NASA CONTRACTOR REPORT 187624

INDENTATION-FLEXURE AND LOW-VELOCITY IMPACT DAMAGE IN GRAPHITE/EPOXY LAMINATES

Young S. Kwon and Bhavani V. Sankar

UNIVERSITY OF FLORIDA
Gainesville, Florida

Grant NAG1-826
March 1992

National Aeronautics and Space Administration

LANGLEY RESEARCH CENTER
Hampton, Virginia 23665-5225

TABLE OF CONTENTS

LIST OF TABLES

LIST OF FIGURES

CHAPTER 1
INTRODUCTION

Recent advances in fabrication of high strength fiber materials, novel fabrication techniques, and reduced cost have made it possible to use fiber reinforced composites in a wide variety of mechanical equipment and consumer products beyond aerospace structures (McConnell, 1991). There are many applications where fiber composites are used as a laminated structure. Composite laminates are very susceptible to impact damage during handling or service. Often the impact damage is in the form of matrix cracks and delaminations which are hard to detect. Research is being conducted in our Center for Advanced Composites and elsewhere to develop an analytical methodology to predict impact damage given the description of the impactor and the target.

In the present study we focus our attention on a class of impact problems where the impact mass is very large (1-15 kg) and the impact velocity is very low (0-3 m/s). Such impacts are typical of handling damage and dropping of objects on composite structures. Previous analytical studies (e.g., Sankar et al., 1990) have shown that for large mass, low-velocity impact, the impact duration is several orders of magnitude higher than the time for the flexural waves to travel to the boundaries of the target, and hence the impact event can be considered as quasi-static. Hence a series of static indentation-flexure tests were performed in the present study using different types of laminates made of graphite/epoxy composite. The load-deflection

relations were recorded. The damage was assessed by ultrasonic C-scanning and also using photo-micrography. The static flexural response and damage were explained by a simple semi-empirical model. Impact tests were performed, and the damage was quantified using similar techniques. The relation between static and dynamic responses was examined.

The descriptions of the material and fabrication procedures are given in Chapter 2. The static test procedure and discussion of results form Chapter 3. Impact tests and results are described in Chapter 4. A comprehensive summary and conclusions are provided in Chapter 5. Complete experimental data and some derivations of formulas used in the semi-empirical models are given in a series of appendices.

CHAPTER 2
SPECIMEN PREPARATION

Fabrication

The graphite/epoxy composite was the sole material used in this research and was fabricated from 305 mm (12 inches) wide Hercules AS4/3501-6 prepreg tapes. Three types of laminates were fabricated: Type A is $\pi/8$ quasi-isotropic laminate $[0,22.5,45,67.5,90,-67.5,-45,-22.5]_{2s}$; Type B is cross-ply laminate $[0,90]_{8s}$; and Type C is $\pi/4$ quasi-isotropic laminate $[0,45,90,-45]_{4s}$.

The prepreg tape was cut into 305 mm squares at various orientations to the fiber direction and stacked according to the stacking sequences to obtain laminate types A, B, and C. The appropriate amount of bleeder and separator materials were prepared. Fiberglass cloth and the porous Teflon film were used as bleeder and separator material respectively. The layup was placed in a vacuum bag (shown in Figure 2.1) with materials required for curing. The schematic diagram for the vacuum bag preparation is shown in Figure 2.2.

The curing was performed by following the cycle recommended by Hercules in an autoclave (Baron-Blakeslee model Bac-24). The autoclave was pressurized to 586 Kpa (85 psi),

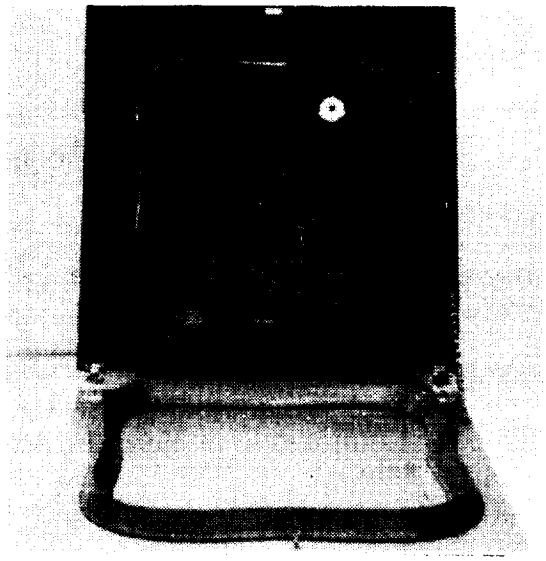

Figure 2.1 Re-usable vacuum bag

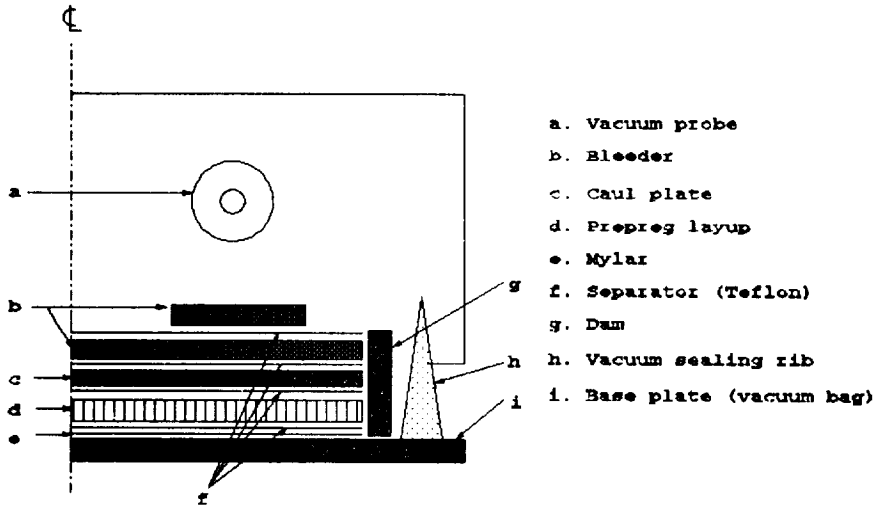

Figure 2.2 Vacuum bag layup for curing

and a vacuum of 635 mm (25 inches) Hg was applied to the vacuum bag at the beginning of the curing process as shown in Figure 2.3. The temperature was raised at the rate of 1.67-2.78°C (3-5°F) per minute until it reached 116°C (240°F) and held for an hour. Then the autoclave pressure was increased to 690 Kpa (100 psi); the vacuum was released; and the temperature was further raised at the same rate to 177°C (350°F) and held for two hours. Then the heat was turned off and the autoclave pressure was released after the temperature went down to 93.3°C (200°F). The cured plate was kept in the autoclave until it had cooled to room temperature.

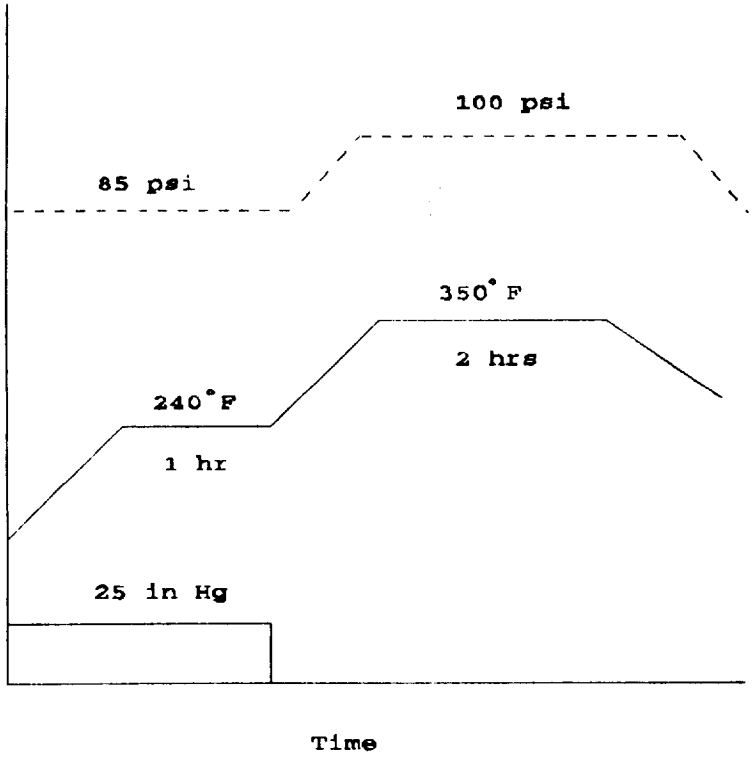

Figure 2.3 Curing cycle for Hercules carbon prepreg tape AS4/3501-6

Material Properties

The properties of the composite material were provided by the prepreg manufacturer. Tensile tests were performed to verify the quality of fabrication.

The specimen preparation and tensile tests were performed according to ASTM standard D3039-76 (ASTM, 1987). The specimen is straight-sided, of constant cross-section, and has adhesively bonded, beveled tabs for gripping. The lamina 0° test specimen is 12.7 mm (0.5 inches) in width and six plies in thickness, while the lamina 90° test specimen is 25.4 mm (1 inches) in width and eight plies in thickness. The overall length of the specimen is 228.7 mm (9 inches), and the test section is 152.4 mm (6 inches). The test specimen geometry is shown in Figure 2.4.

The wedge-section friction grips were utilized for the tensile loading on MTS material tester. The specimen was loaded monotonically to failure at a rate of 2 mm/min. Electrical resistance strain gages were mounted on the specimen to determine the specimen strains in fiber and transverse directions. The strain gages were monitored by digital oscilloscope, Nicolet 4094. Stress-strain curves were plotted to obtain the Young's moduli and Poisson's ratios.

Five tensile tests were conducted for 0° and 90° test specimens. The results are presented in Table 2.1.

The 0° tensile modulus at room temperature provided by the manufacturer is 148 Gpa. Thus the quality of the composite fabricated for this research is proven to be fairly adequate.

Table 2.1 Elastic constants from tensile tests

Specimen No.	0°test specimen		90°test specimen	
	E_1(Gpa)	ν_{12}	E_2(Gpa)	ν_{21}
1	167	0.34	18.9	0.030
2	161	0.29	17.0	0.020
3	142	0.31	18.4	0.036
4	148	0.36	17.3	0.024
5	153	0.29	18.5	0.031
Average	154	0.32	18.0	0.028

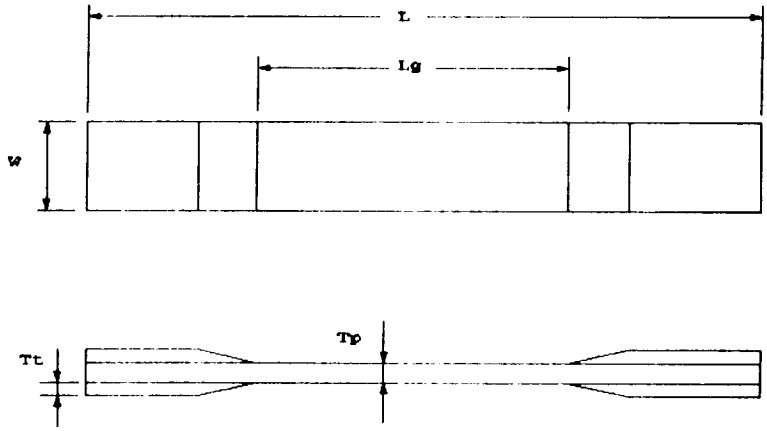

Dimension (in mm)

	W	L	Lg	Tt	Tp
0° specimen	12.7	228.7	152.4	2.0	0.75
90° specimen	25.4	228.7	152.4	2.0	1.0

Figure 2.4 Geometry of tensile test specimen

CHAPTER 3
STATIC INDENTATION TESTS

Overview

This chapter describes static indentation tests performed on graphite/epoxy laminates in order to gain a better understanding of damage initiation and progression in plates of different sizes and laminate configurations due to indentation by different diameter indenters. It is expected that a thorough understanding of the damage due to static indentation will shed light on damage mechanisms during impacts due to large masses at low velocities.

As mentioned in Chapter 2, three types of laminate configurations were used: Type A is $\pi/8$ quasi-isotropic laminate $[0,22.5,45,67.5,90,-67.5,-45,-22.5]_{2s}$; Type B is cross-ply laminate $[0,90]_{8s}$; and Type C is $\pi/4$ quasi-isotropic laminate $[0,45,90,-45]_{4s}$. Square specimens were cut from cured laminates. The sides of the specimens were about an inch longer than the diameter of the support rings used in the indentation tests. Thus the specimens can be considered as simply supported circular plates. The support ring diameters were 50.8 mm, 76.2 mm, and 101.6 mm. The two steel indenters had hemispherical nose of diameters 6.35 mm and 25.4 mm respectively.

The indentation test setup consisted of a loading apparatus, recording devices and data processing devices as given below:

- MTS Material Tester

- Digital Oscilloscope (Nicolet 4094 & XF-44 Recorder)

- LVDT (Schaevitz model 500 MHR)

- Analog Transducer Amplifier (Schaevitz model ATA-101)

- Specimen Support Fixture (see Appendix A)

- Computing Facilities (VAX mainframe and microcomputers)

The tests were conducted under stroke control at the rate of 0.02 mm/s. The load and plate center deflection data were acquired at the rate of 5 samples/second and were recorded by the Nicolet XF-44 recorder. The data were transferred to a microcomputer from the oscilloscope and were processed by software available in the mainframe and in the microcomputer.

After indentation tests the specimens were C-scanned at a facility at NASA Langley Research Center. Some of the specimens were sectioned and polished for the purpose of photo-micrographic studies. The damage was also assessed by cutting small beam specimens out of the damaged area and testing them under three-point flexure.

Results and Discussions

The load-deflection diagrams of all the tests are presented in Appendix B. Some plots are presented in Figures 3.1 through 3.9 for the purpose of discussion. The general observations about the indentation damage and effects of layup, plate diameter, and indenter diameter are discussed in the following section.

Some General Observations on the Load-Deflection Diagrams

There are some common features in the load-deflection diagrams for the three different types of laminates A, B, and C. Referring to Figure 3.1, the initial portion of the loading curve OA shows some nonlinearity, which can be attributed to local indentation at small loads. As the load is increased, the plate deflection becomes much higher than the amount of indentation, and the load-deflection curve is almost linear (AB in Figure 3.1). One could hear intermittent crackling noise, typical of matrix cracking, but no apparent stiffness loss was observed during this stage. When the load reached a critical value, denoted by D in Figure 3.1, there was a sudden load drop. The noise level and the amount of load drop associated with

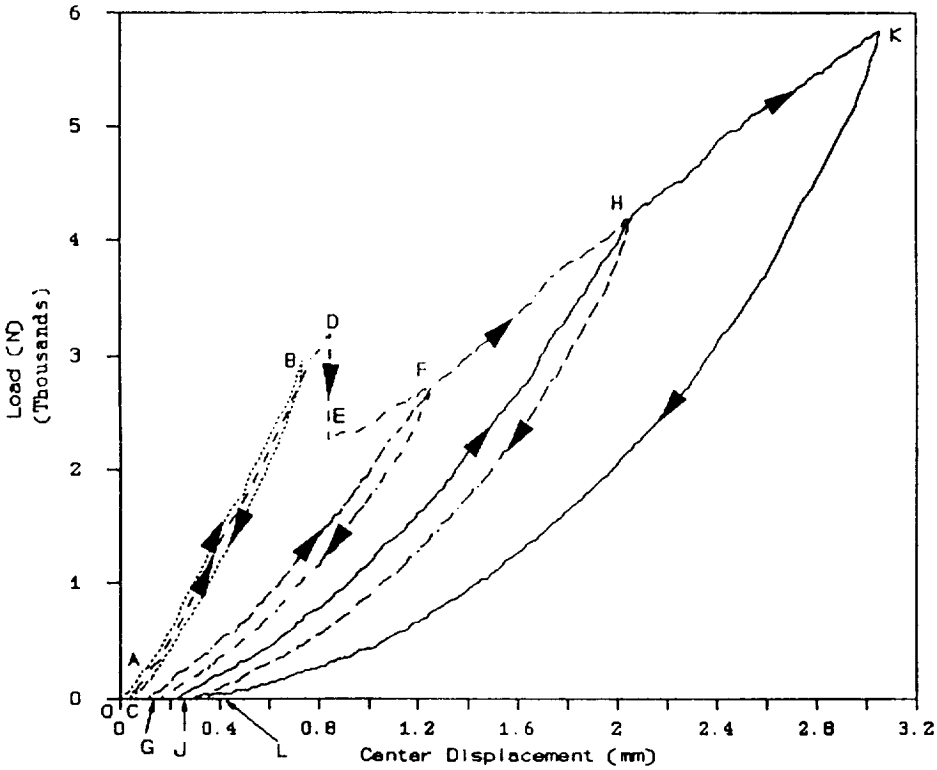

Figure 3.1 Typical load-deflection curve for graphite/epoxy laminates

failure (see Figures 3.6-3.9 for comparison) were highest for the cross-ply laminates (Type B), lowest in the $\pi/8$ quasi-isotropic laminates (Type A), and in-between in the $\pi/4$ quasi-isotropic laminates (Type C). It is suspected that the load drop is caused by initiation and unstable propagation of delaminations.

After the first observable failure, there is a significant loss of plate stiffness denoted by the reduced slope of the subsequent unloading and reloading curves, e.g., FG and GF, HJ and JH, etc in Figure 3.1. As will be seen later, the delaminations grow in a stable manner as the load is increased. The loading curve EFHK represents yielding of the plate and hence will be called the yield curve. The yield curve is almost a straight line until the central deflection is about 3 mm (note that the average plate thickness is 3.8 mm). Thereafter there is a sudden increase in the slope of the yield curve (e.g., Figures 3.6-3.9). The slopes of the unloading curves at this stage are sometimes greater than the stiffness of the undamaged plate and were highly nonlinear also. The nonlinearities can be attributed to (a) large deflection of the plate; (b) membrane action in the delaminated plies; and (c) friction between various contacting surfaces, e.g., between the indenter and the plate, between delaminations, and between the plate and the support.

Some specimens were unloaded even before the first observable failure (BC in Figure 3.1), and there were some energy losses indicated by the hysteresis loop (area OBC). This energy loss can be attributed mainly to material damage, and to some extent to friction at contact areas. When unloaded at higher loads, the unloading and reloading curves were highly nonlinear (e.g., FG and GF, HJ and JH).

The area between the corresponding unloading and reloading curves, e.g., FG and GF, is the measure of frictional energy dissipation. The area between an unloading curve and the next reloading curve, e.g., FG and JH, is an example of energy dissipation due to material damage, mostly delaminations.

Figures 3.2 through 3.5 are for a single specimen that underwent multiple loading, unloading, and reloading. For example, Figure 3.3 represents the behavior of a specimen previously damaged by the loading cycle shown in Figure 3.2. In fact, Figure 3.1 is the superposition of all the load-deflection curves shown in Figures 3.2-3.5.

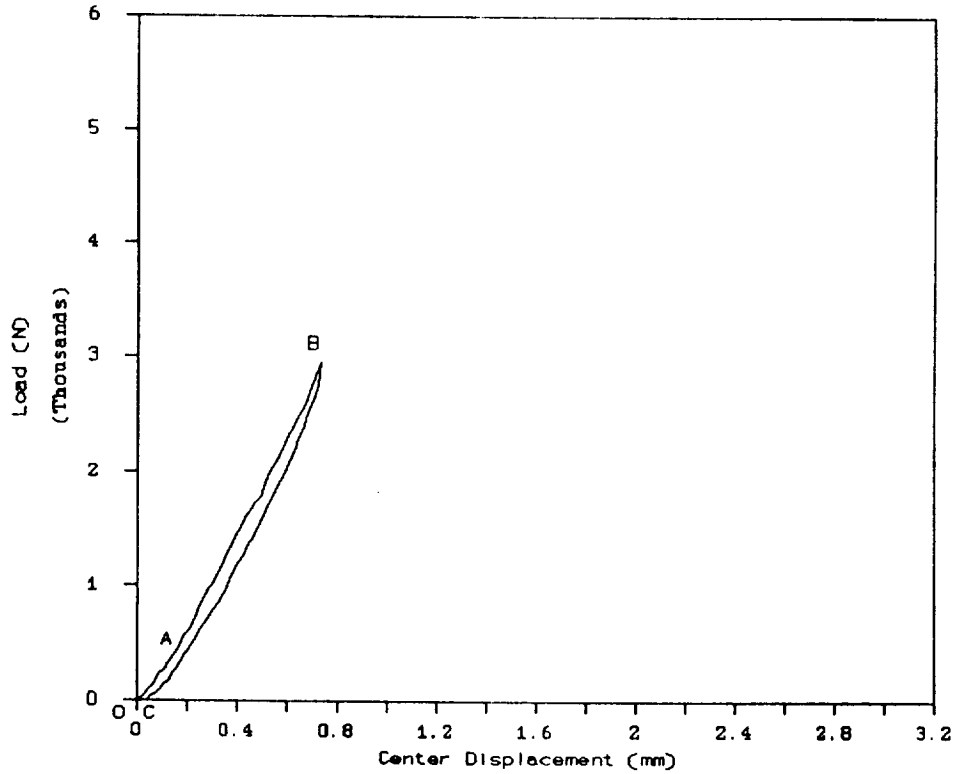

Figure 3.2 Initial part of multiple reloading test

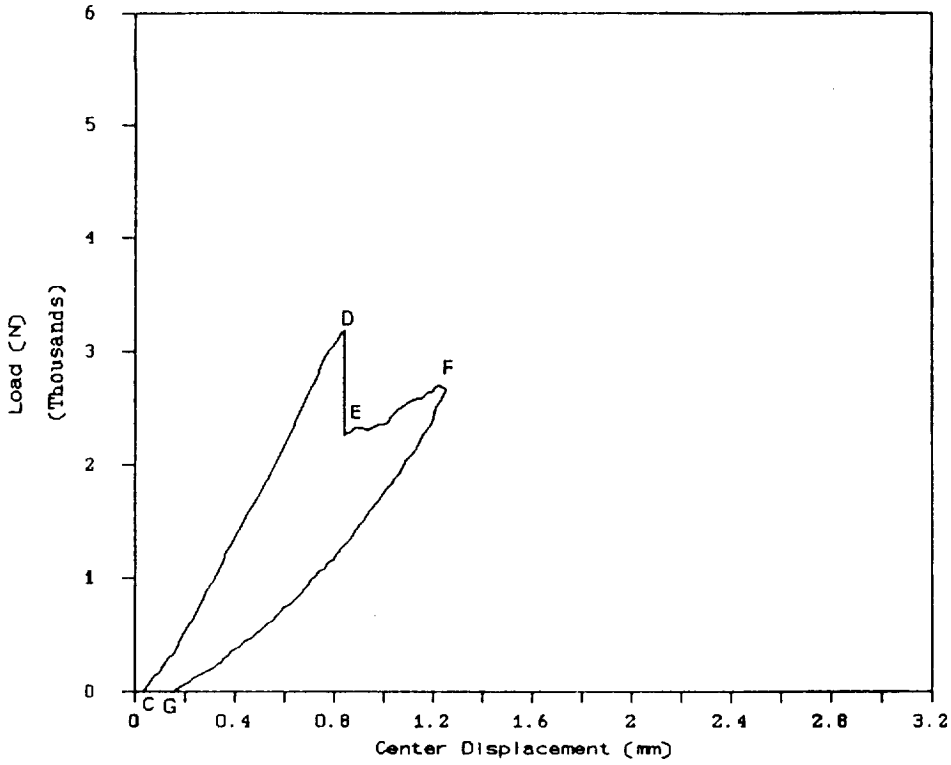

Figure 3.3 The second part of multiple reloading test

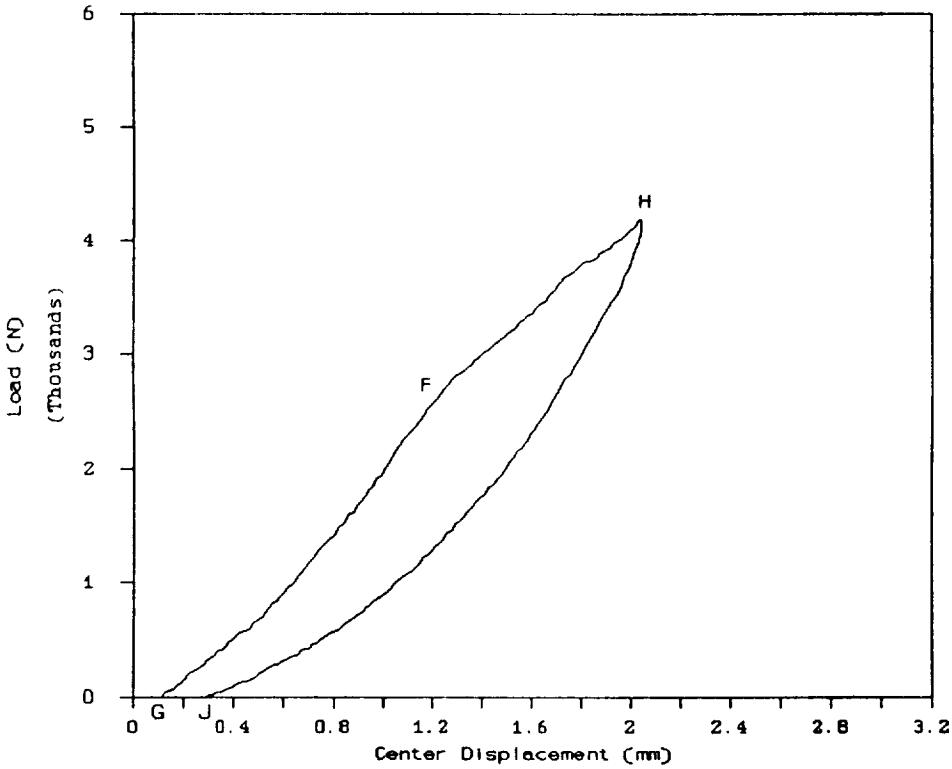

Figure 3.4 The third part of multiple reloading test

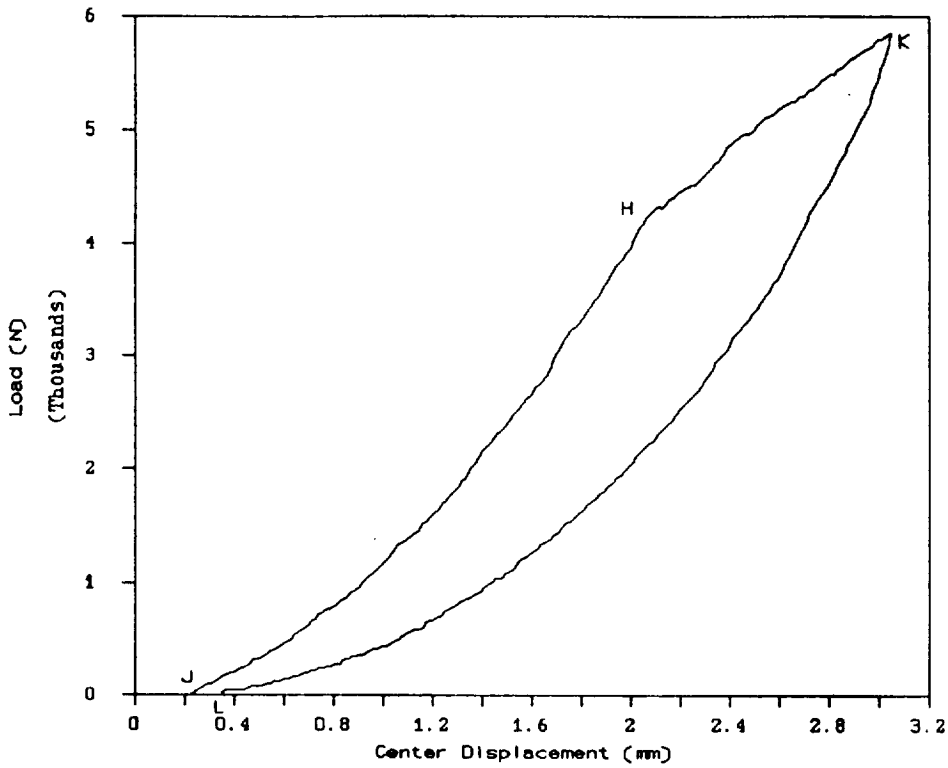

Figure 3.5 The fourth part of multiple reloading test

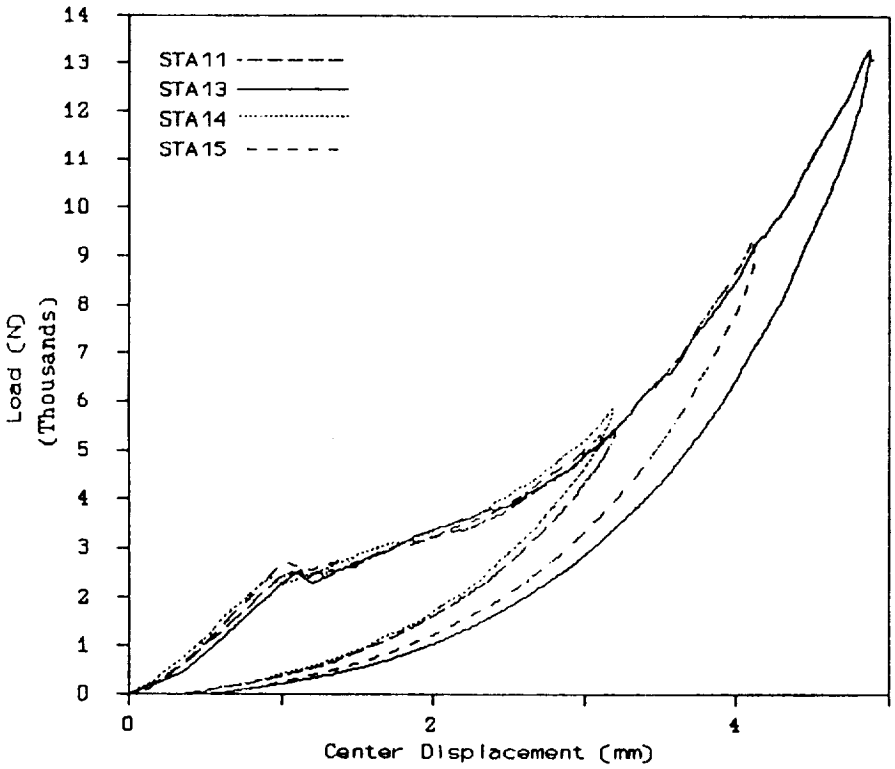

Figure 3.6 Static indentation test for laminate type A:indenter-25.4 mm dia.; support-50.8 mm dia.

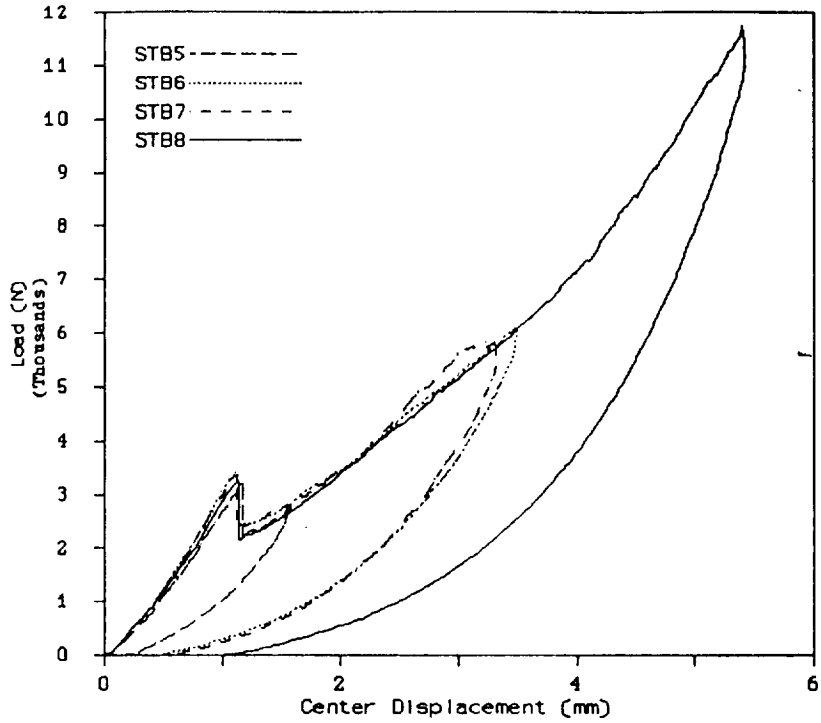

Figure 3.7 Static indentaion test for laminate type B:indenter-25.4 mm dia.; support-50.8 mm dia.

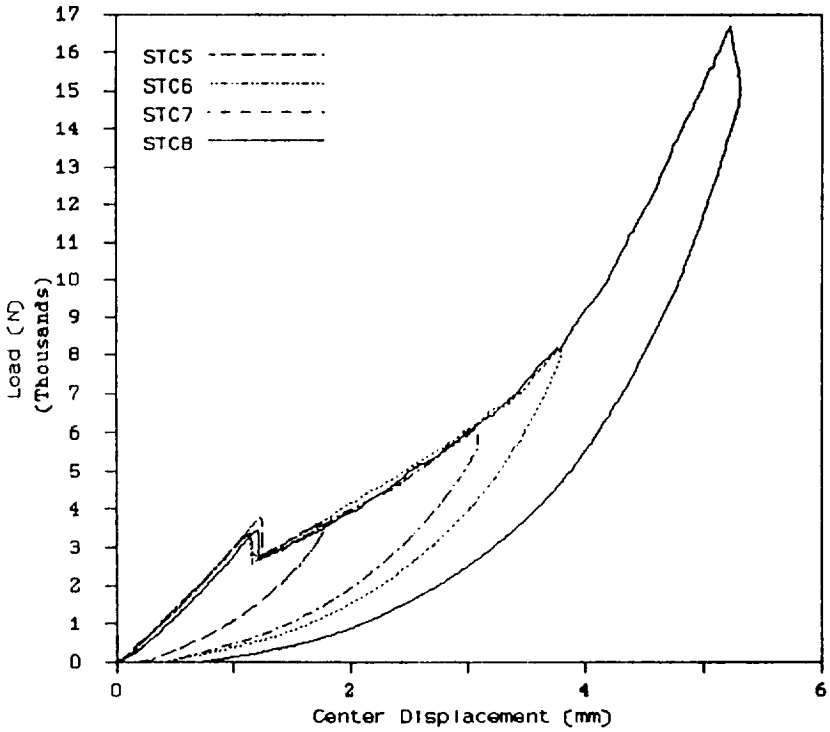

Figure 3.8 Static indentation test for laminate type C:indenter-25.4 mm dia.; support-50.8 mm dia.

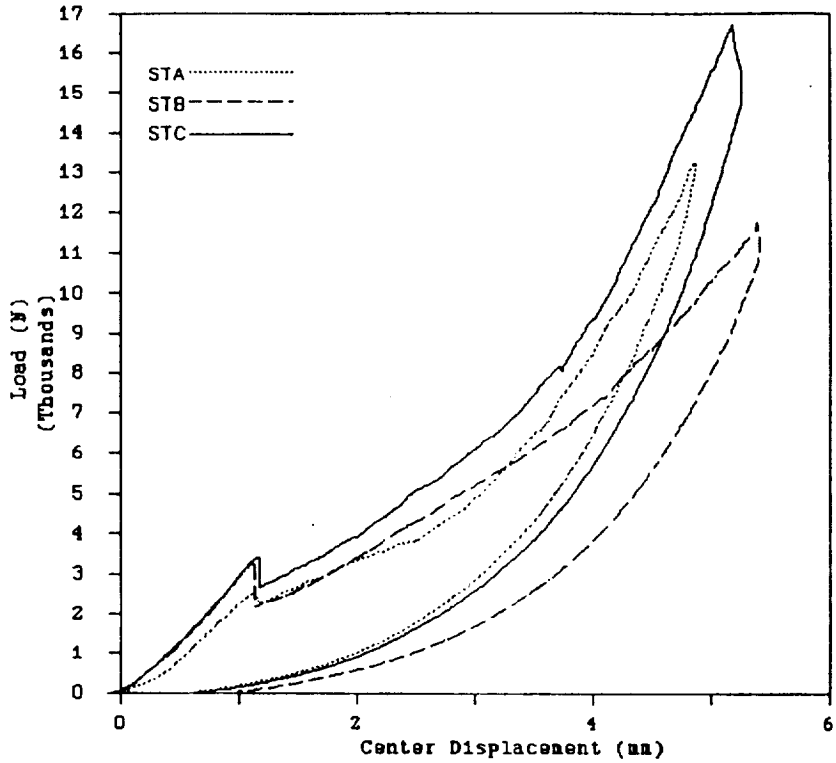

Figure 3.9 Static indentation test for laminate types A, B and C:indenter-25.4 mm dia.; support-50.8 mm dia.

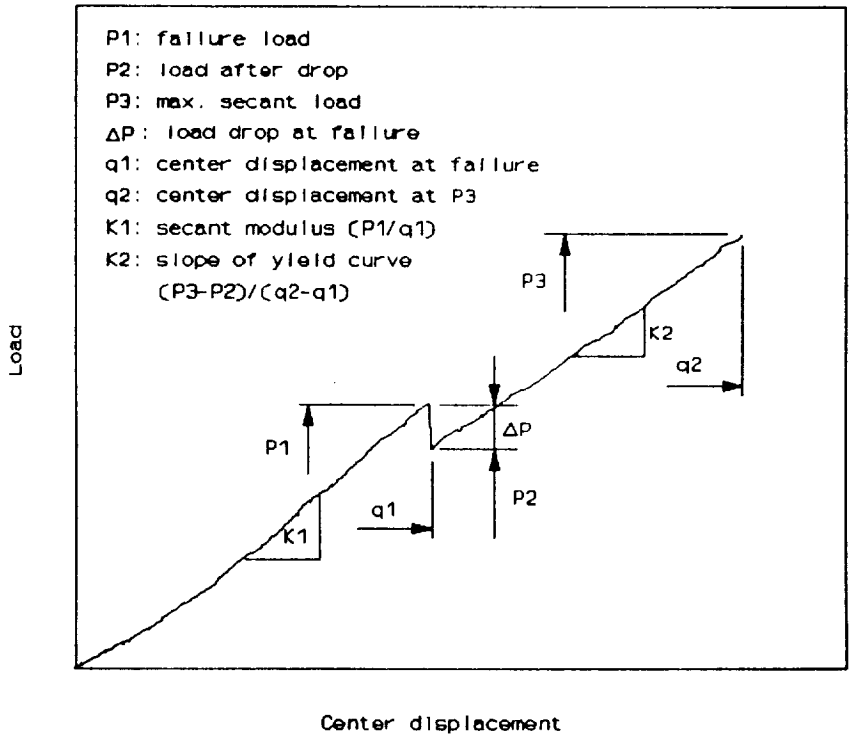

Figure 3.10 Sketch of load-displacement (P-q) relation

There were no significant visible damages either on the front surface or back surface even when the loads were as high as 10,000 N. The indenter always left a small dent at the point of contact.

A sketch of a typical load-deflection curve is shown in Figure 3.10 (see Appendix C for the data). The sketch will be used for the purpose of discussion of results in the following sections.

Loading up to Initial Observable Failure

A sample load-deflection diagram for the behavior before the first observable load drop is shown in Figure 3.2. Except for the initial nonlinear contact behavior, the loading curve can be considered almost linear. The area between the loading and unloading curves in this figure represents energy dissipation due to formation of microcracks and some frictional effects. Figure 3.11 depicts the failure load P_1 for the initial observable damage for different types of laminates, different diameter support rings, and the two indenters (see Figure 3.10 for definition of P_1). For each combination of test parameters three repeat tests were performed. For all cases shown, the failure load due to 25.4 mm diameter indenter was about 30% higher than that for 6.35 mm diameter indenter. The only explanation seems to be that for a given load the contact radius is proportional to the cube root of the indenter radius (Sankar, 1985), and hence the contact pressure is reduced. This may have an effect on the load at which matrix cracks initiate a delamination in the plate.

In all cases shown in Figure 3.11, Type A ($\pi/8$) laminates failed at significantly lower loads compared to the B and C Types. The Type C laminates

($\pi/4$) performed better than the cross-ply laminates (Type B) under the 50.8 mm ring support, but failed at slightly lower loads under 76.2 and 101.6 mm supports.

It seems that the interlaminar shear stresses in conjunction with the flexural stresses are responsible for initiation of delaminations. The interlaminar shear stress distribution (τ_{rz}) is parabolic away from the contact region but skewed very near the contact region (Sankar, 1989). If there were only shear stresses, the matrix material will be subjected to tensile stresses (principal stresses) in the 45° planes, which are responsible for the matrix cracks (see Mohr's circle in Figure 3.12). The effect of flexure is to add a compressive normal stress (σ_{rr}) above the mid-plane and tensile normal stress below the mid-plane of the laminate. The compressive stresses will reduce the magnitude of the principal stresses and hence delay the onset of transverse cracks. The larger the support ring diameter, the larger are the flexural stresses. This could explain the increase in failure loads for Type A and Type B laminates with increase in the support ring diameter. The failure loads for $\pi/4$ laminates were slightly reduced with the increase in the support ring diameter. This suggests that there is a need for a detailed stress analysis of laminates under indentation-flexure in order to understand the initiation of microcracks and delaminations.

The center deflections at the instant of failure are presented in Figure 3.13. It should be mentioned that the center deflection is the displacement of the indenter, which includes both the plate deflection and local indentation.

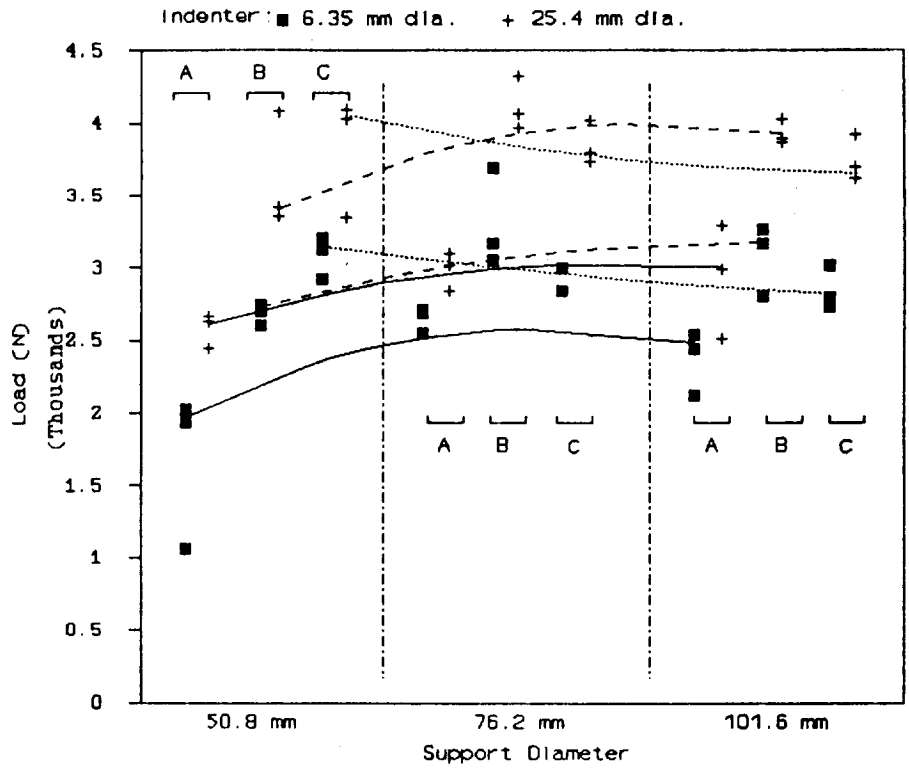

Figure 3.11 Failure load(P_1) for laminate types A, B and C

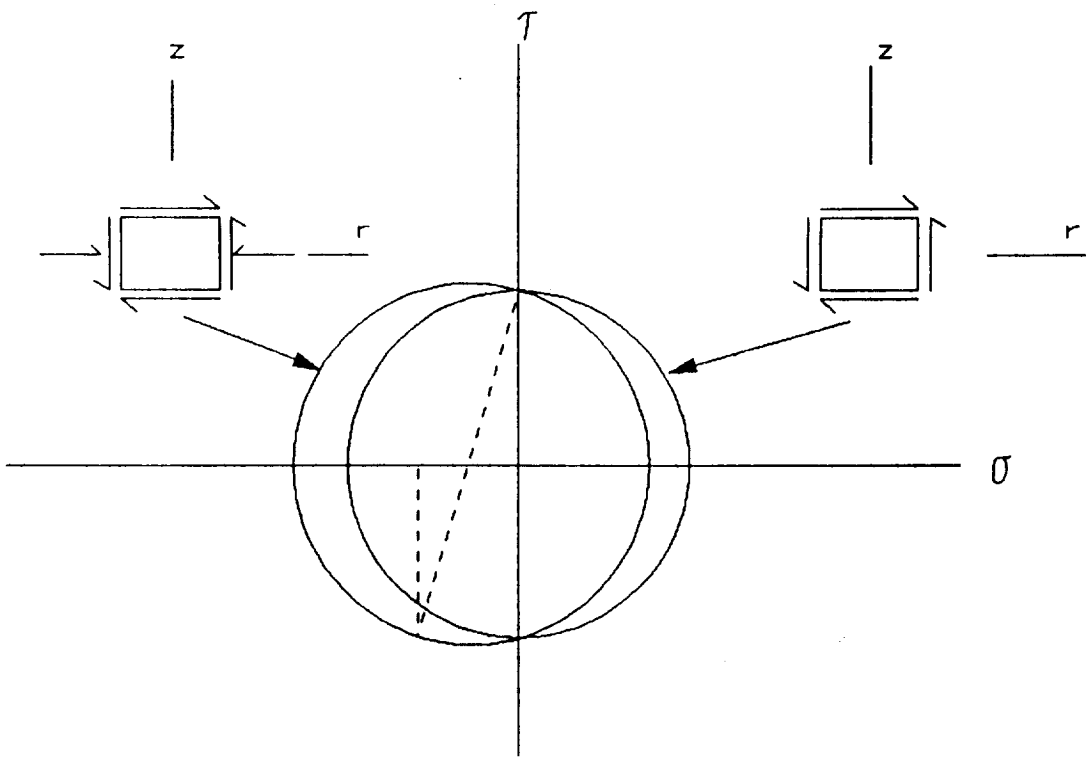

Figure 3.12 Mohr's circle with the effect of flexure

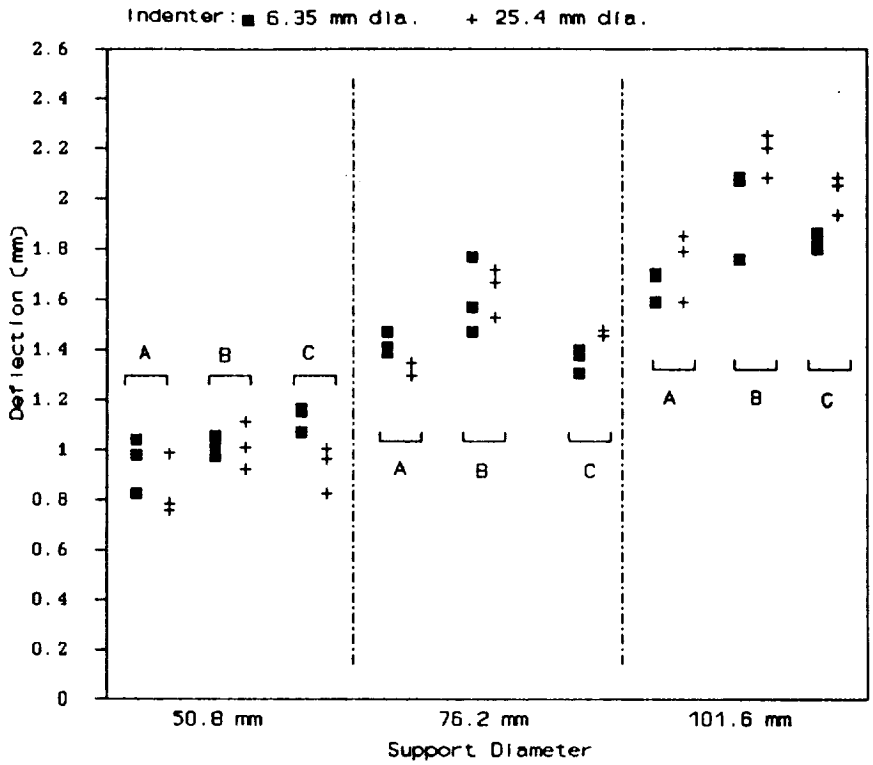

Figure 3.13 Center deflection (q_1) at failure

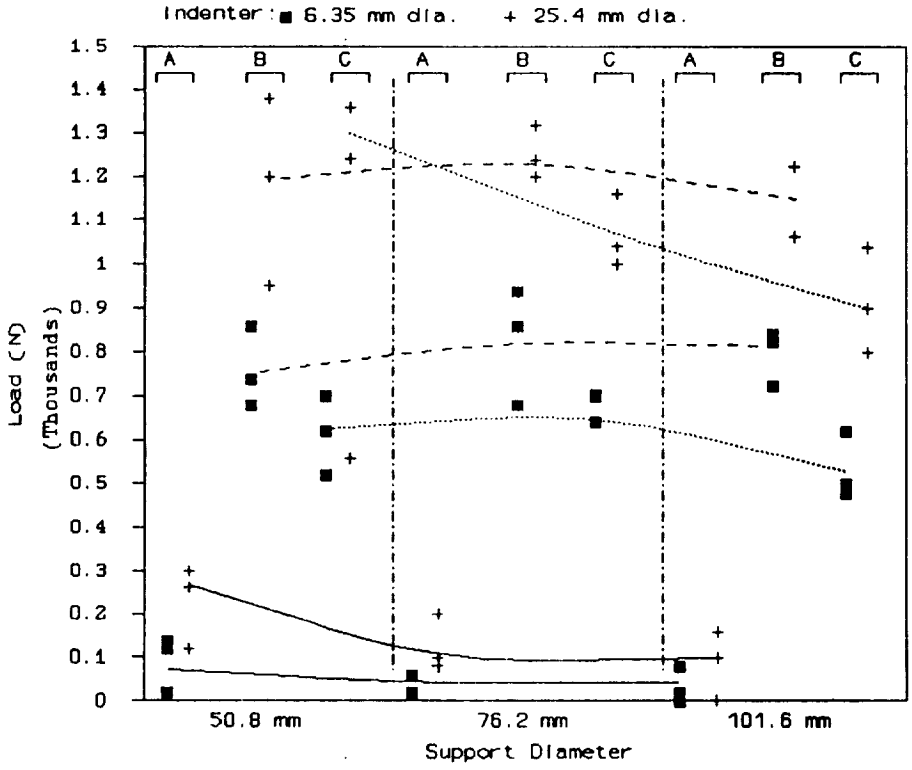

Figure 3.14 Load drop (ΔP) at failure

It is interesting to see that for a given support ring size, the center deflection at failure does not depend on the indenter diameter very much.

After the unstable failure, there is a significant load drop in the displacement controlled tests. The load drop for different sets of test parameters are shown in Figure 3.14. In general the load drop is higher, if the failure load is higher. The $\pi/8$ laminates do not show much load drop, which indicates that the failure is not sudden, but similar to yielding of ductile materials. The load drop in the case of cross-ply laminates is in general higher than for the $\pi/4$ quasi-isotropic laminates.

The flexural stiffness of the undamaged laminates (k_1) under different test conditions is shown in Figure 3.15. It is interesting to note that the stiffness is apparently greater under the 25.4 mm indenter than the 6.35 mm indenter. The bigger indenter causes larger contact area and lesser indentation. Since indentation is also included in the deflection, the apparent stiffness of the plate is higher for larger diameter indenter. In fact the effect of indenter size diminishes for larger plate diameters. Type C laminates have the highest flexural stiffness, and Type A have the lowest.

As the loading continues, the delaminations caused by the initial failure continue to grow in a stable manner. Before we discuss the unloading and reloading tests, it will be instructive to look at the ultrasonic C-scan results.

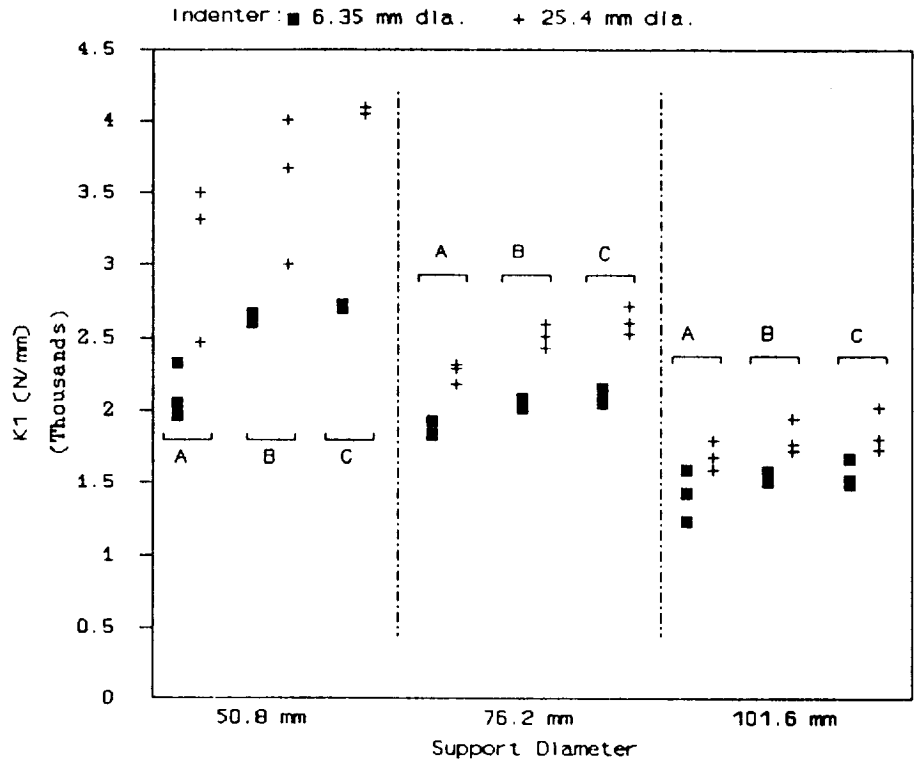

Figure 3.15 Secant modulus (K_1) before failure

Ultrasonic C-Scan Results

The damaged specimens were C-scanned to map the area of delamination. The damage pattern was almost circular in all cases. This may be due to the quasi-isotropic nature of the laminates and the circular support used in the tests. In Figure 3.18 the delamination radii are plotted against the maximum contact force applied during the test for $\pi/4$ laminates (Type C). In the case of Type C laminates the delamination radius was directly proportional to the maximum load irrespective of the indenter size or the plate size. A linear relation between the delamination radius and the maximum load was obtained using least square curve fitting. There were some scatter in the data for the Type A and Type B laminates as seen in Figures 3.16

and 3.17. However it was decided to use a linear fit for all the results. The delamination radius b can be expressed as $b=BP_{max}$, where B is the constant of proportionality. The constant B in mm/N units for the $\pi/8$, cross-ply and $\pi/4$ laminates respectively were found as 0.005295, 0.004334, and 0.003863. Thus one can see that $\pi/4$ laminates have better delamination resistance than cross-ply laminates, and cross-ply laminates are better than $\pi/8$ laminates.

The data for delamination areas are presented in Appendix D. Sample C-scan outputs are shown in Figure 3.19.

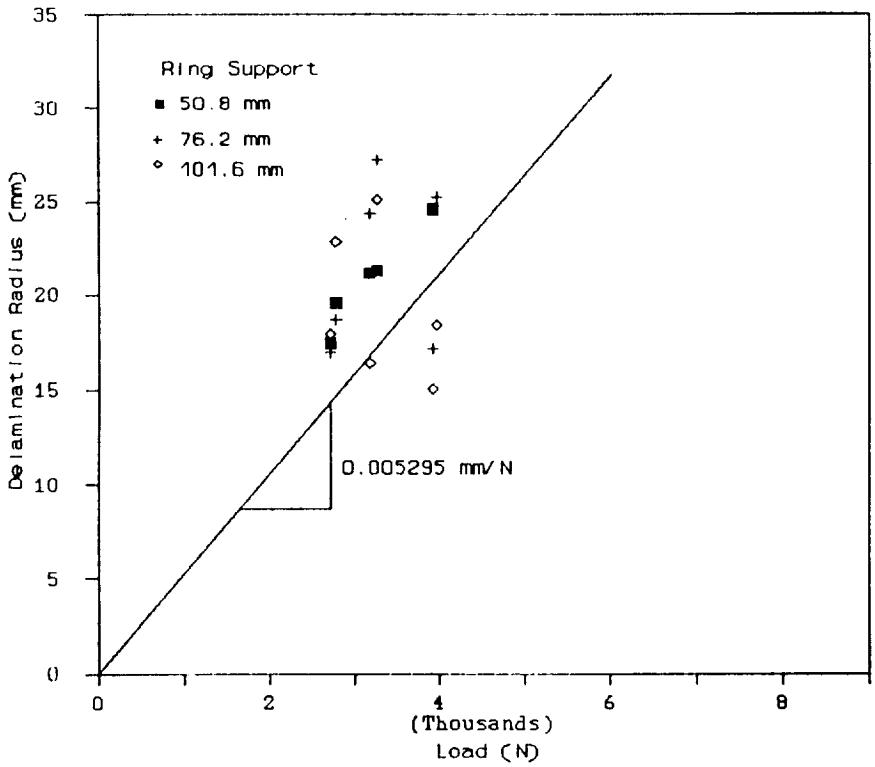

Figure 3.16 Delamination radius vs. maximum static load for laminate type A

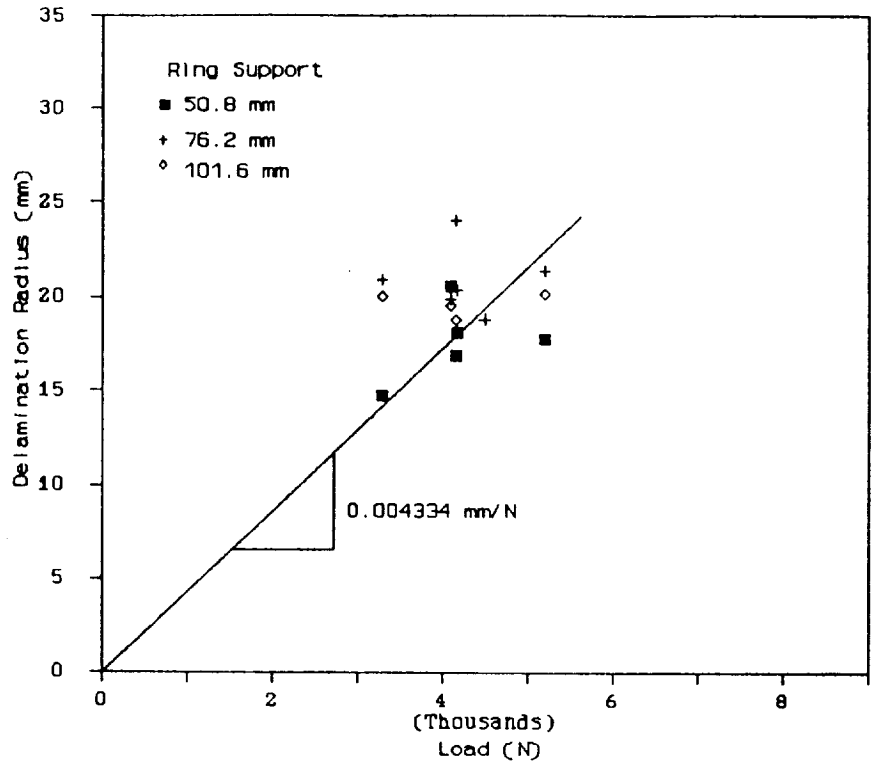

Figure 3.17 Delamination radius vs. maximum static load for laminate type B

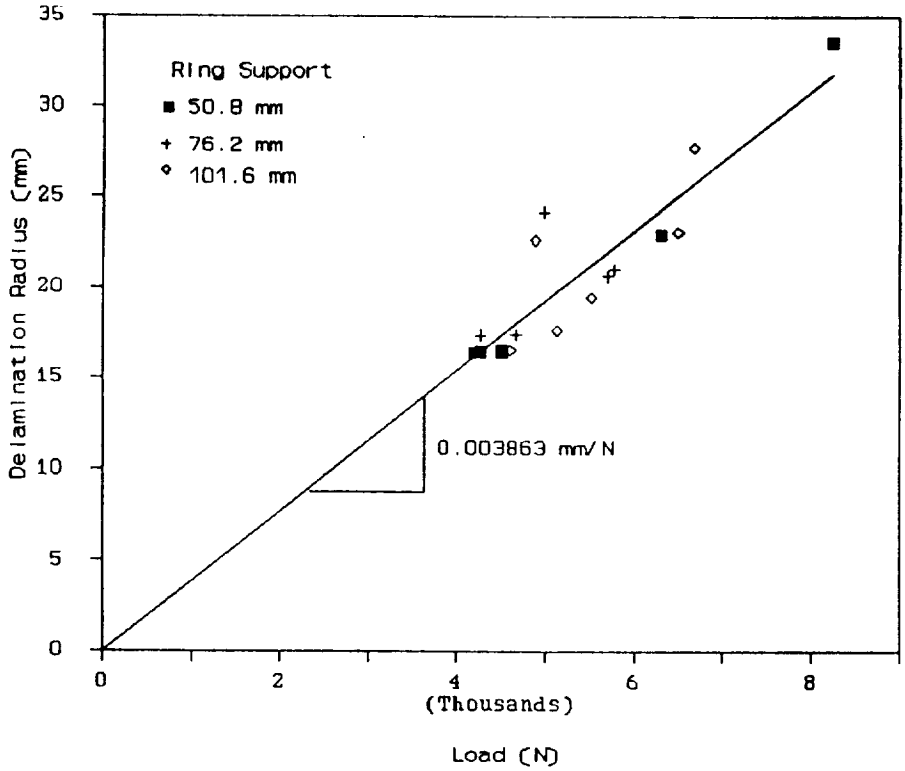

Figure 3.18 Delamination radius vs. maximum static load for laminate type C

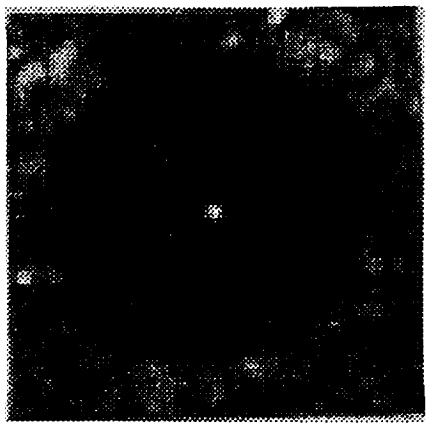

(a)

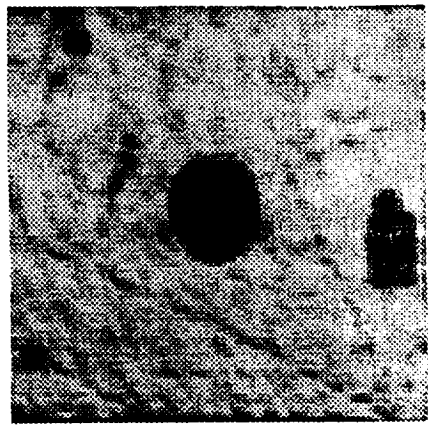

(b)

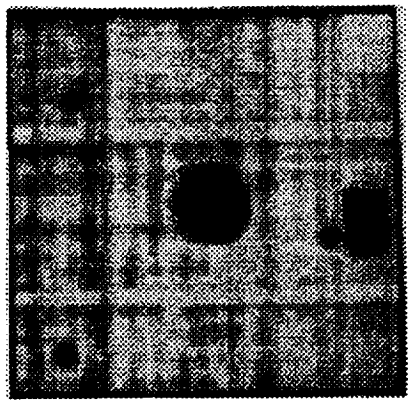

(c)

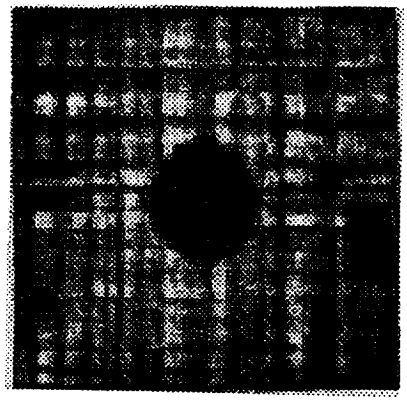

(d)

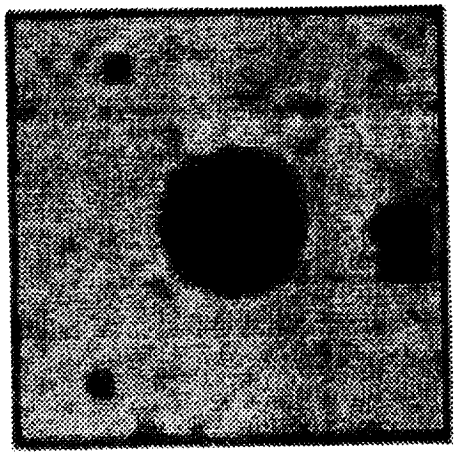

(e)

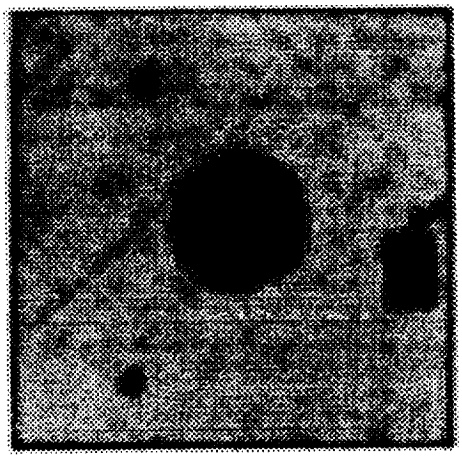

(f)

Figure 3.19 Samples of ultrasonic C-scan results: (a)STA11 (b)STA24 (c)STB18 (d)STB20 (e)STC20 (f)STC22

Loading, Unloading, and Reloading Curves

The discussion in this section pertains to loading after the initial observable load drop. As the loading continues, the delamination also grows in a stable manner. The loading curve (yield curve) is almost a straight line. In fact a simple plate fracture mechanics analysis described in the section **Analytical Models** shows that the yield curve has to be a straight line. The unloading curves are highly nonlinear (see Figure 3.1). The stiffness is higher at the instant of unloading and gradually decreases as the load is reduced. When reloaded the load-deflection is again nonlinear with stiffness increasing as the load is increased. The nonlinear load-deflection behavior is largely due to the membrane action of the delaminated plies (Bostaph and Elber, 1982, and Elber, 1983). The area formed by the unloading and reloading curves represents the energy dissipated by friction between contacting surfaces.

Fractographic Studies

The plates damaged by indentation-flexure tests were sectioned along a diametrical plane, polished, and observed in an optical microscope. Three specimens, one for each laminate type, were selected. In each specimen the loading was stopped immediately after the first observable load drop. A fourth specimen was Type C laminate in which loading was stopped just before the anticipated sudden failure. The schematic diagrams of delaminations are shown in Figures 3.20a-3.20d. As seen from Figure 3.20d, there are delaminations even before the sudden load

drop occurs. That substantiates the conclusion that the crackling noise heard during loading was due to both matrix cracking and initiation of small delaminations. The load drop and the associated *bang* are due to connecting of various delaminations and unstable delamination propagation. It should be mentioned that the delamination patterns were not strictly axisymmetric. We were able to observe the spiralling stair-case type damage pattern as reported by Dost and others (1988). There were no delaminations in the top portion of the laminates. The envelope of delamination fronts in all the layers resembled a conical tent. A simple plate model is presented in the section **Analytical Models** to support this observation. Some selected photo-micrographs are presented in Figures 3.21 and 3.22. These pictures show typical matrix cracks and accompanying delaminations.

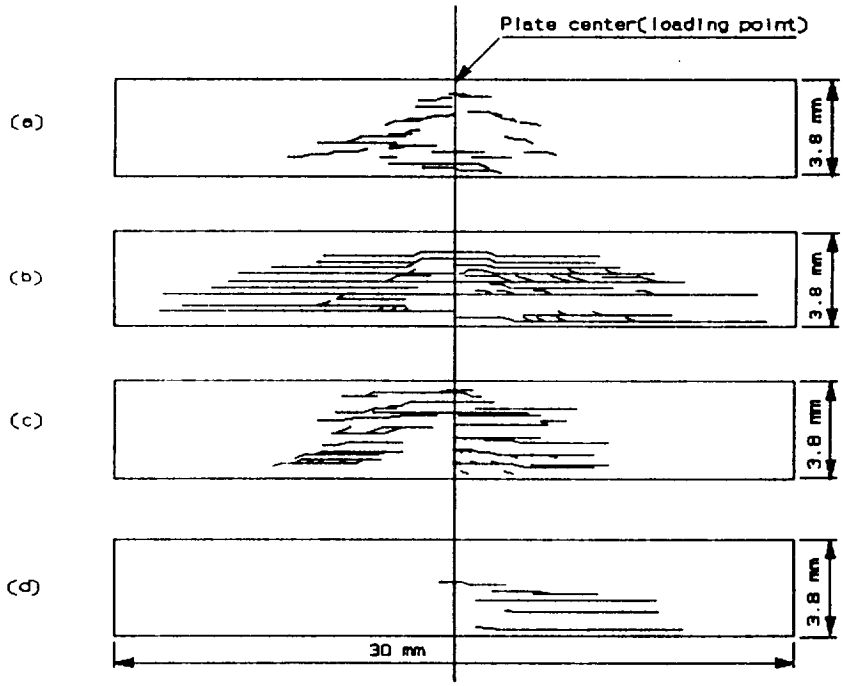

Figure 3.20 Schematics of delaminations and matrix cracks:(a)laminate A; (b)laminate B; (c)laminate C; and (d)laminate C. Cases(a-c): after initial load drop; Case(d): before load drop

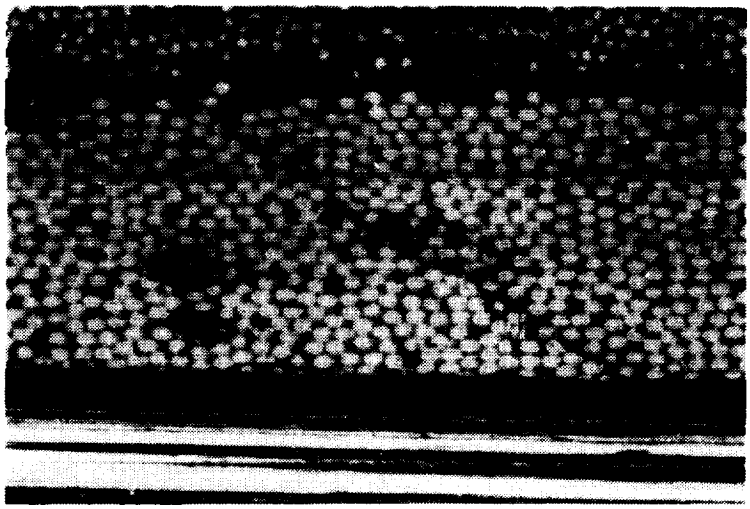

Figure 3.21 Typical view of matrix crack initiation from a void during loading(400x)

Figure 3.22 Matrix cracks and delamination formed immediately after failure(100x)

Stiffness Loss Due to Indentation Damage

One of the plates subjected to indentation was sectioned into several beams, and the flexural rigidities of the damaged beams were measured using three-point bending tests. The specimen considered was a cross-ply laminate (Specimen Number STB10). The support ring diameter was 50.8 mm, and the indenter diameter was 25.4 mm. The loading-unloading diagram for this laminate is given in Appendix B. The damaged plate was sectioned into seven beams. The width of each beam was about 10.2 mm, and the span for the three-point bending tests was 50.8 mm as shown in Figure 3.23. The load-deflection diagrams obtained from the three-point bend tests are shown in Figure 3.24. Beam 1 is undamaged and represents the stiffness of the intact plate. Beams 2 and 6 are symmetrical about the center and have the same amount of damage. Beam 4, which was at the center of the laminate, had suffered severe damage in the indentation test as indicated by the reduced stiffness in flexure. The residual stiffness information from such tests will be useful in verifying damage models that may be developed in the future.

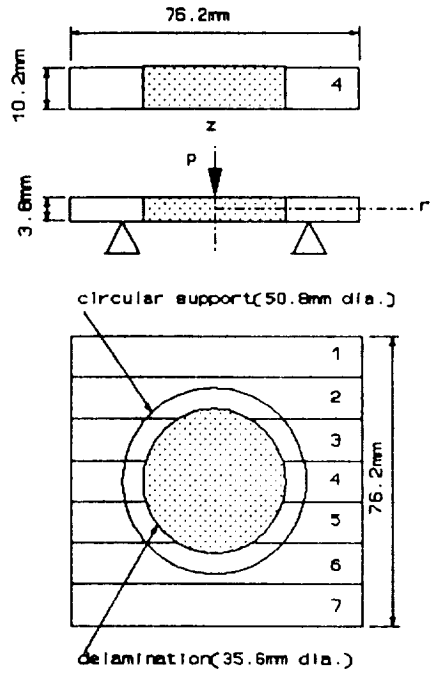

Figure 3.23 Flexural test on damaged specimen (STB10)

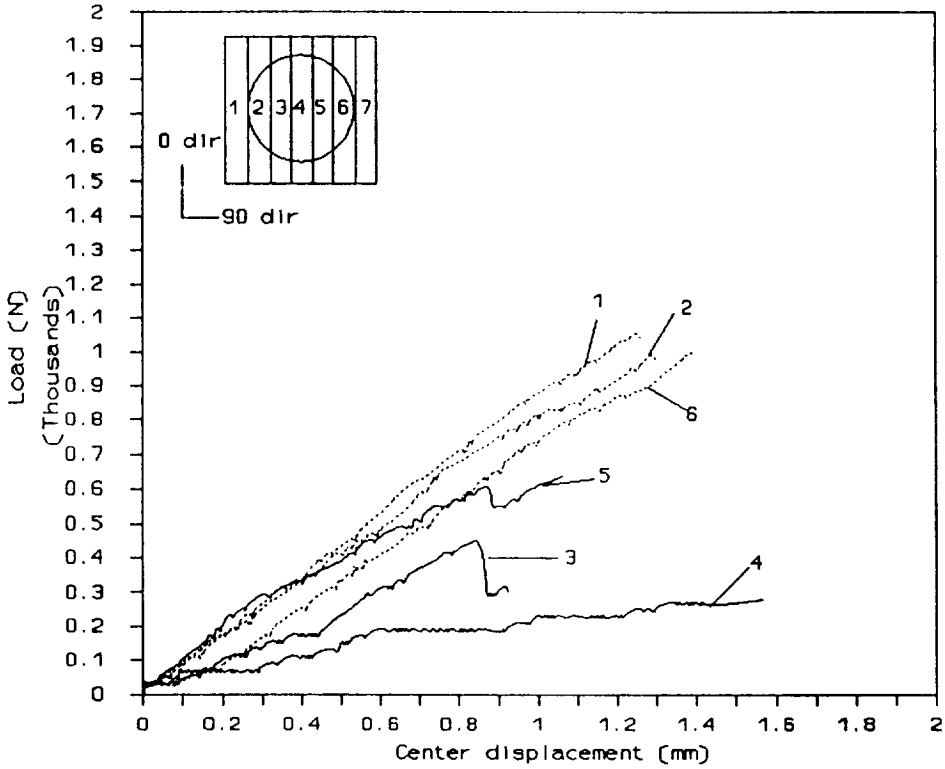

Figure 3.24 Load-displacement curves from the three-point bending tests for the portions of damaged plate (STB10)

Analytical Models

In this section we derive simple analytical models to predict some of the observations made in static tests. The analytical models pertain to the prediction of delamination pattern in static tests, and the shape of the yield curve in static tests. In both models the plate is assumed to be homogeneous and transversely isotropic.

Delamination Pattern in Static Tests

The expressions for the normal and the shear stresses in a simply supported circular plate subjected to a central load are (Timoshenko and Woinowsky-Krieger, 1959):

$$\sigma_{rr}=\frac{12z}{(1-\nu^2)h^3}\left[M_r(1-\frac{\nu^2}{r})+\nu M_t(-1+\frac{1}{r})\right]$$
$$\tau_{rz}=\frac{1.5P}{2\pi rh}\left[\frac{h^2}{4}-z^2\right] \qquad (3.1)$$

where the bending moments, M_r and M_t, are:

$$M_r = \frac{P}{4\pi}(1+\nu)\log\frac{a}{r}$$
$$M_t = \frac{P}{4\pi}\left[(1+\nu)\log\frac{a}{r}+1-\nu\right] \qquad (3.2)$$

In the above expressions P is the central load, a is the plate radius and ν is the Poisson's ratio, which is assumed to be equal to 0.3 for the purpose of illustration. The principal stresses at any point are:

$$\sigma_{1,2} = \frac{\sigma_{rr}}{2} \pm \sqrt{\left(\frac{\sigma_{rr}}{2}\right)^2 + \tau_{rz}^2} \tag{3.3}$$

The contour of constant tensile principal stress for a unit load is shown in Figure 3.25. Referring to the delamination patterns shown in Figure 3.20, one can note that the envelope of the delamination fronts (referred to as conical tents in a previous section) is similar to the iso-principal stress curves. This suggests that the tensile principal stresses may govern the initiation of microcracks and delaminations. The subsequent growth of delaminations may be governed by their initial radius and location along the thickness. For example, a finite element analysis by Pinheiro (1991) shows that the strain energy release rate is higher for delaminations at the midplane of a laminated beam than that at other positions.

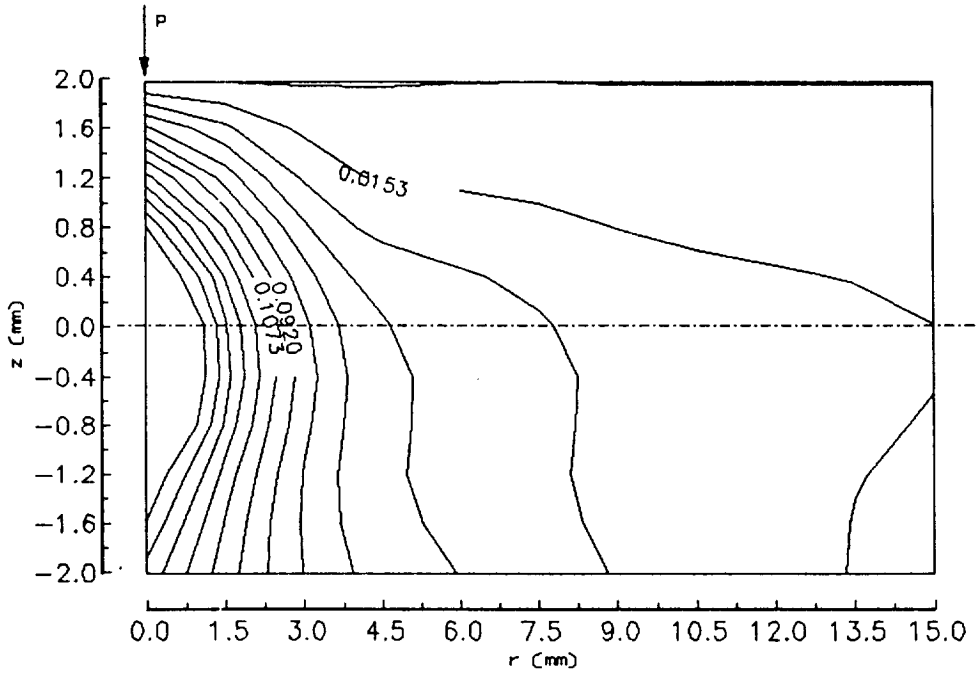

Figure 3.25 Contour of constant tensile principal stresses for a unit load

Strain Energy Release Rate

The discussion in this section pertains to the yield curve or growth of delaminations. A simple analysis shows that the yield curve has to be a straight line. The strain energy release rate due to an axisymmetric delamination in a circular plate can be derived based on a plate delamination model. Let us consider a circular plate containing a circular delamination. As the load is increased the delamination continues to grow. Let G_c be the critical strain energy release rate for delamination growth.

During the steady growth of delaminations, the strain energy release rate is equal to the critical strain energy release rate and can be expressed as

$$G_c = \frac{1}{2} P^2 \frac{\partial C}{\partial A} \tag{3.4}$$

where C is the compliance of the plate, P is the applied load and A is the delamination area. For the sake of simplicity we consider a single delamination. The compliance C can be expressed as $C=q/P$ where q is the center deflection. Then

$$\begin{aligned} G_c &= \frac{1}{2} P \frac{\partial q}{\partial A} \\ &= \frac{1}{2} P \frac{\partial q}{\partial P} \frac{\partial P}{\partial A} \end{aligned} \tag{3.5}$$

From experimental results we have for $b=BP$(see previous section). Where b is the delamination radius, $A=\pi b^2$, and B is a constant. Hence

$$\frac{\partial A}{\partial P} = 2\pi B^2 P \tag{3.6}$$

Substituting in (5) we obtain

$$G_c = \left[4\pi B^2 \frac{\partial P}{\partial q}\right]^{-1} \tag{3.7}$$

If G_c is assumed to be a constant for the particular material and lay-up, then we find that $\partial P/\partial q$ must also be a constant. The term $\partial P/\partial q$ is actually the slope of the yield curve, e.g., FHK in Figure 3.1. Test results from various plates have shown that the yield curve is indeed a straight line. The values of the slope, K_2, for various combinations of test parameters are shown in Figure 3.26.

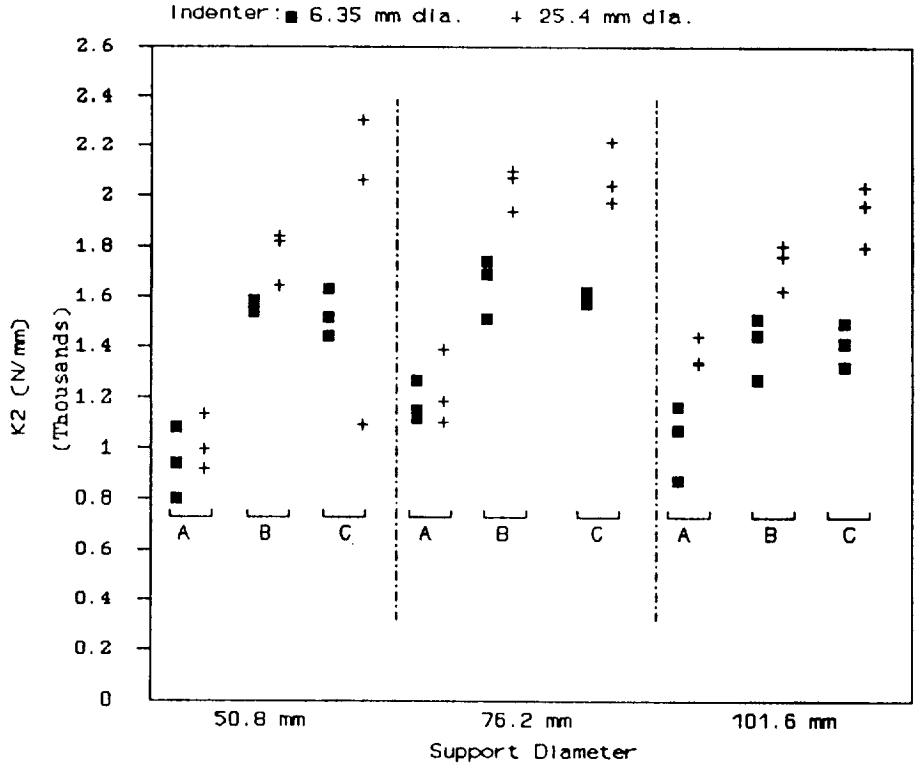

Figure 3.26 Slope of yield curve (K_2)

CHAPTER 4
LOW-VELOCITY IMPACT TESTS

Background

Low-velocity impact tests were conducted on composite laminates in order to compare the response and damage with corresponding behavior under static loading. The laminate types, indenter, and support ring diameters were the same as used in static tests. The equipment used in impact studies consisted of the following:

- Pendulum Impact Facility
- Digital Oscilloscope (Nicolet 4094 & Nicolet XF-44 Recorder)
- Computing Facilities; VAX mainframe and microcomputers

Pendulum Impact Test Equipment

The impact pendulum is depicted in Figure 4.1. It is a modified version of the one described by Sjöblom, Hartness, and Cordell (1988). It is easier to measure the rebound velocity of the impactor in a pendulum impact facility than in a drop tower impact facility. The impact and rebound velocities were measured by using two pairs of phototransistors and light emitting diodes with two 10 MHz counters. The impact force was measured by using an instrumented tup, Dynatup 8496-1, and a Vishay 2310 strain gage conditioner. The digital oscilloscope, Nicolet 4094, was used for

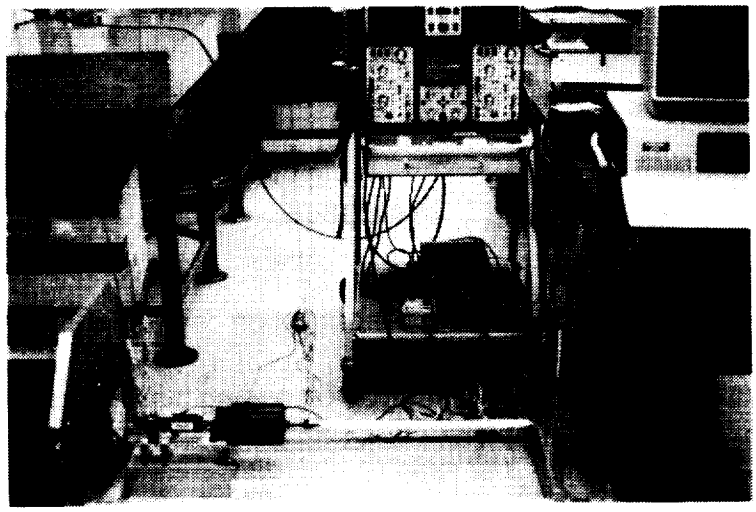

(a)

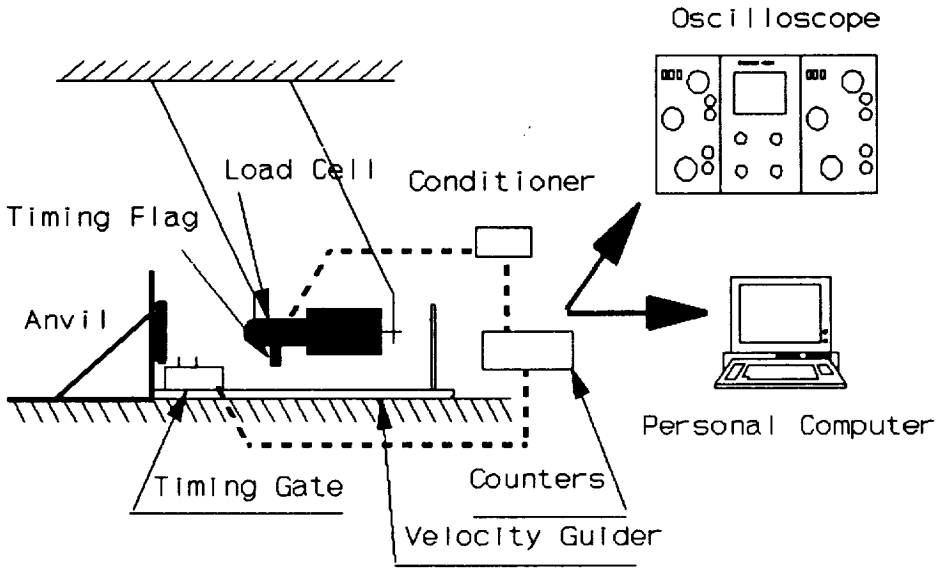

(b)

Figure 4.1 Pendulum impact facility:(a)photo of full setup and (b)schematic diagram of setup

recording the impact force history during the event. The personal computer was also utilized to record the impact and rebound velocities and to compute the impact energy and energy imparted to the target. A gauge was used to measure the drop height of the impactor to ensure repeatable impacts. The maximum velocity obtainable was about 2 m/s. The maximum mass the tup can carry was about 15 kg. The support for the specimen was fixed on the anvil mechanically. The support used for the pendulum impact facility was the same ring support used for the static indentation tests described in the previous chapter. Only the 50.8 mm diameter ring support was used in impact studies.

Calibration of the Load Cell

According to Ireland (1974), it is necessary to calibrate the load cell dynamically for the instrumented impact testing. The different components in the load cell might react differently due to the differences in load introduction rates between static and impact loading. Having the impact and the rebound velocities measured, we can calibrate the load cell dynamically so that the average force is correct. Consider the impact event depicted in Figure 4.2. Assume that the load is proportional to output signal.

$$F_a = C\, F_m \tag{4.1}$$

$$I_a = \int -F_a\, dt = m(V_r - V_i) \tag{4.2}$$

$$I_m = \int -F_m \, dt \tag{4.3}$$

Where,

F_a = actual force
F_m = measured force
C = correction factor
I_a = actual impulse momentum
I_m = measured impulse momentum
V_i = impact velocity
V_r = rebound velocity

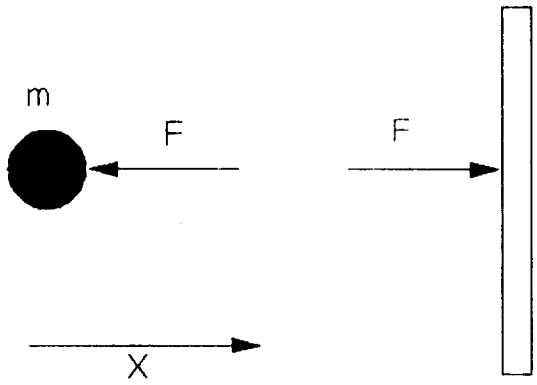

Figure 4.2 Definition of coordinate system

By substituting equation (4.1) into equation (4.3), the correction factor can be expressed in terms of impulse momenta as

$$C = \frac{I_a}{I_m} \tag{4.4}$$

The actual impulse momentum can be calculated easily with the measured impact and rebound velocities. The total mass of the pendulum used in this study was 13.98 kg. The measured impulse momentum can be found by integrating the force-time curve.

The calibration was performed by repeating the test at ten different impact velocities in the current study. The final factor C was found by averaging the results from the ten trials as seen in Table 4.1. The measured impact force by the load cell used in this study was higher than the actual impact force by 8.3 %.

The static calibration for the load cell is essential to obtain a calibration factor to interpret the output voltage as a force. The static calibration factor was obtained by employing a MTS material tester as a reference calibrator; the result was 1,500 N/V.

Table 4.1 Dynamic calibration of load cell

Test No.	$V_i(m/s)$	$V_r(m/s)$	I_a	I_m	C
1	0.584	0.498	15.122	16.887	0.895
2	0.351	0.314	9.297	10.216	0.910
3	0.812	0.716	21.361	22.990	0.929
4	0.903	0.792	23.696	25.259	0.938
5	0.490	0.416	12.666	14.065	0.901
6	0.629	0.525	16.133	18.140	0.889
7	0.718	0.564	17.922	20.143	0.890
8	0.810	0.651	20.425	22.675	0.901
9	0.947	0.839	24.968	26.601	0.939
10	1.132	1.069	30.770	31.445	0.979
				Average	0.917

The dynamic calibration factor of the load cell used in this study was found to be 1,375.5 N/V, which was 91.7% of the static calibration factor, 1,500 N/V. The impact history was accessed by an oscilloscope, Nicolet 4094, and recorded by Nicolet

XF-44 Recorder. The impact history was simply the force-time curve, and the force was measured in voltage difference by the load cell and multiplied by dynamic calibration factor to obtain the true impact force.

Force-Displacement Relation

From the experimentally measured impact force history, and the impact velocity, a relation between the contact force and impactor displacement can be derived. The governing equation for the impact problem is defined as:

$$\begin{aligned} m\ddot{x} &= -F(t) \\ x(0) &= 0 \\ \dot{x}(0) &= V_0 \end{aligned} \tag{4.5}$$

where m is the impactor mass, x is the impactor displacement, V_0 is the initial velocity, and $F(t)$ is the contact force. The acceleration and velocity at any time can be expressed in terms of displacements using the finite difference approximation as follows:

$$\ddot{x}_2 \approx \frac{x_3 - 2x_2 + x_1}{(\Delta t)^2} \tag{4.6}$$

$$\dot{x}_2 \approx \frac{x_3 - x_2}{\Delta t} \tag{4.7}$$

where Δt is the time increment between the adjacent points and x_i is the displacement at station i (see Figure 4.3). By substituting the above relation into the governing equation of motion (4.5), we obtain

$$\frac{m(x_3 - 2x_2 + x_1)}{(\Delta t)^2} = -F_2 \tag{4.8}$$

Solving for x_3,

$$x_3 = \frac{-F_2(\Delta t)^2}{m} + 2x_2 - x_1 \tag{4.9}$$

The displacement at node *3* can be computed if the displacement at the node *1* and *2* are known. At $t=0$, the initial displacement x is taken as zero. By using the velocity relation (4.7), the initial velocity at node *1* can be written as:

$$\dot{x}_1 = \frac{x_2 - x_1}{\Delta t} = V_0 \tag{4.10}$$

Solving for displacement x_2, we obtain

$$x_2 = V_0 \, \Delta t \tag{4.11}$$

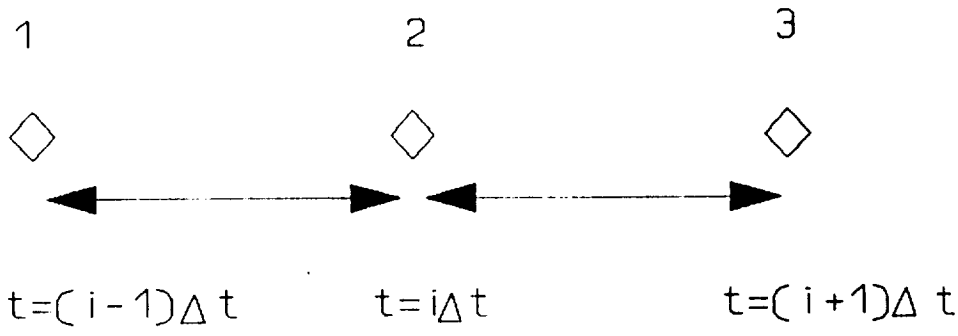

Figure 4.3 Finite difference scheme

Results and Discussion

The impact force history (F-t) and corresponding force-deflection (F-q) relations for all the tests conducted are presented in Appendix E. The results also include the impact energy and the energy imparted to the specimen. The energy imparted is actually equal to the difference between the initial and final kinetic energies of the impactor computed from the impact and rebound velocities.

The contact force-deflection relations from some of the impact tests for the three types of laminates are presented in Figures 4.4-4.6. The dynamic load-deflection behavior is compared with corresponding static behavior in Figures 4.7-4.9. Until the initial failure indicated by the sudden load drop, the dynamic stiffness was slightly higher than the static stiffness k_1. After the initial failure the load-deflection relations followed the static curves. Types B and C showed some high frequency oscillations superposed over the static curves. Type A laminates displayed a yielding point as they did in static tests. In Type A laminates, yielding occurred at the same load as in the static tests for low impact velocities ($v_0 < 0.77$ *m/s*). However, for higher velocities ($v_0 > 0.77$ *m/s*) yielding occurred at a lower load (see Figure 4.4 for comparison), and the load-deflection relations deviated from the static curves considerably. It is not clear if this was due to variations in the specimens.

The areas of delamination in impacted specimens were measured using ultrasonic C-scanning. The results are presented in Appendix D along with results from static tests. In Figures 4.10-4.12 the delamination radii are plotted against the maximum contact force experienced by the specimen during impact. These figures

display corresponding static results also. The delamination radii are found to be proportional to the maximum force. A least square curve fitting of impact data shows that in all three types of laminates, the delamination radius for a given maximum contact force is slightly lower in impact tests than in static tests. The explanation could be as follows. Consider the free body diagram of the circular disc cut out from the plate shown in Figure 4.13. Let $\bar{m}$ be the mass of the disc, $\bar{a}$ be the average acceleration of the disc, and τ be the average shear stress τ_{rz} acting on the periphery of the disc. Then for dynamic equilibrium

$$P - 2\pi rh\tau = \bar{m}\bar{a} \tag{4.12}$$

Solving for the average shear stress,

$$\tau_{rz} = \tau = \frac{1}{2\pi rh}(P - \bar{m}\bar{a}) \tag{4.13}$$

Equation (4.13) shows that for a given force P the interlaminar shear τ_{rz} will be higher for static case, and hence the delamination radius will also be larger.

Prediction of Impact Response and Damage

It has been found that for all the impact tests we conducted, the load-deflection relations were similar to the ones for the corresponding static tests. Hence the static load-deflection relations can be used to model the impact response.

A typical static curve (e.g., Figure 3.10) can be modeled by three empirical formulas. For the initial loading portion upto the first observable load drop, the load-

deflection relation can be expressed as

$$P = K_1 q, \quad q<q_1 \tag{4.14}$$

where P is the contact force, q is the plate deflection, K_1 is the slope of the static curve, and q_1 is the deflection at which load drop ΔP occurs. After the load drop, the load-deflection follows the yield curve given by

$$P = (K_1 q_1 - \Delta P) + K_2(q - q_1), \quad q > q_1 \tag{4.15}$$

The above relation is valid as long as the load is increasing. Once the unloading begins, i.e., contact force starts decreasing, the load-deflection follows the unloading curve approximated as a parabola (see Figure 3.1) given by

$$P = P_{max}\left(\frac{q}{q_{max}}\right)^2 \tag{4.16}$$

where P_{max} and q_{max} are the load and deflection at the point of unloading. In fact the exponent in (4.16) can be estimated accurately by curve fitting the static unloading curves. This formula neglects the residual deformation at the end of the contact/impact process. In fact the unloading process is not critical in estimating the maximum impact force. The equation of motion of the impactor is given by

$$M\ddot{q} = -P(q) \tag{4.17}$$

where M is the impactor mass, and $\ddot{q}$ is the acceleration. The force function $P(q)$ is chosen from equations (4.14-4.16) depending on the contact force and deflection.

The equation of motion can be numerically integrated to obtain force-time history. The constants K_p, q_p, ΔP and K_2 are obtained from one simple static test. The above procedure was tried for several impact tests and the agreement between the measured and predicted impact response, in particular the maximum contact force, was excellent. A sample comparison is shown in Figure 4.14. Now from the maximum predicted contact force, one can predict the delamination radius using the C-scan results for the static tests. The delamination radius obtained using C-scan for impact tests on Type C laminates is plotted in Figure 4.12 along with corresponding static results. For a given maximum contact force, the delamination radius in impact tests is slightly smaller than in static tests. Thus static tests provide a conservative estimate of the delamination radius.

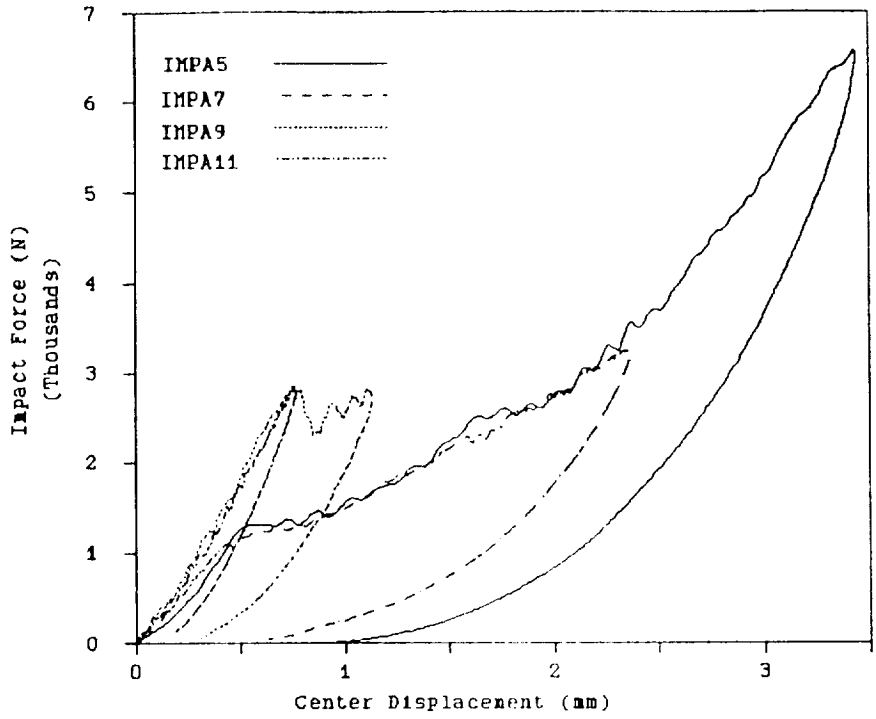

Figure 4.4 Dynamic responses of laminate type A:force-displacement curve

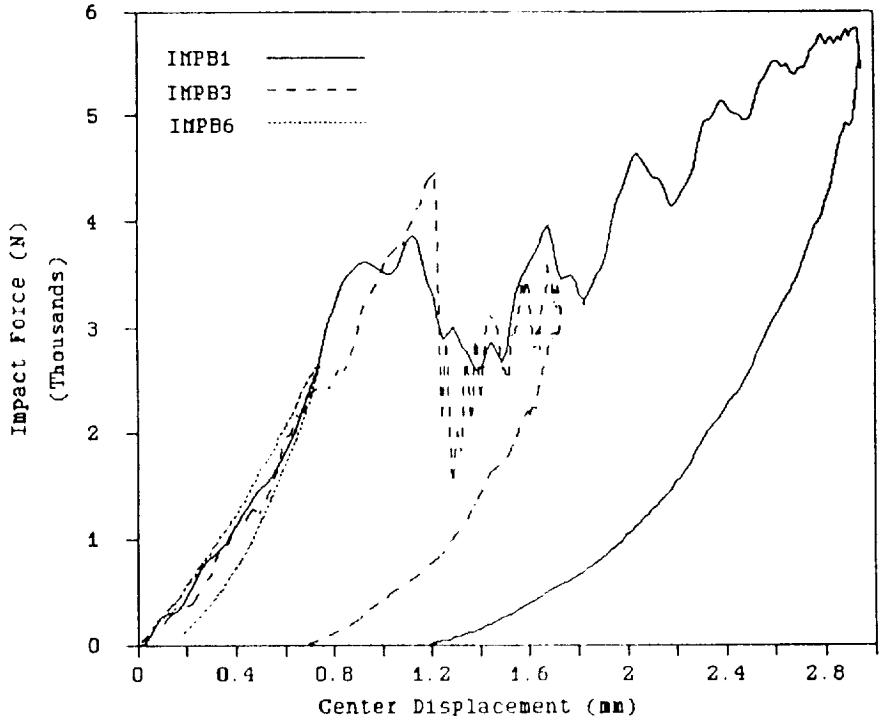

Figure 4.5 Dynamic responses of laminate type B:force-displacement curve

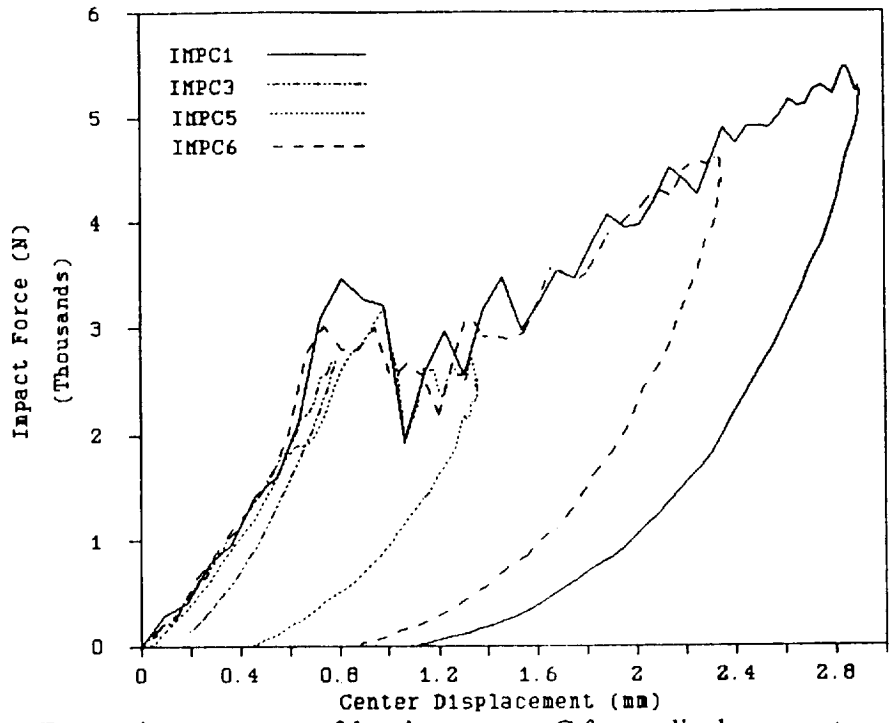

Figure 4.6 Dynamic responses of laminate type C:force-displacement curve

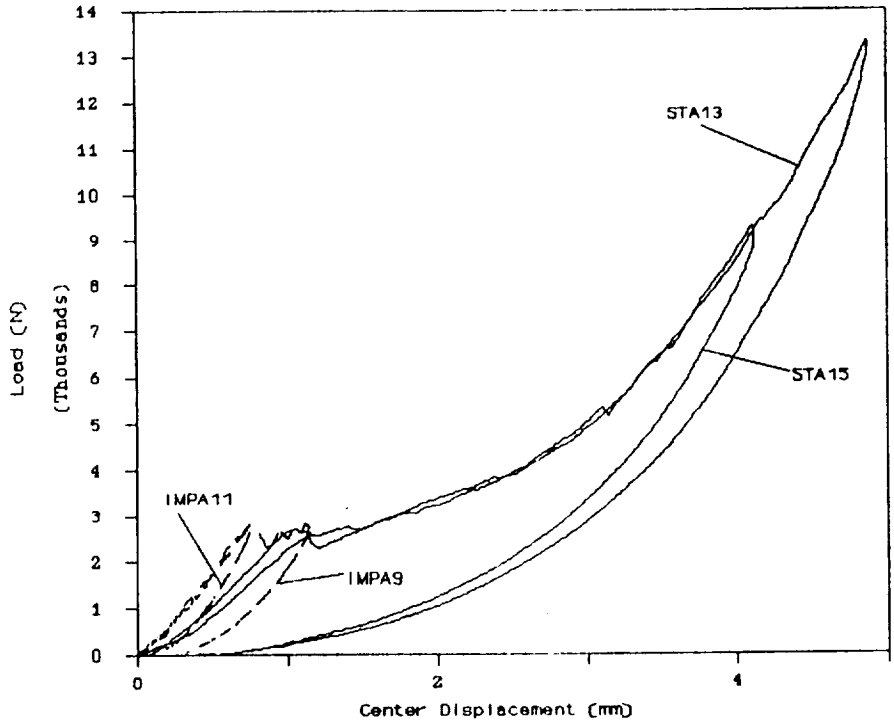

Figure 4.7 Responses of laminate type A:static and dynamic

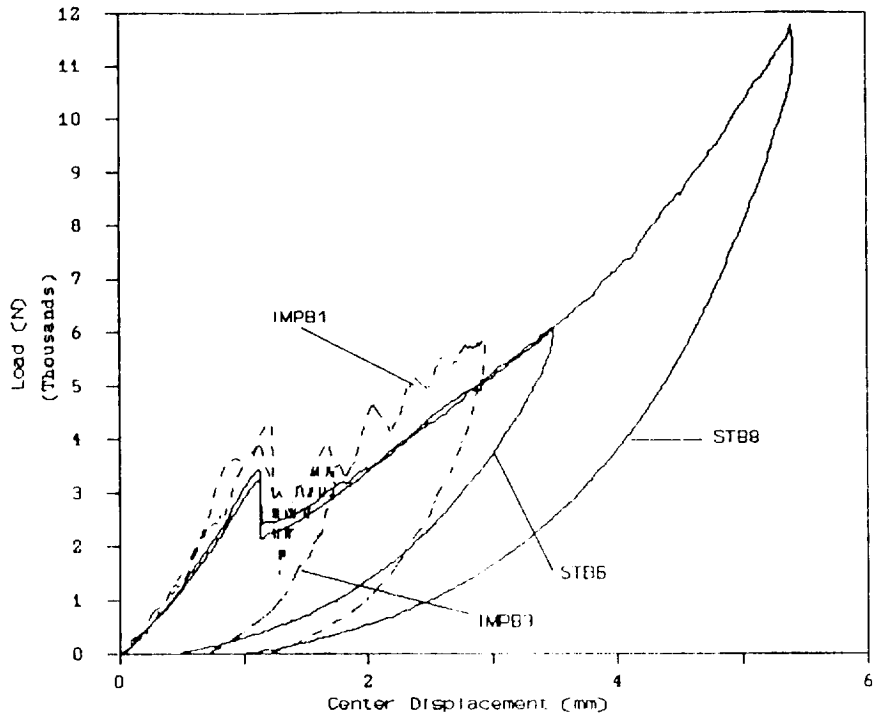

Figure 4.8 Responses of laminate type B:static and dynamic

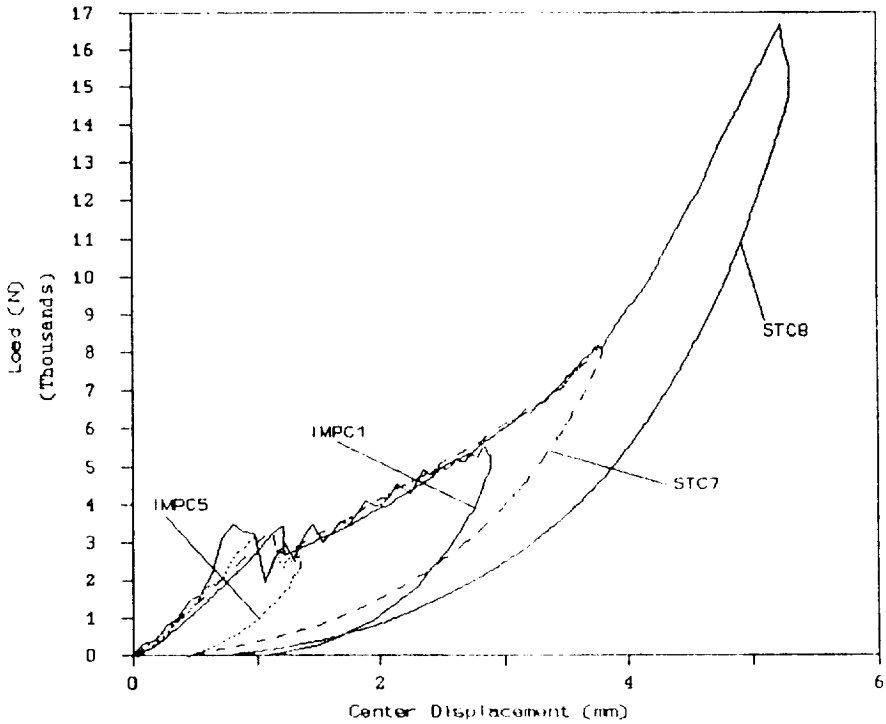

Figure 4.9 Responses of laminate type C:static and dynamic

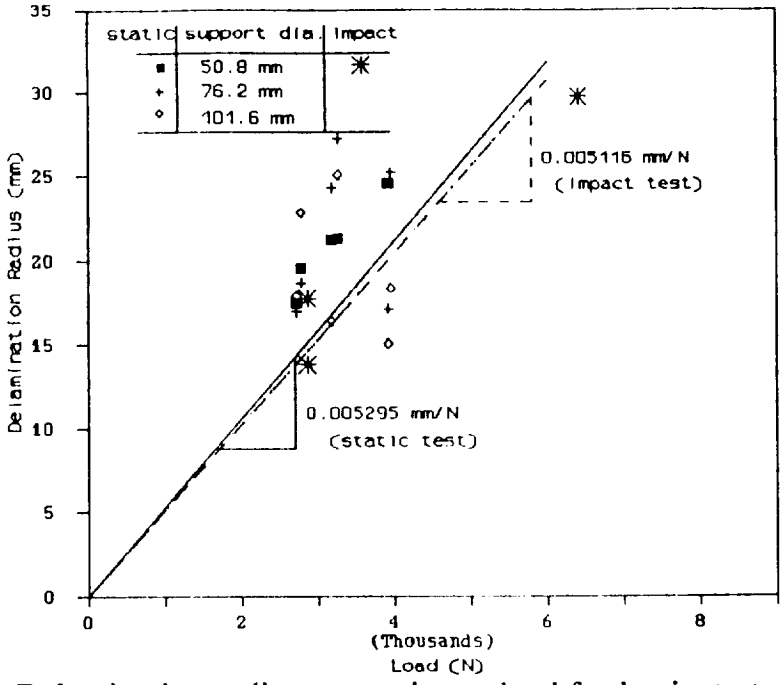

Figure 4.10 Delamination radius vs. maximum load for laminate type A:static and dynamic cases

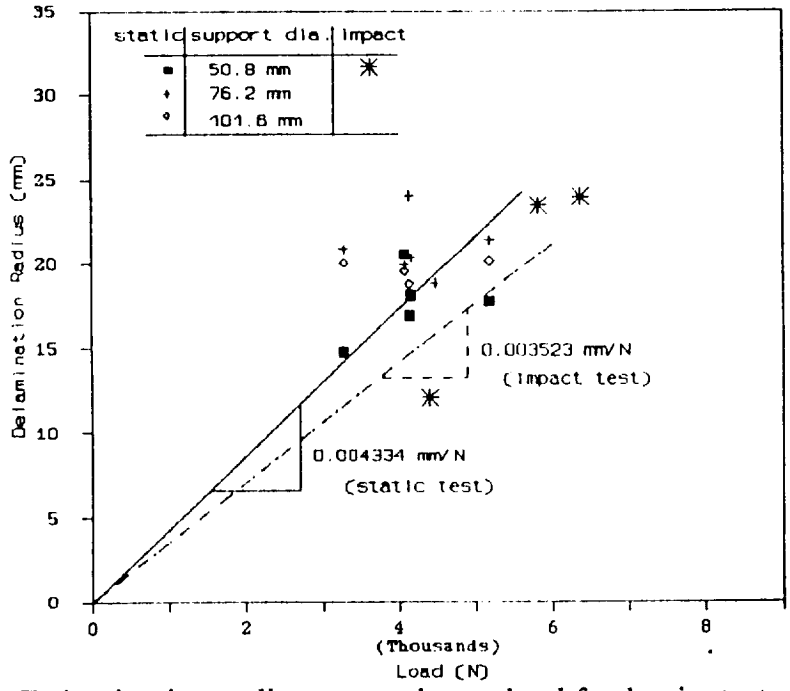

Figure 4.11 Delamination radius vs. maximum load for laminate type B:static and dynamic cases

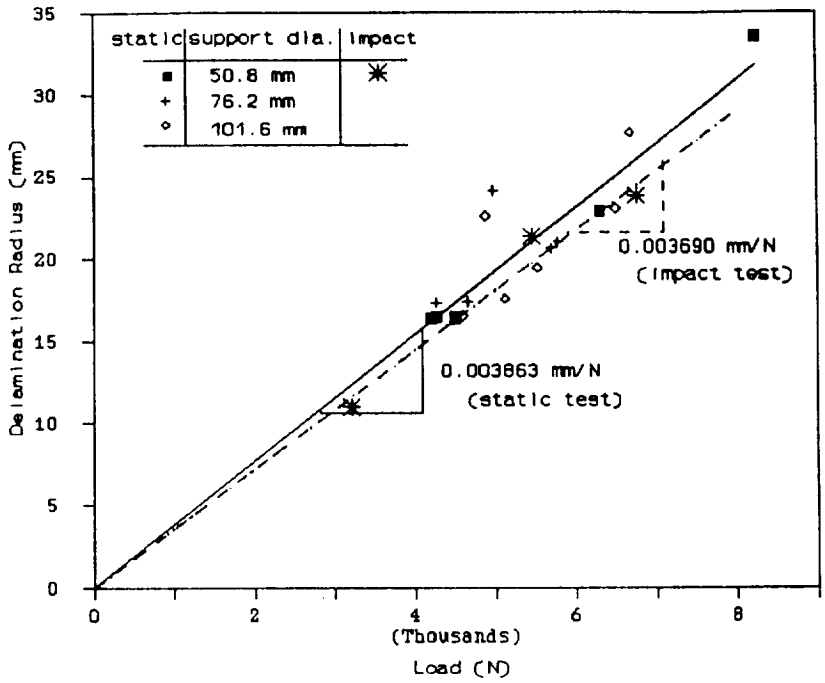

Figure 4.12 Delamination radius vs. maximum load for laminate type C:static and dynamic cases

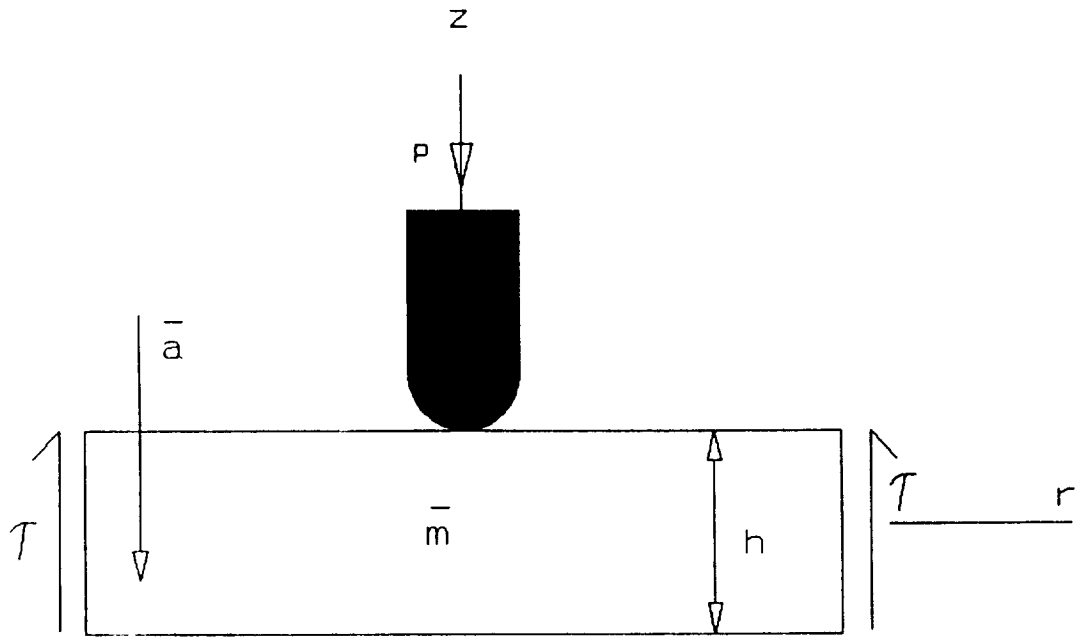

Figure 4.13 Free body diagram of circular plate under a concentrated impact load

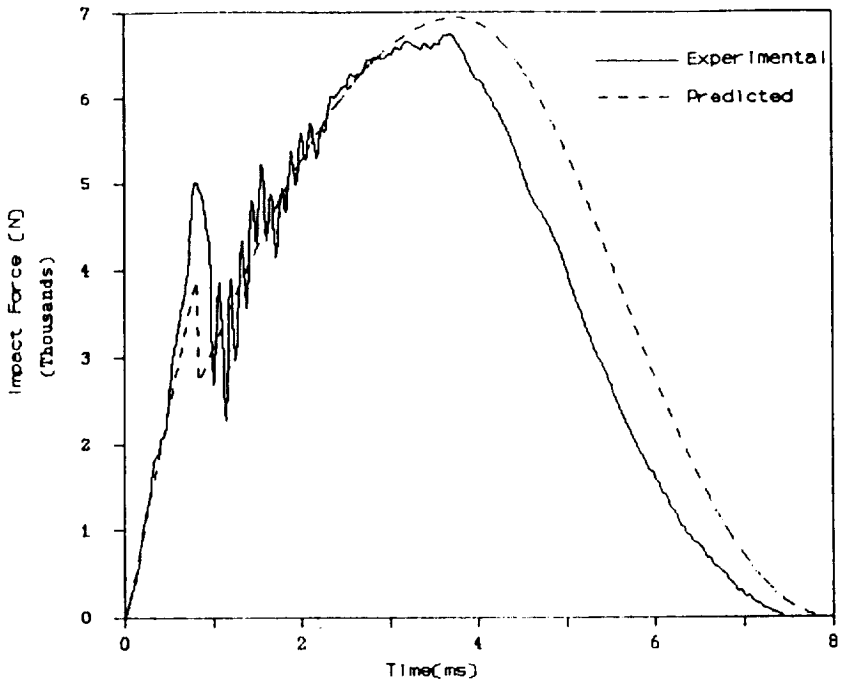

Figure 4.14 Impact force history for laminate type C:impactor mass-13.98 Kg; impact velocity-1.27 m/s

CHAPTER 5
SUMMARY AND CONCLUSIONS

Summary and Discussion

Quasi-isotropic and cross-ply graphite/epoxy laminated circular plates were statically indented using steel indenters with hemispherical nose. The specimens were loaded, unloaded, and reloaded several times. The damage in the laminates was assessed by ultrasonic C-scanning and photo-micrographic techniques. Low-velocity impact tests were performed on similar specimens with steel impactors in a pendulum impact facility. The impact force history was recorded. The displacement of the indenter as a function of time was computed numerically by integrating the acceleration, which was obtained from the impact force history and the impactor mass. The impact damage was quantified using the same techniques as with statically damaged specimens. The similarities between static and impact responses were discussed.

Three types of laminates were used in the study: Type A - $\pi/8$ quasi-isotropic, Type B - cross-ply, and Type C - $\pi/4$ quasi-isotropic. All laminates were symmetric, consisted of 32 plies, and were about 3.8 mm thick. Three circular rings - diameters 50.8 mm, 76.2 mm, and 101.6 mm - were used as supports for the plates in the indentation tests. Two steel indenters - hemispherical nose diameters 6.35 mm and

25.4 mm - were used in the tests. The static tests were stroke controlled at a rate of 0.02 mm/s.

There were some common features in the load-deflection diagrams obtained from the static tests on various specimens. As the load is increased, some crackling sound could be heard which may be an indication of matrix cracking and onset of small delaminations. The stiffness of the plate was not much affected by these damages as seen from the load deflection diagrams. When unloaded at small loads (below 2,000 N) there was a very small area enclosed by the loading and unloading curves. This area represents the energy dissipated mostly by the damages corresponding to the crackling noise.

The load-deflection curves were nonlinear at very small loads because of local indentation effects. As the plate deflection increased, the load-deflection relations became almost linear. However, the apparent plate stiffness was higher for the larger indenter, and this effect was much more pronounced in the case of smaller diameter ring support. This was because of the larger area of contact under the bigger indenter.

As the load is further increased, a sudden failure occurs with significant load drop in the stroke controlled tests. The failure is accompanied by a breaking noise similar to the **bang** typical of impact tests. The load drop and the associated noise level were the largest in the cross-ply laminates and the smallest in the $\pi/8$ laminates. In all tests the failure load due to the 25.4 mm diameter indenter was about 30% higher than that for the 6.35 mm indenter. However, the center

deflection at failure for a given laminate type and support ring did not depend on the indenter size. In general $\pi/4$ quasi-isotropic laminates performed better than the cross-ply laminates. The failure loads for the $\pi/8$ laminates were the lowest. Unlike the other two types, failure of $\pi/8$ laminates was similar to yielding of ductile materials. In $\pi/8$ laminates the load drop at failure was almost negligible.

The initial unstable failure was due to the sudden appearance of delaminations. This was confirmed by the ultrasonic C-scanning and photo-micrographs of failed specimens. It was found that the delaminations cause increase in thickness of the plates, but no detailed quantitative studies were conducted to relate the thickness change and damage.

As the specimen was loaded further, the delaminations grew steadily in a stable manner. The loading curve (or the yield curve) was a straight line until the delaminations ceased to grow, and other nonlinear effects such as the large deflection and friction came into the picture. The delaminations were almost circular in all cases. A linear relationship existed between the delamination radius and the maximum force applied during the indentation tests. For a given maximum force the $\pi/8$ laminates had the largest delaminations and the $\pi/4$ laminates had the smallest. A simple plate delamination model confirmed that the yield curve must be a straight line, if the delamination radius is directly proportional to the maximum force applied.

A high degree of nonlinearity was exhibited during unloading and reloading of the plates. The small area between corresponding unloading and reloading curves represents the energy loss due to friction, mostly between delamination surfaces.

The impact force histories recorded during low-velocity impact tests were used to generate the relationship between the contact force and the plate deflection in the dynamic tests. The force-deflection diagrams were similar to that obtained in static tests. Thus, the initiation and propagation of delaminations during impact can be explained from the corresponding behavior in static tests. For a given maximum force, the delamination radius in impact tests was slightly smaller than that in static tests. This was explained by the inertial effects in the vibrating plate in impact tests.

Conclusions

The combination of interlaminar shear stresses and flexural stresses initiates matrix cracking and delaminations in laminated plates subjected to indentation type loads. It is not yet clear if one type of damage leads to the other or both initiate independent of each other. Further photo-micrographic studies are warranted to pin-point the sequence of events. The damages accumulate and cause sudden failure due to creation of several large size delaminations in the plate. The traditional $\pi/4$ quasi-isotropic laminates performed better than the $\pi/8$ and cross-ply laminates of same thickness in the sense that they withstood large forces before the unstable failure. The $\pi/8$ laminates, though, failed at lower loads, exhibiting a ductile type of yielding, which may be desirable in some applications. The experimental data thus far collected will be very useful in detailed finite element modeling of the static tests and in identifying the mechanisms responsible for matrix cracking and delamination initiation.

The load-deflection behavior in impact tests is very similar to the corresponding static behavior before and after damage. Hence the static response curves can now be used to predict damage due to large impact masses at very low velocities. From the load-deflection diagrams and the extent of damage obtained from very few static indentation-flexure tests, and with the impact analysis program (Sankar et al., 1990), now it will be possible to predict impact damage in similar specimens for several combinations of impact masses and velocities.

APPENDIX A
SPECIMEN SUPPORT FIXTURE

This specimen support fixture was designed and fabricated to meet the requirements of the current research by the author. The fixture was made to be utilized for the static indentation test on a material tester such as the MTS machine.

The major frame of the fixture consists of a base plate, two I-shaped beams, and a support mount as shown in Figure A.1. All components are made of aluminum except the support mount which is made of steel. The stiffness of the fixture is very high and suitable for the present plate flexure tests.

The fixture frame is equipped with an LVDT holding bar, which is adjustable in position by translation and rotation. The support mount is also made to be utilized in the low velocity impact pendulum setup for the current research.

The various types and sizes of specimen support can be made to fit onto the support mount.

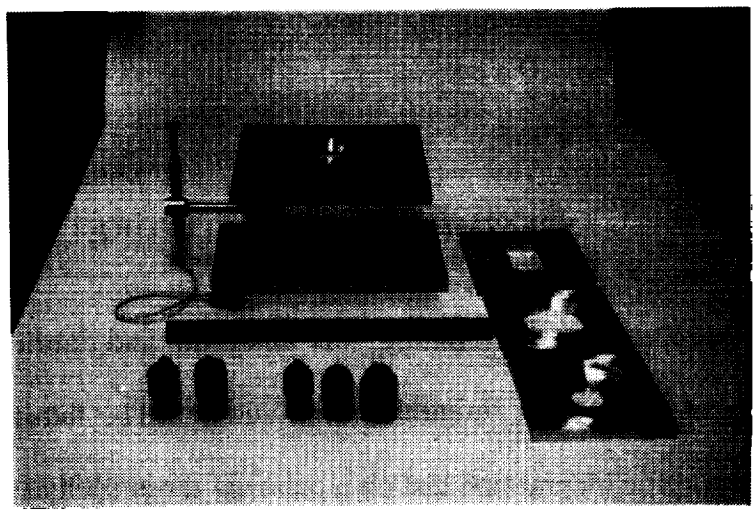

(a)

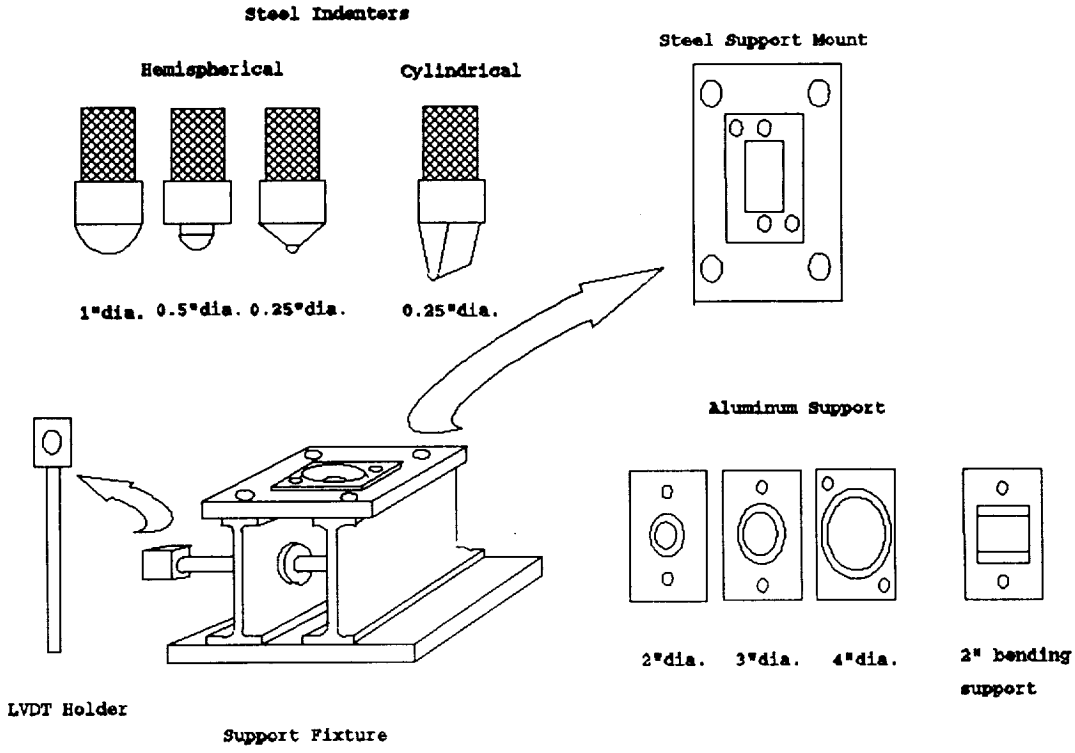

(b)

Figure A.1 Specimen support fixture: (a)photo of fixture and (b)schematic diagram of fixture

APPENDIX B
LOAD-DISPLACEMENT DIAGRAMS FOR STATIC INDENTATION TESTS

In this appendix the load-center deflection diagrams for all static indentation tests are presented. The specimen I.D., indenter diameter, and plate diameter (or support diameter) for laminate Types A, B, and C are presented in Tables B.1, B.2, and B.3, respectively. It should be noted that the center deflection is actually the indenter displacement, which includes plate deflection and local indentation.

Table B.1 Combination of indenter and support for the static test on laminate type A

Specimen I.D.	Indenter Diameter(mm)	Support Diameter(mm)
STA11	25.4	50.8
STA12	25.4	50.8
STA13	25.4	50.8
STA14	25.4	50.8
STA15	25.4	50.8
STA16	25.4	50.8
STA17	25.4	50.8
STA18	25.4	101.6
STA19	25.4	76.2
STA20	6.35	50.8
STA21	6.35	50.8

Table B.1--continued.

Specimen I.D.	Indenter Diameter(mm)	Support Diameter(mm)
STA22	6.35	101.6
STA23	6.35	50.8
STA24	6.35	76.2
STA25	6.35	76.2
STA26	6.35	76.2
STA27	25.4	76.2
STA28	25.4	76.2
STA29	25.4	101.6
STA30	25.4	101.6
STA31	6.35	101.6
STA32	6.35	101.6

Table B.2 Combination of indenter and support for the static test on laminate type B

Specimen I.D.	Indenter Diameter(mm)	Support Diameter(mm)
STB5	25.4	50.8
STB6	25.4	50.8
STB7	25.4	50.8
STB8	25.4	50.8
STB9	25.4	50.8
STB10	25.4	50.8
STB11	25.4	101.6
STB12	25.4	76.2
STB13	6.35	50.8

Table B.2--continued

Specimen I.D.	Indenter Diameter(mm)	Support Diameter(mm)
STB14	6.35	50.8
STB15	6.35	101.6
STB16	6.35	50.8
STB17	6.35	76.2
STB18	6.35	76.2
STB19	6.35	76.2
STB20	25.4	76.2
STB21	25.4	76.2
STB22	25.4	101.6
STB23	25.4	101.6
STB24	6.35	101.6
STB25	6.35	101.6

Table B.3 Combination of indenter and support for the static test on laminate type C

Specimen I.D.	Indenter Diameter(mm)	Support Diameter(mm)
STC5	25.4	50.8
STC6	25.4	50.8
STC7	25.4	50.8
STC8	25.4	50.8
STC9	25.4	50.8
STC10	25.4	50.8
STC11	25.4	101.6
STC12	25.4	76.2

Table B.3--continued

Specimen I.D.	Indenter Diameter(mm)	Support Diameter(mm)
STC13	6.35	50.8
STC14	6.35	50.8
STC15	6.35	101.6
STC16	6.35	50.8
STC17	6.35	76.2
STC18	6.35	76.2
STC19	6.35	76.2
STC20	25.4	76.2
STC21	25.4	76.2
STC22	25.4	101.6
STC23	25.4	101.6
STC24	6.35	101.6
STC25	6.35	101.6

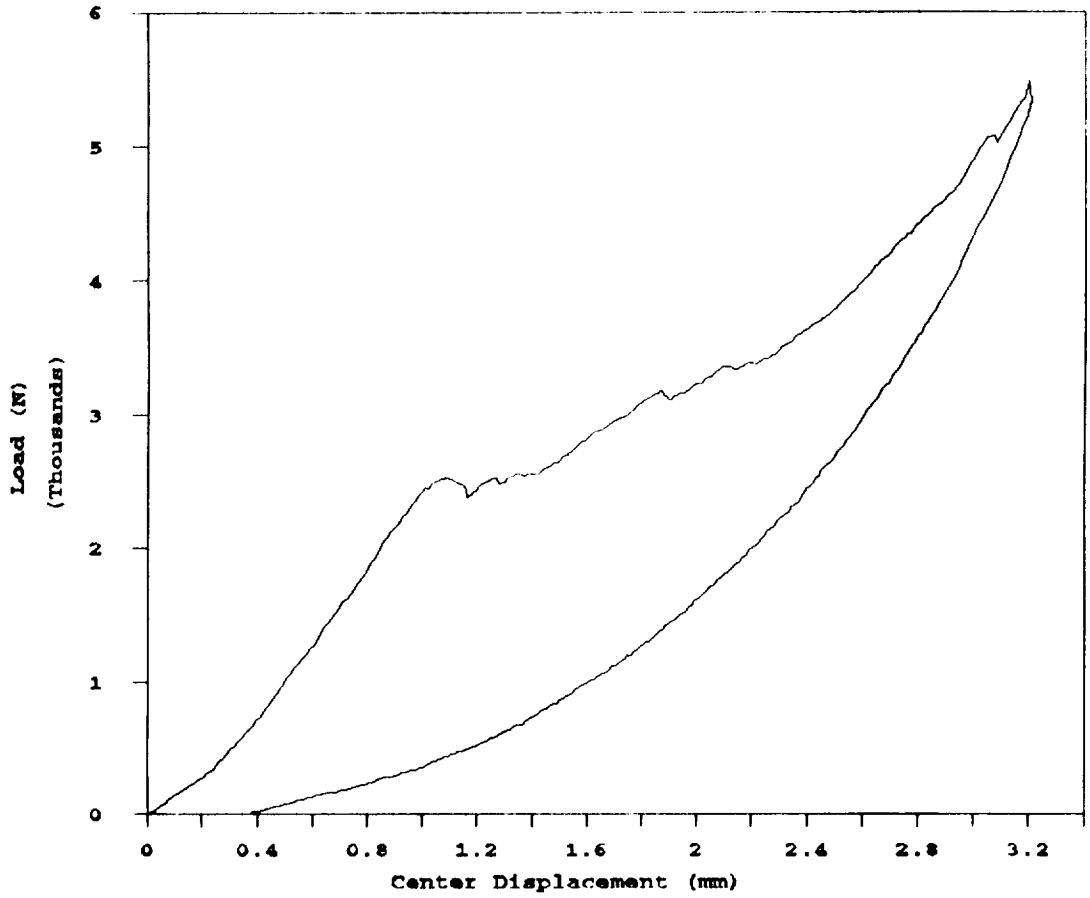

Figure B.1 Load-displacement diagram of STA11

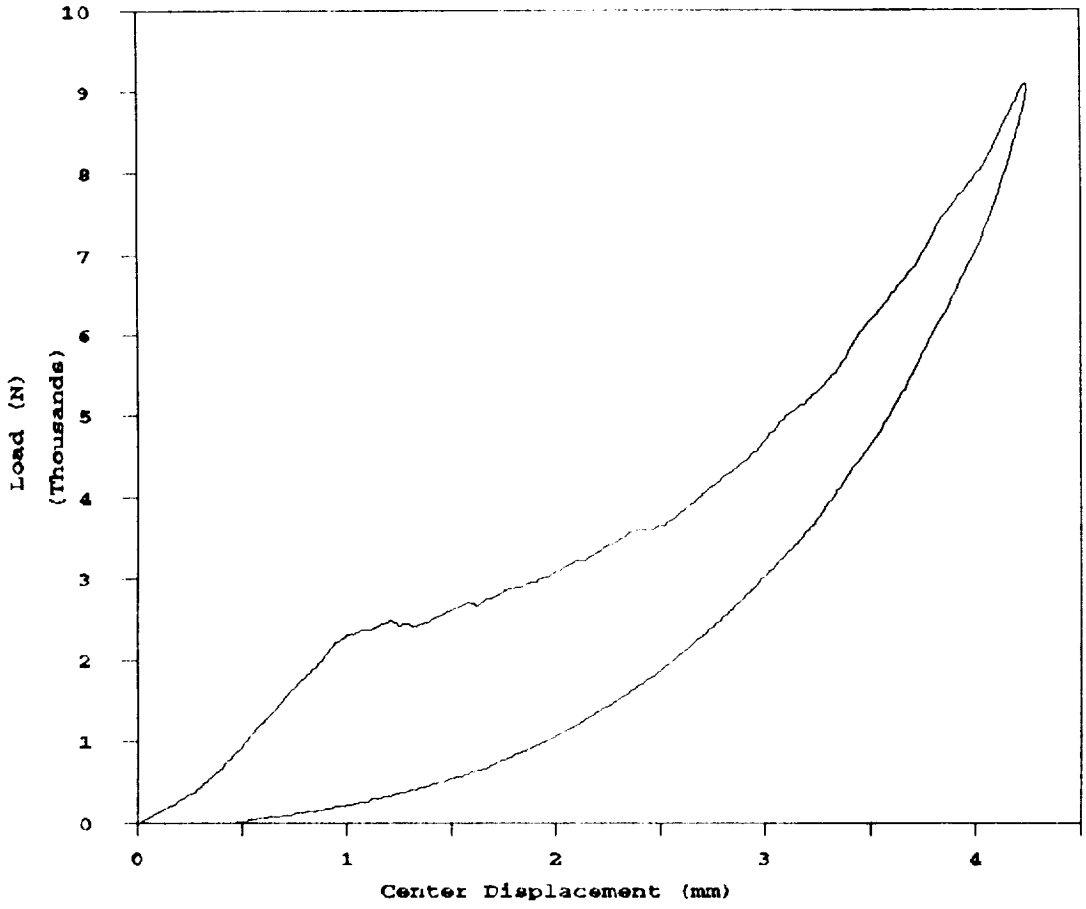

Figure B.2 Load-displacement diagram of STA12

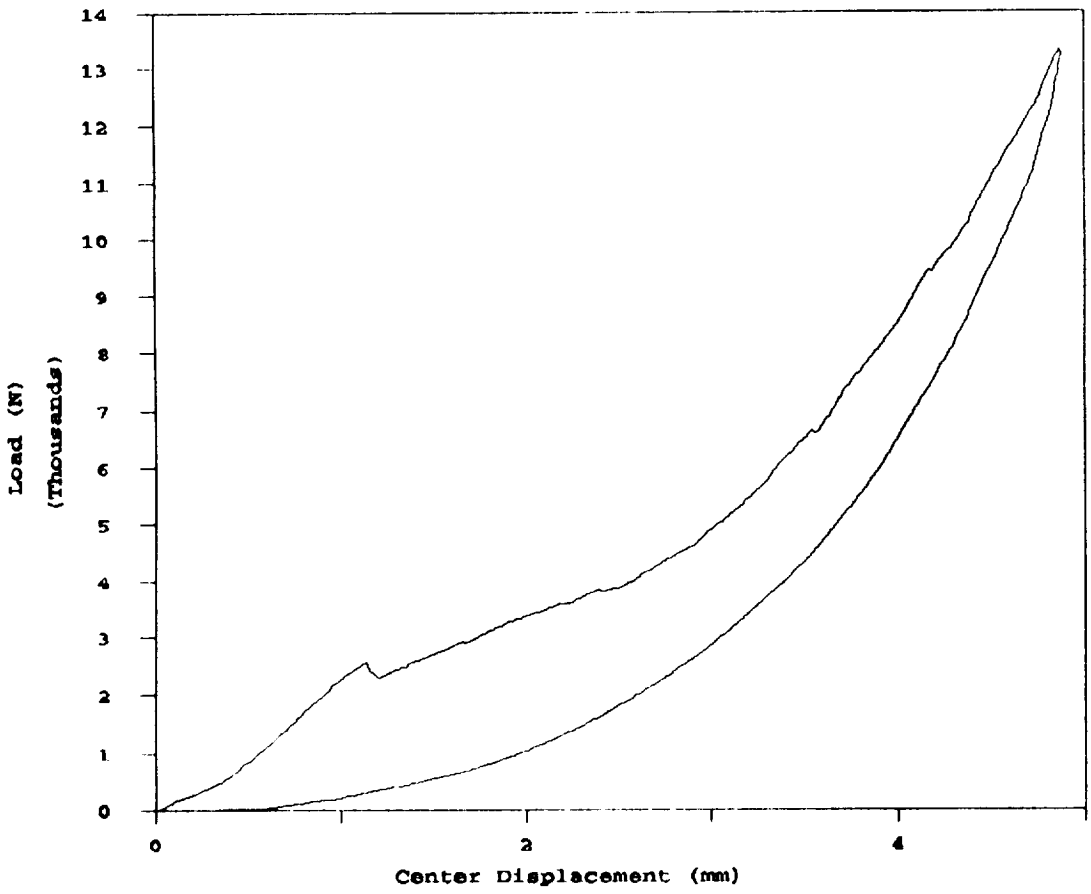

Figure B.3 Load-displacement diagram of STA13

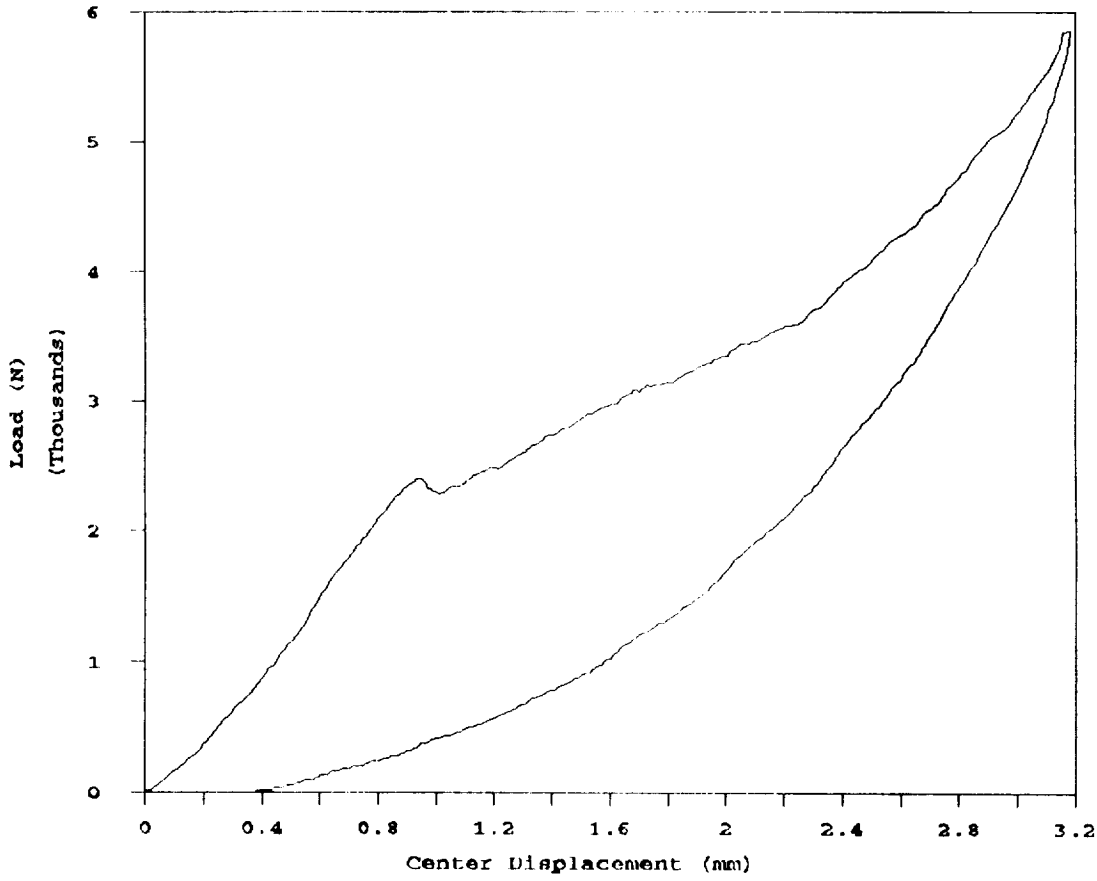

Figure B.4 Load-displacement diagram of STA14

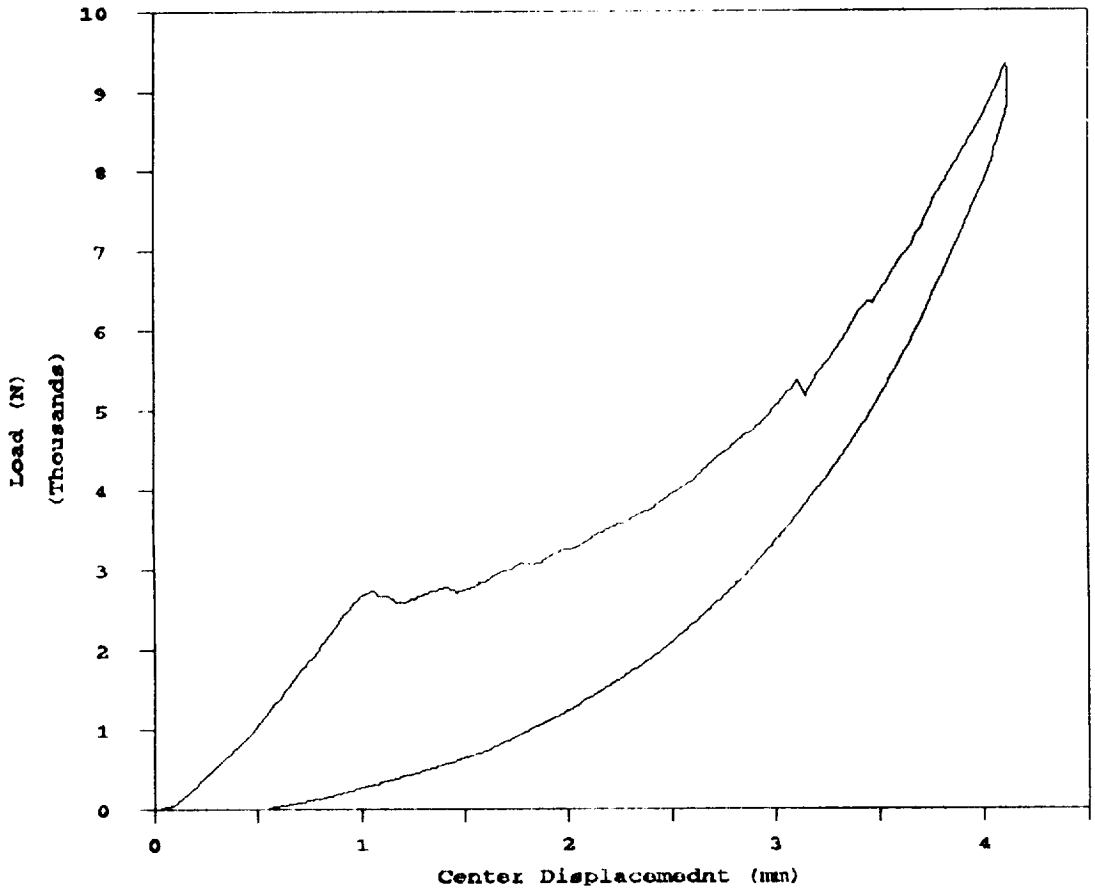

Figure B.5 Load-displacement diagram of STA15

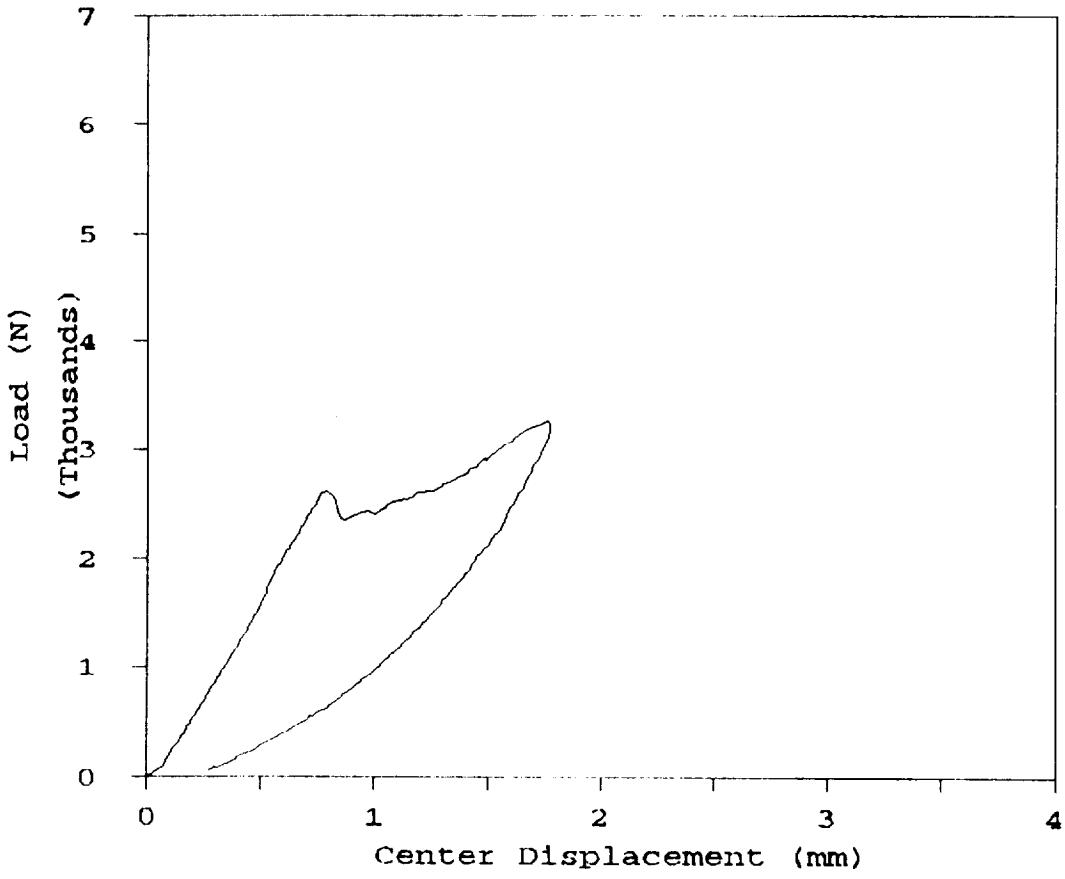

Figure B.6 Load-displacement diagram of STA16

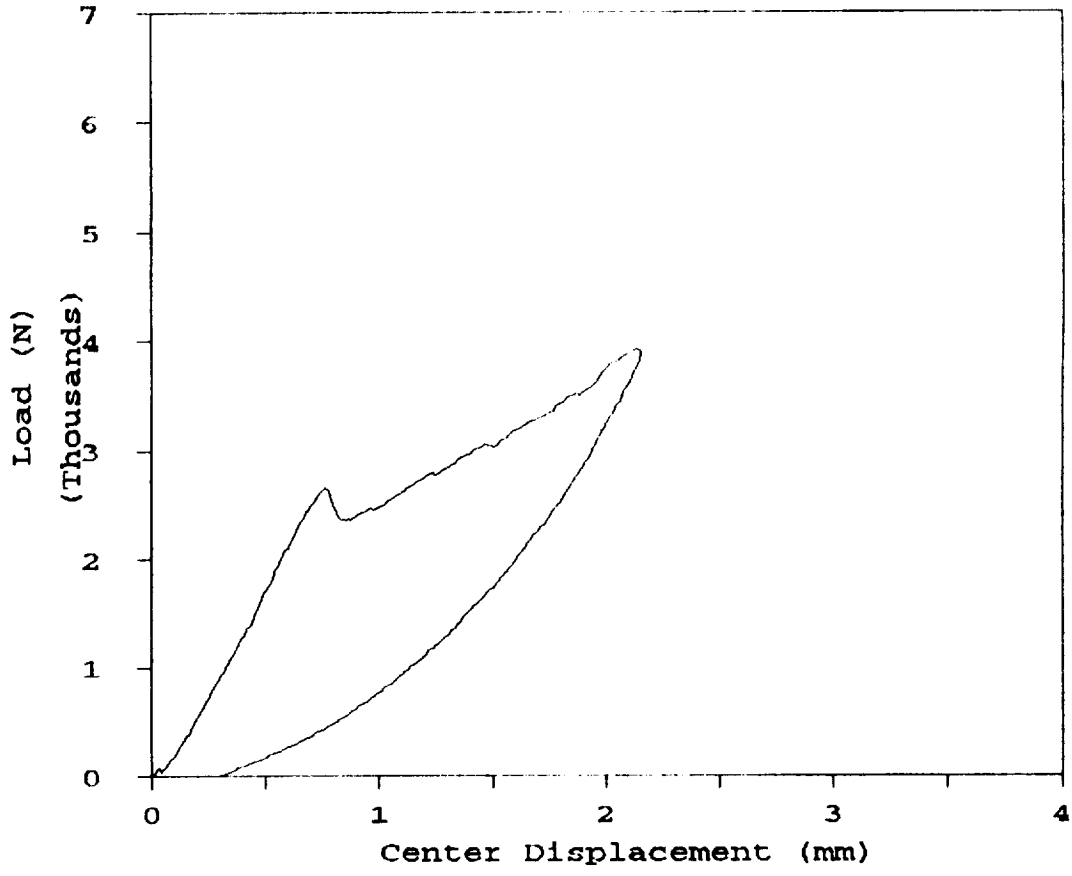

Figure B.7 Load-displacement diagram of STA17

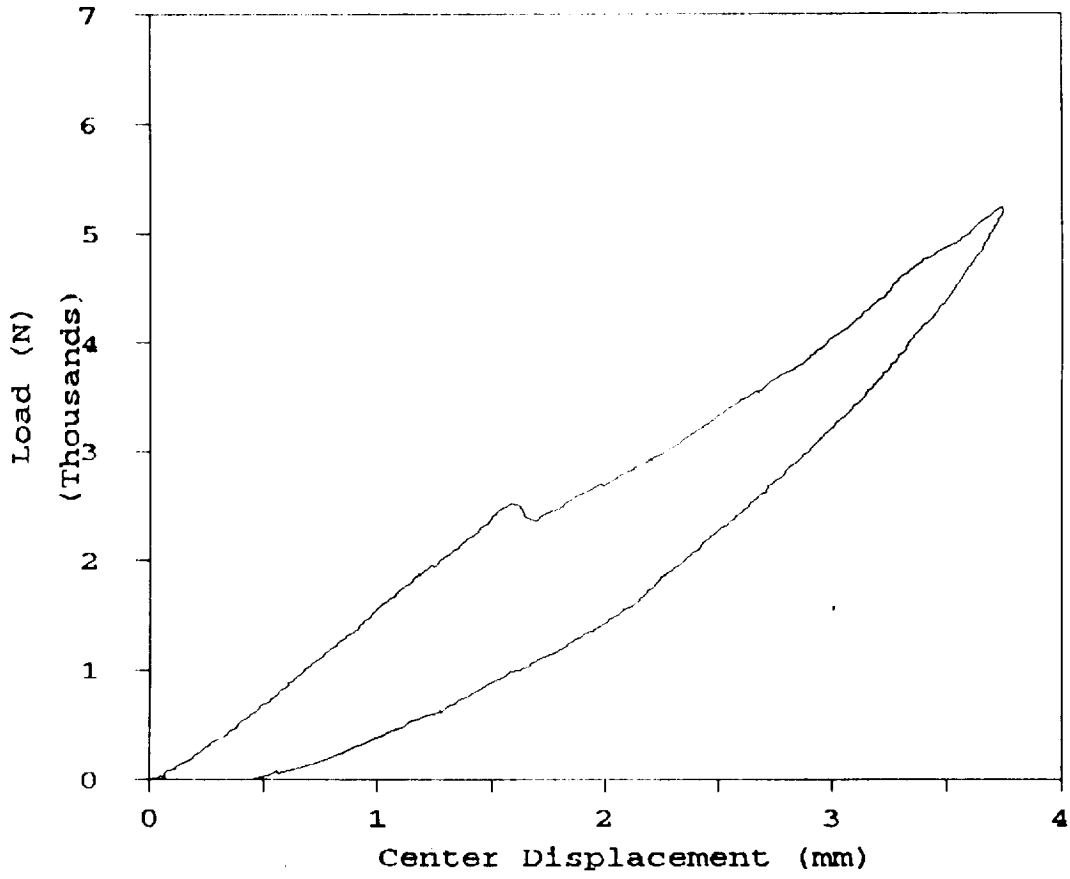

Figure B.8 Load-displacement diagram of STA18

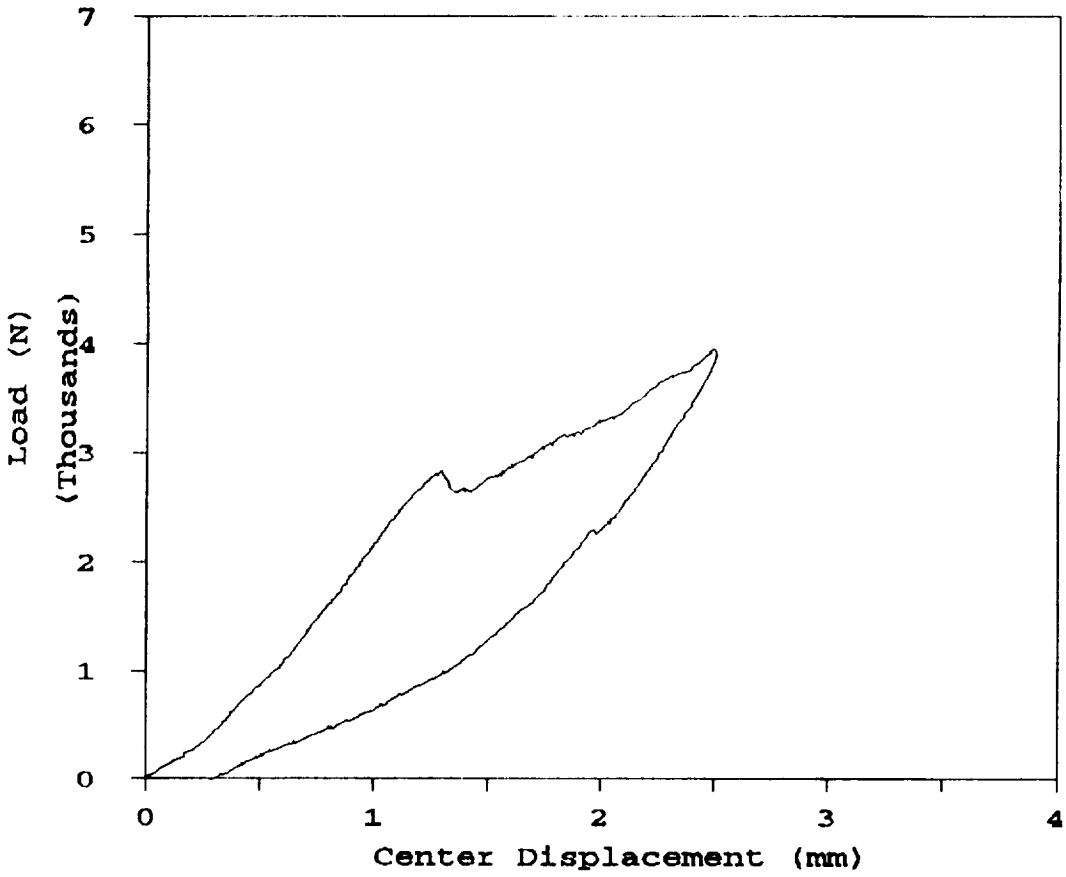

Figure B.9 Load-displacement diagram of STA19

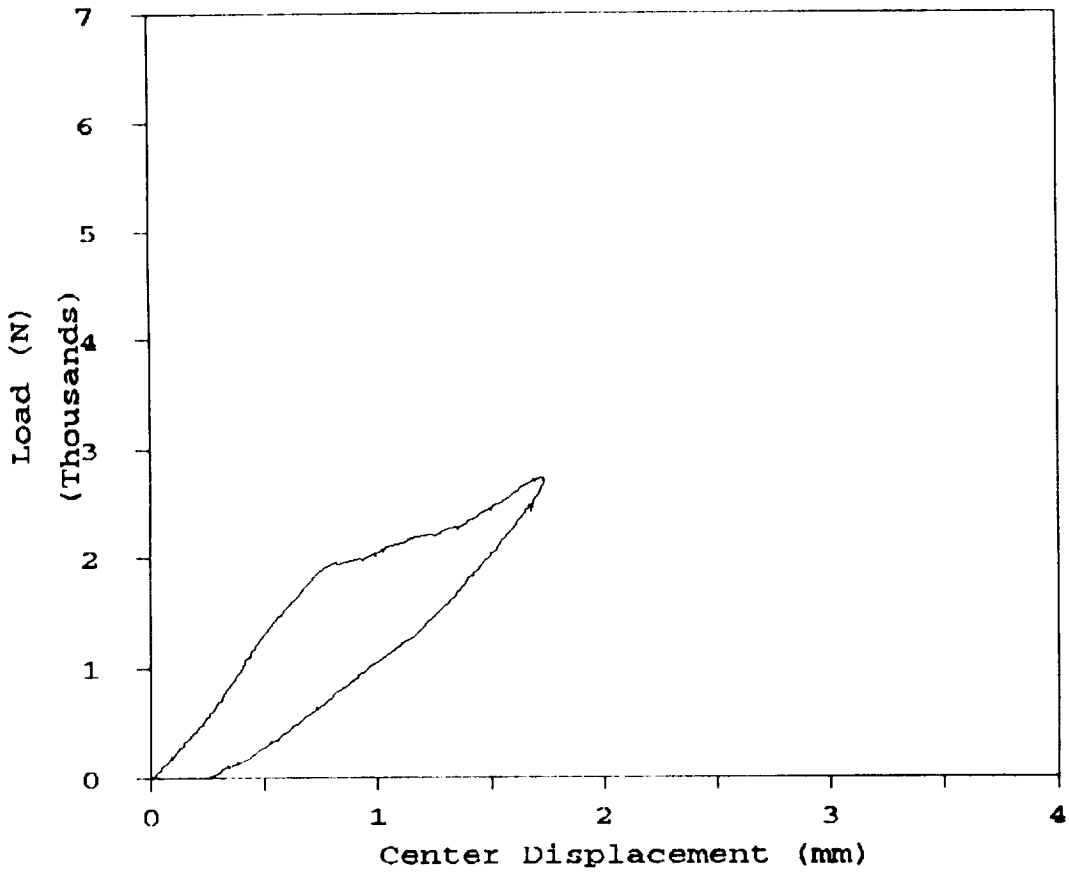

Figure B.10 Load-displacement diagram of STA20

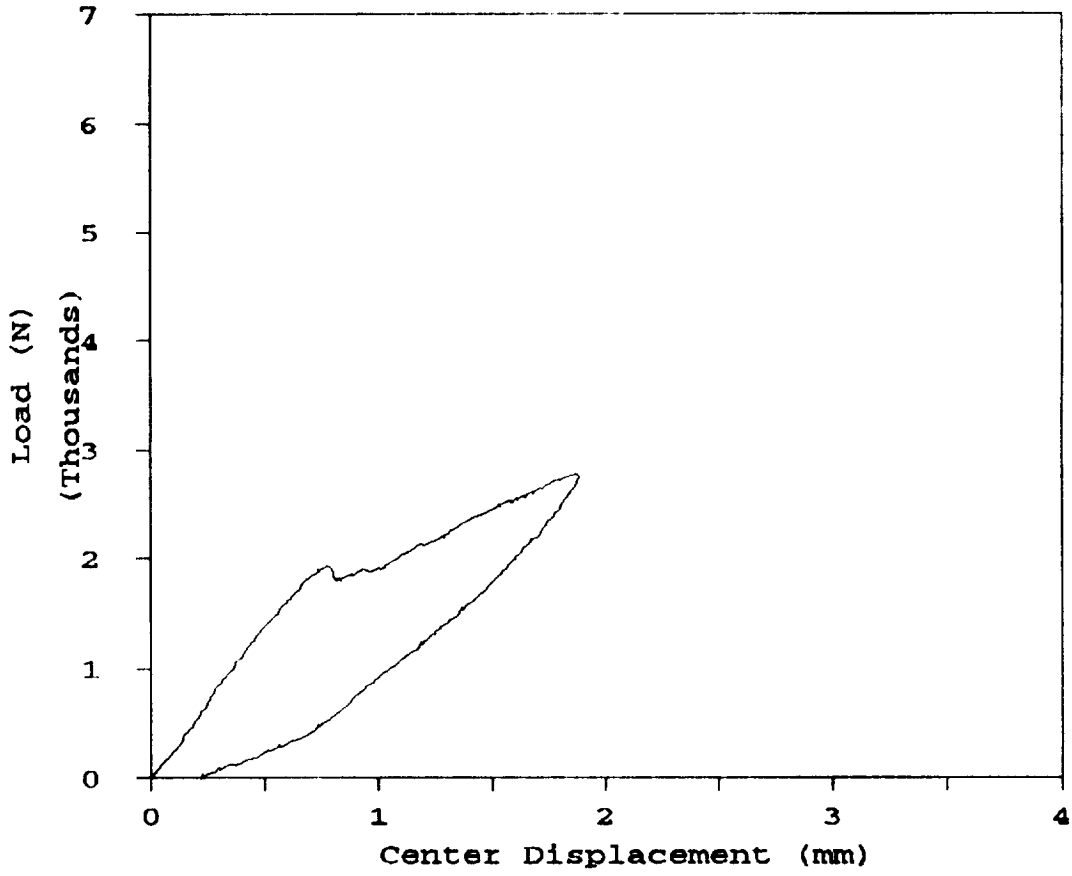

Figure B.11 Load-displacement diagram of STA21

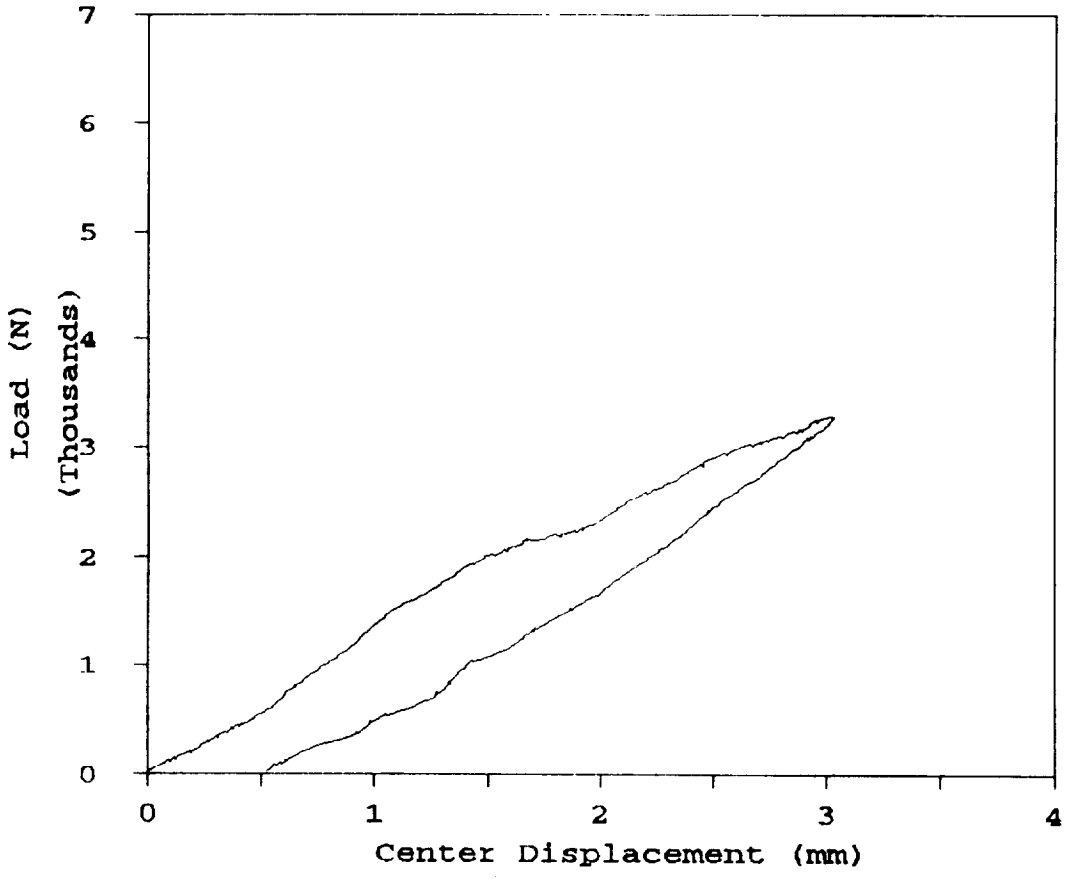

Figure B.12 Load-displacement diagram of STA22

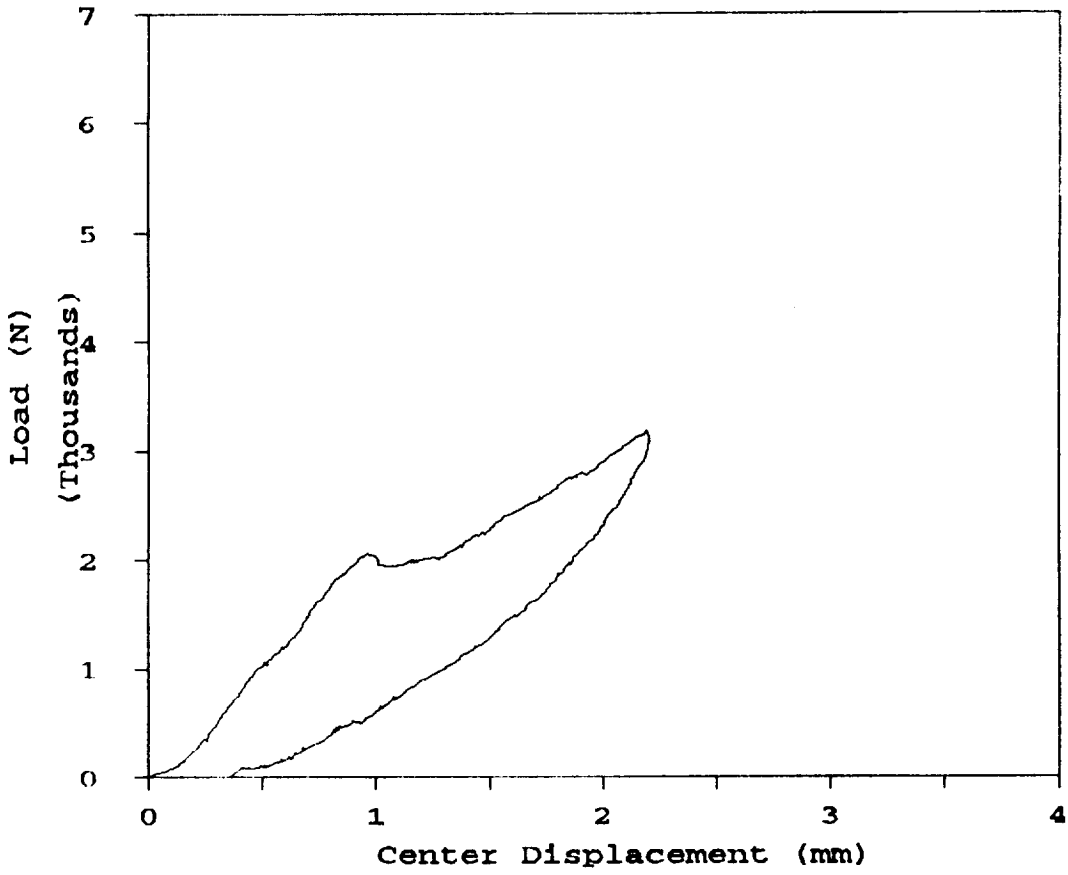

Figure B.13 Load-displacement diagram of STA23

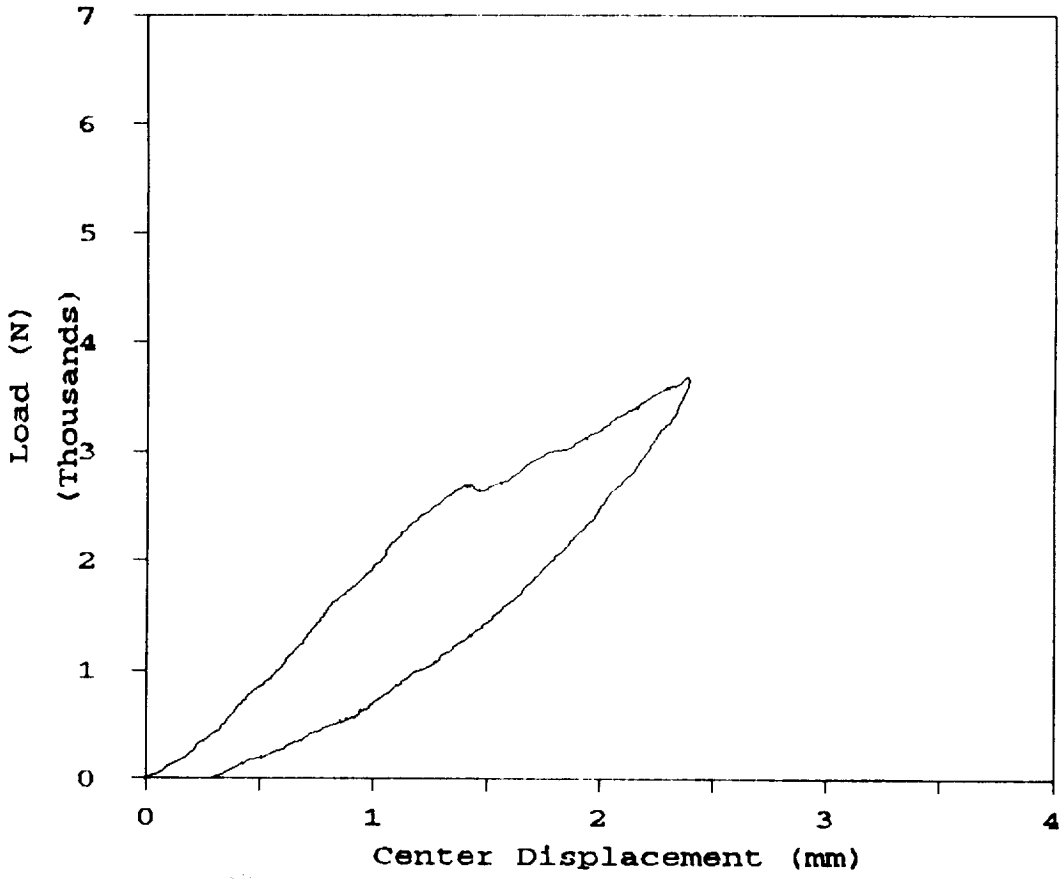

Figure B.14 Load-displacement diagram of STA24

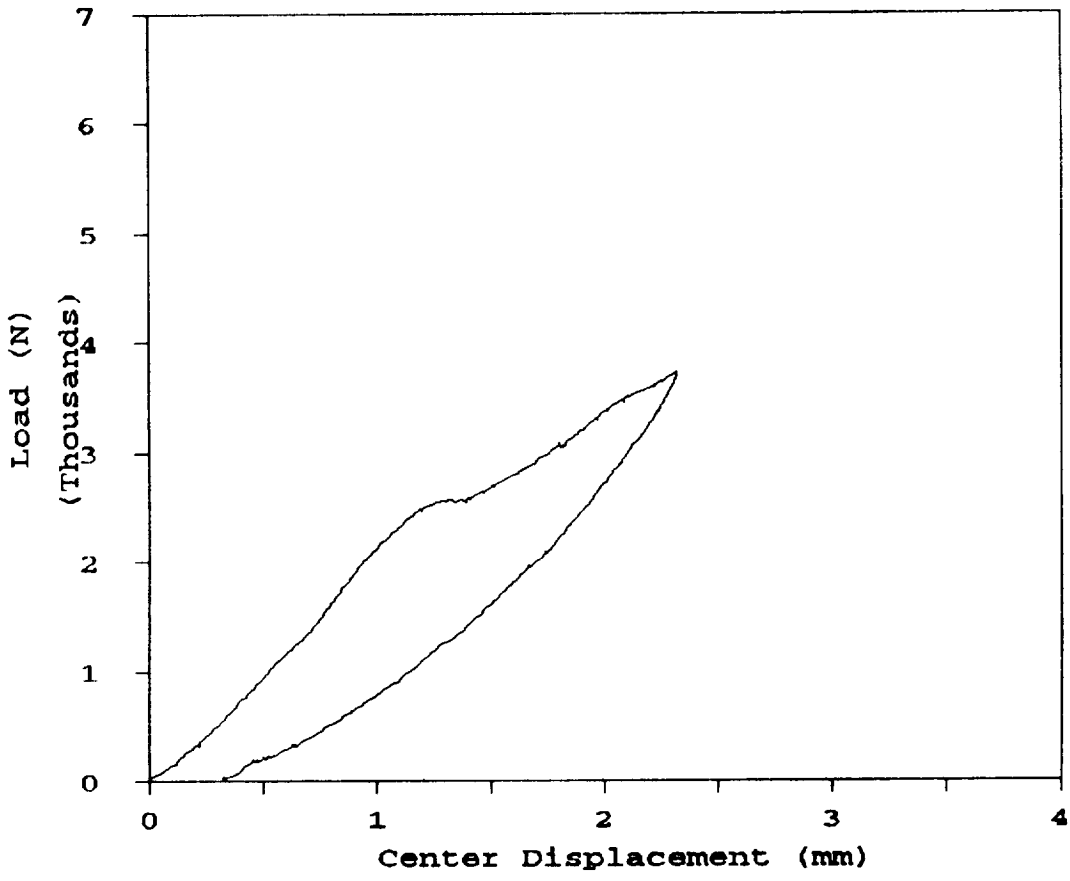

Figure B.15 Load-displacement diagram of STA25

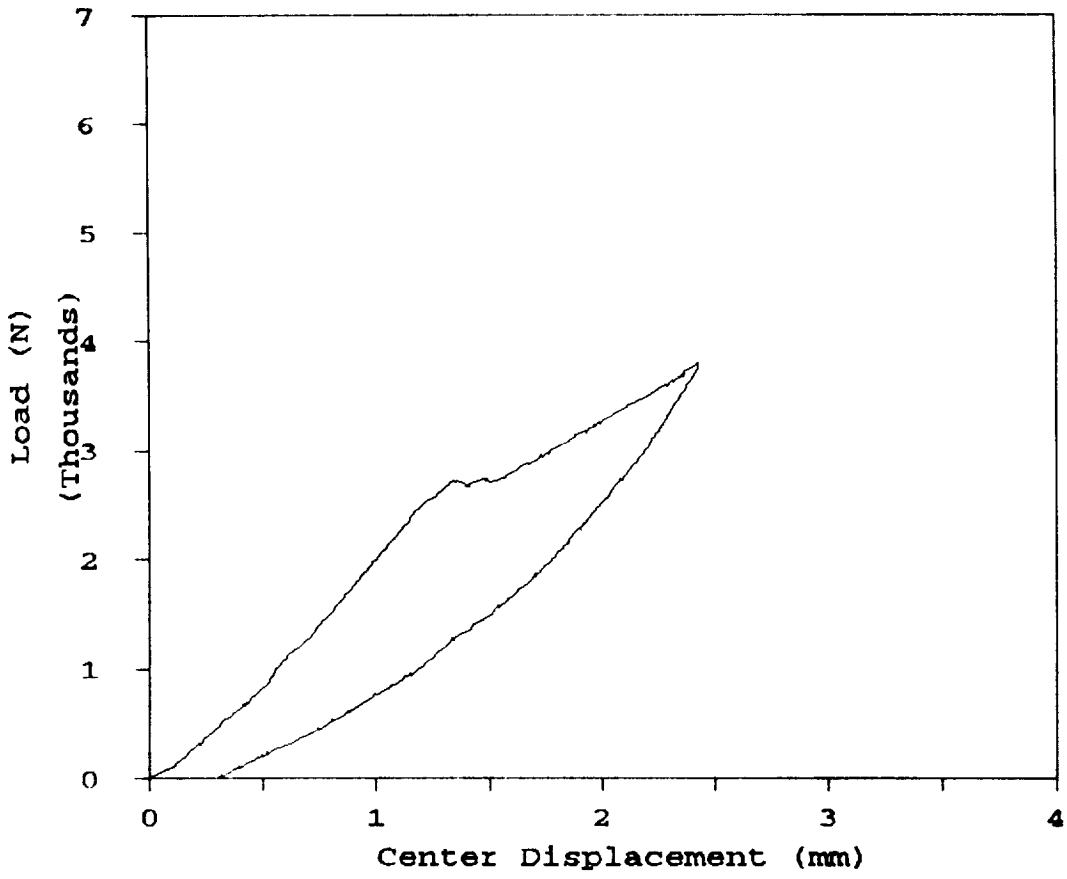

Figure B.16 Load-displacement diagram of STA26

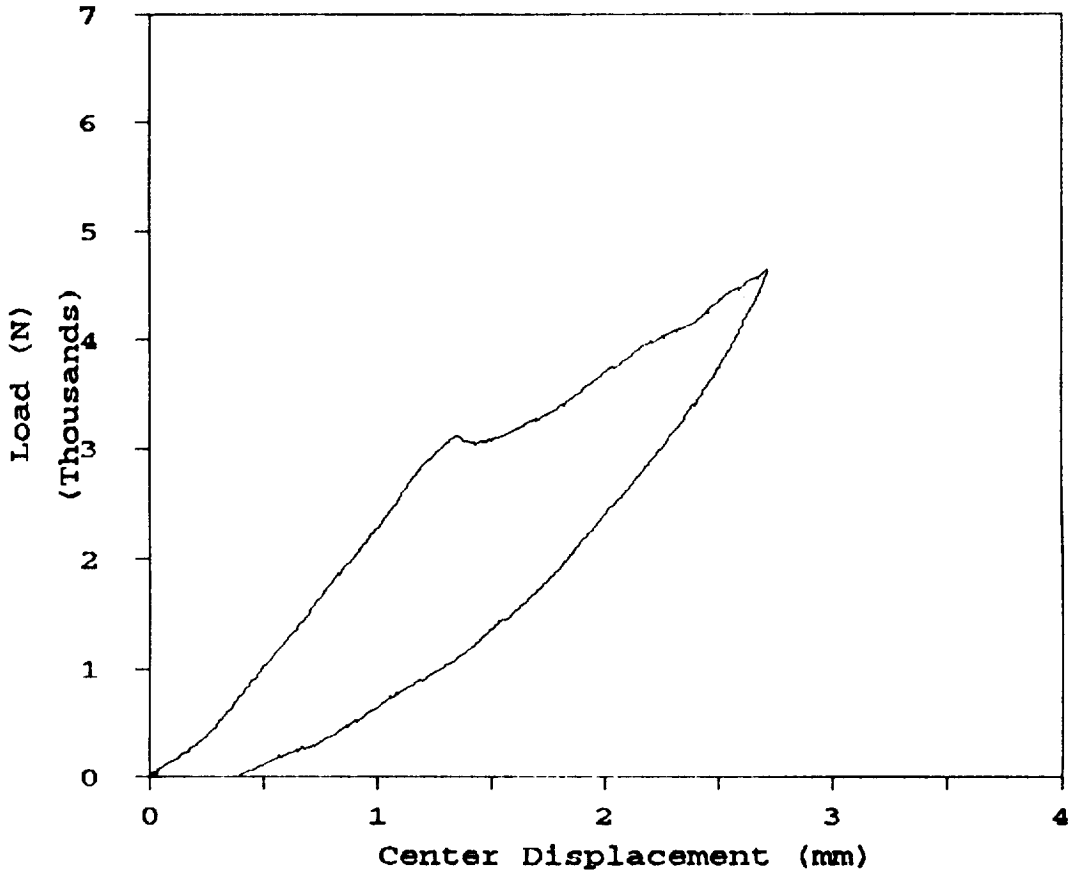

Figure B.17 Load-displacement diagram of STA27

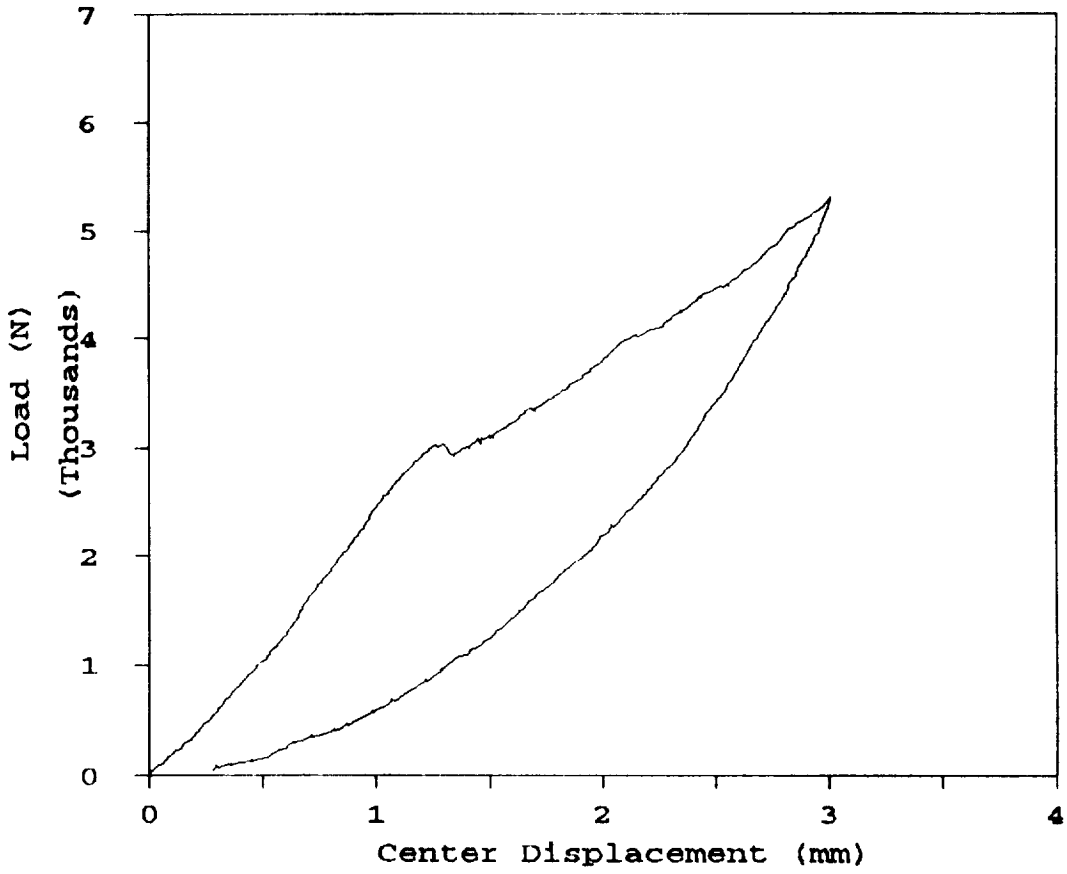

Figure B.18 Load-displacement diagram of STA28

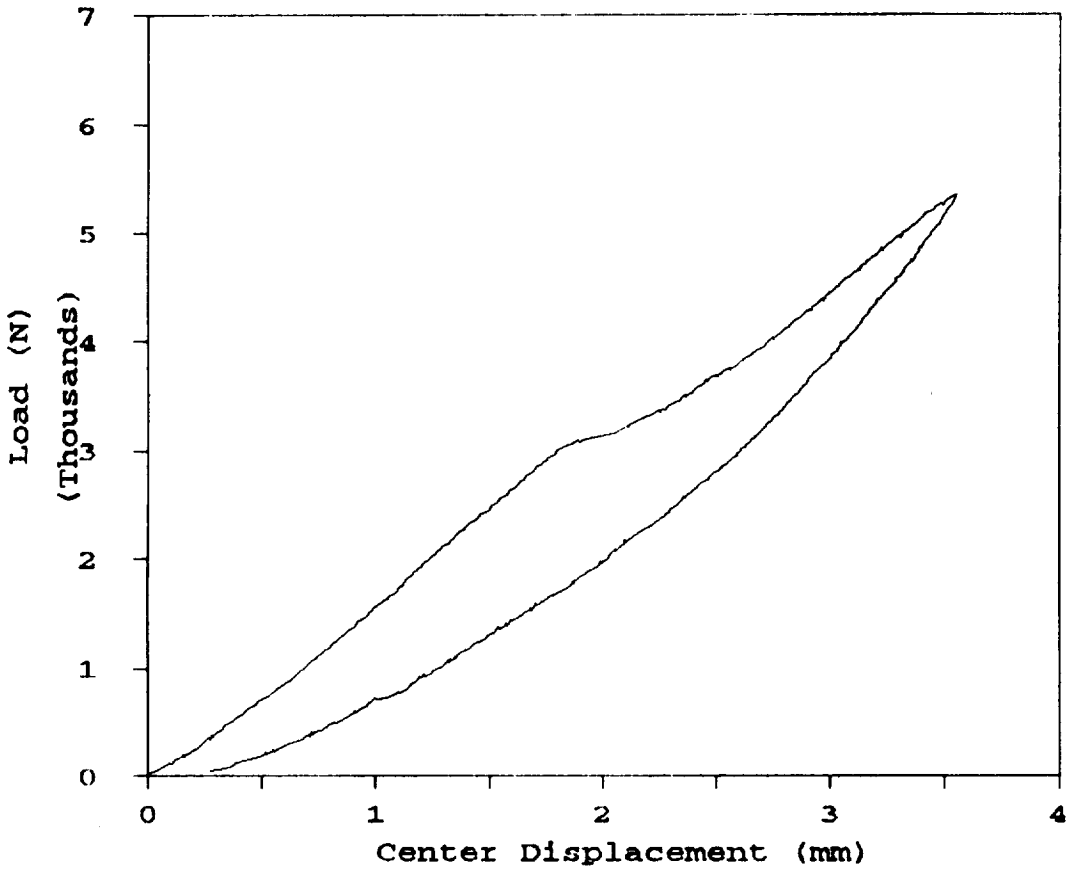

Figure B.19 Load-displacement diagram of STA29

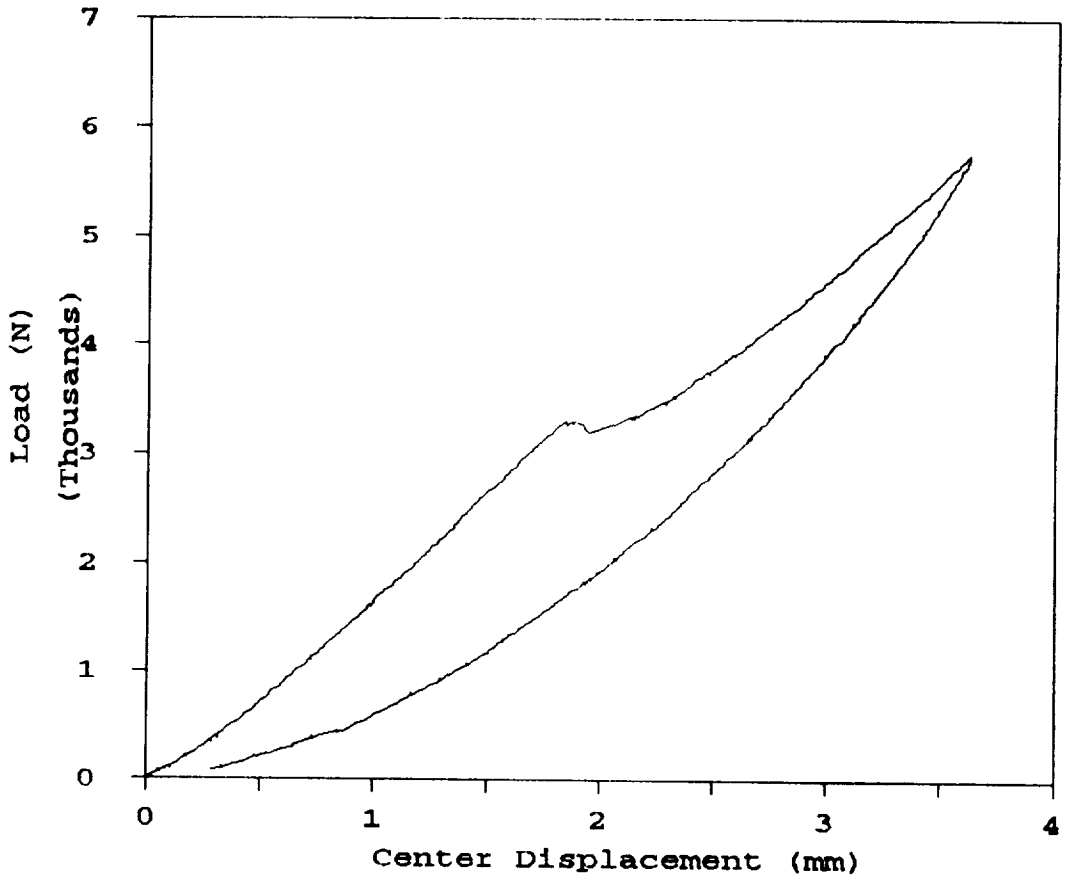

Figure B.20 Load-displacement diagram of STA30

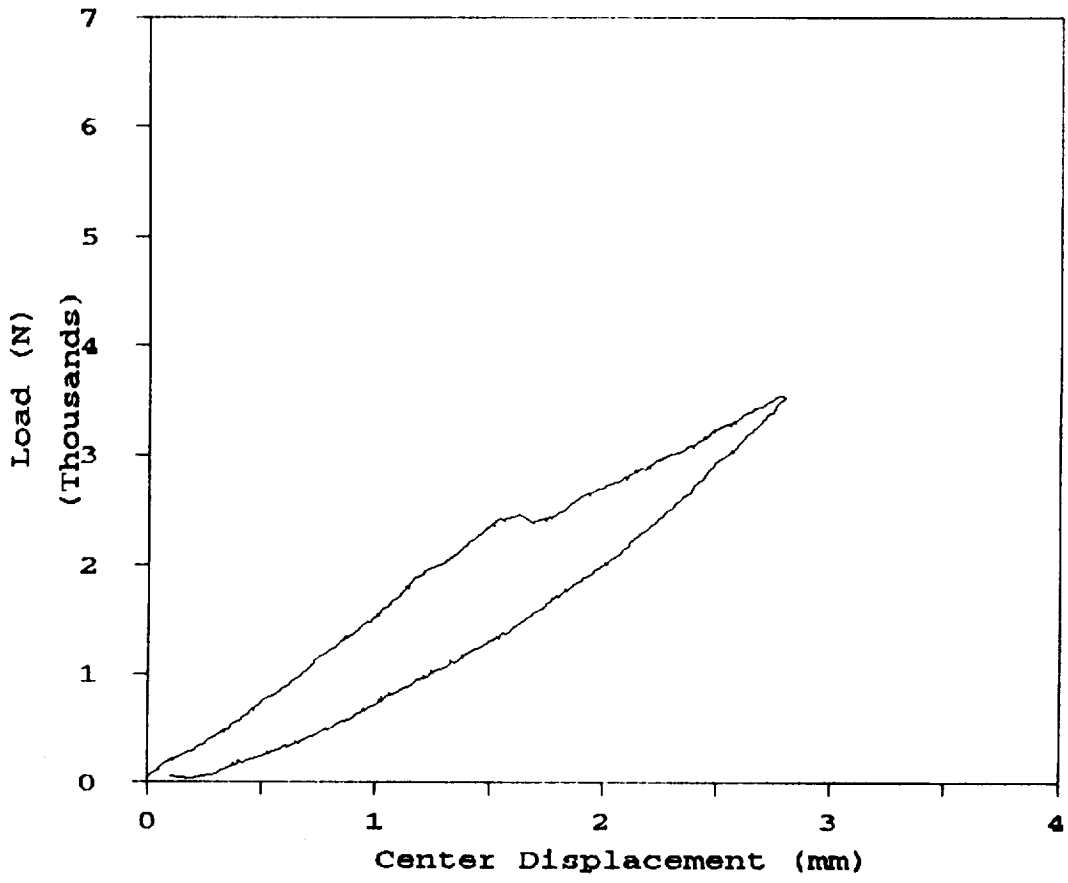

Figure B.21 Load-diaplacement diagram of STA31

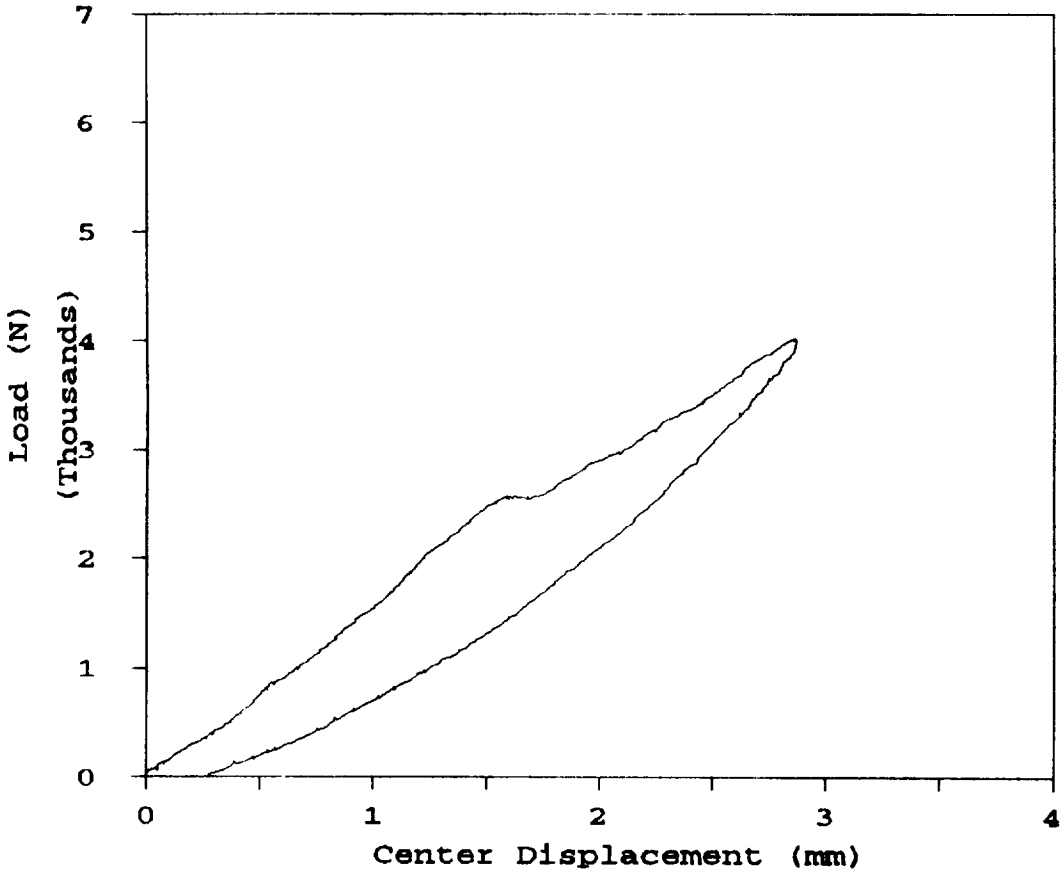

Figure B.22 Load-displacement diagram of STA32

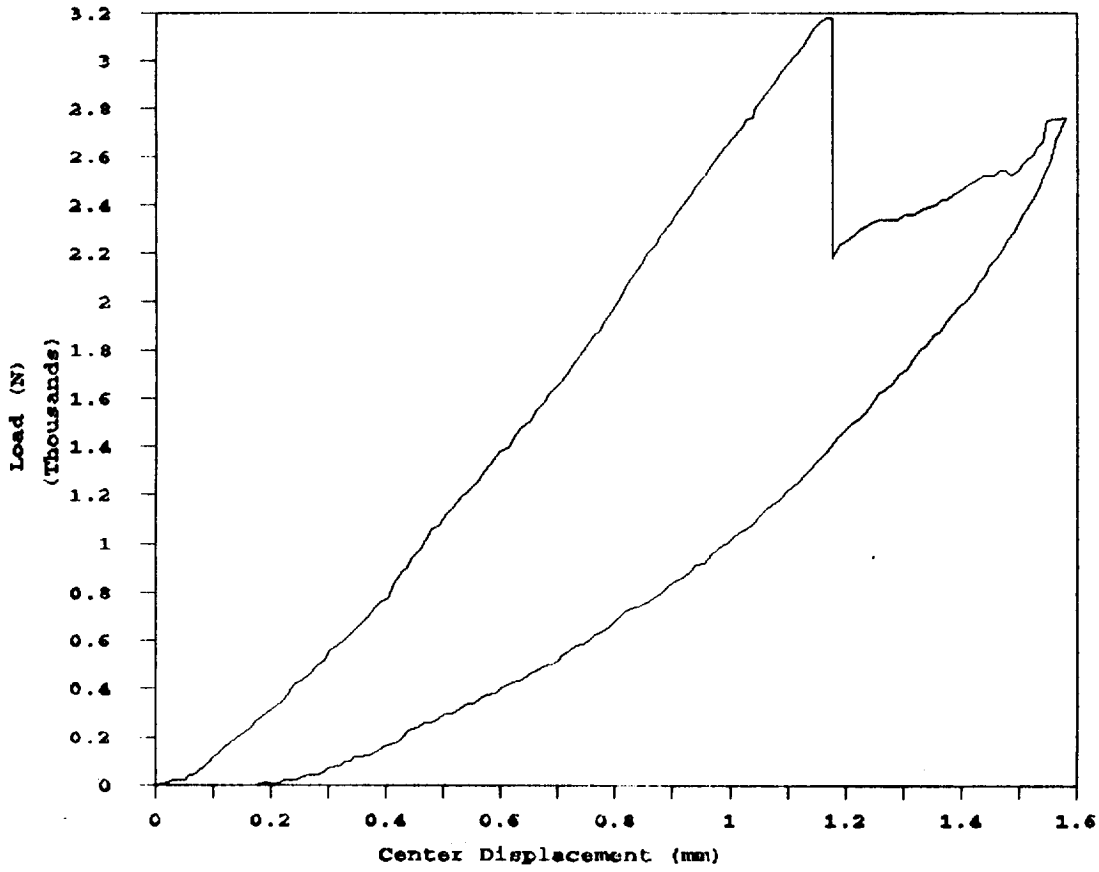

Figure B.23 Load-displacement diagram of STB5

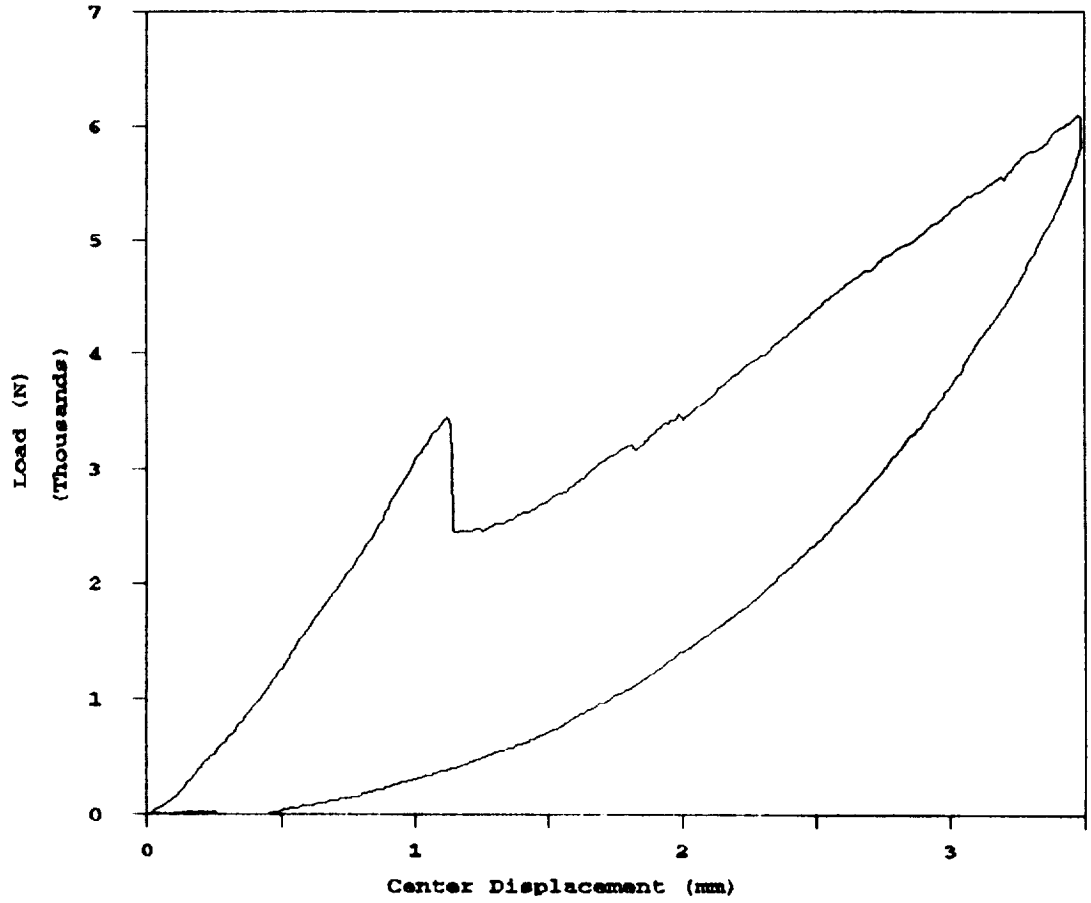

Figure B.24 Load-displacement diagram of STB6

C-2

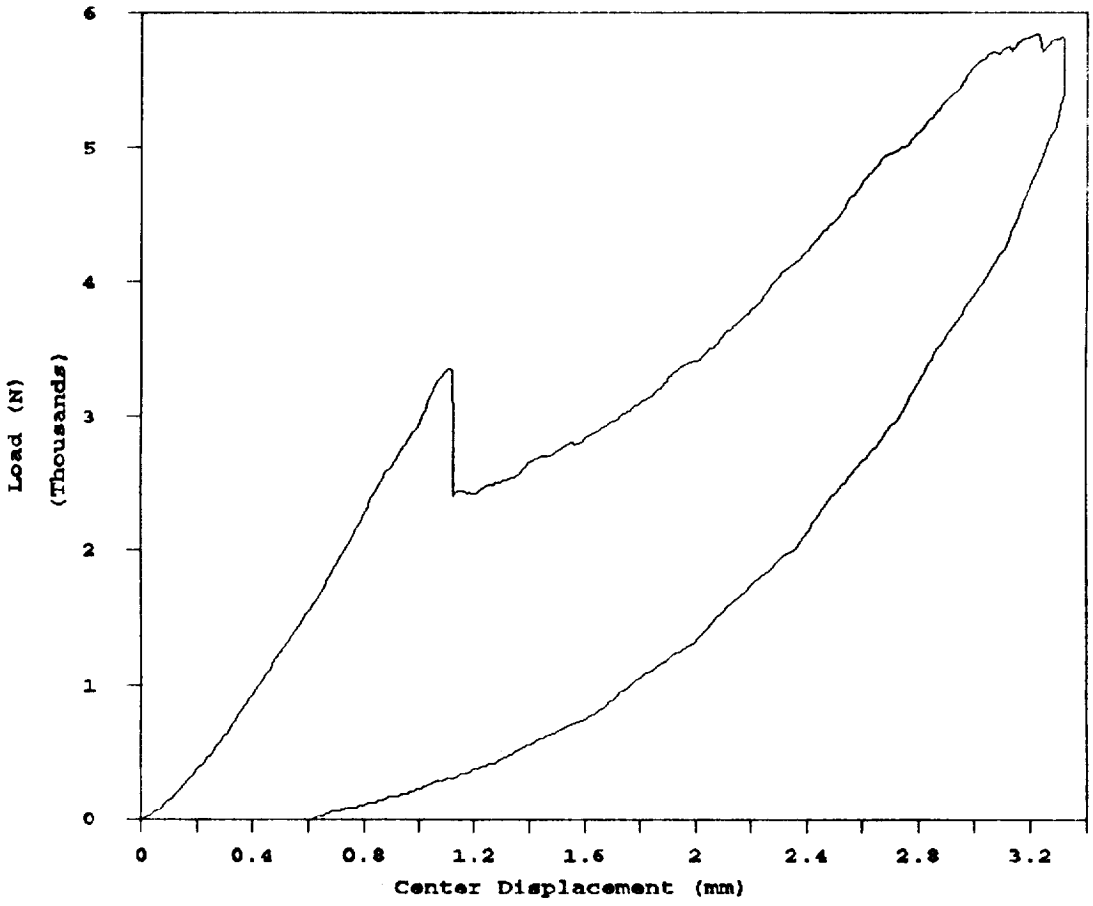

Figure B.25 Load-displacement diagram of STB7

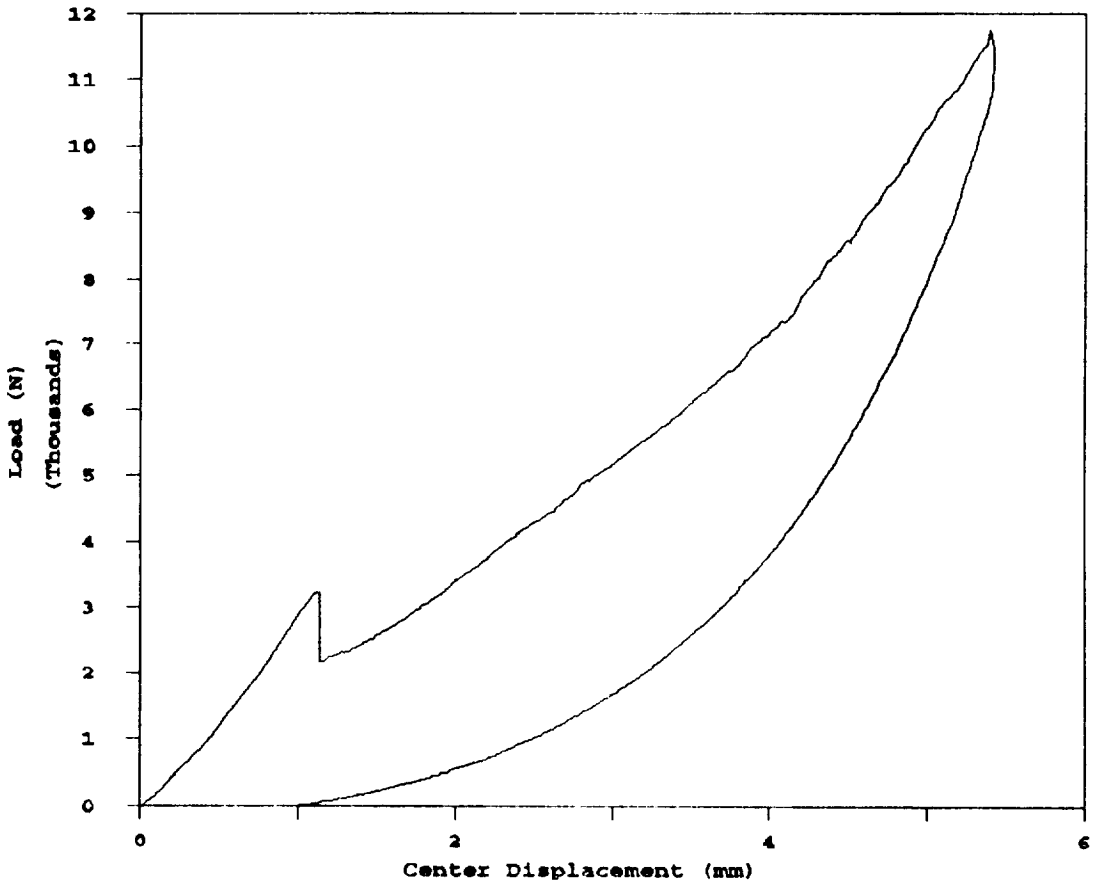

Figure B.26 Load-displacement diagram of STB8

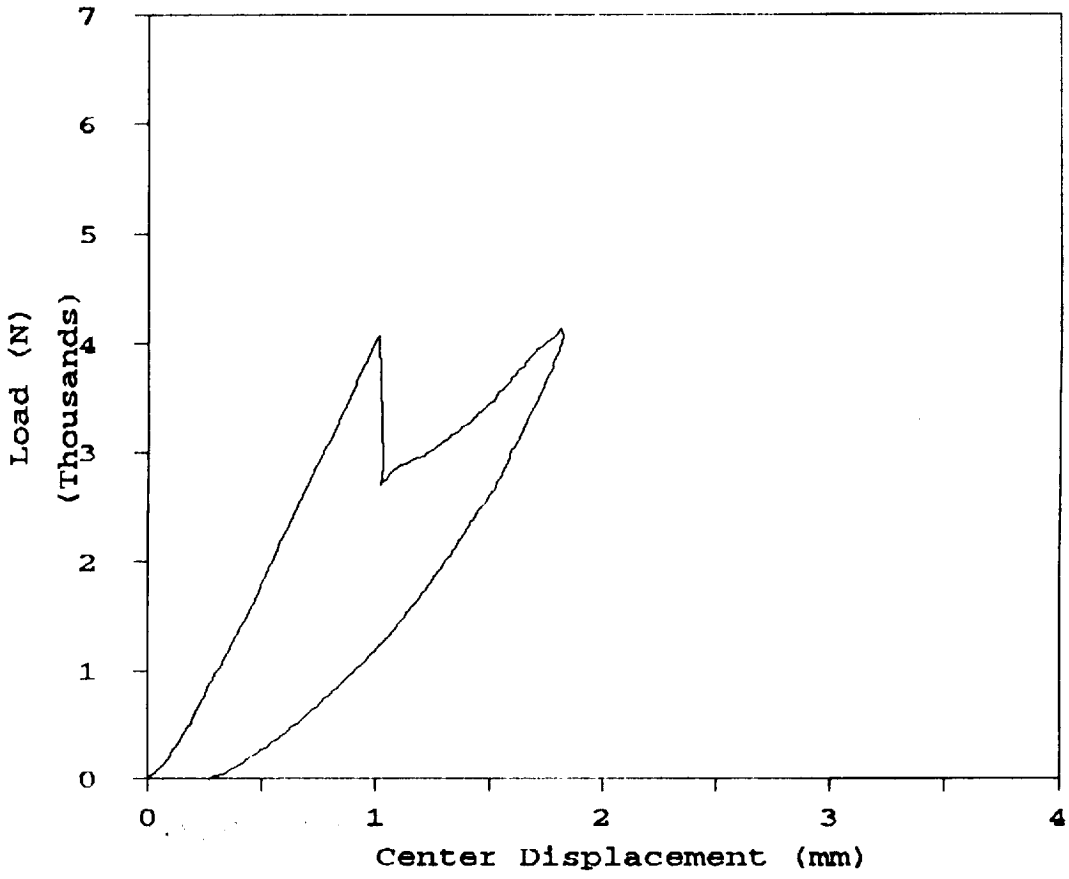

Figure B.27 Load-displacement diagram of STB9

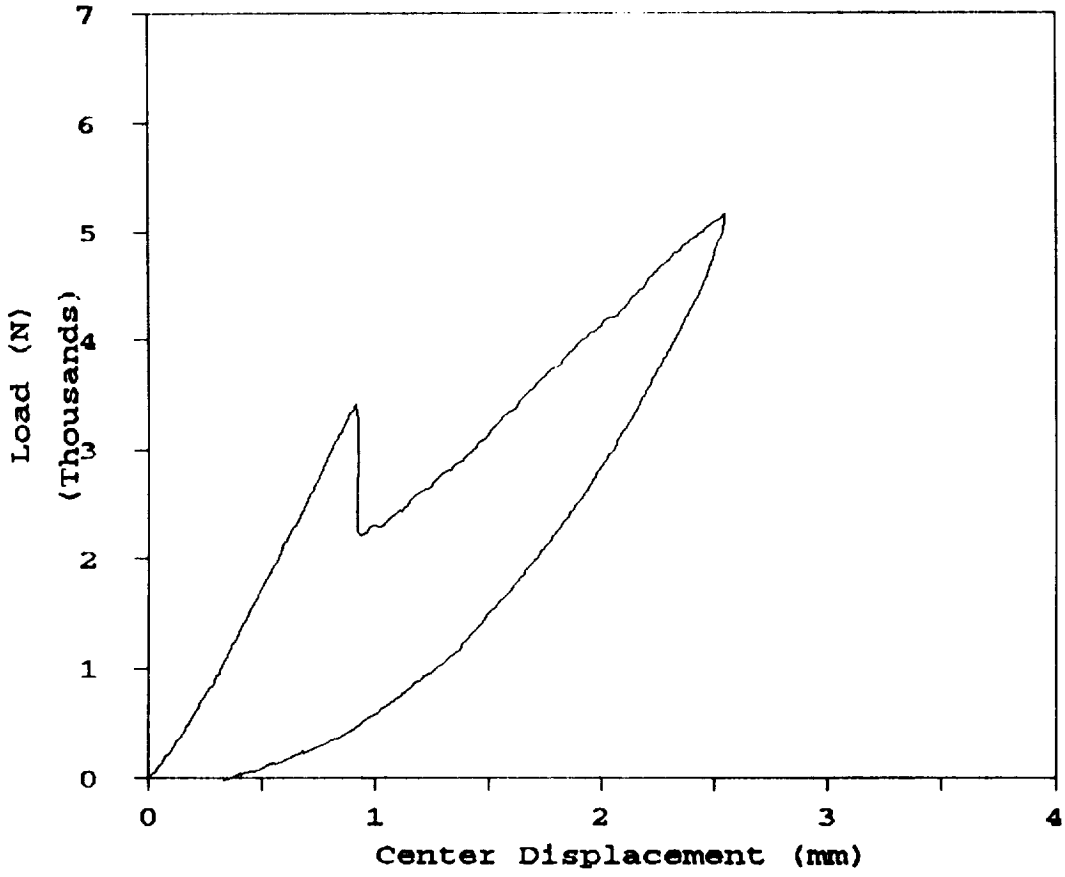

Figure B.28 Load-displacement diagram of STB10

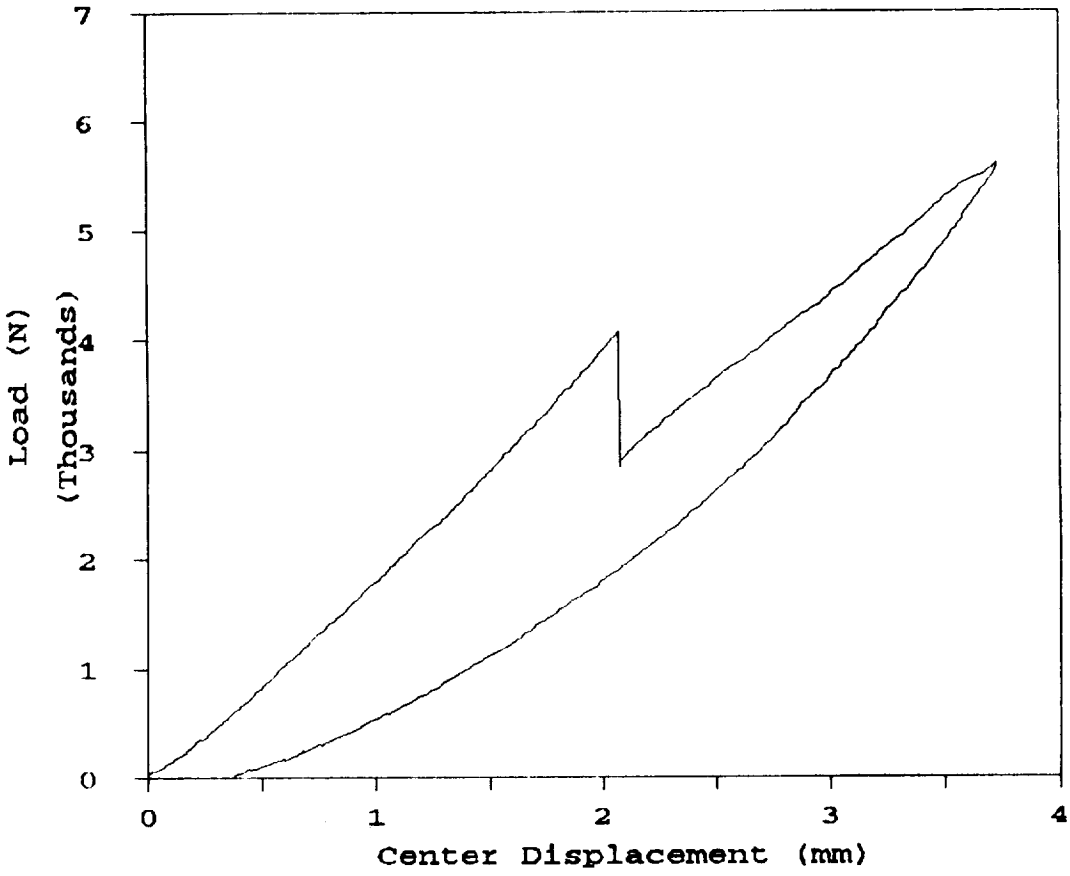

Figure B.29 Load-displacement diagram of STB11

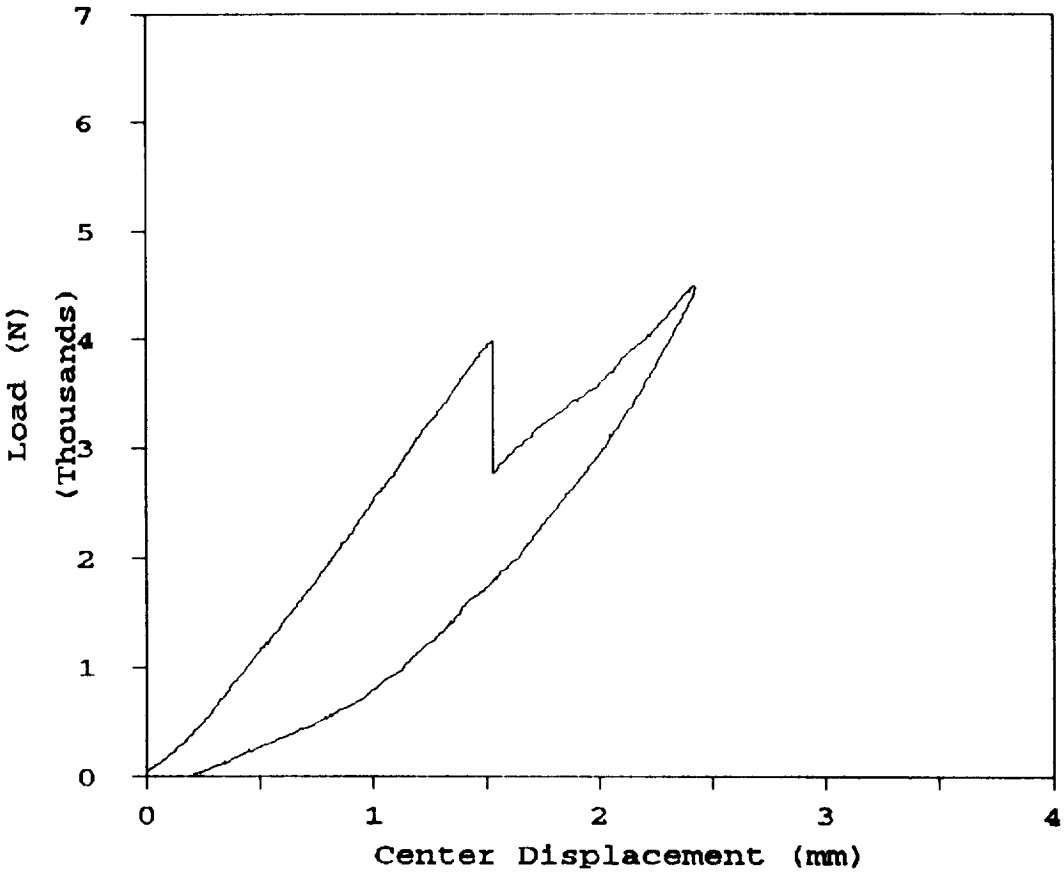

Figure B.30 Load-displacement diagram of STB12

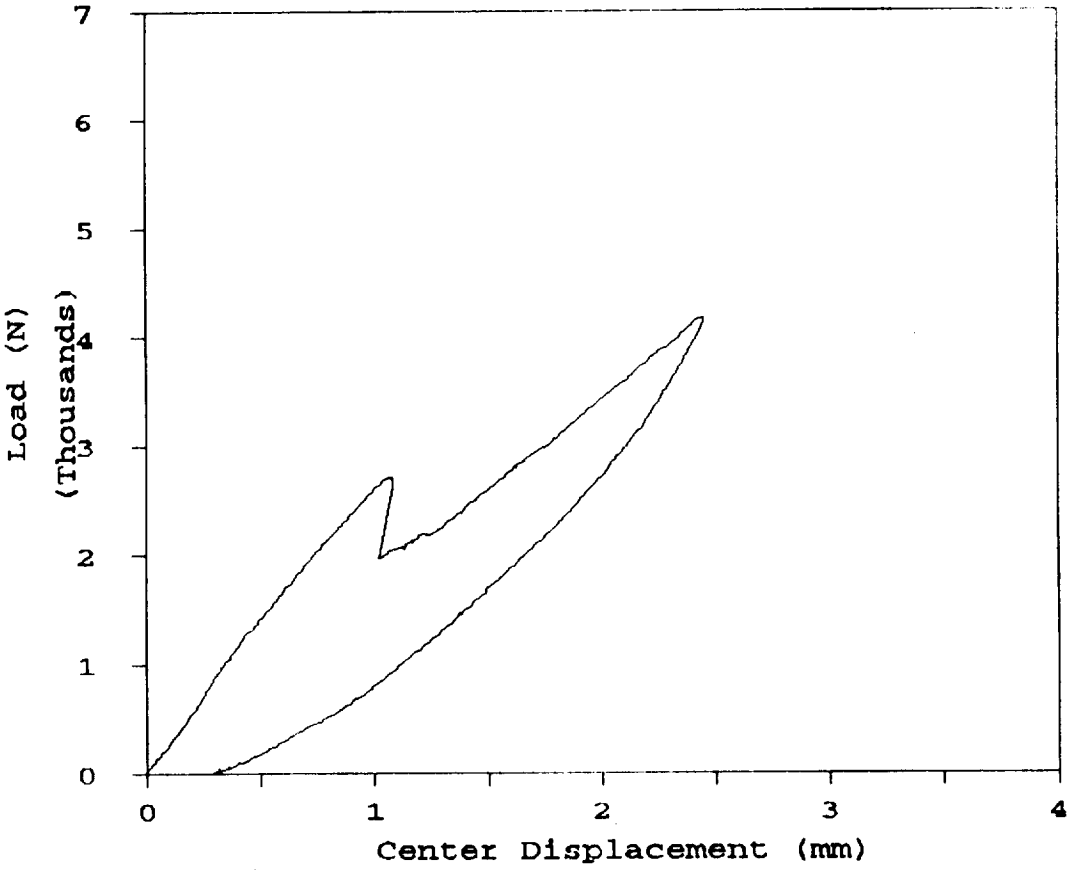

Figure B.31 Load-displacement diagram of STB13

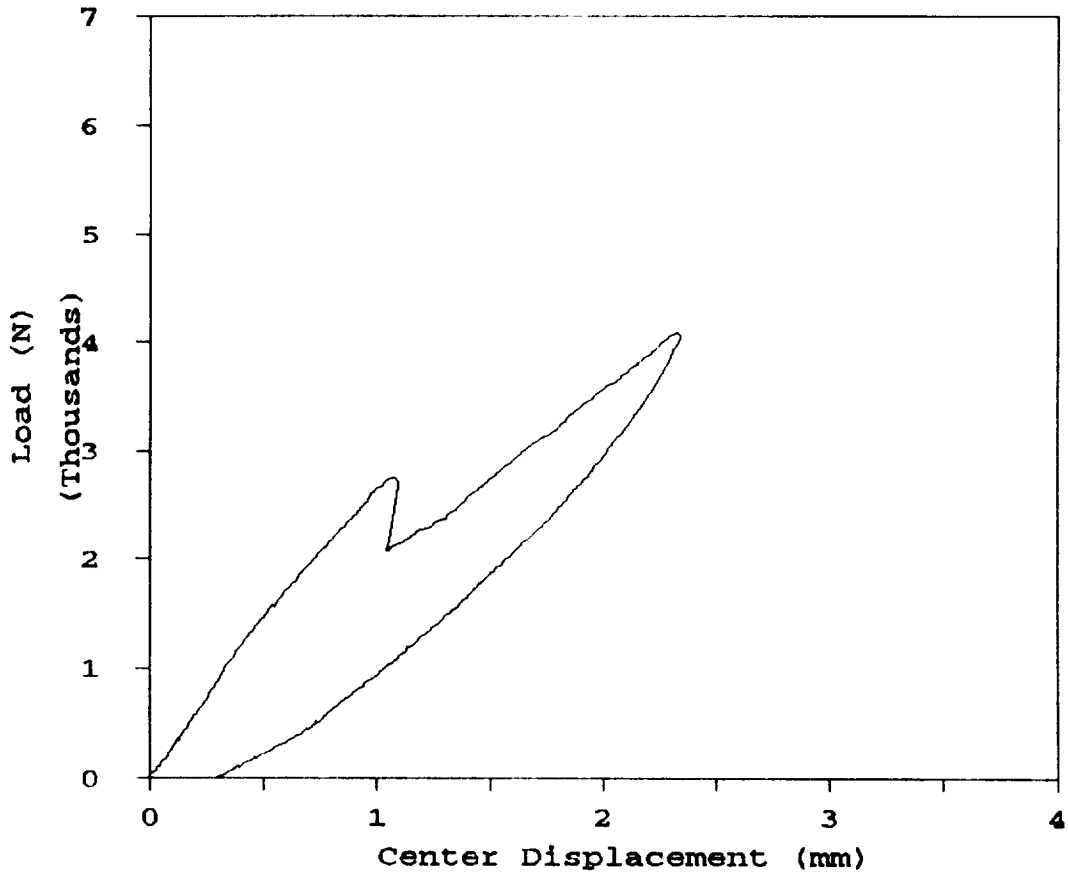

Figure B.32 Load-displacement diagram of STB14

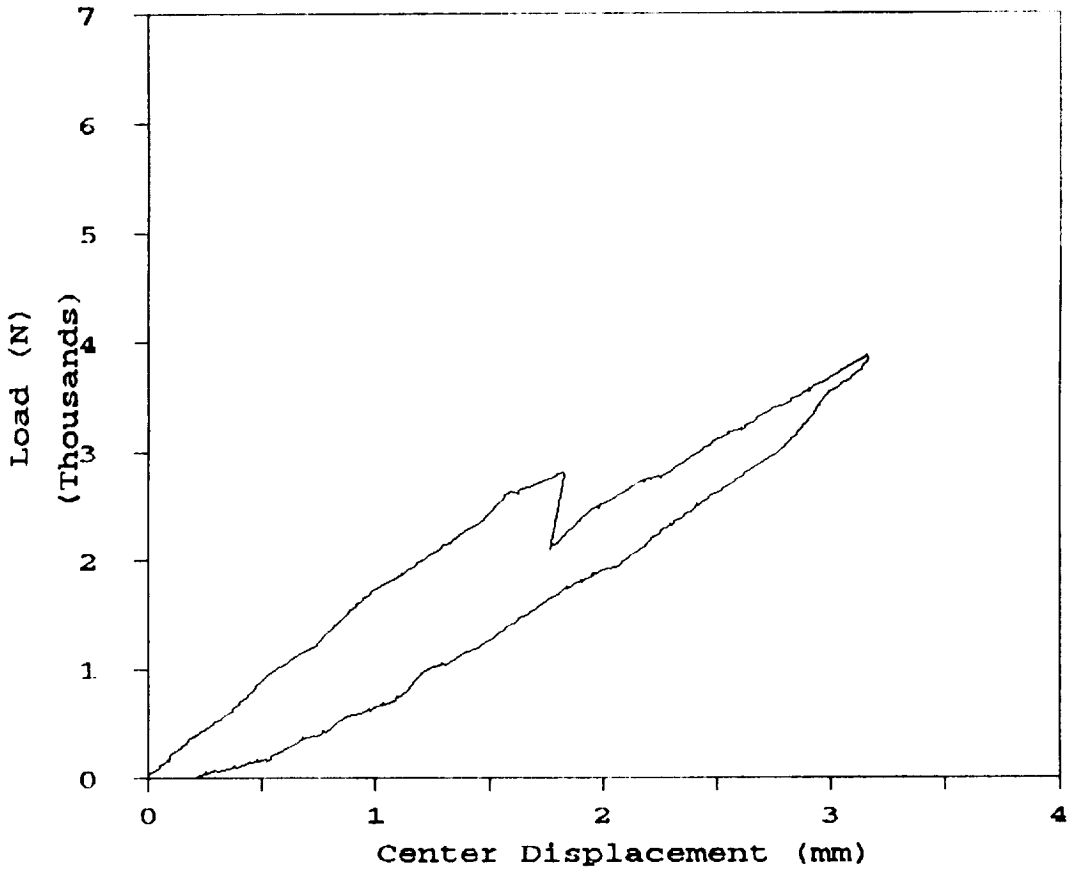

Figure B.33 Load-displacement diagram of STB15

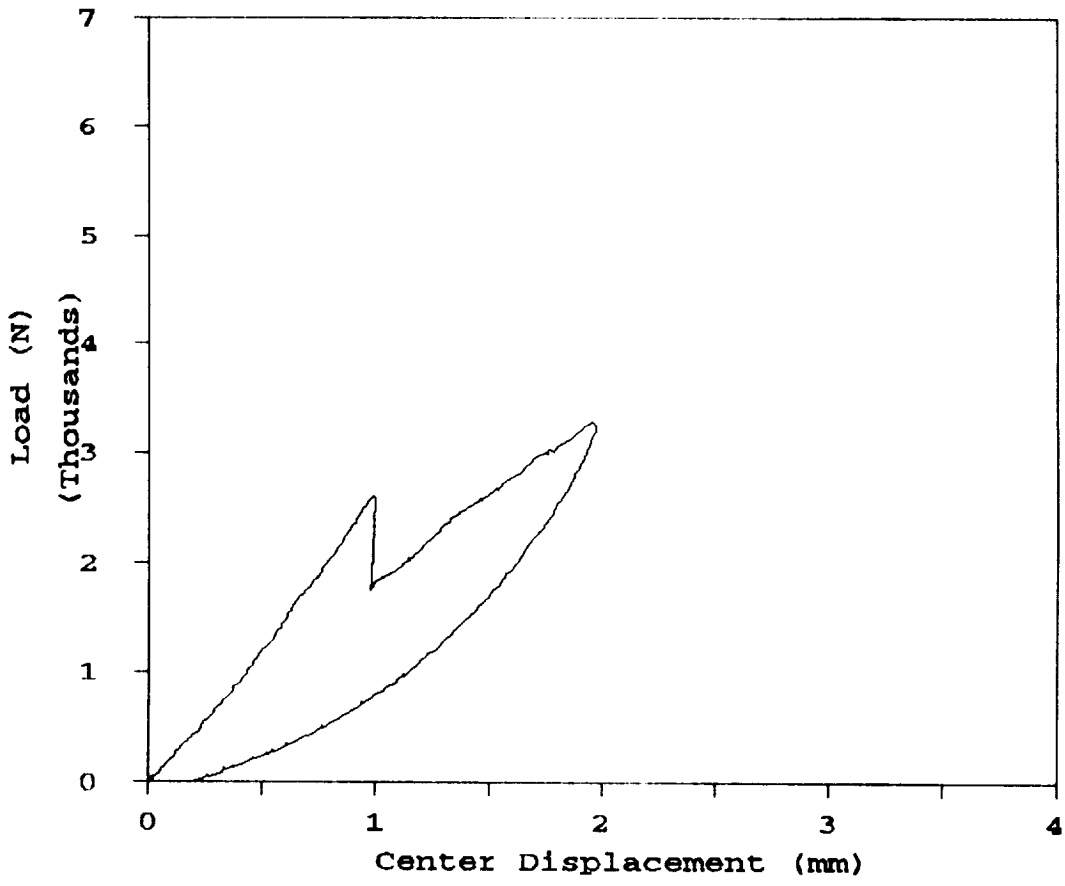

Figure B.34 Load-displacement diagram of STB16

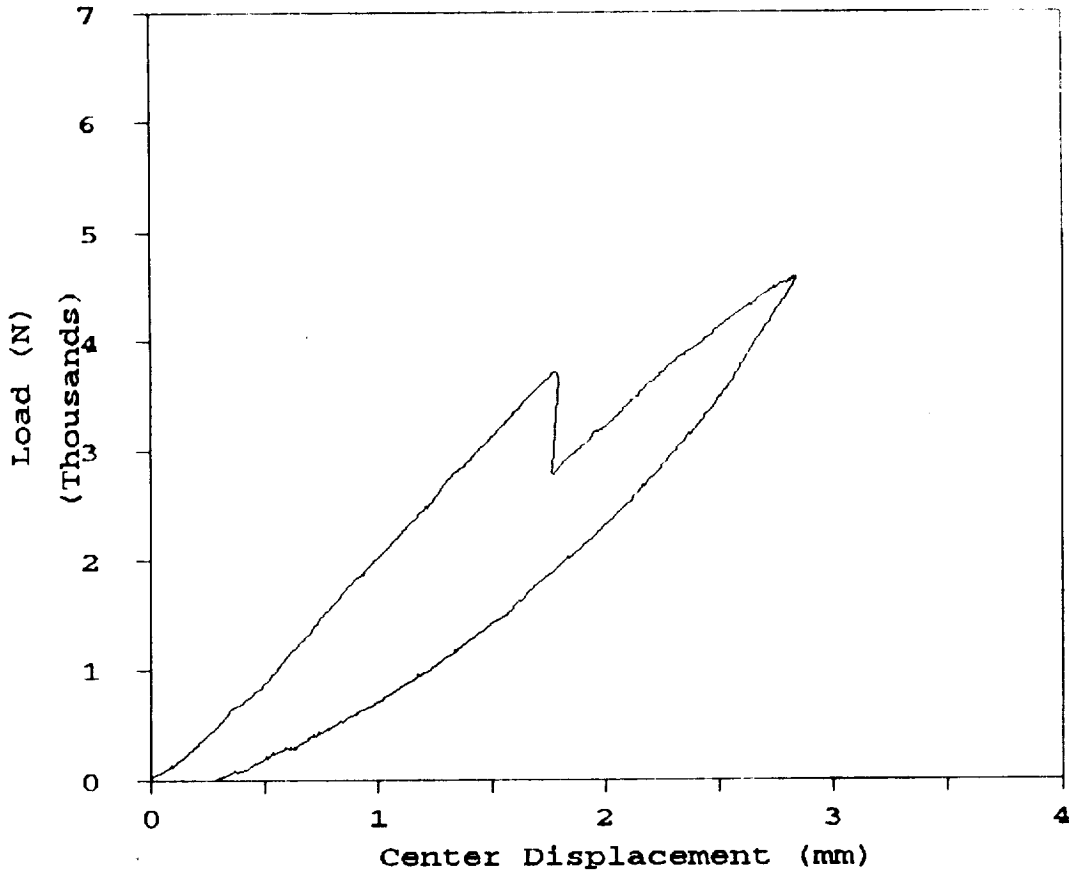

Figure B.35 Load-displacement diagram of STB17

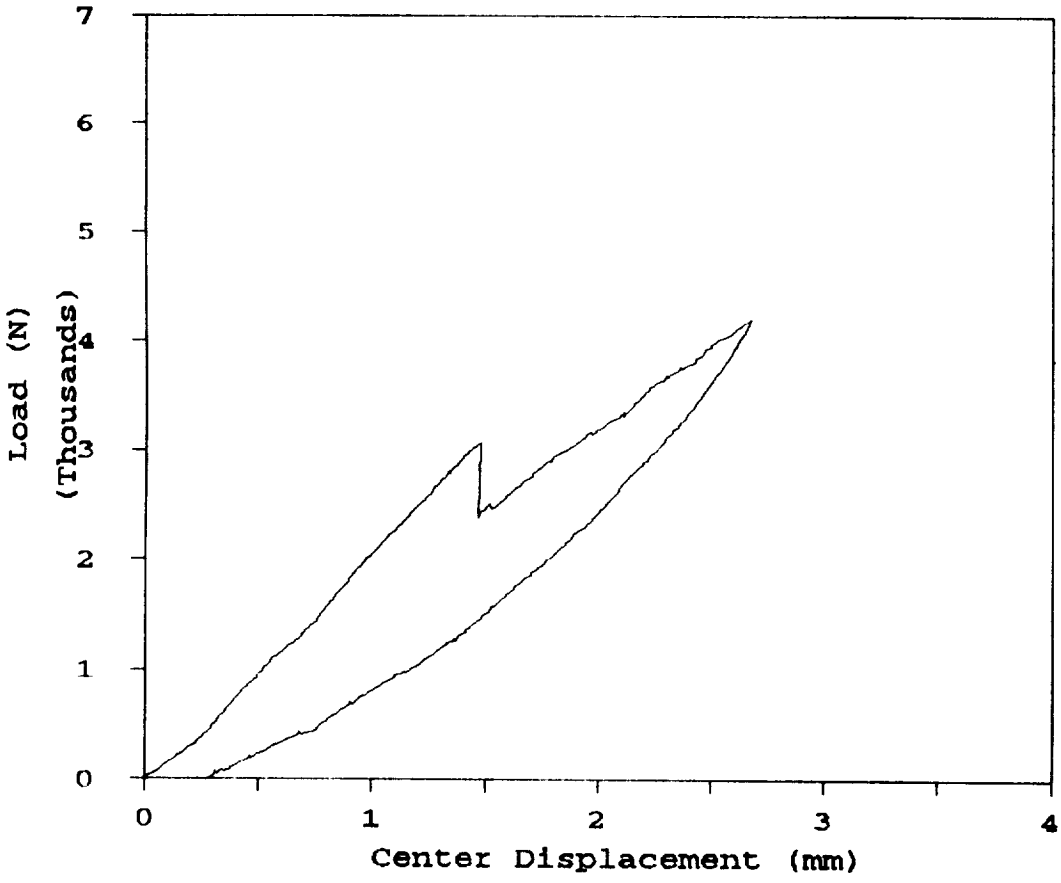

Figure B.36 Load-displacement diagram of STB18

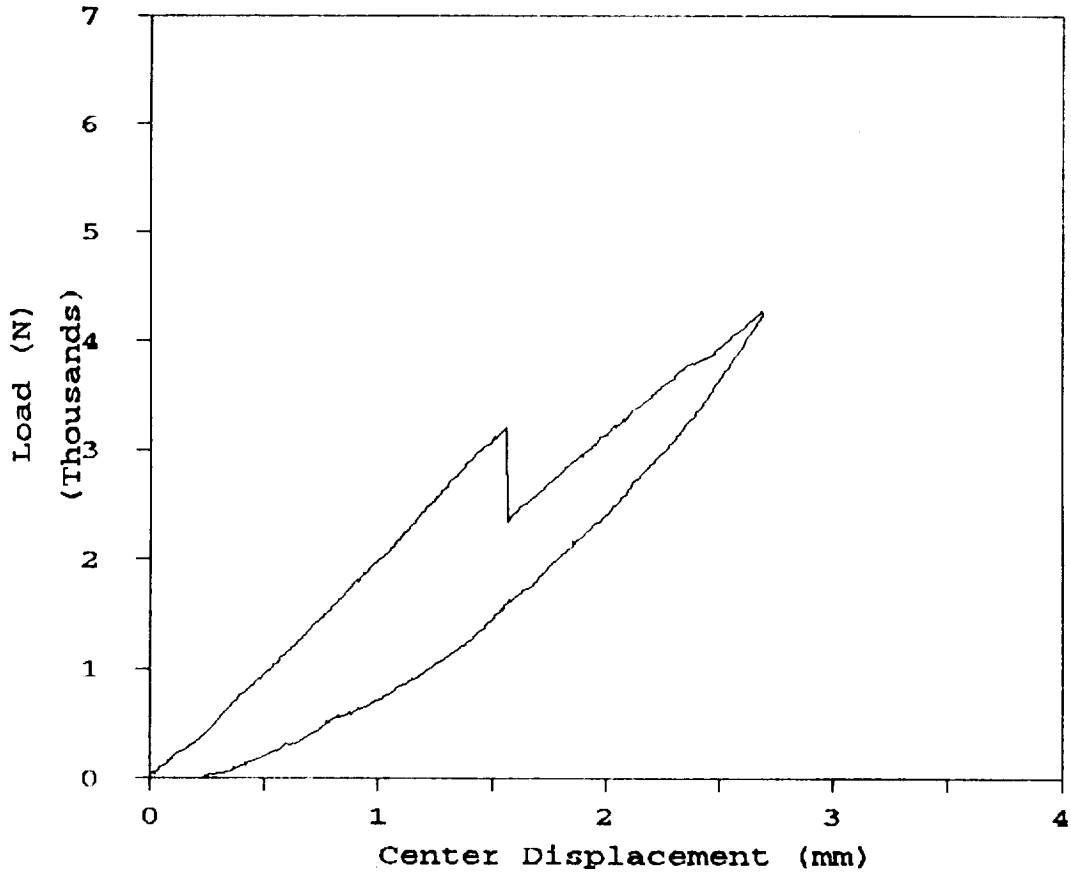

Figure B.37 Load-displacement diagram of STB19

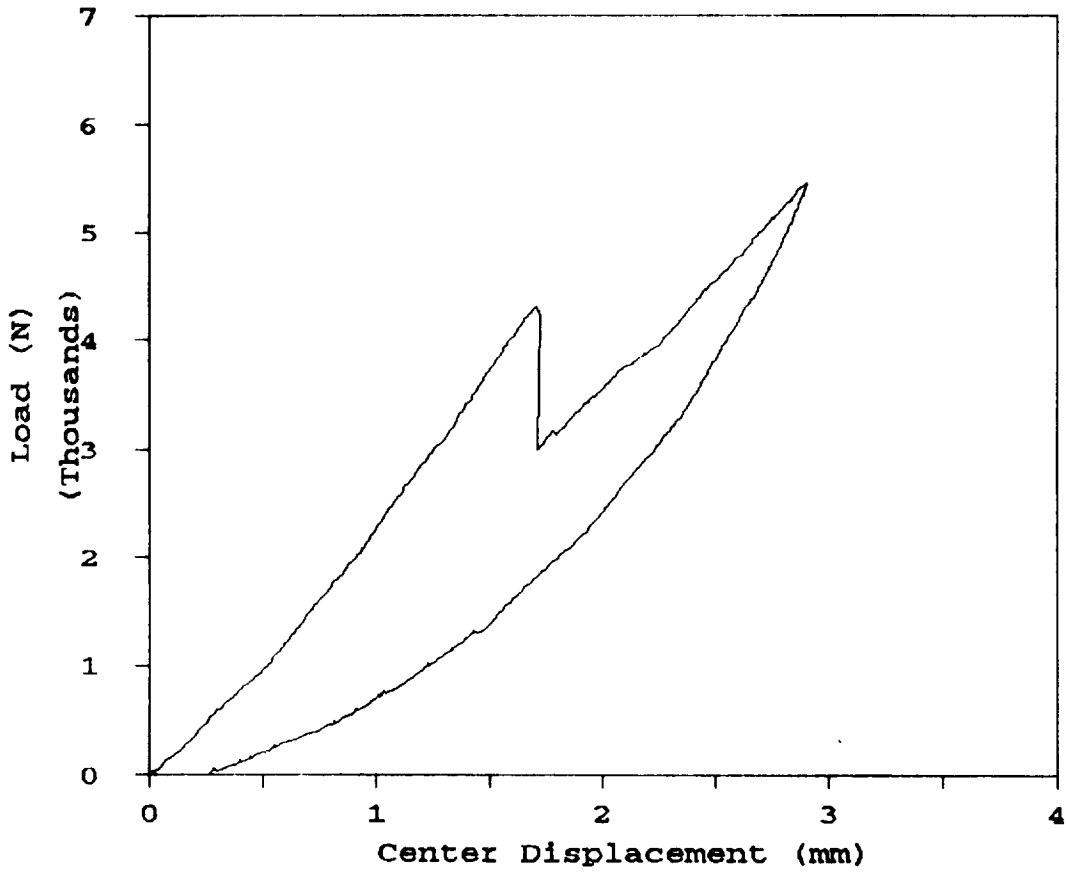

Figure B.38 Load-displacement diagram of STB20

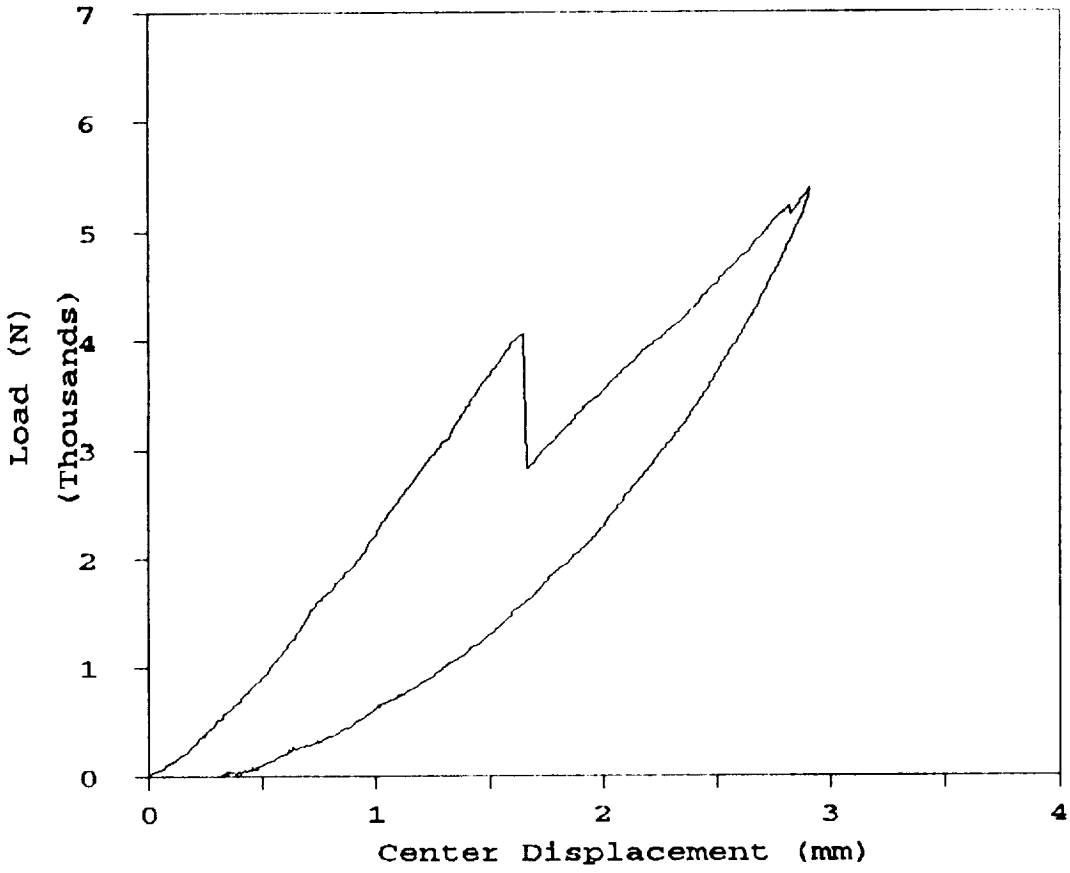

Figure B.39 Load-displacement diagram of STB21

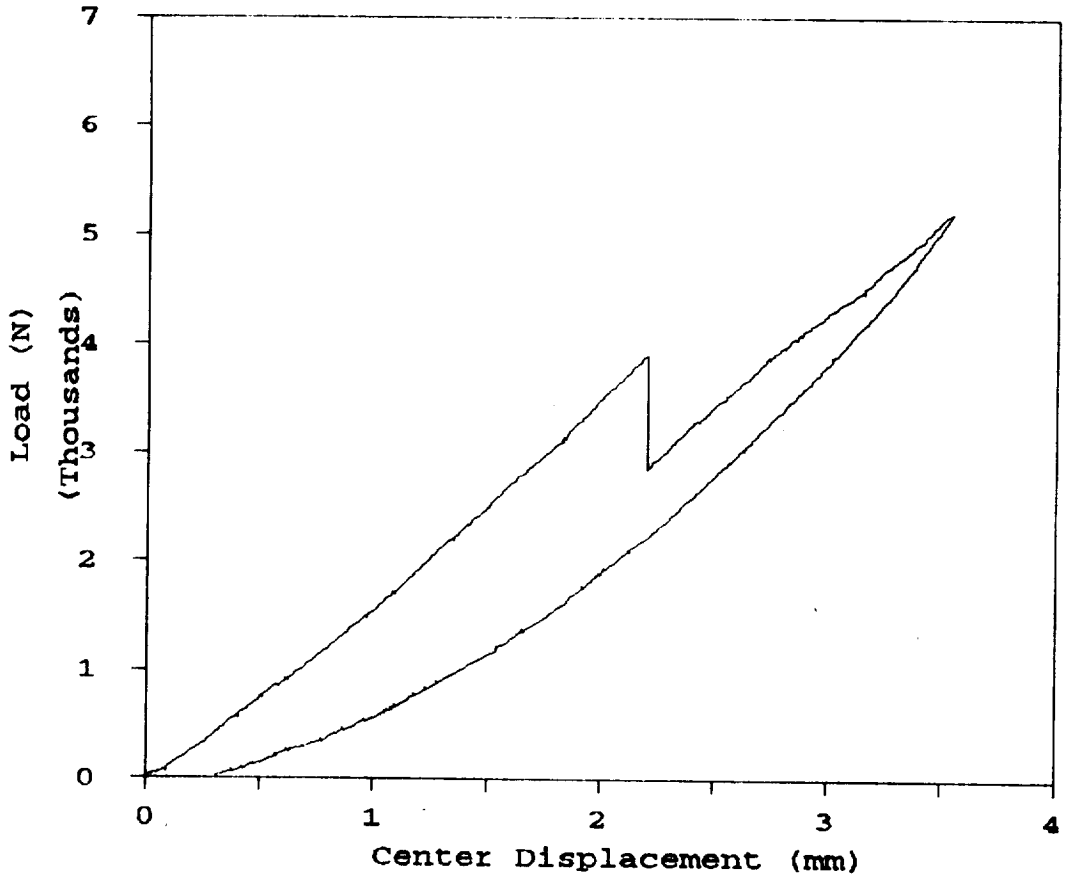

Figure B.40 Load-displacement diagram of STB22

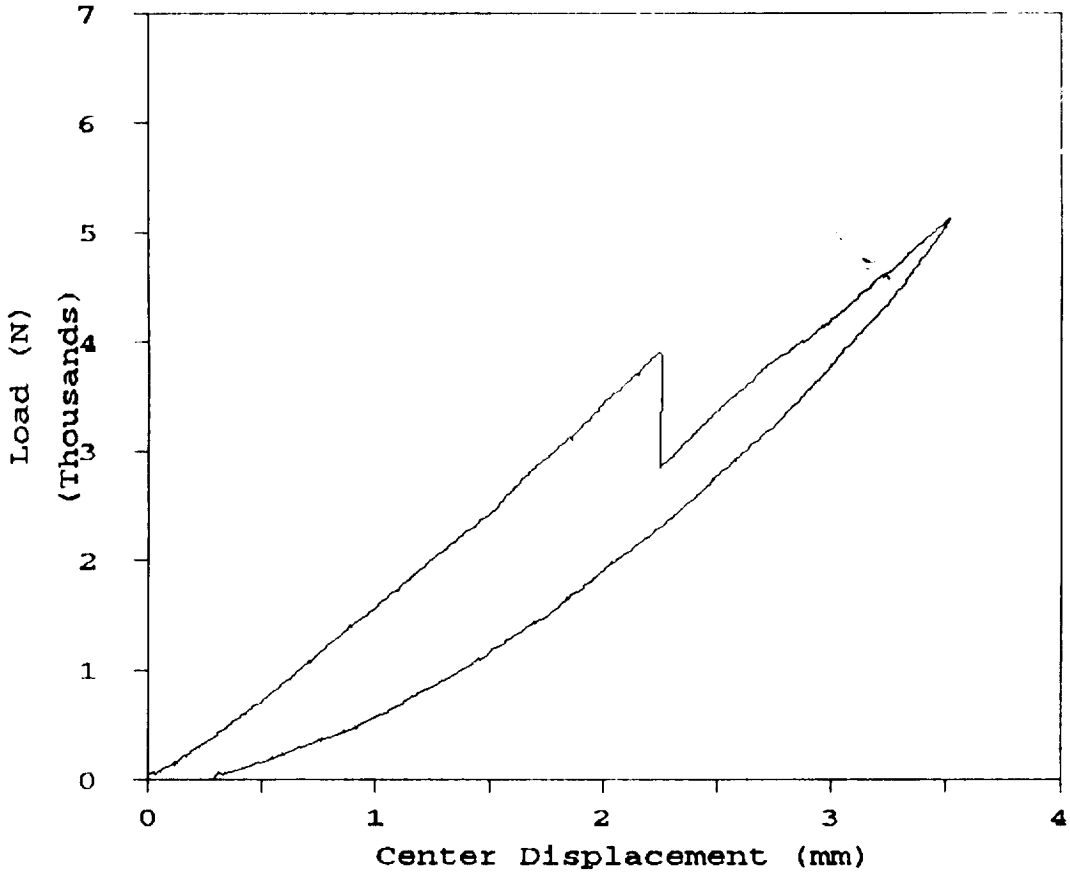

Figure B.41 Load-displacement diagram of STB23

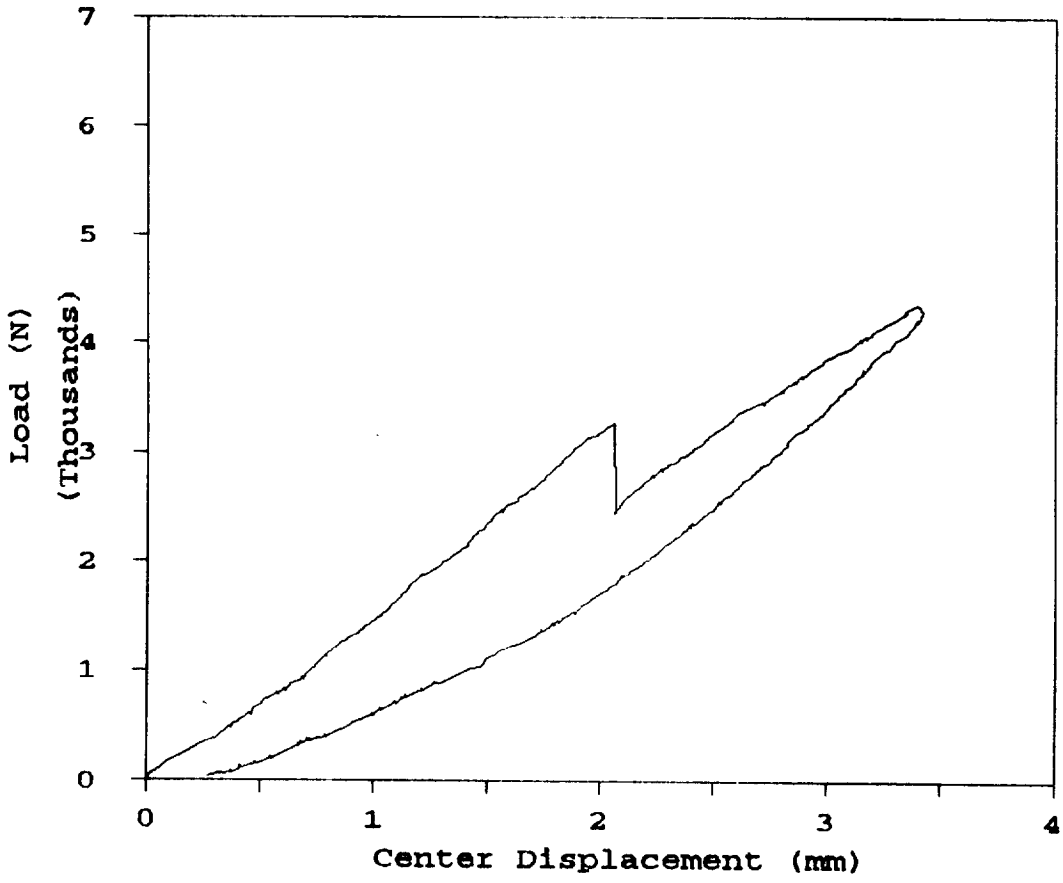

Figure B.42 Load-displacement diagram of STB24

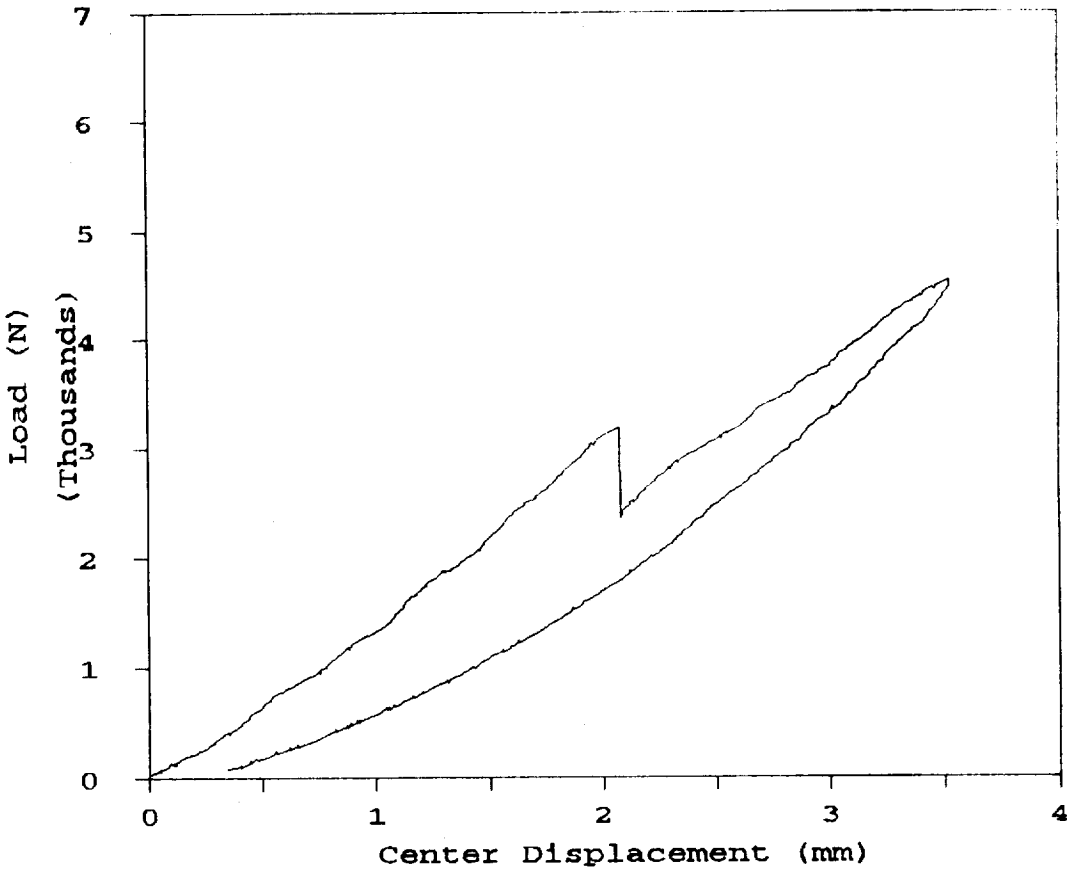

Figure B.43 Load-displacement diagram of STB25

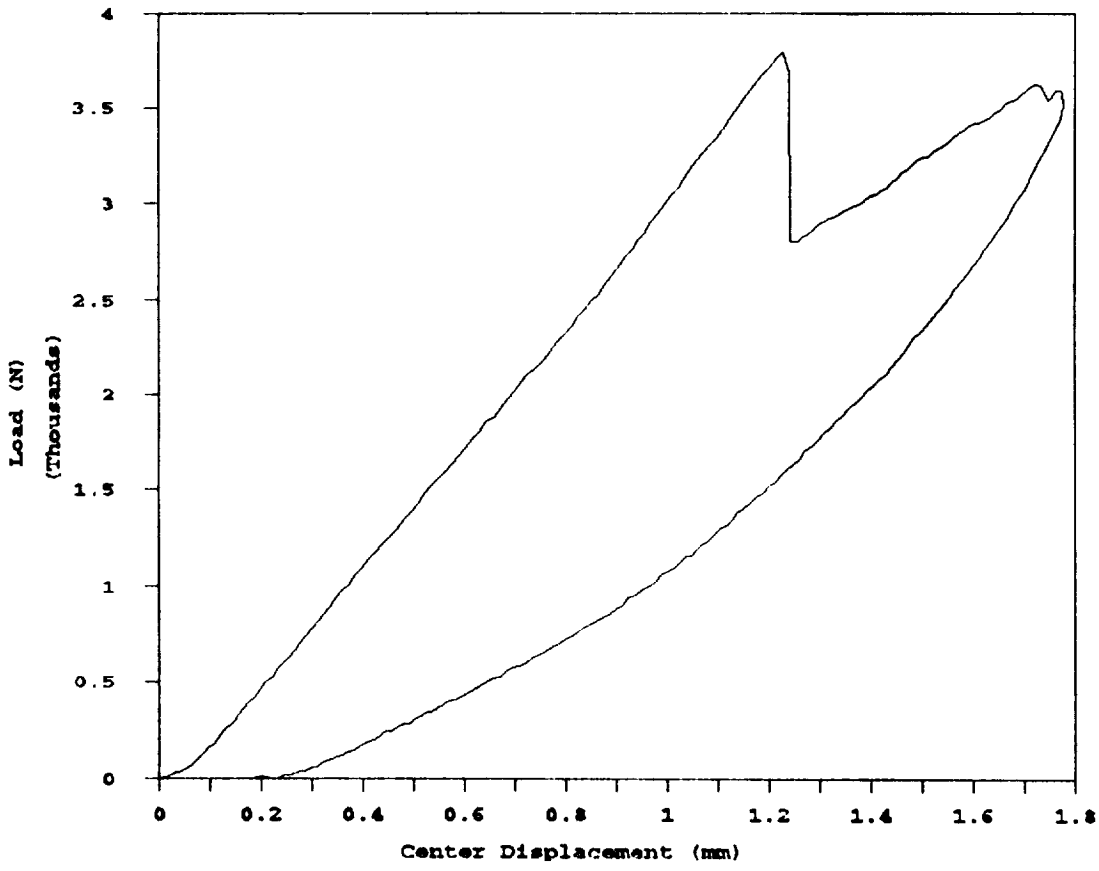

Figure B.44 Load-displacement diagram of STC5

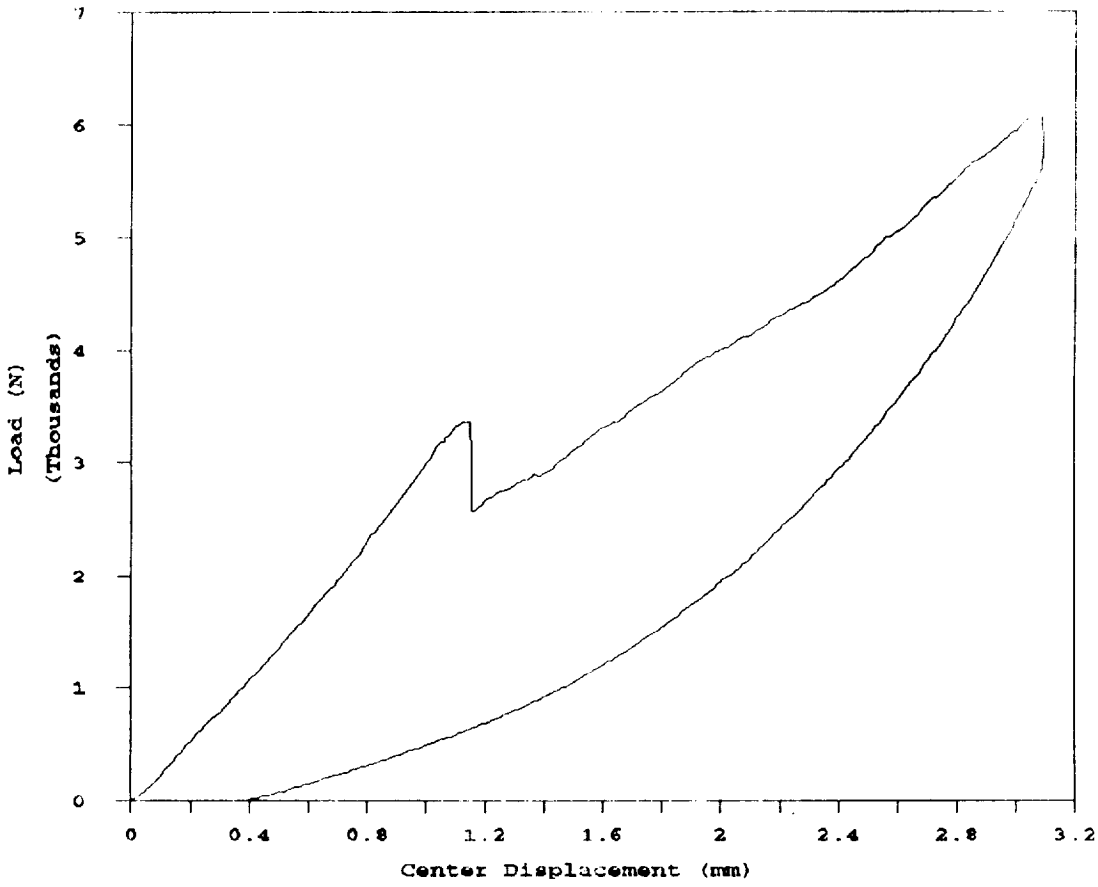

Figure B.45 Load-displacement diagram of STC6

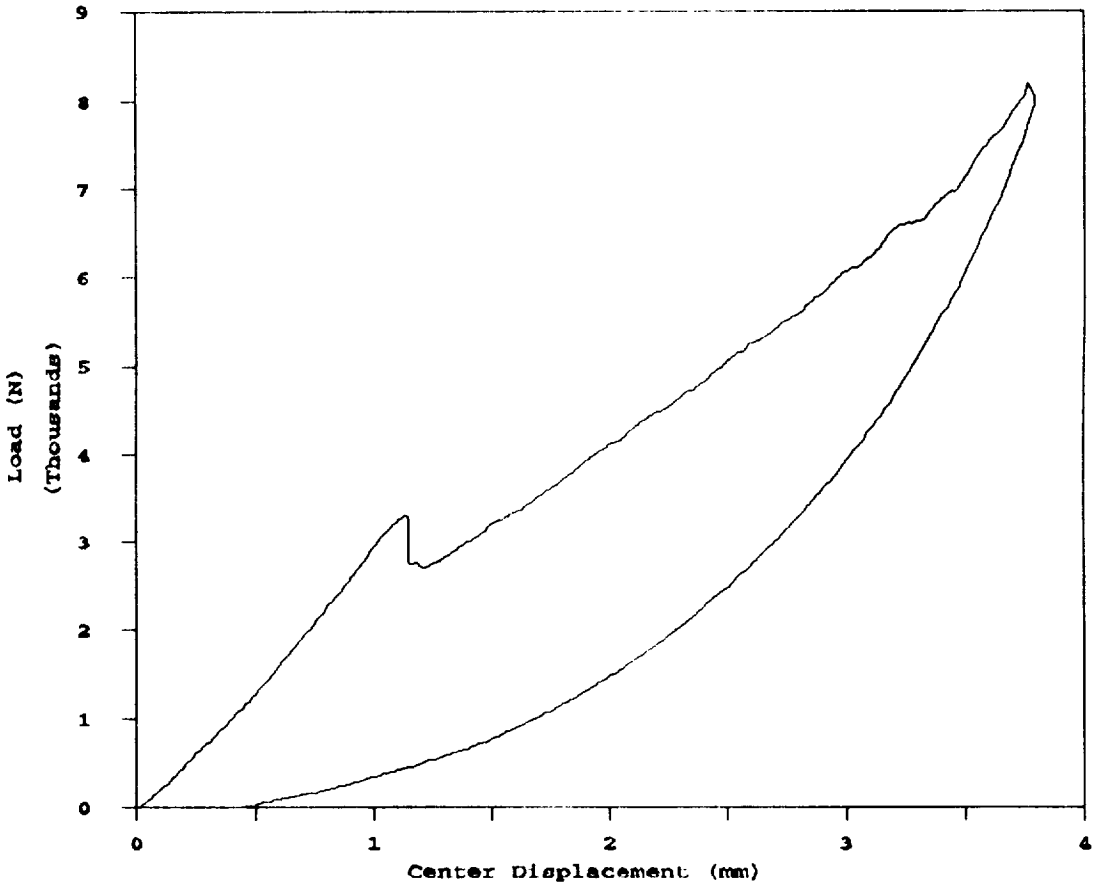

Figure B.46 Load-displacement diagram of STC7

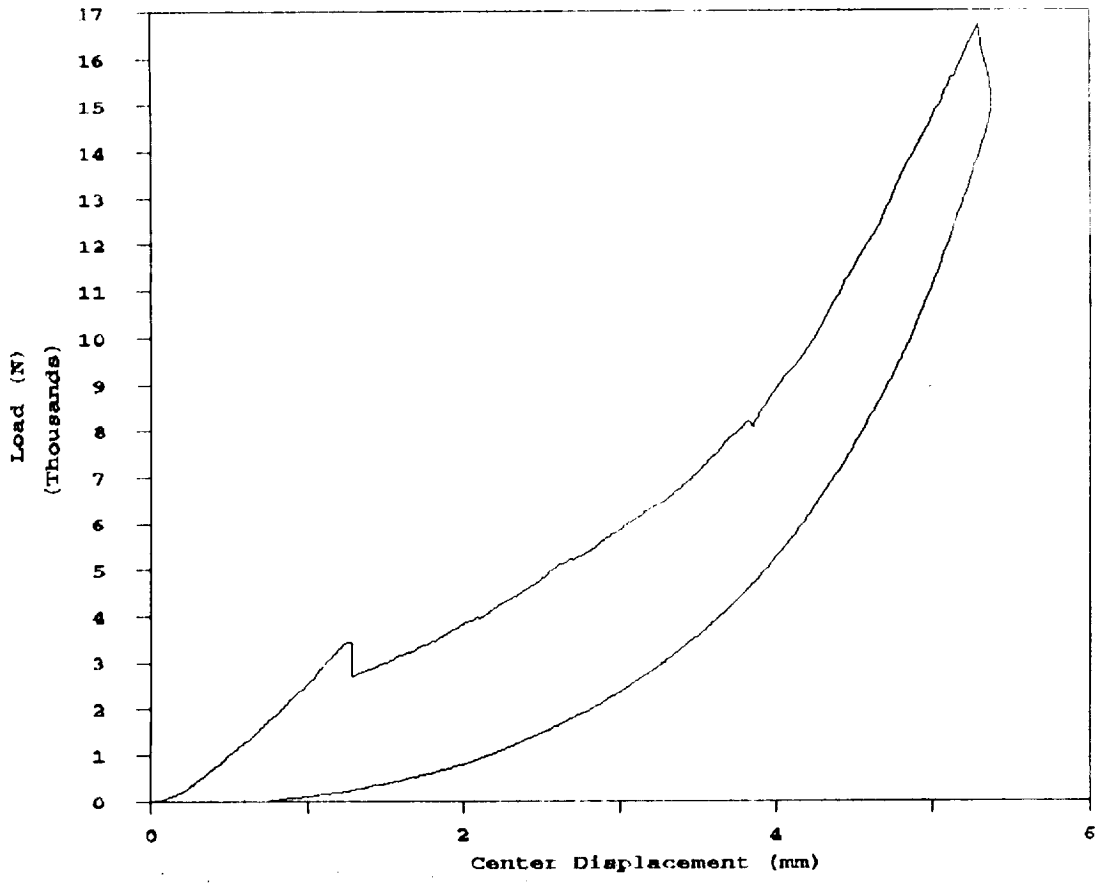

Figure B.47 Load-displacement diagram of STC8

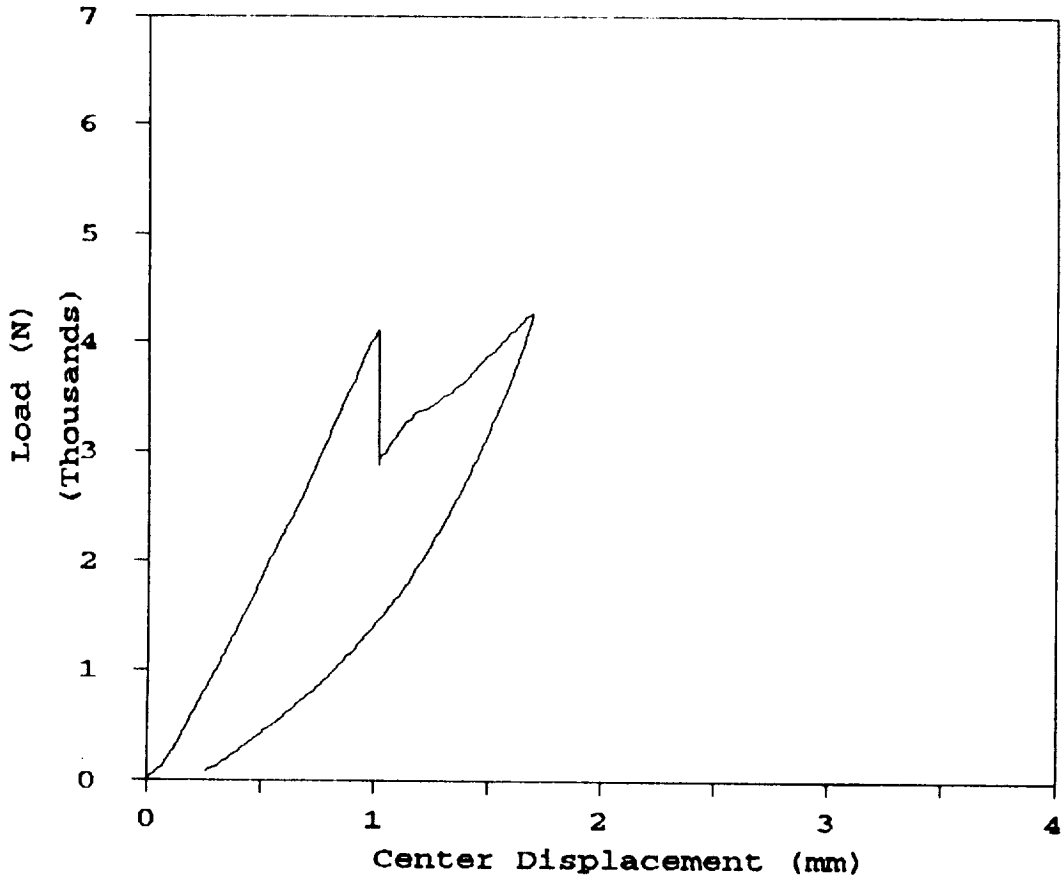

Figure B.48 Load-displacement diagram of STC9

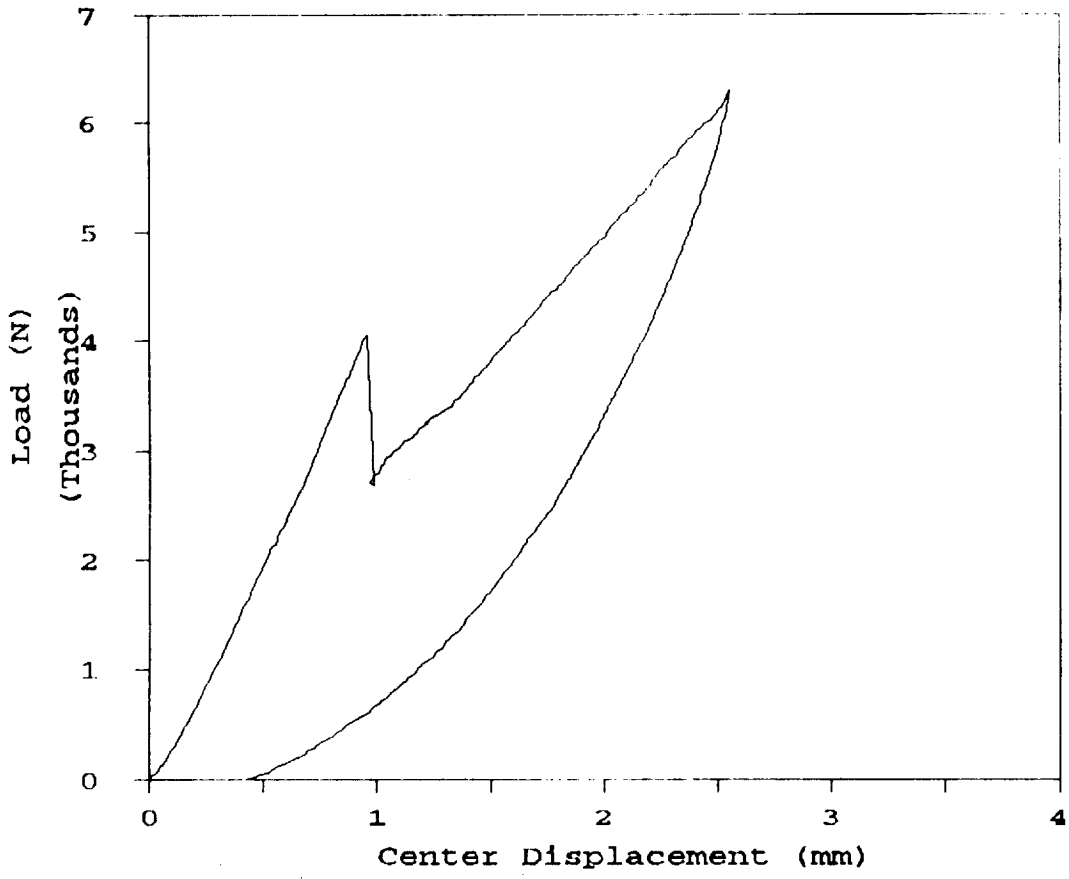

Figure B.49 Load-displacement diagram of STC10

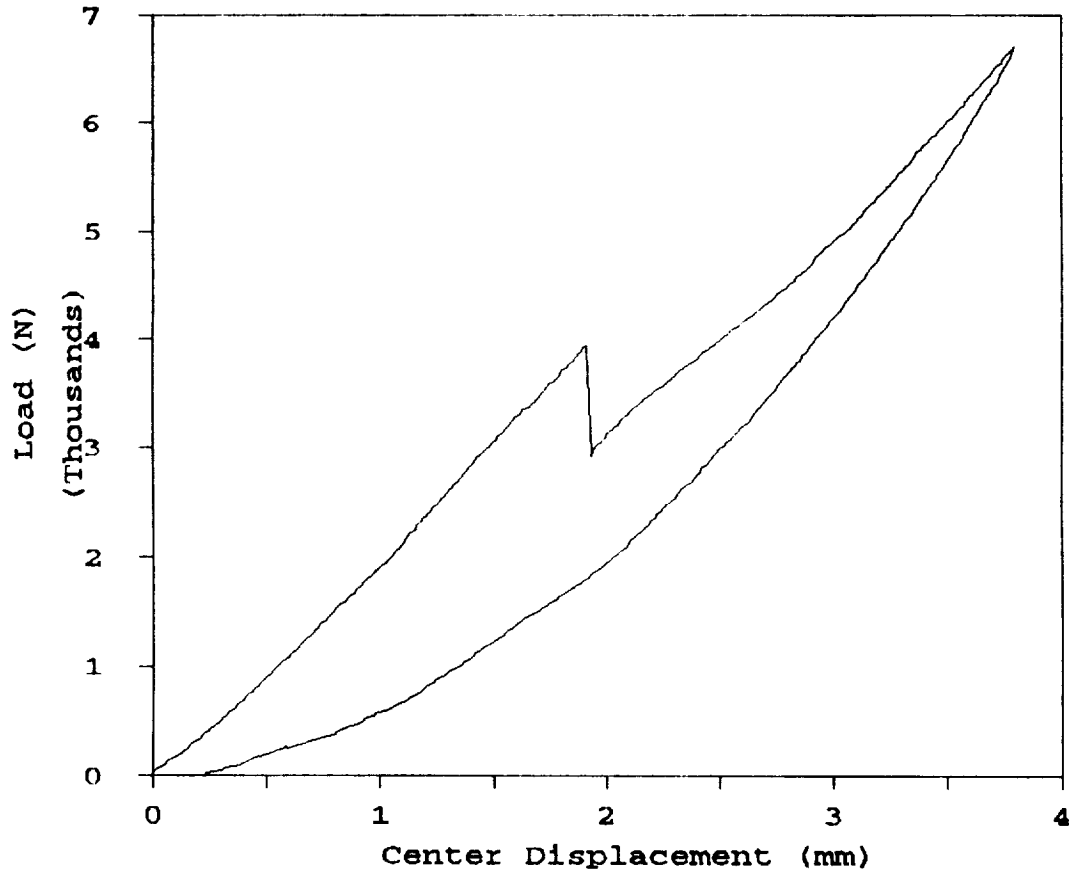

Figure B.50 Load-displacement diagram of STC11

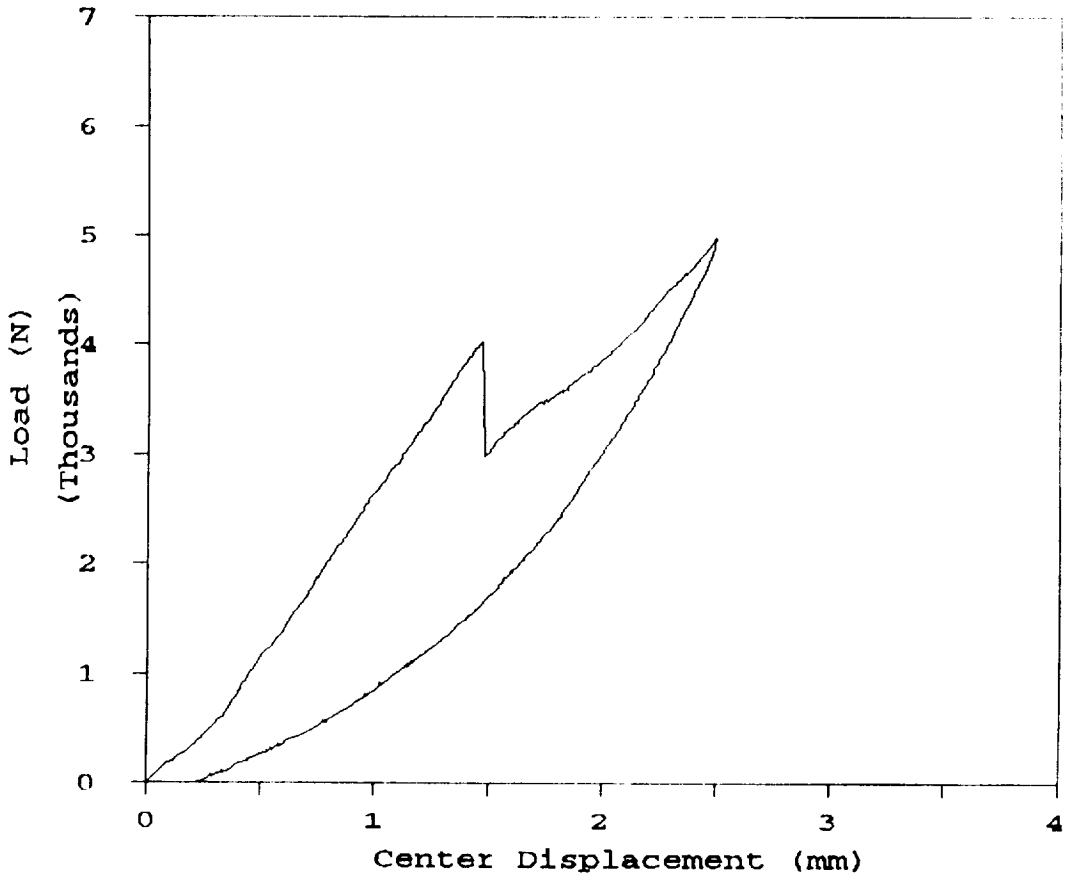

Figure B.51 Load-displacement diagram of STC12

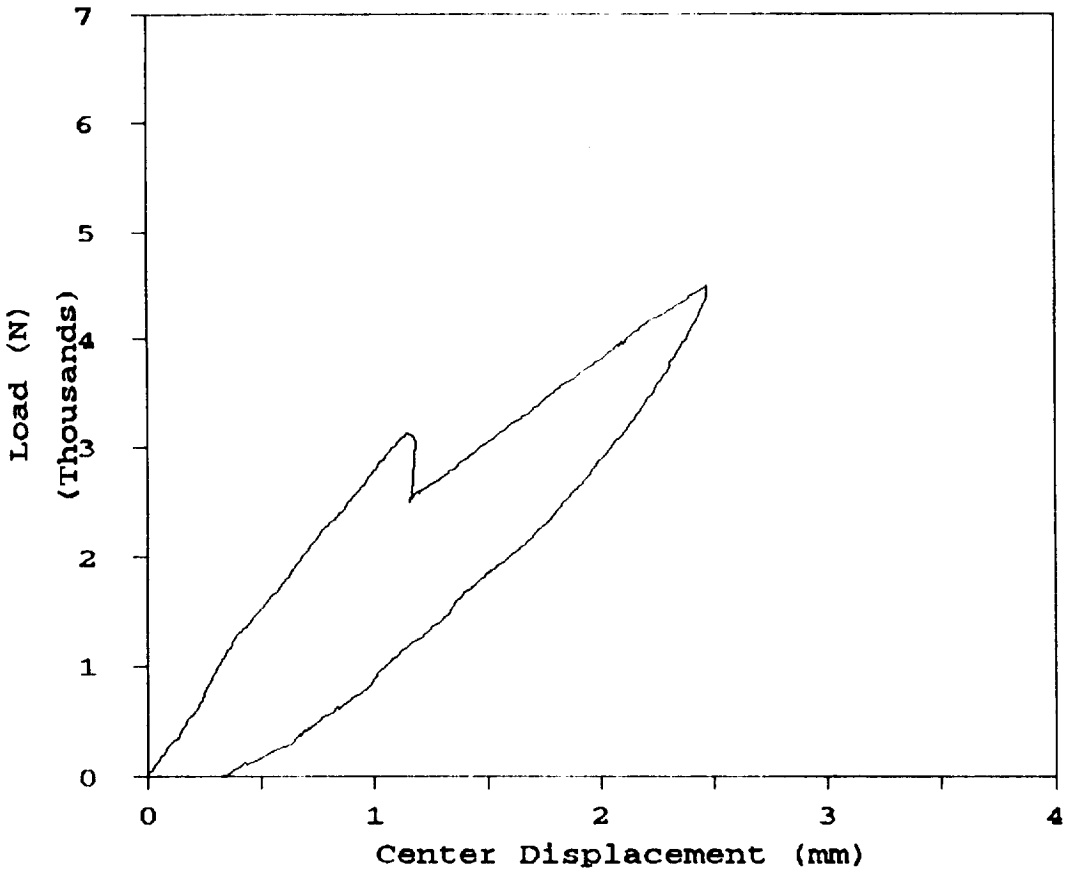

Figure B.52 Load-displacement diagram of STC13

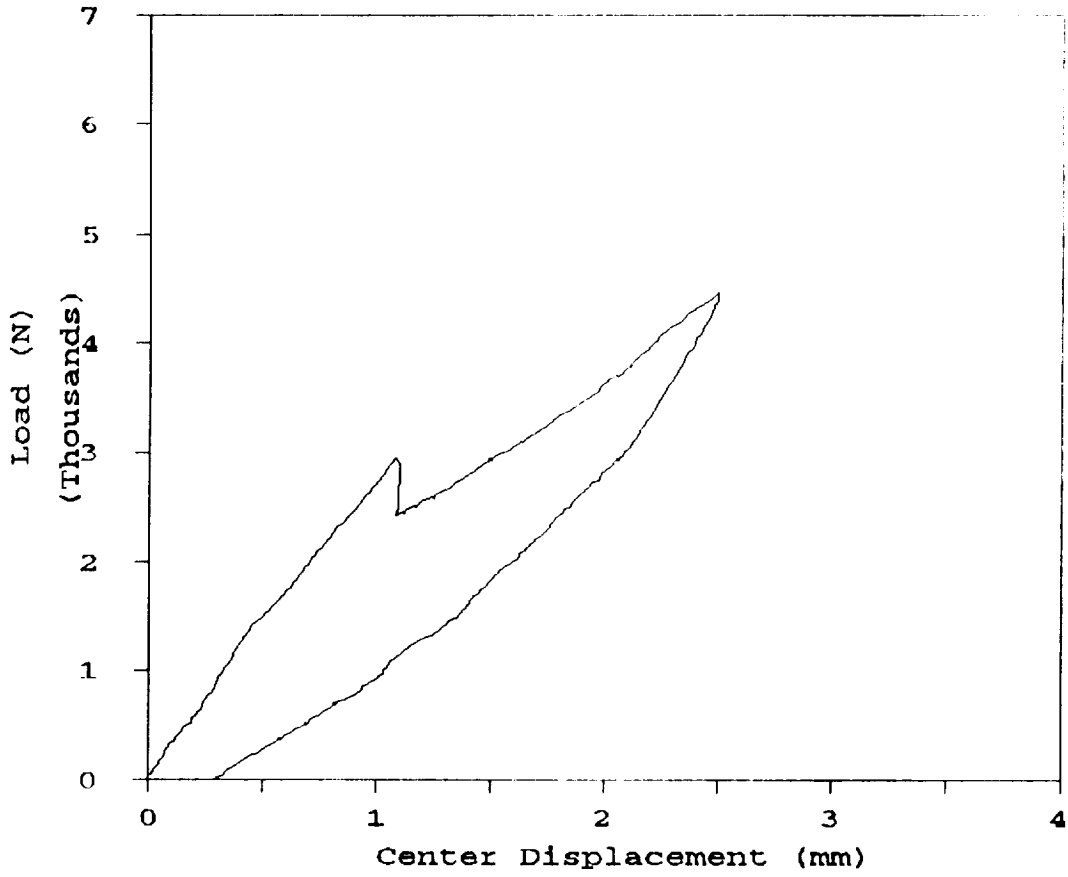

Figure B.53 Load-displacement diagram of STC14

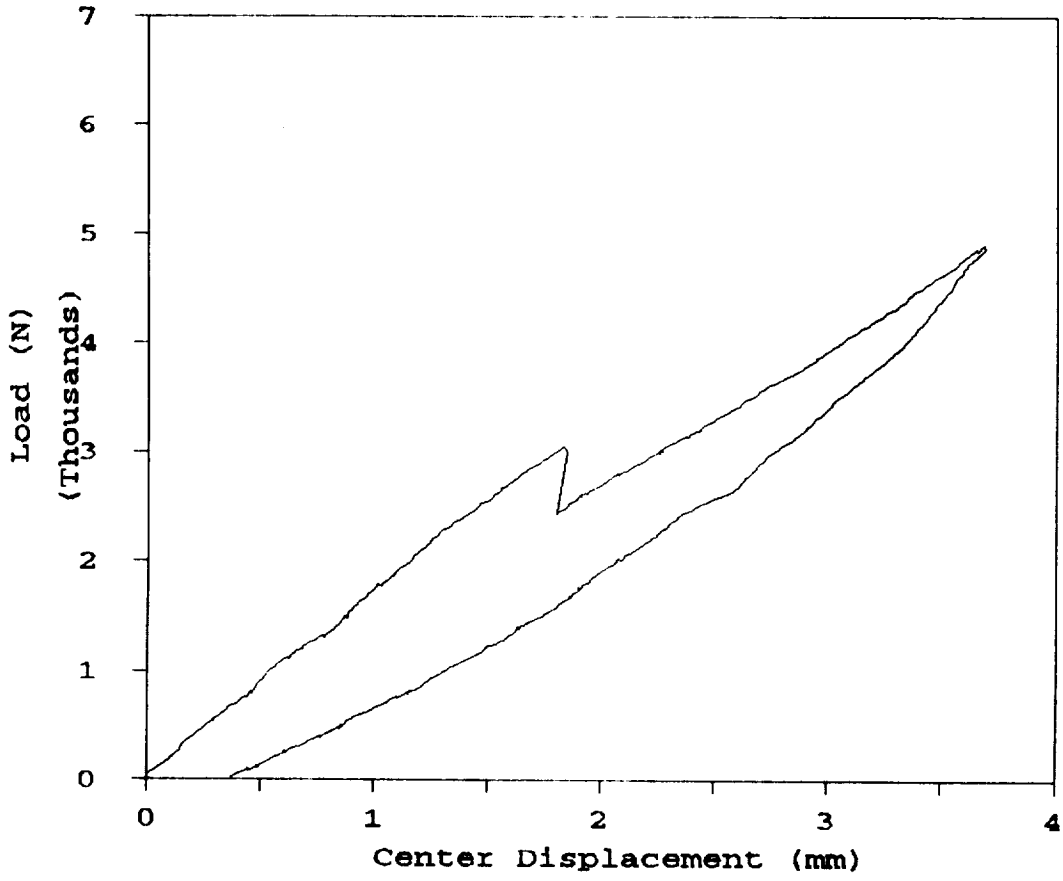

Figure B.54 Load-displacement diagram of STC15

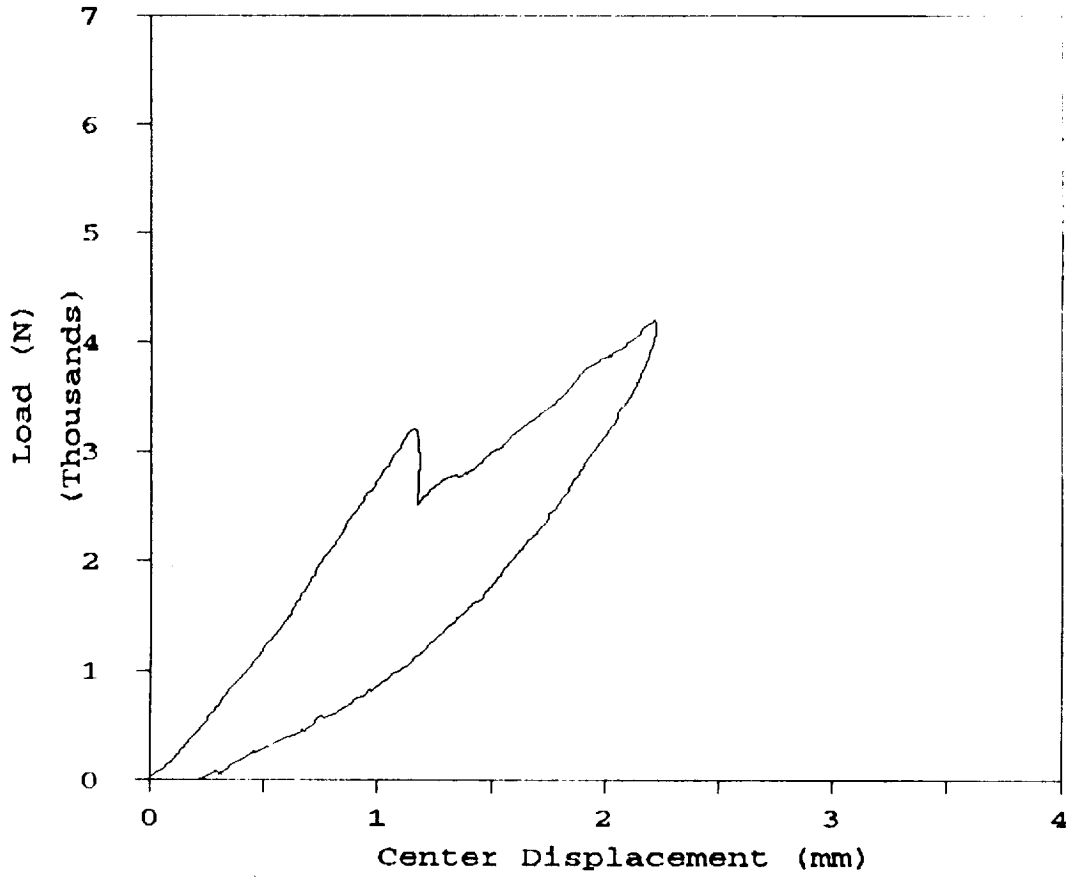

Figure B.55 Load-displacement diagram of STC16

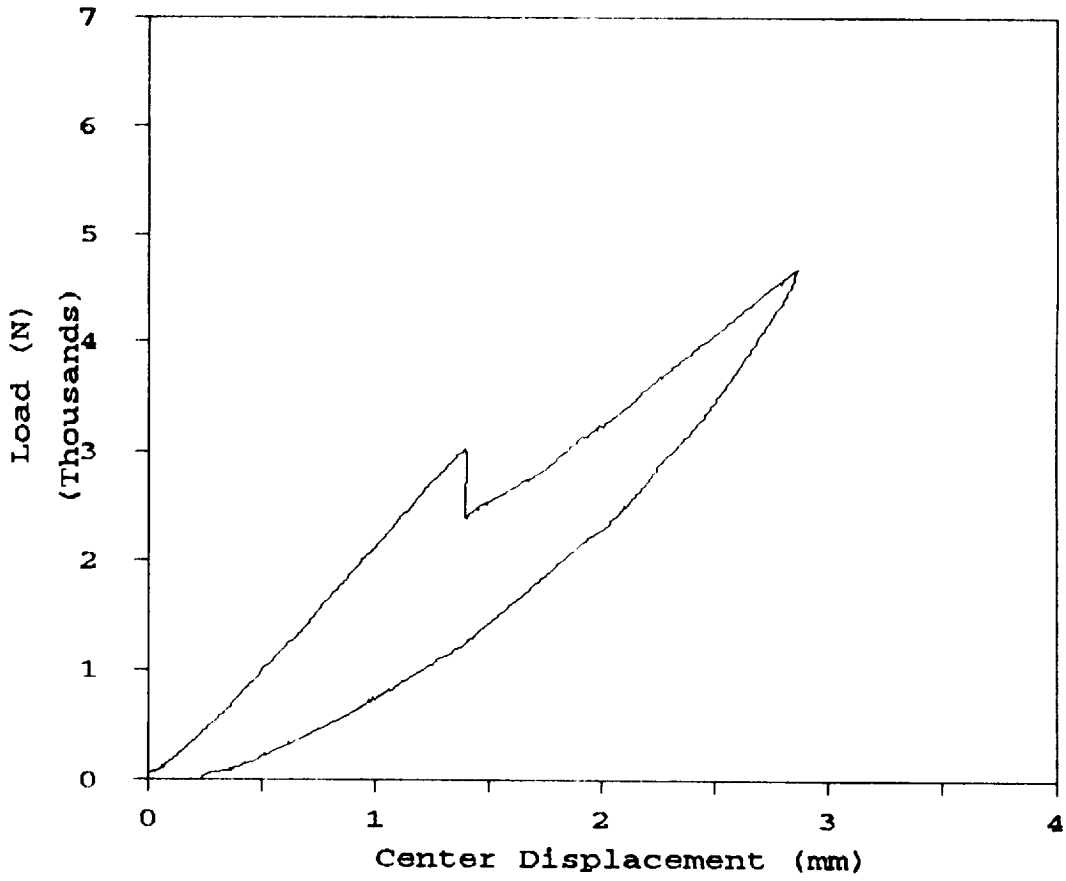

Figure B.56 Load-displacement diagram of STC17

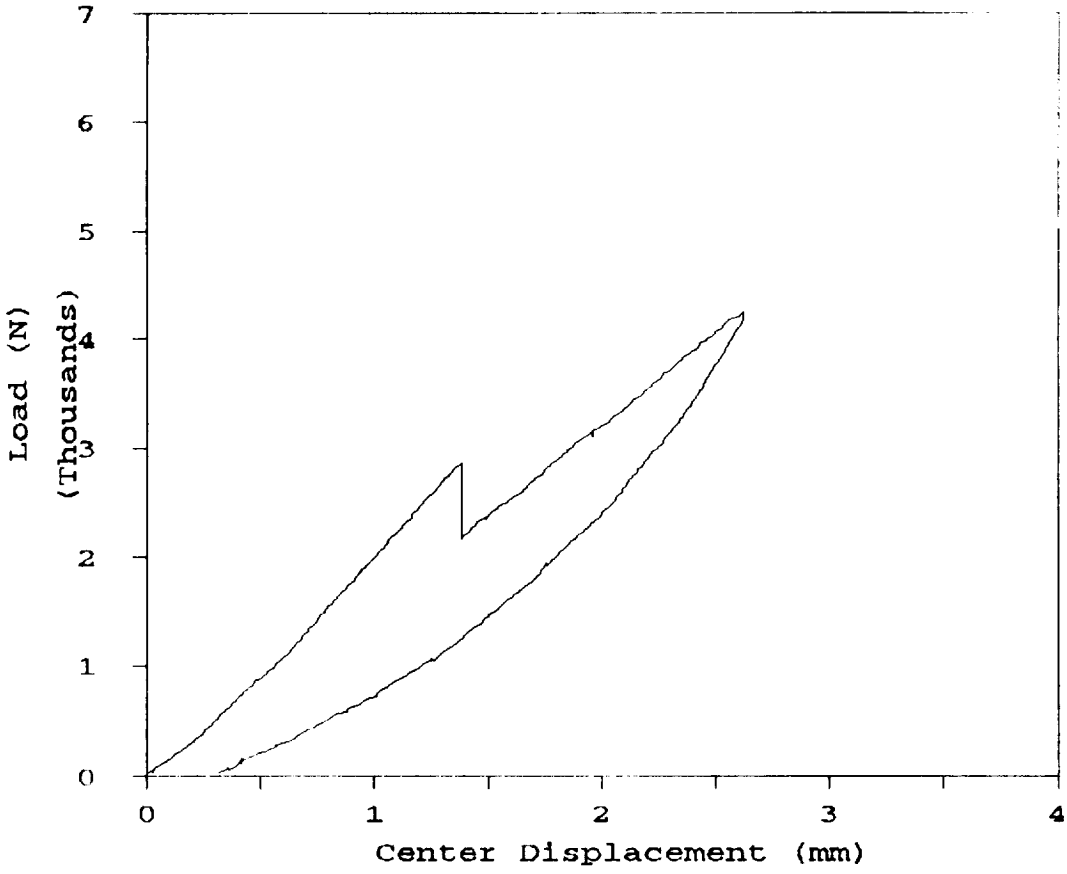

Figure B.57 Load-displacement diagram of STC18

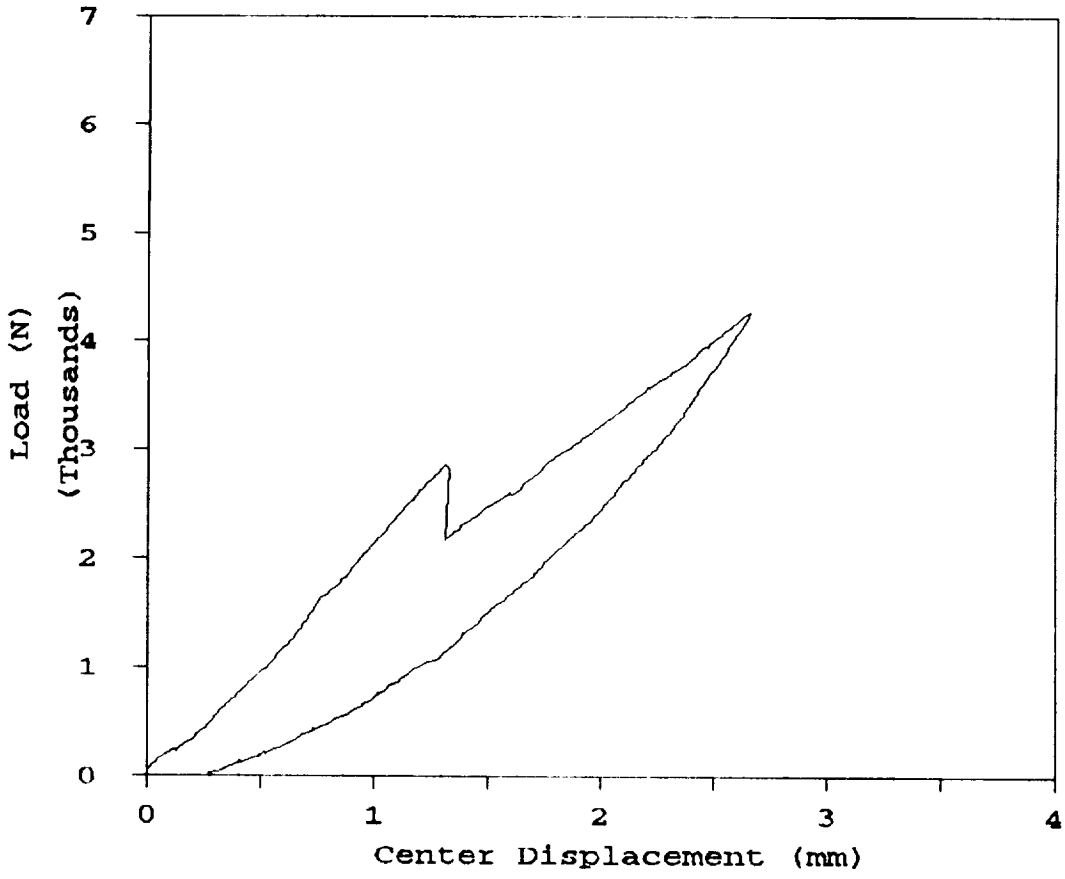

Figure B.58 Load-displacement diagram of STC19

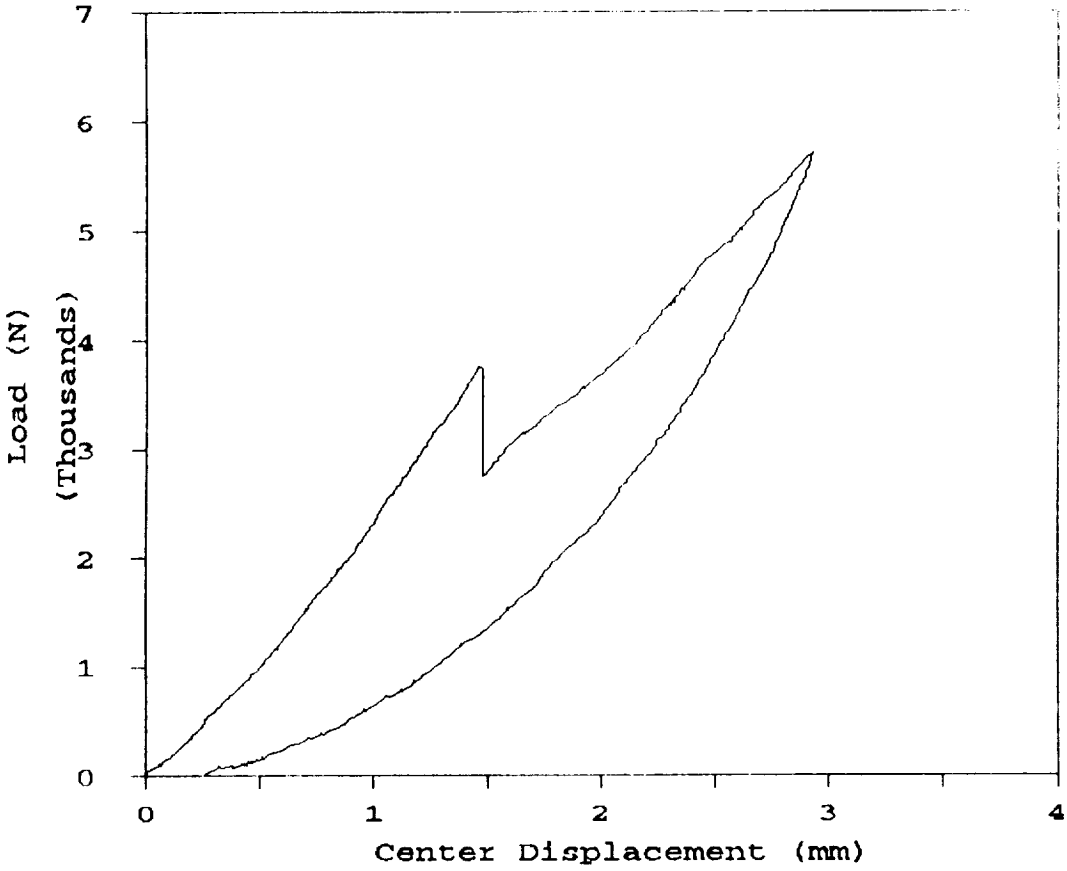

Figure B.59 Load-displacement diagram of STC20

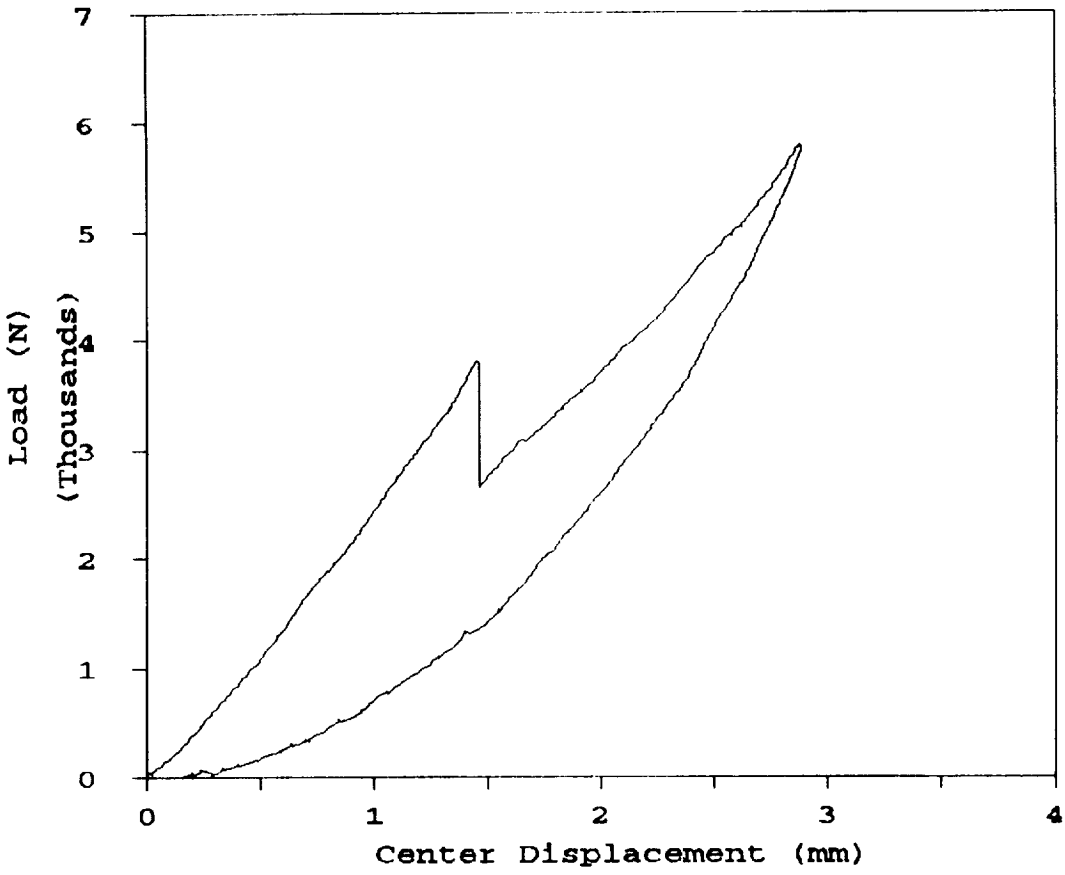

Figure B.60 Load-displacement diagram of STC21

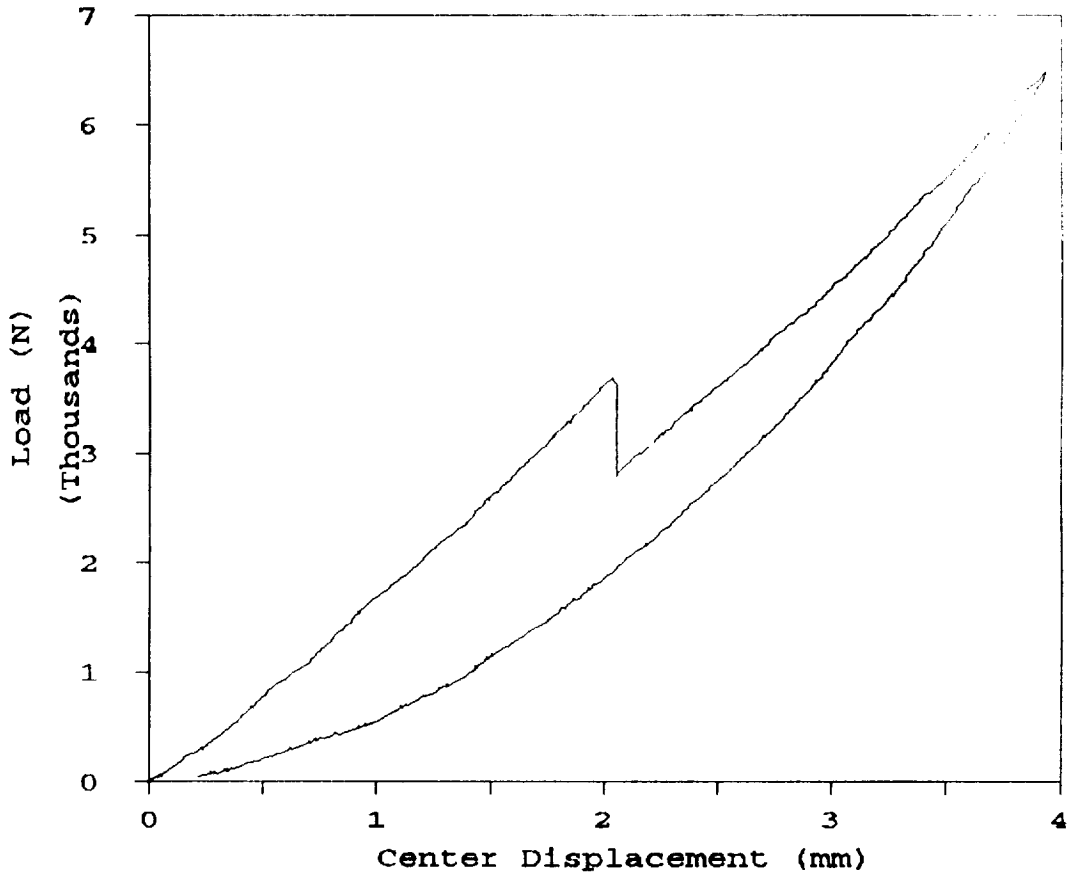

Figure B.61 Load-displacement diagram of STC22

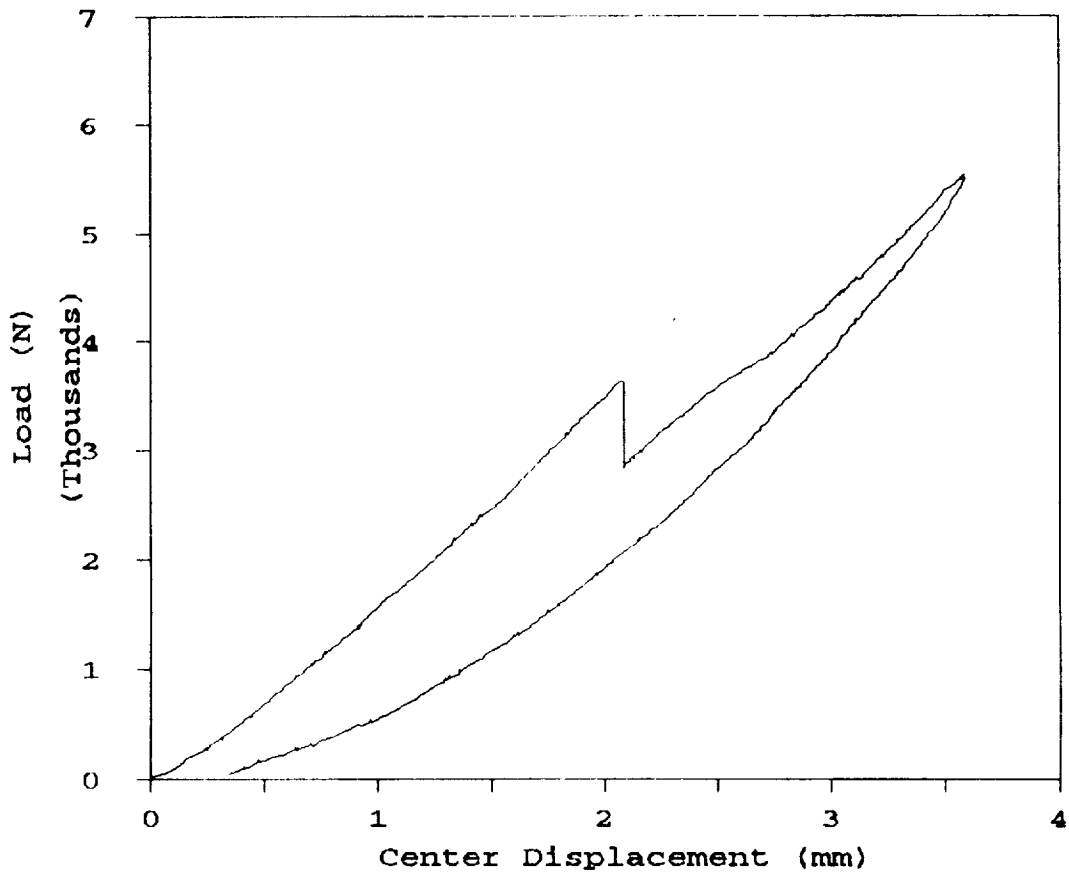

Figure B.62 Load-displacement diagram of STC23

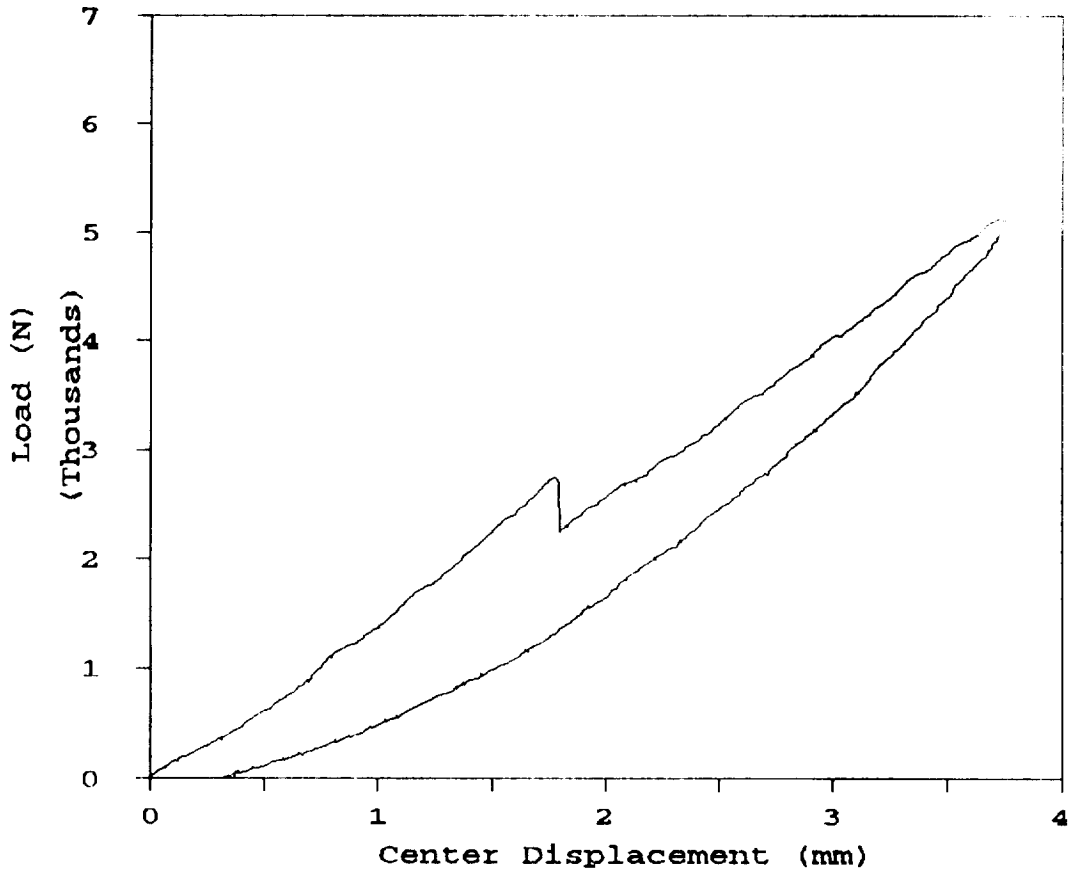

Figure B.63 Load-displacement diagram of STC24

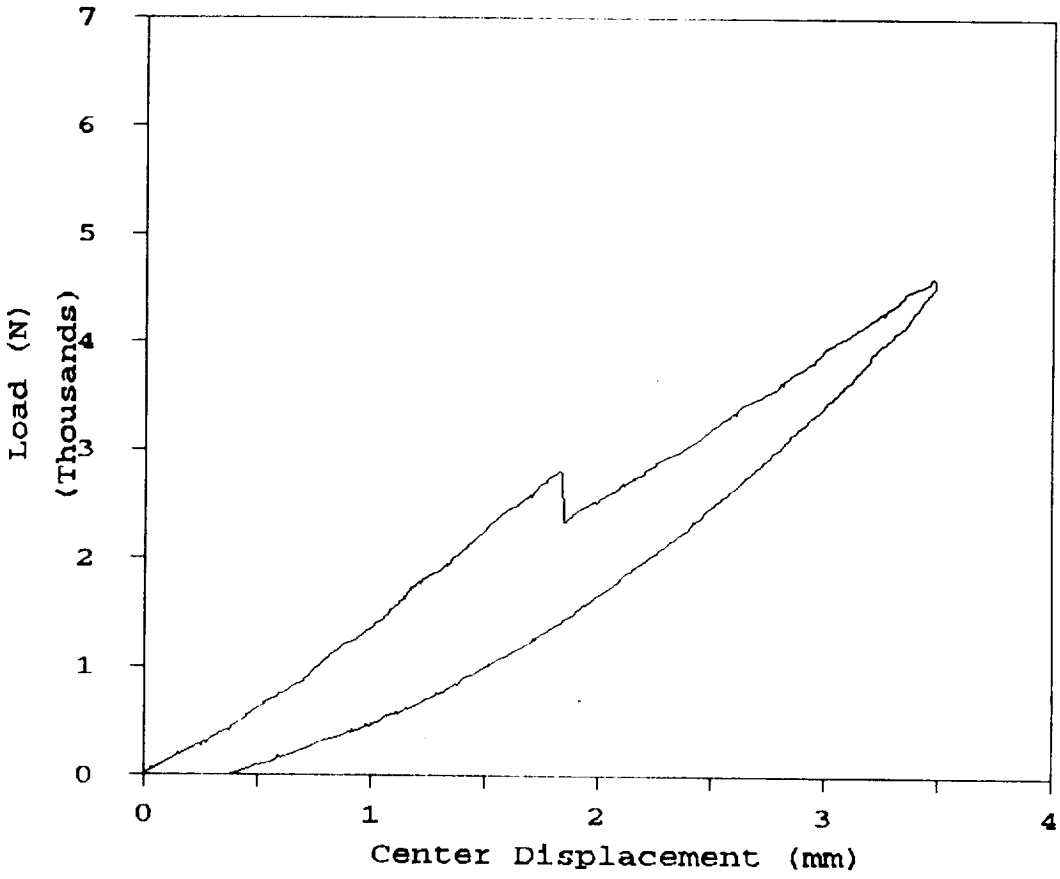

Figure B.64 Load-displacement diagram of STC25

APPENDIX C
DATA FOR LOAD-DISPLACEMENT DIAGRAMS

The plate stiffness (K_1), the load and the center displacement at the first observable failure (P_1 and q_1 respectively), the load drop at the first observable failure (ΔP), and the slope of the yield curve (K_2) for various specimens are presented in this appendix. Figure C.1 is the key for various data presented in Table C.1.

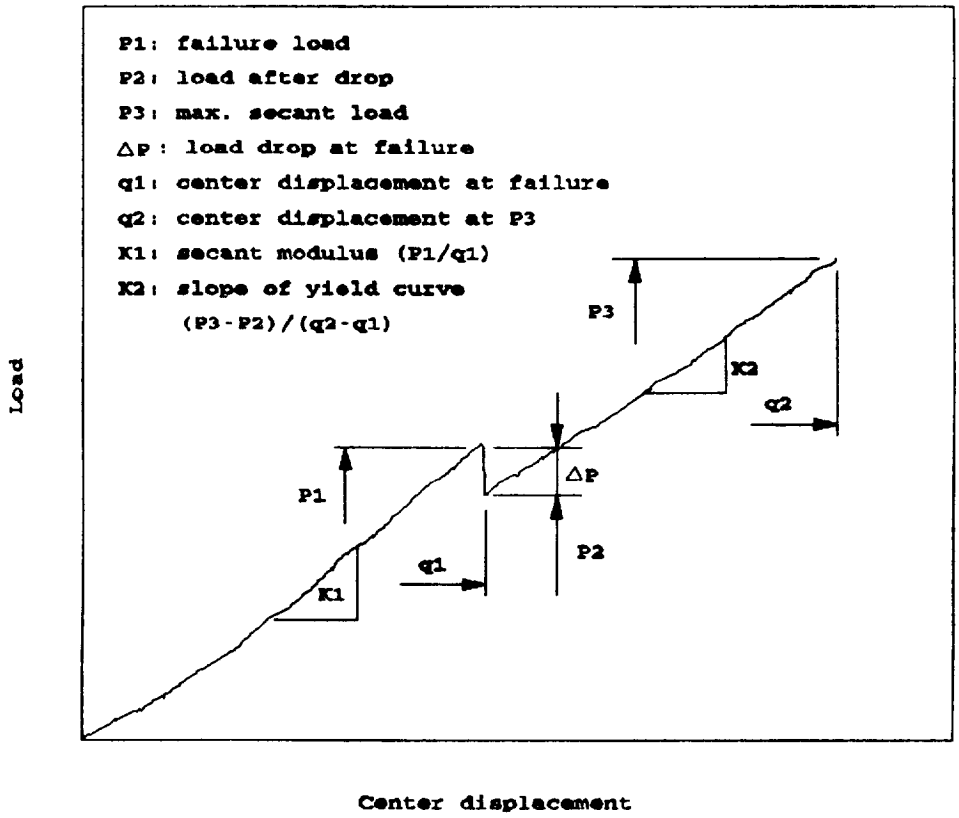

Figure C.1 Sketch of typical load-displacement diagram

Table C.1 Data for load-displacement diagrams of static indentation tests

		I.D.	P_1	q_1	P_2	ΔP	P_3	q_2	K_1	K_2
			N	mm	N	N	N	mm	N/mm	N/mm
6.35 mm dia. indenter	50.8 mm dia. support	STA20	2020.81	0.98679	2000.8	20.008	2200.88	1.23543	2047.86	804.70
		STA21	1940.78	0.83398	1800.72	140.056	2781.11	1.87257	2327.13	943.96
		STA23	1060.82	1.05154	1940.78	120.048	3181.27	2.19373	1959.82	1086.1
		STB13	2701.08	1.02046	1960.78	740.296	4161.66	2.44755	2646.92	1542.2
		STB14	2741.10	1.05672	0260.82	680.272	4081.63	2.32841	2593.97	1589.1
		STB16	2601.04	0.97643	1740.70	860.344	3281.31	1.95545	2663.83	1573.6
		STC13	3121.25	1.15773	2501	620.248	4501.8	2.47345	2696.01	1520.7
		STC14	2921.17	1.08262	2400.96	520.208	4441.78	2.49676	2698.24	1443.1
		STC16	3201.28	1.17327	2501	700.28	4201.68	2.21445	2728.51	1633.4
		STA24	2701.08	1.46853	2641.06	60.024	3701.48	2.38798	1839.31	1153.3

Table C.1--continued

6.35 mm dia. indenter

76.2 mm dia. support

I.D.	P_1	q_1	P_2	ΔP	P_3	q_2	K_1	K_2
	N	mm	N	N	N	mm	N/mm	N/mm
STA25	2561.02	1.39083	2541.02	20.008	3721.49	2.31546	1841.36	1276.7
STA26	2721.09	1.41155	2661.06	60.024	3801.52	2.42424	1927.73	1126.2
STB17	3701.48	1.77156	2761.10	940.376	4561.82	2.83605	2089.39	1691.6
STB18	3061.22	1.47112	2380.95	680.272	4201.68	2.67547	2080.88	1511.8
STB19	3181.27	1.57213	2320.93	860.344	4261.70	2.68583	2023.54	1742.6
STC17	3001.2	1.40378	2360.94	640.256	4661.86	2.86195	2137.94	1578.0
STC18	2841.14	1.38306	2140.86	700.28	4221.69	1.36493	2054.24	1623.3
STC19	2841.14	1.31313	2140.86	700.28	4261.70	2.65475	2163.64	1580.8
STA22	2120.85	1.70422	2120.85	0	3261.30	3.01476	1244.47	870.22
STA31	2440.98	1.69386	2360.94	80.032	3521.41	2.77648	1441.07	1071.9
STA32	2541.02	1.58767	2521.01	20.008	4001.6	2.86195	1600.47	1191.9

Table C.1--continued

		I.D.	P_1	q_1	P_2	ΔP	P_3	q_2	K_1	K_2
			N	mm	N	N	N	mm	N/mm	N/mm
6.35 mm dia. indenter	101.6 mm dia. support	STB15	2801.12	1.76379	2080.83	720.288	3861.54	3.15721	1588.13	1277.9
		STB24	3261.30	2.06682	2420.97	840.336	4341.74	3.3929	1577.9	1448.5
		STB25	3161.26	2.08236	2340.94	820.328	4521.81	3.51981	1518.12	1517.2
		STC15	3021.21	1.80782	2400.96	620.248	4881.95	3.68039	1671.19	1324.9
		STC24	2741.10	1.79746	2240.90	500.2	5122.05	3.72183	1524.98	1497.2
		STC25	2801.12	1.8648	2320.93	480.192	4601.84	3.47578	1502.10	1415.9
25.4 mm dia. indenter	50.8 mm dia. support	STA14	2440.98	0.98862	2320.93	119.994	3363.34	2.03160	2469.07	999.41
		STA16	2621.05	0.79254	2360.94	260.104	3261.30	1.76638	3307.15	924.55
		STA17	2661.06	0.76146	2360.94	300.12	3921.57	2.13416	3494.69	1136.9
		STB7	3361.34	1.12147	2406.96	954.382	5842.34	3.21367	2997.27	1642.0
		STB9	4081.63	1.02046	2701.08	1380.55	4141.66	1.813	3999.80	1817.7

Table C.1--continued

25.4 mm dia. indenter

	I.D.	P_1	q_1	P_2	ΔP	P_3	q_2	K_1	K_2
		N	mm	N	N	N	mm	N/mm	N/mm
50.8 mm dia. support	STB10	3421.37	0.93499	2220.89	1200.48	5182.07	2.54338	3659.26	1841.1
	STC7	3357.34	0.82892	2799.12	558.223	4297.72	2.20176	4050.25	1091.6
	STC9	4101.64	1.01269	2861.14	1240.49	4261.70	1.69127	4050.24	2064.0
	STC10	4041.62	0.98679	2681.07	1360.54	6302.52	2.55892	4095.72	2303.5
76.2 mm dia. support	STA19	2841.14	1.29759	2641.06	200.08	3961.58	2.49158	2189.55	1106.0
	STA27	3101.24	1.34939	3021.21	80.032	4641.86	2.71173	2298.25	1189.6
	STA28	3021.21	1.30277	2921.17	100.04	5302.12	3.00958	2319.06	1395.0
	STB12	3961.58	1.53069	2761.10	1200.48	4481.79	2.41647	2588.10	1942.6
	STB20	4321.73	1.71717	3001.2	1320.53	5462.18	2.90339	2516.77	2074.6
	STB21	4061.62	1.67055	2821.13	1240.49	5182.07	2.79202	2431.31	2105.2
	STC12	4021.61	1.48148	2981.19	1040.42	4981.99	2.49417	2714.59	1975.7

Table C.1--continued

		I.D.	P_1	q_{1i}	P_2	ΔP	P_3	q_2	K_1	K_2
			N	mm	N	N	N	mm	N/mm	N/mm
25.4 mm dia. indenter		STC20	3741.50	1.47889	2741.10	1000.4	5702.28	2.93188	2529.94	2038.0
		STC21	3801.52	1.46076	2641.06	1160.46	5782.31	2.88008	2602.43	2213.2
	101.6 mm dia. support	STA18	2521.01	1.58767	2360.94	160.064	5242.10	3.73996	1587.87	1338.6
		STA29	3001.2	1.79487	3001.2	0	5362.14	3.5483	1672.10	1346.5
		STA30	3301.32	1.84667	3201.28	100.4	5762.30	3.61564	1787.72	1447.7
		STB11	4041.62	2.07718	2821.13	1220.49	5482.19	3.71147	1945.72	1628.3
		STB22	3901.56	2.20409	2841.14	1060.42	5202.08	3.54053	1770.15	1766.6
		STB23	3881.55	2.25071	2821.13	1060.42	5102.04	3.51204	1724.59	1808.3
		STC11	3921.57	1.93473	2881.15	1040.42	6682.67	3.79694	2026.9	2041.4
		STC22	3701.48	2.05128	2801.12	900.36	6052.6	3.93421	1804.47	1965.8
		STC23	3621.45	2.08495	2821.13	800.32	5522.21	3.58197	1736.95	1804.3

APPENDIX D
DELAMINATION AREA

Plates damaged in static and impact tests were C-scanned in a facility at NASA Langley Research Center, Hampton, Virginia. The data were recorded by means of image processing, so that the areas of damages could be measured conveniently by using a commercial graphic software "IMAGE[1]" in a Macintosh microcomputer. The data for the projected delamination area and the corresponding maximum load are presented in the following tables.

Static Indentation Test

Table D.1 Delamination area vs. static load for laminate type A

Specimen	Applied Max. Load(N)	Delamination Area(mm^2)
STA16	3261	1432
STA17	3922	1903
STA18	5242	1981
STA19	3962	2329
STA20	2721	961
STA21	2781	1206
STA22	3261	716
STA23	3181	1419

[1] Image Processing and Analysis by Wayne Rasband, National Institute of Health, Research Services Branch, NIMH

Table D.1--continued

Specimen	Applied Max. Load(N)	Delamination Area(mm^2)
STA24	3701	929
STA25	3721	910
STA26	3802	1103
STA27	4642	1865
STA28	5302	2000
STA29	5362	1013
STA30	5762	1645
STA31	3521	852
STA32	4002	1065

Table D.2 Delamination area vs. static load for laminate type B

Specimen	Applied Max. Load(N)	Delamination Area(mm^2)
STB9	4142	897
STB10	5182	994
STB11	5582	1110
STB12	4482	1819
STB13	4162	1032
STB14	4082	1329
STB15	3862	1277
STB16	3281	684
STB17	4562	1445
STB18	4202	1303
STB19	4262	1245
STB20	5462	1374
STB21	5382	1116
STB22	5202	1039

Table D.2--continued

Specimen	Applied Max. Load(N)	Delamination Area(mm^2)
STB23	5102	1032
STB24	4342	1200
STB25	4522	1265

Table D.3 Delamination area vs. static load for laminate type C

Specimen	Applied Max. Load(N)	Delamination Area(mm^2)
STC7	8247	3542
STC9	4262	852
STC10	6303	1658
STC11	6683	2419
STC12	4982	1839
STC13	4502	858
STC14	4500	845
STC15	4882	1613
STC16	4202	845
STC17	4662	955
STC18	4222	845
STC19	4262	948
STC20	5702	1342
STC21	5782	1394
STC22	6503	1677
STC23	5522	1194
STC24	5122	974
STC25	4602	865

Table D.4 Delamination area vs. impact load for laminate type A

Specimen	Applied Impact Load(N)	Delamination Area(mm^2)
IMPA9	2875	910
IMPA11	2855	581
IMPA12	6356	2768

Table D.5 Delamination area vs. impact load for laminate type B

Specimen	Applied Impact Load(N)	Delamination Area(mm^2)
IMPB1	5819	1748
IMPB3	4409	458
IMPB9	6370	1819

Table D.6 Delamination area vs. impact load for laminate type C

Specimen	Applied Impact Load(N)	Delamination Area(mm^2)
IMPC1	5496	1477
IMPC5	3192	394
IMPC7	6748	1845

APPENDIX E
FORCE HISTORY OF LOW-VELOCITY IMPACT TESTS

Force-time and force-displacement curves from the low-velocity impact test for three laminate types are presented in this appendix. The results of impact tests for each laminate are given in the following tables.

Table E.1 Results of impact test for laminate Type A

Specimen No.	Impact Vel.(m/s)	Rebound Vel.(m/s)	Impact Energy(J)	Imparted Energy(J)
IMPA5	1.17	0.68	9.57	6.34
IMPA7	0.77	0.44	4.14	2.79
IMPA9	0.54	0.29	2.04	1.45
IMPA10	0.57	0.29	2.27	1.68
IMPA11	0.38	0.25	1.01	0.57
IMPA12	1.27	0.81	11.27	6.69

Table E.2 Results of impact test for laminate Type B

Specimen No.	Impact Vel.(m/s)	Rebound Vel.(m/s)	Impact Energy(J)	Imparted Energy(J)
IMPB1	1.19	0.60	9.90	7.38
IMPB2	1.16	0.56	9.41	7.21
IMPB3	0.74	0.35	3.82	2.97
IMPB5	0.31	0.21	0.67	0.36
IMPB6	0.36	0.24	0.91	0.50

Table E.2--continued

Specimen No.	Impact Vel.(m/s)	Rebound Vel.(m/s)	Impact Energy(J)	Imparted Energy(J)
IMPB8	0.64	0.30	2.86	2.23
IMPB9	1.27	0.74	11.27	7.45

Table E.3 Results of impact test for laminate Type C

Specimen No.	Impact Vel.(m/s)	Rebound Vel.(m/s)	Impact Energy(J)	Imparted Energy(J)
IMPC1	1.15	0.57	9.24	6.97
IMPC2	0.76	0.38	4.04	3.03
IMPC3	0.37	0.25	0.96	0.52
IMPC4	0.53	0.25	1.96	1.53
IMPC5	0.58	0.29	2.35	1.76
IMPC6	0.95	0.48	6.31	4.70
IMPC7	1.27	0.76	11.27	7.24

Note that all the impact tests conducted were under the simply supported condition with a 50.8 mm diameter circular support and a 25.4 mm diameter hemispherical steel impactor.

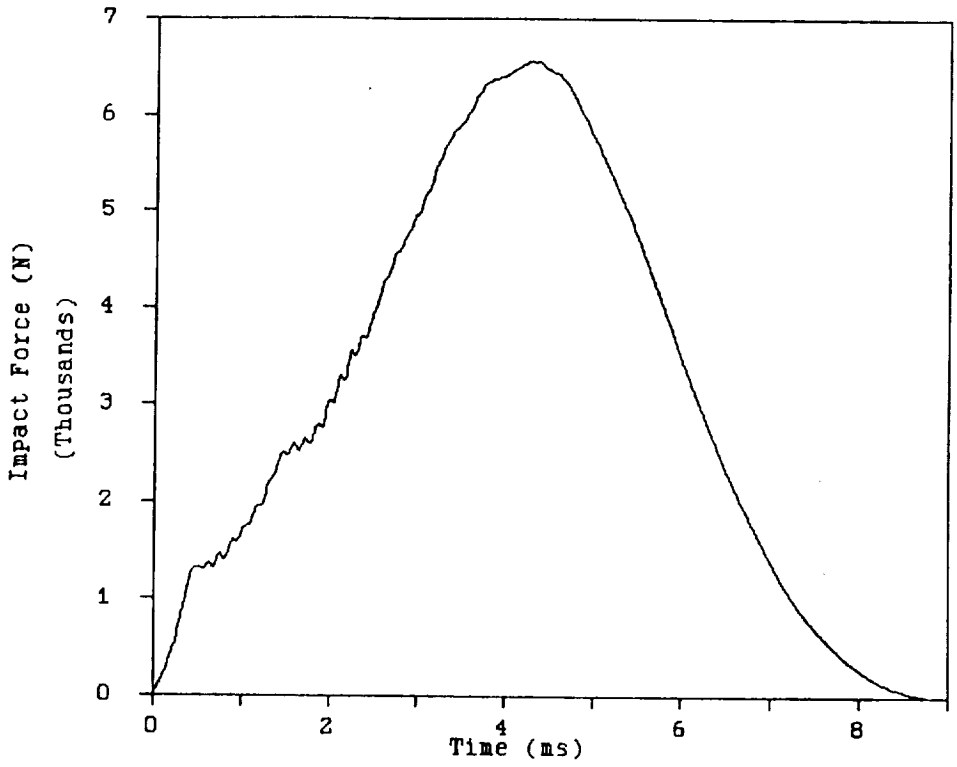

(a)

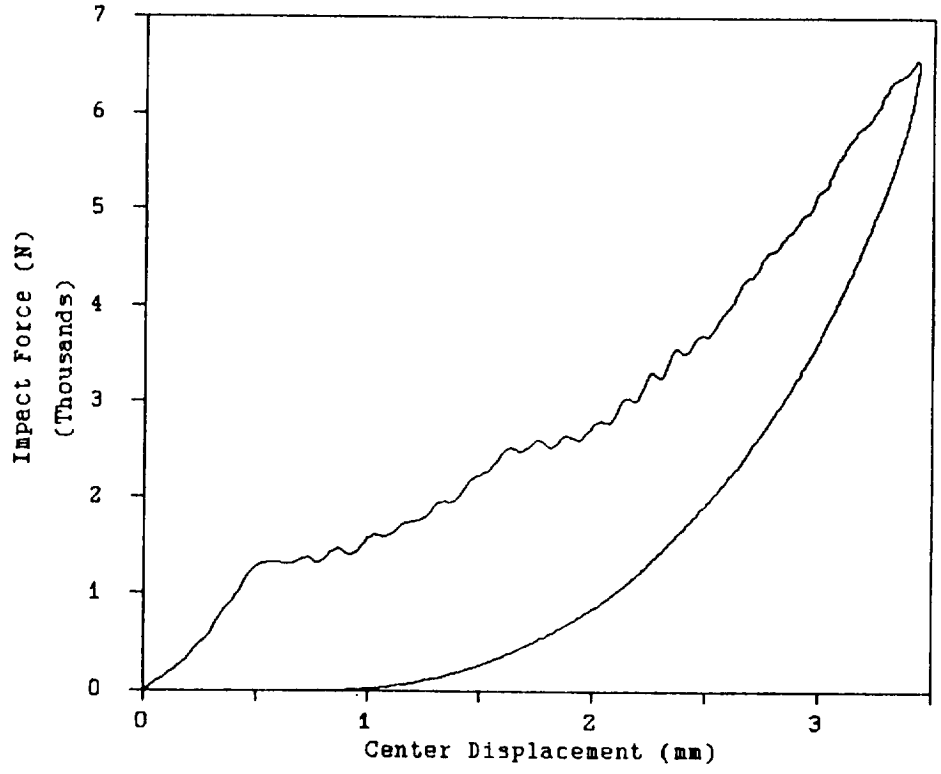

(b)

Figure E.1 Impact force history of IMPA5:(a) force vs. time and (b) force vs. displacement

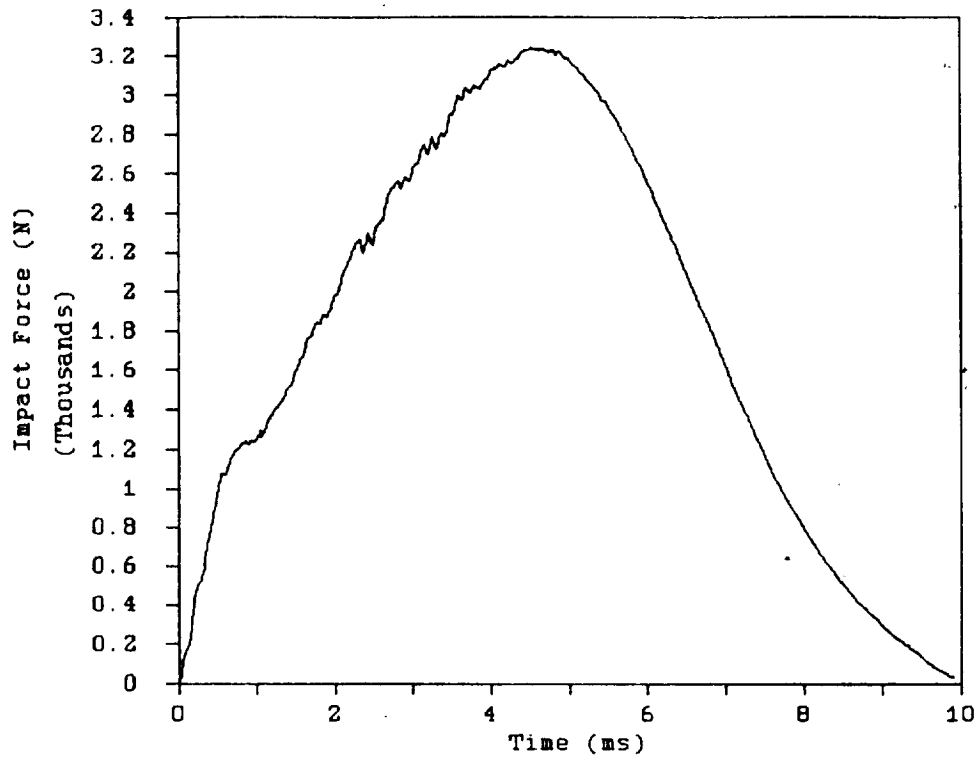

(a)

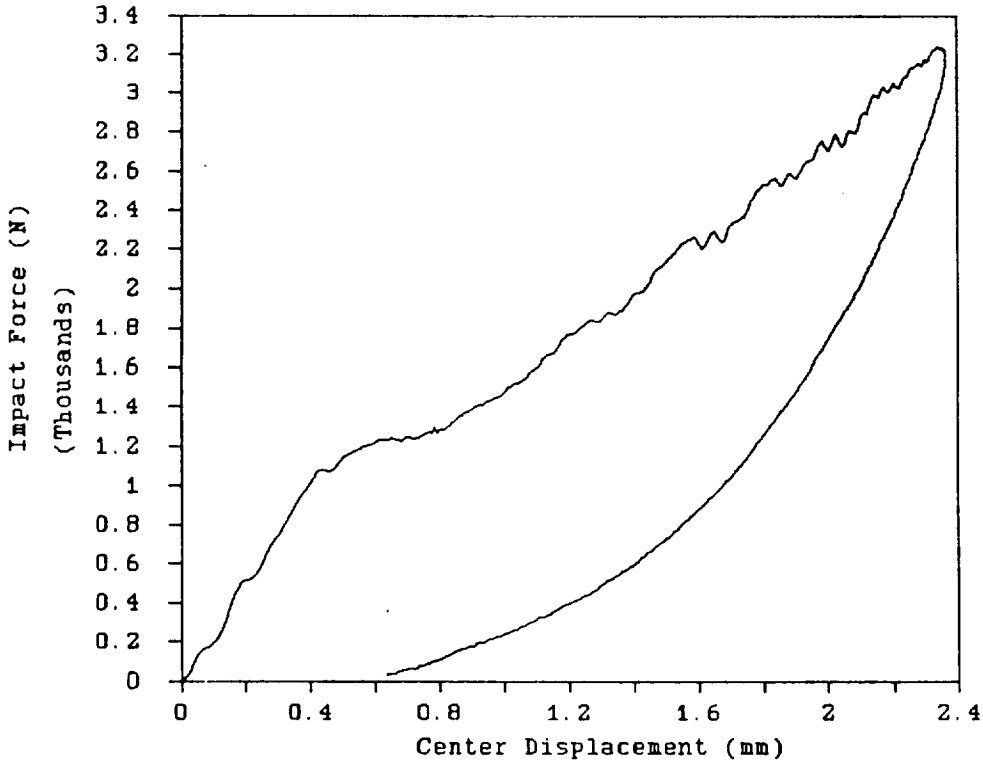

(b)

Figure E.2 Impact force history of IMPA7:(a) force vs. time and (b) force vs. displacement

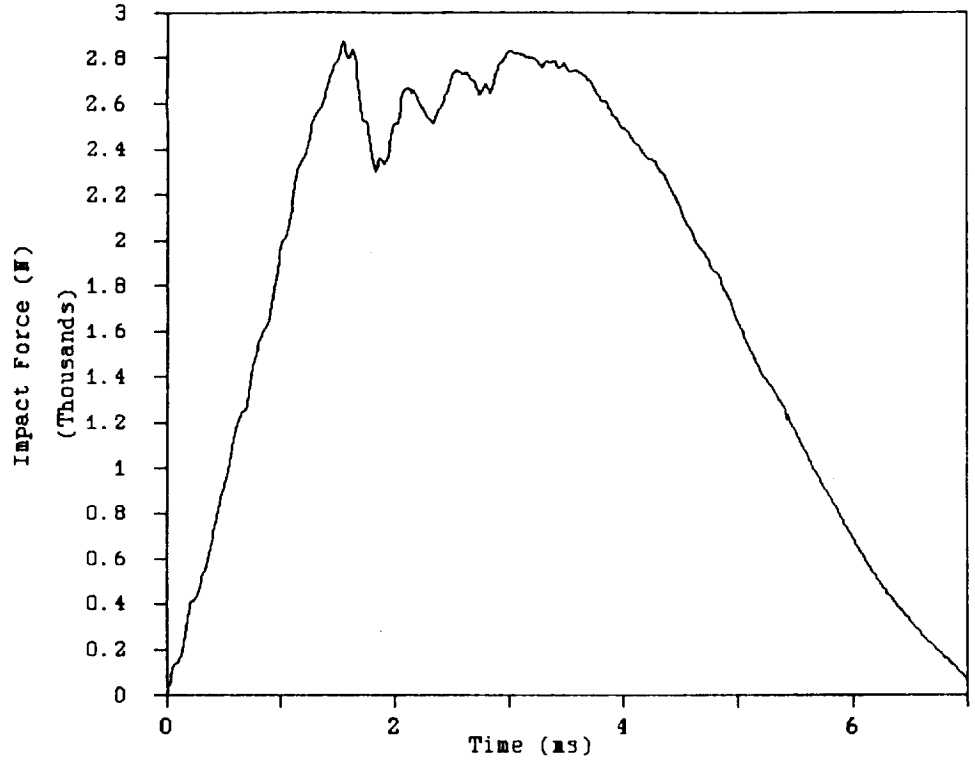

(a)

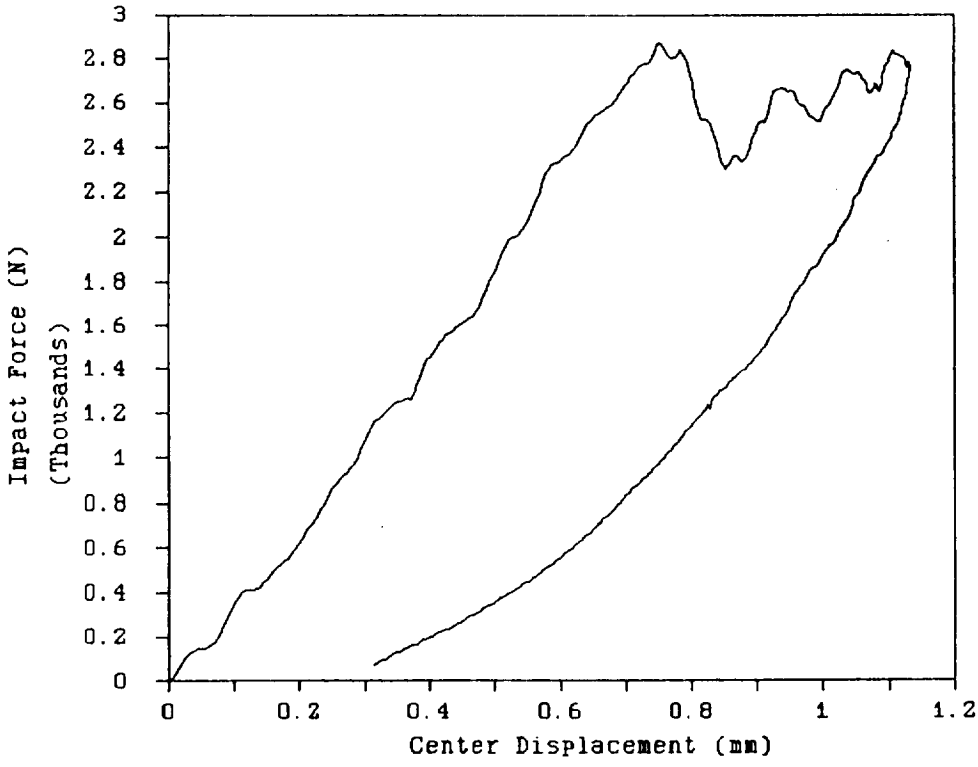

(b)

Figure E.3 Impact force history of IMPA9:(a) force vs. time and (b) force vs. displacement

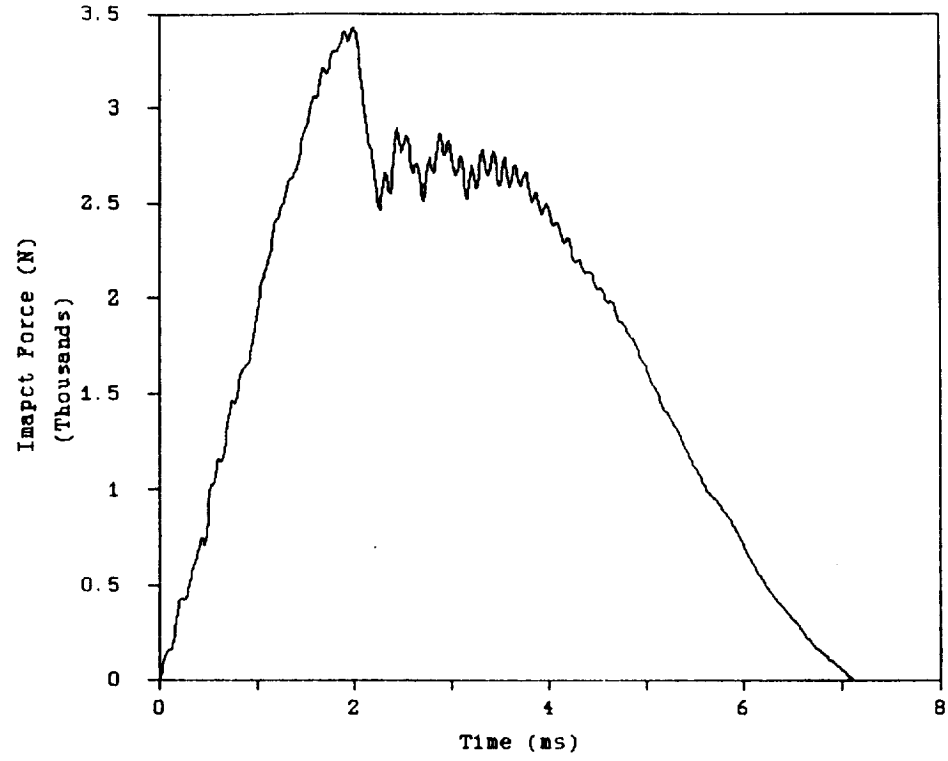

(a)

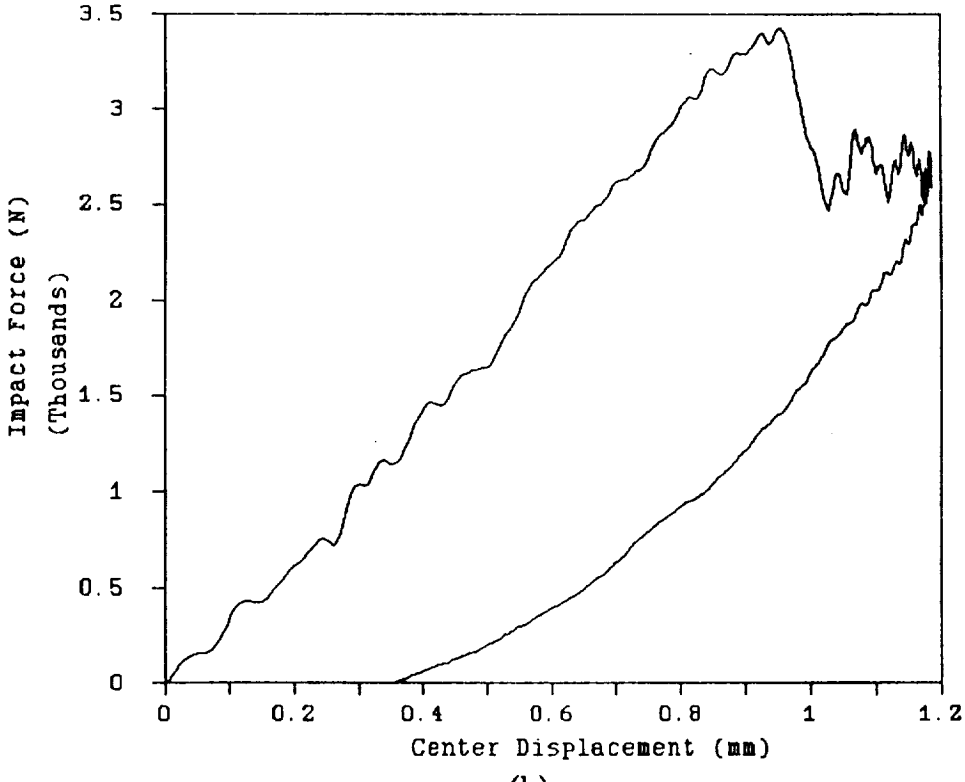

(b)

Figure E.4 Impact force history of IMPA10:(a) force vs. time and (b) force vs. displacement

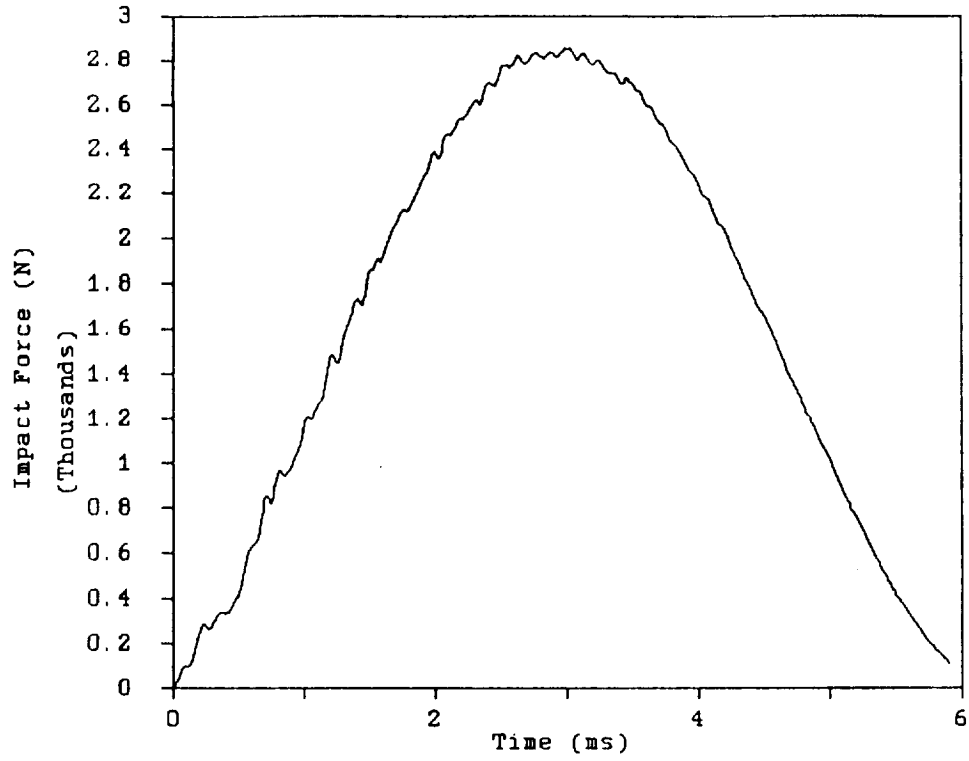

(a)

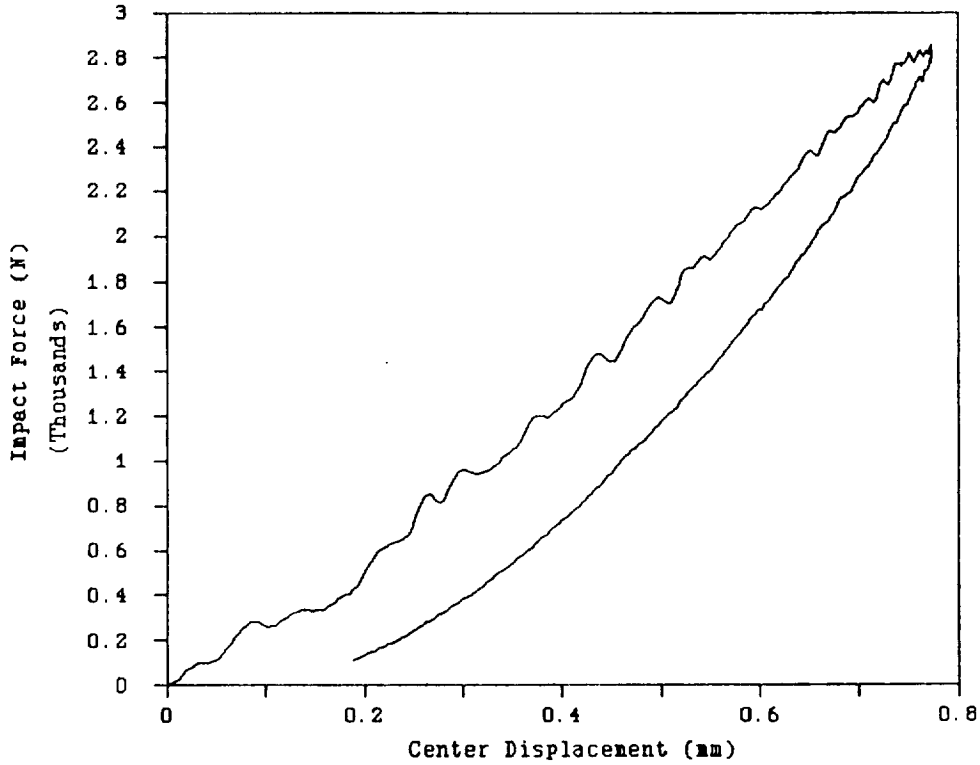

(b)

Figure E.5 Impact force history of IMPA11:(a) force vs. time and (b) force vs. displacement

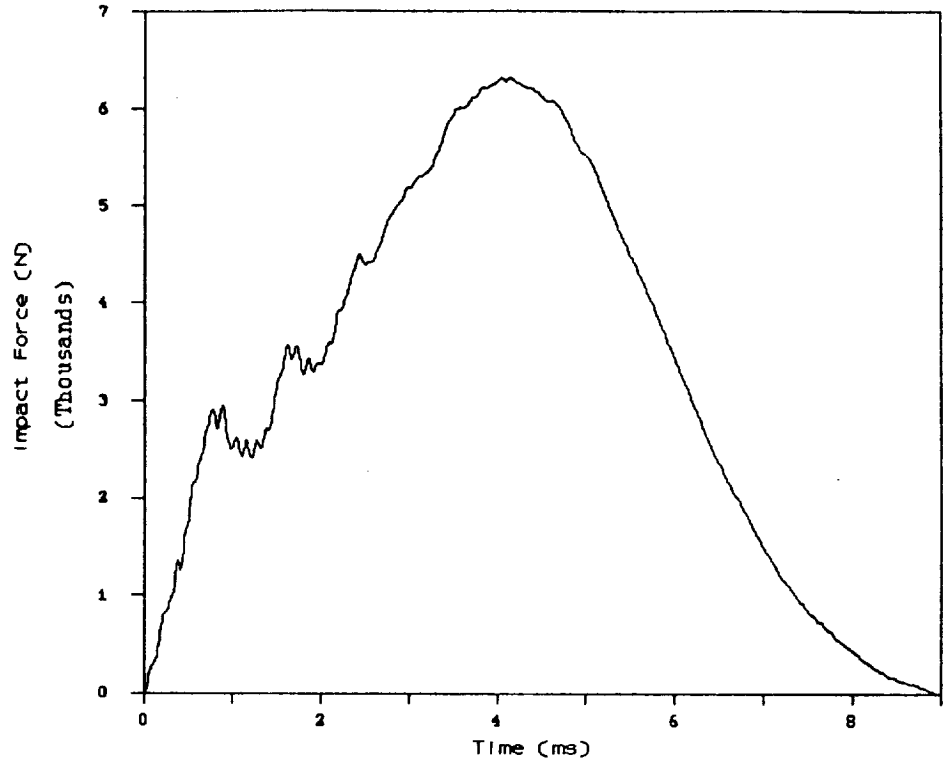

(a)

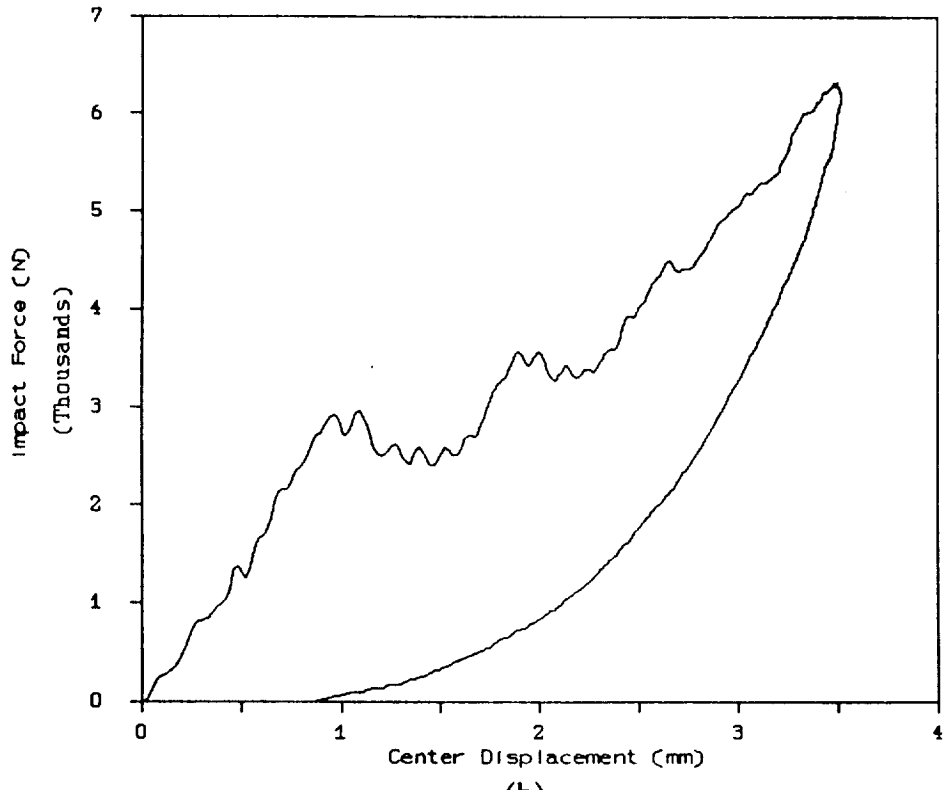

(b)

Figure E.6 Impact force history of IMPA12:(a) force vs. time and (b) force vs. displacement

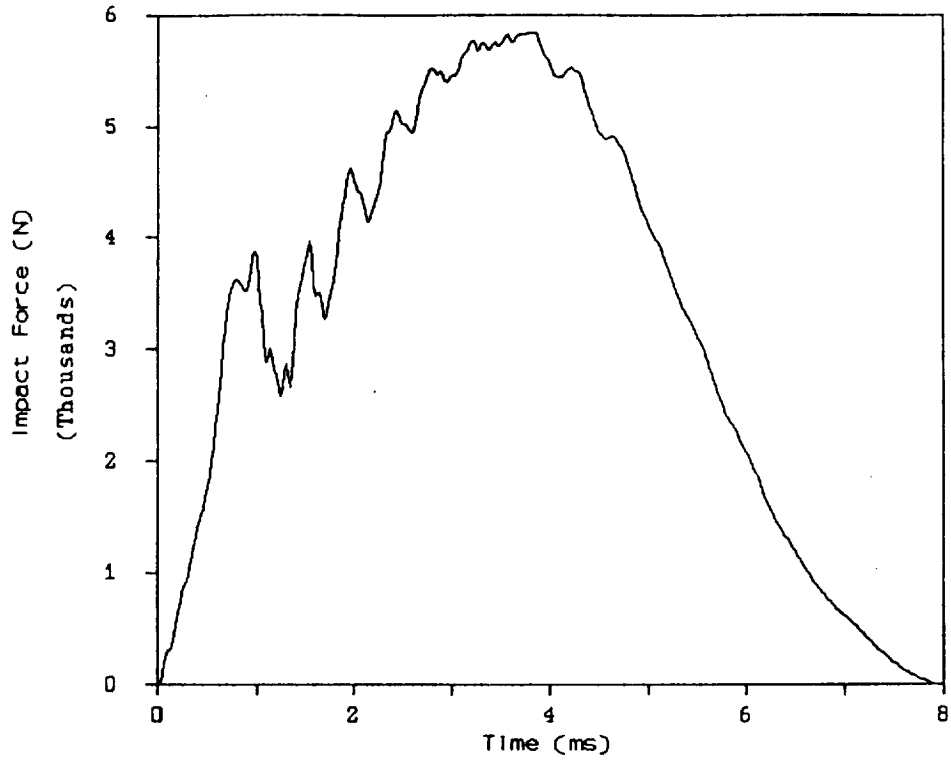

(a)

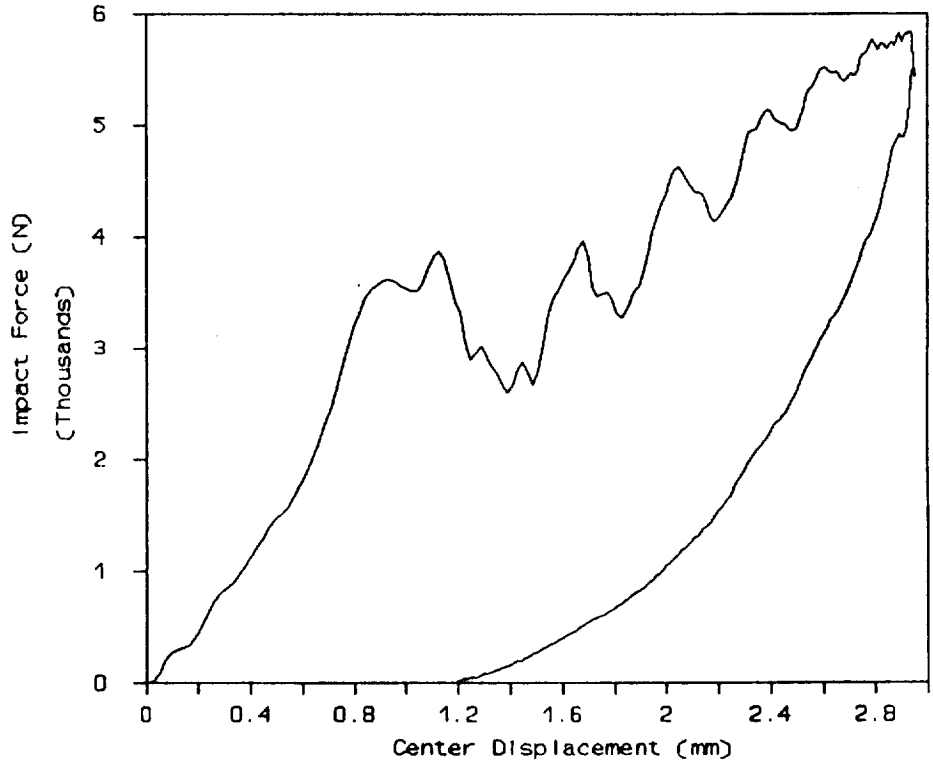

(b)

Figure E.7 Impact force history of IMPB1:(a) force vs. time and (b) force vs. displacement

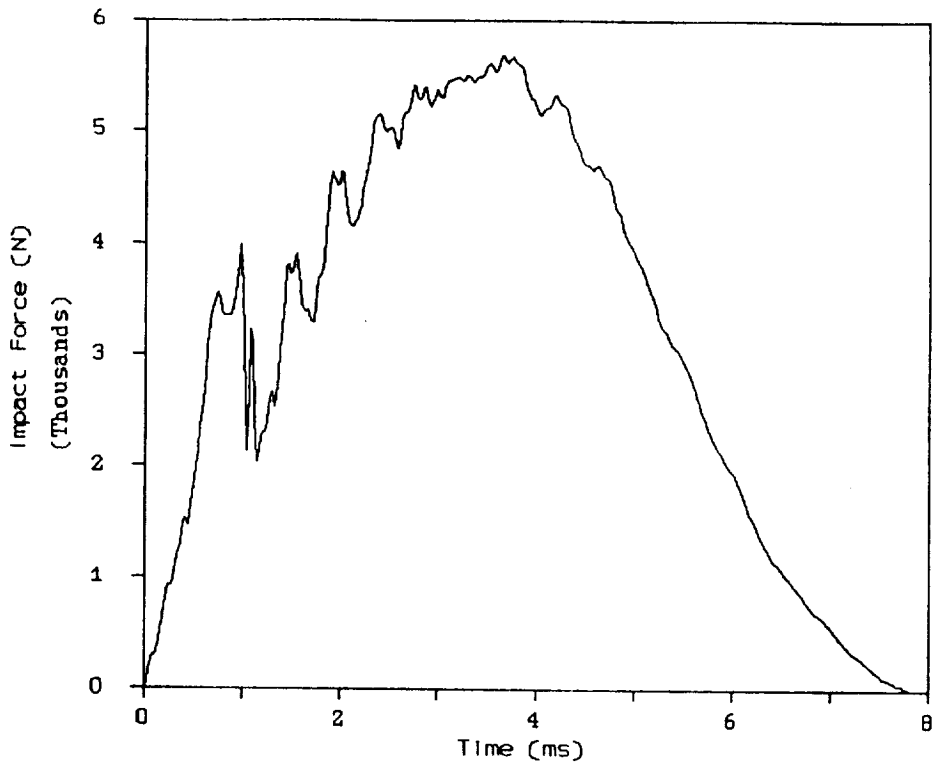

(a)

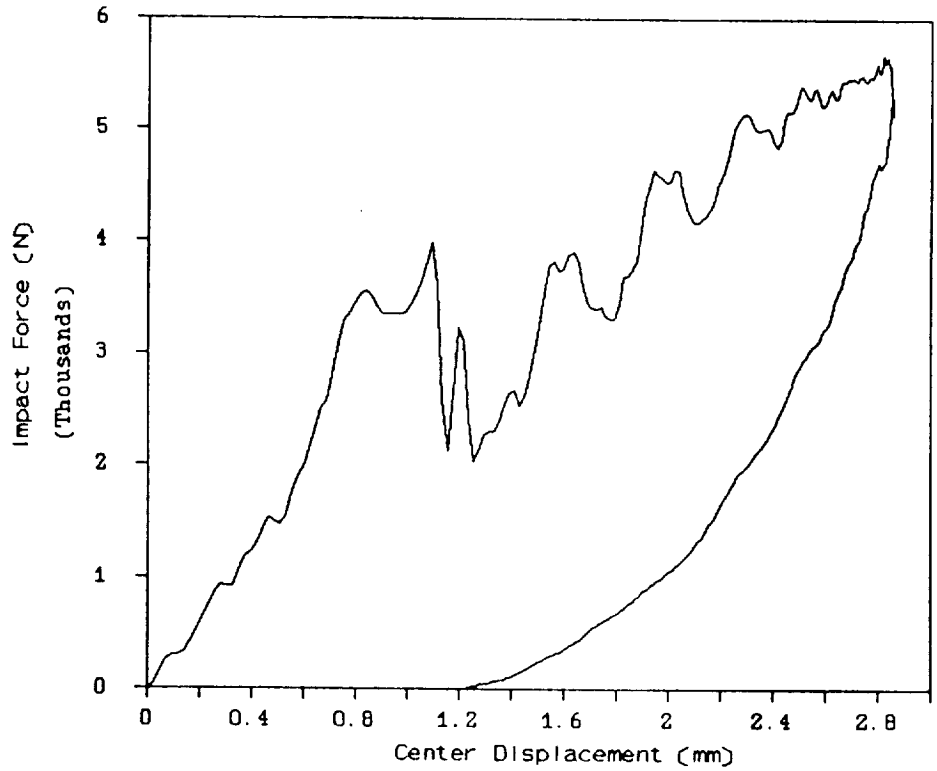

(b)

Figure E.8 Impact force history of IMPB2:(a) force vs. time and (a) force vs. d<xplacement

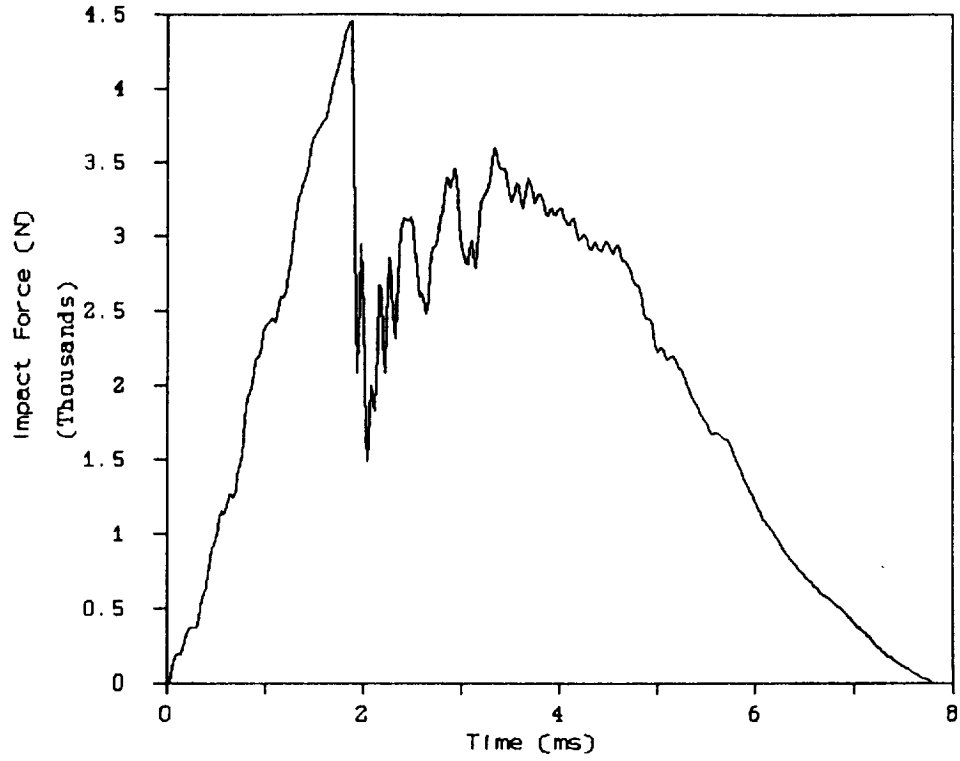

(a)

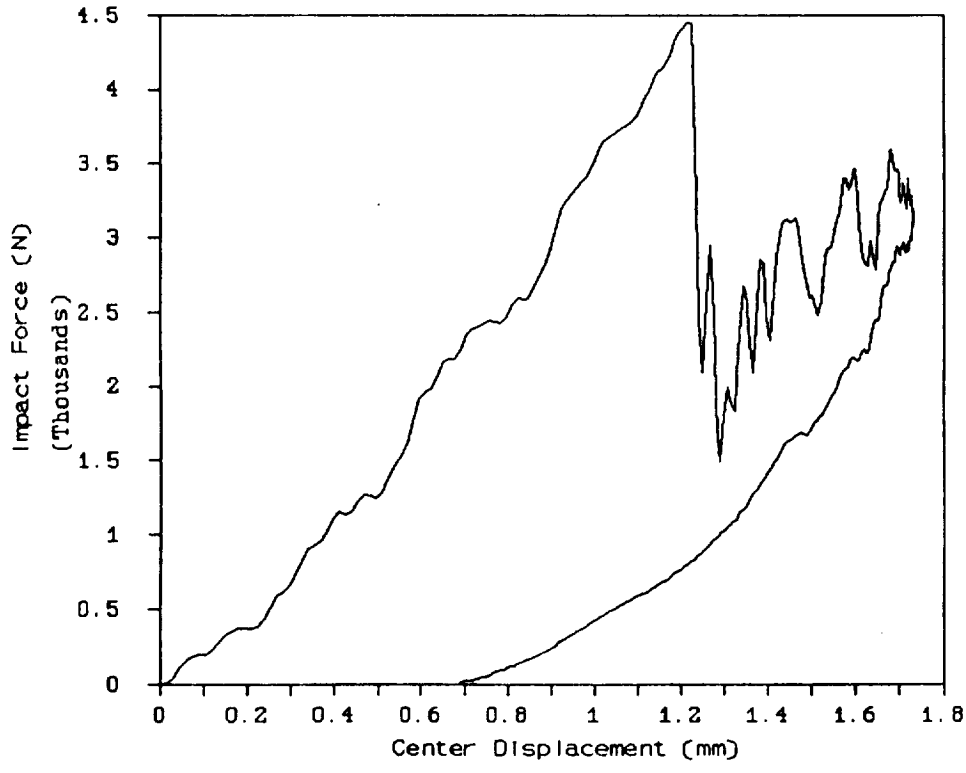

(b)

Figure E.9 Impact force history of IMPB3:(a) force vs. time and (b) force vs. displacement

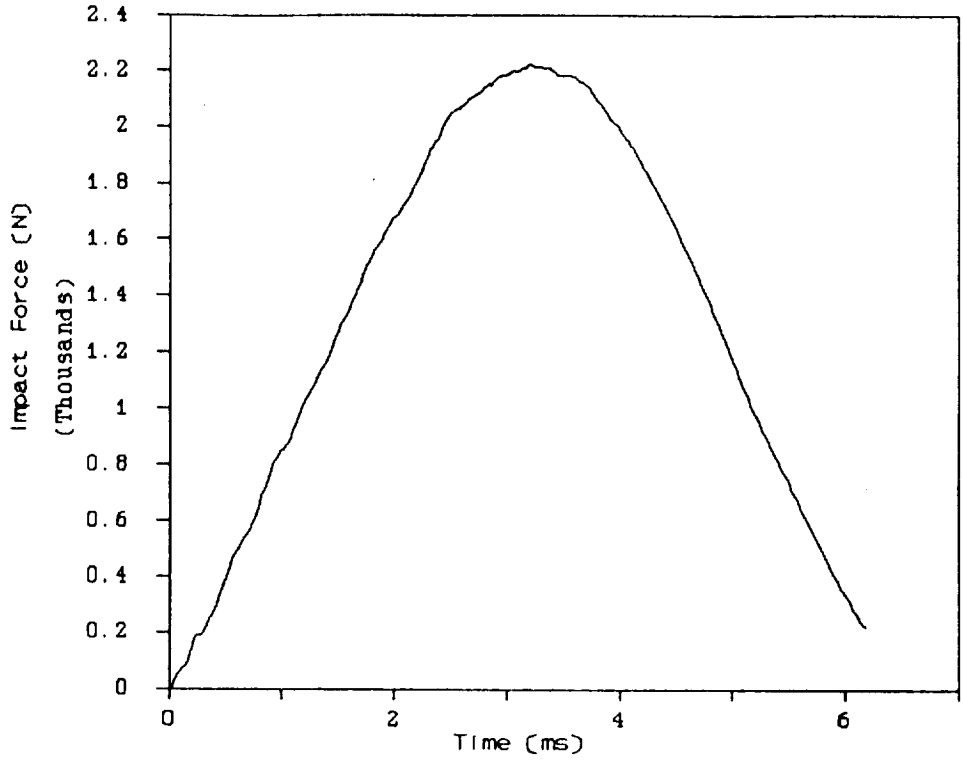

(a)

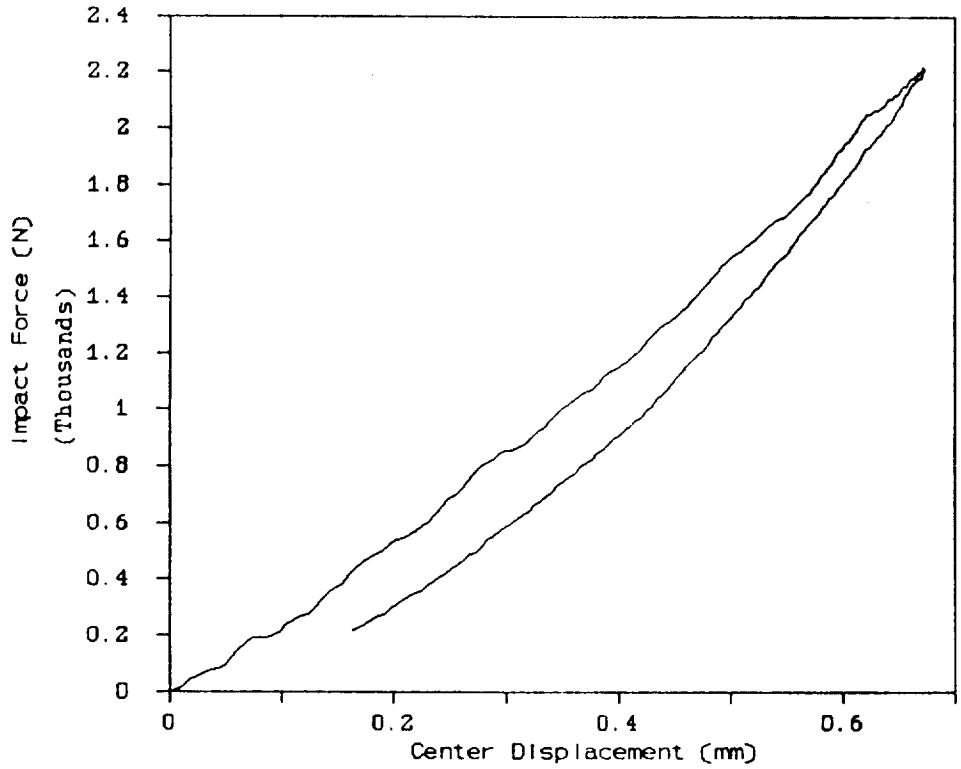

(b)

Figure E.10 Impact force history of IMPB5:(a) force vs. time and (b) force vs. displacement

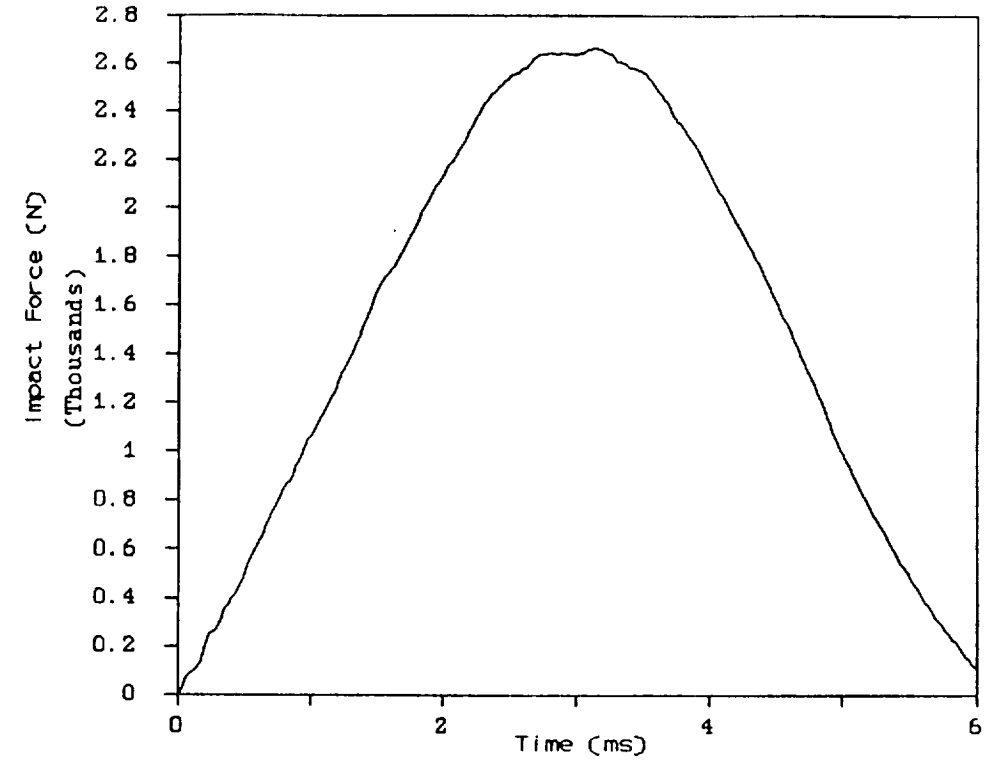

(a)

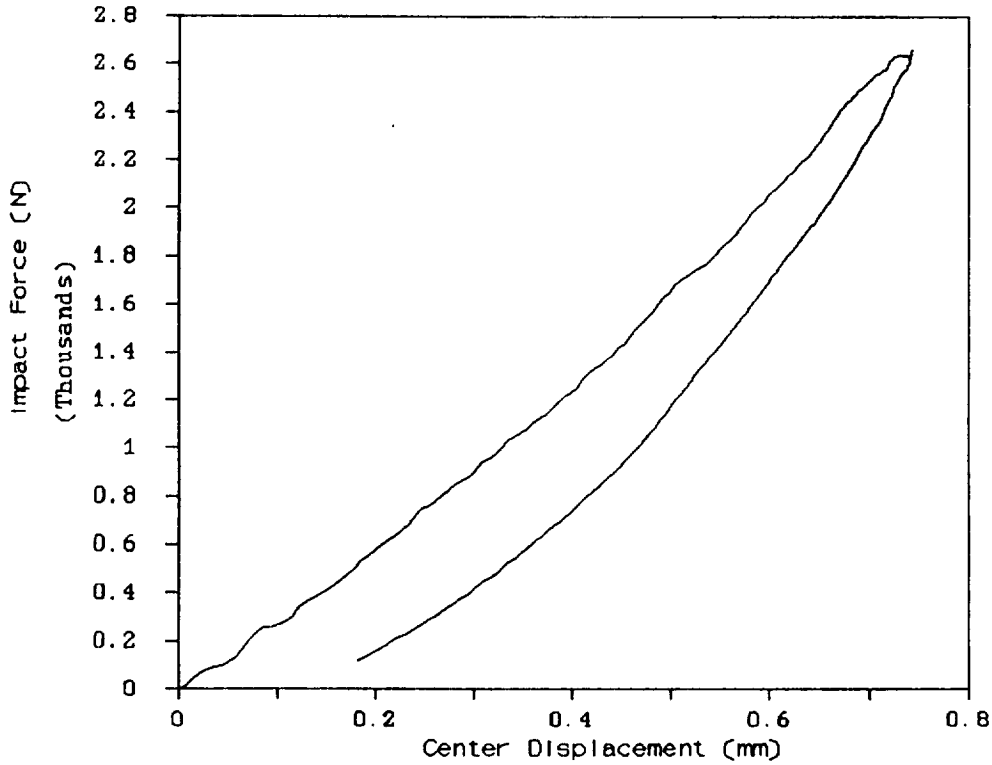

(b)

Figure E.11 Impact force history of IMPB6:(a) force vs. time and (b) force vs. displacement

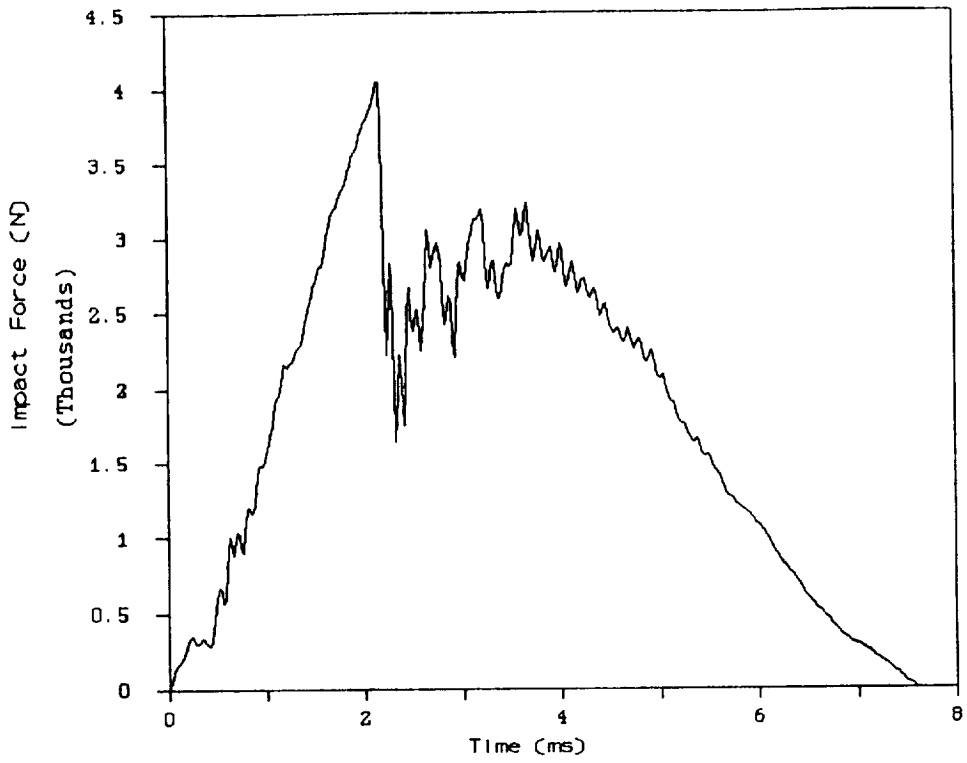

(a)

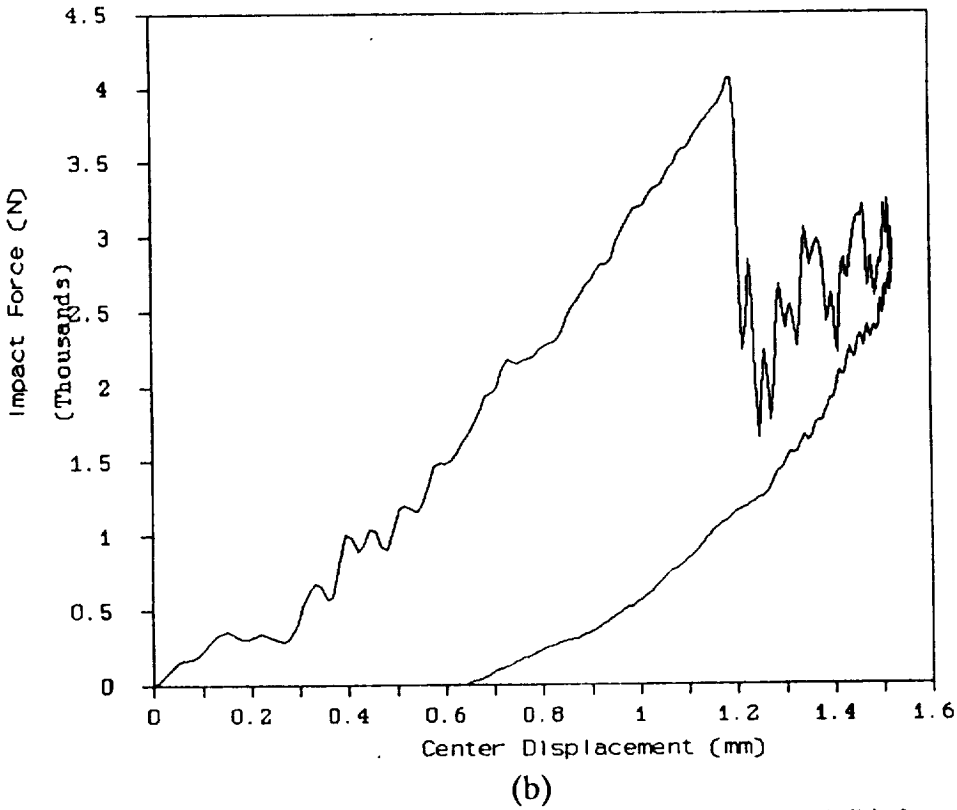

(b)

Figure E.12 Impact force history of IMPB8:(a) force vs. time and (b) force vs. displacement

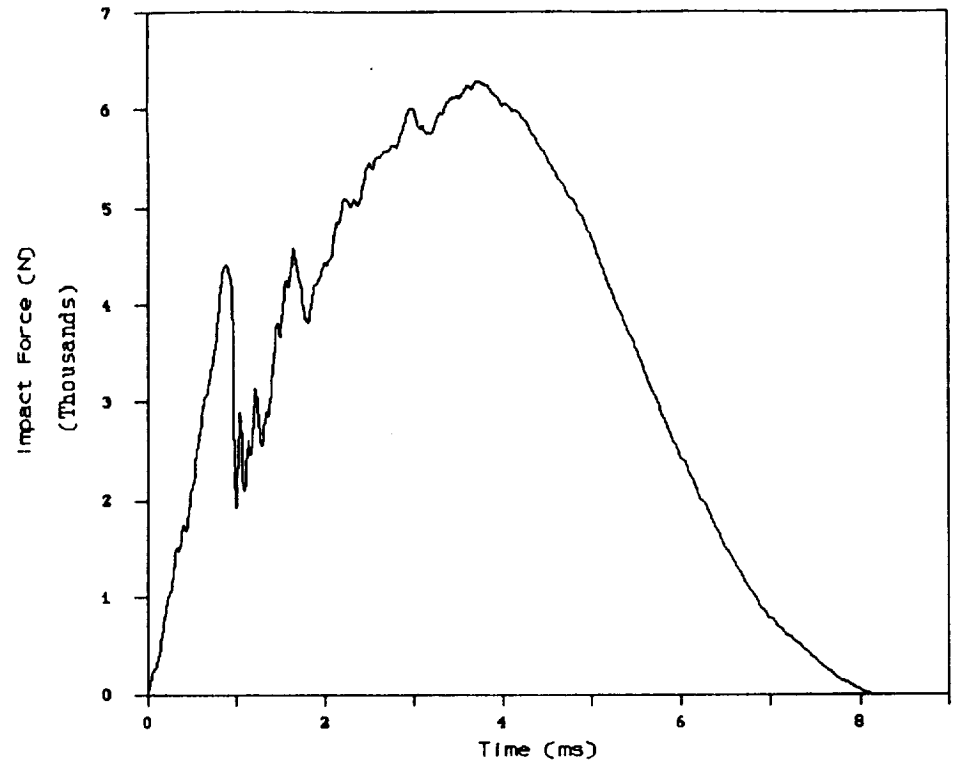

(a)

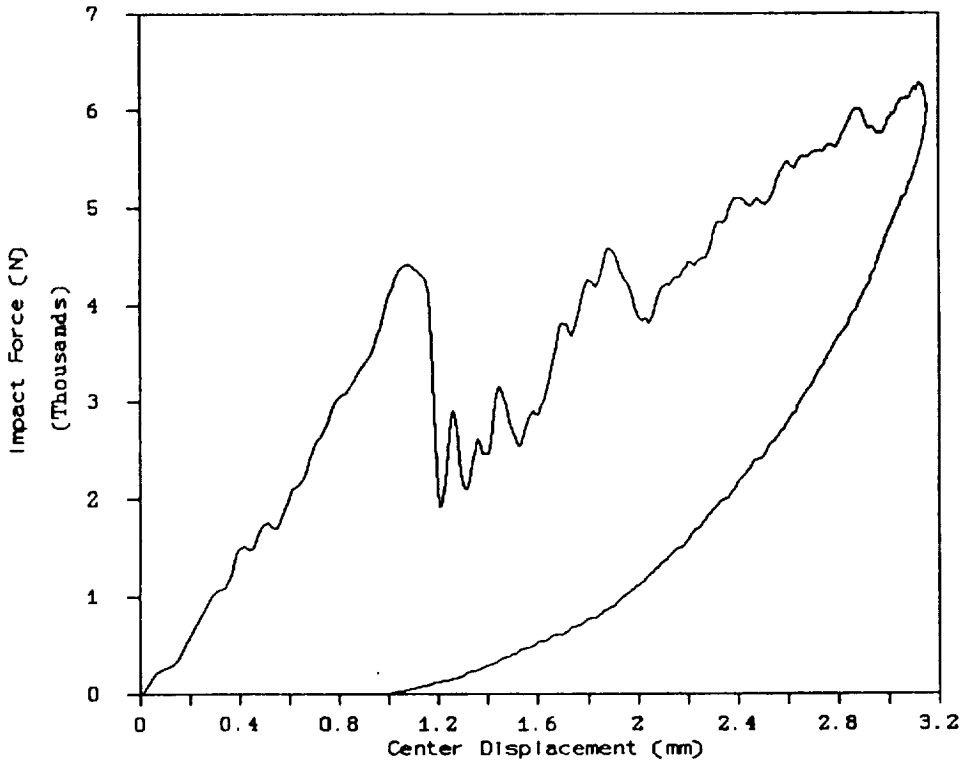

(b)

Figure E.13 Impact force history of IMPB9:(a) force vs. time and (b) force vs. displacement

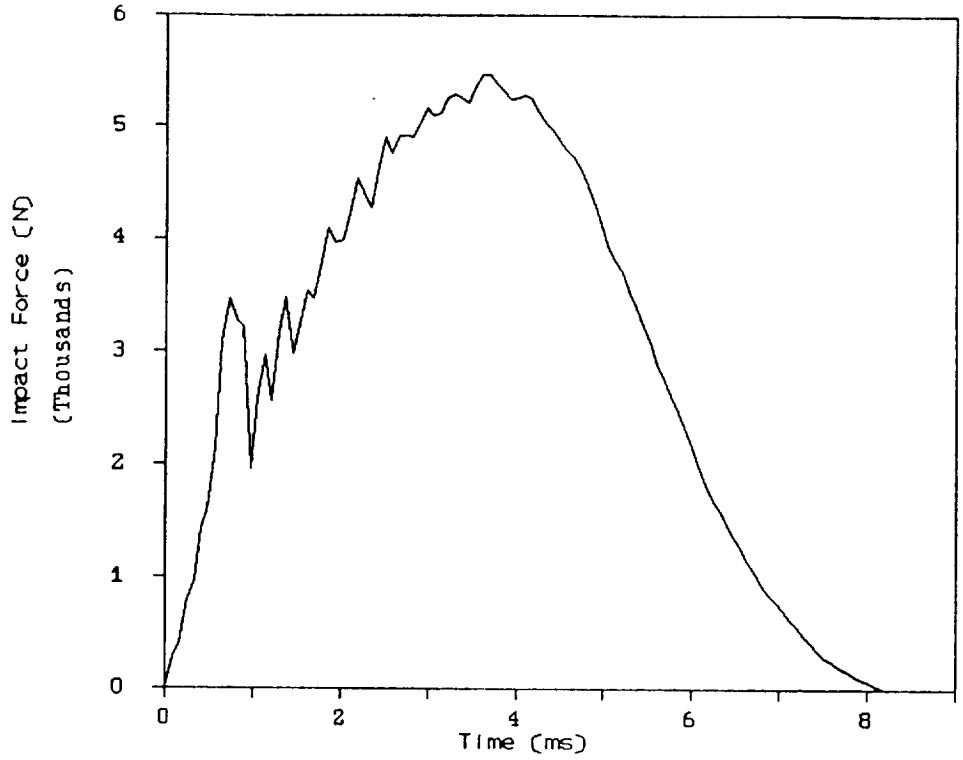

(a)

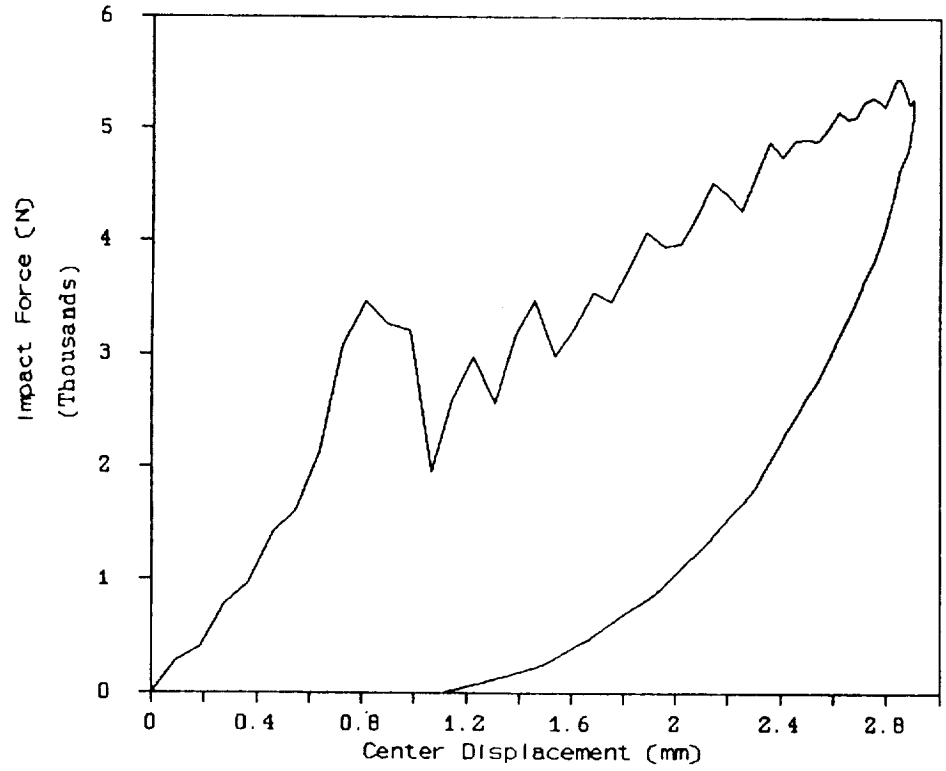

(b)

Figure E.14 Impact force history of IMPC1:(a) force vs. time and (b) force vs. displacement

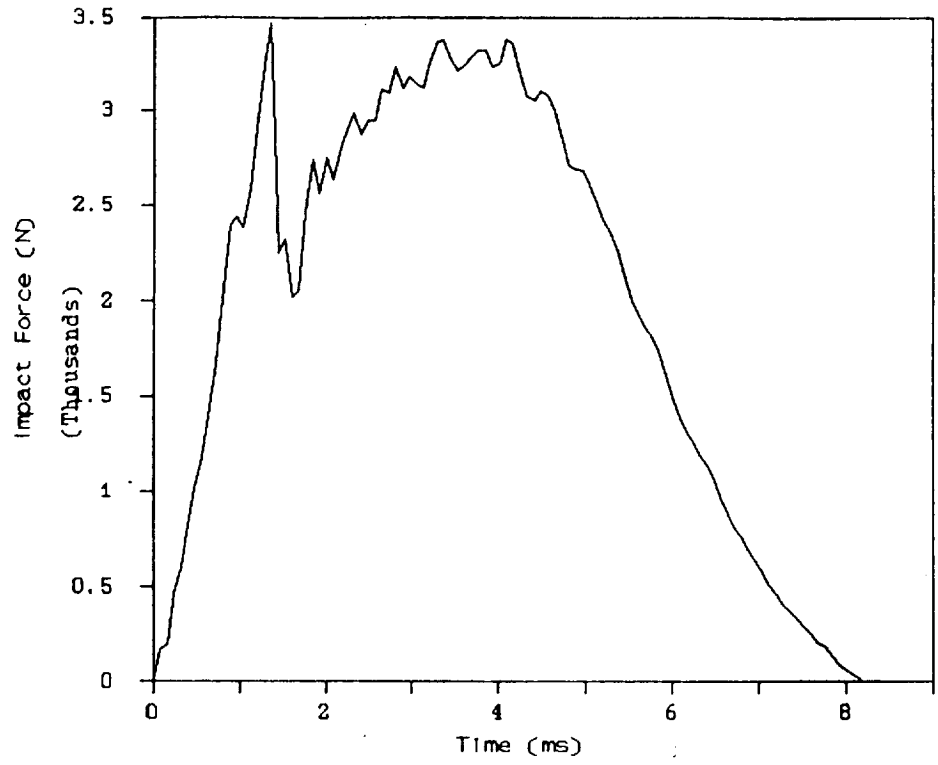

(a)

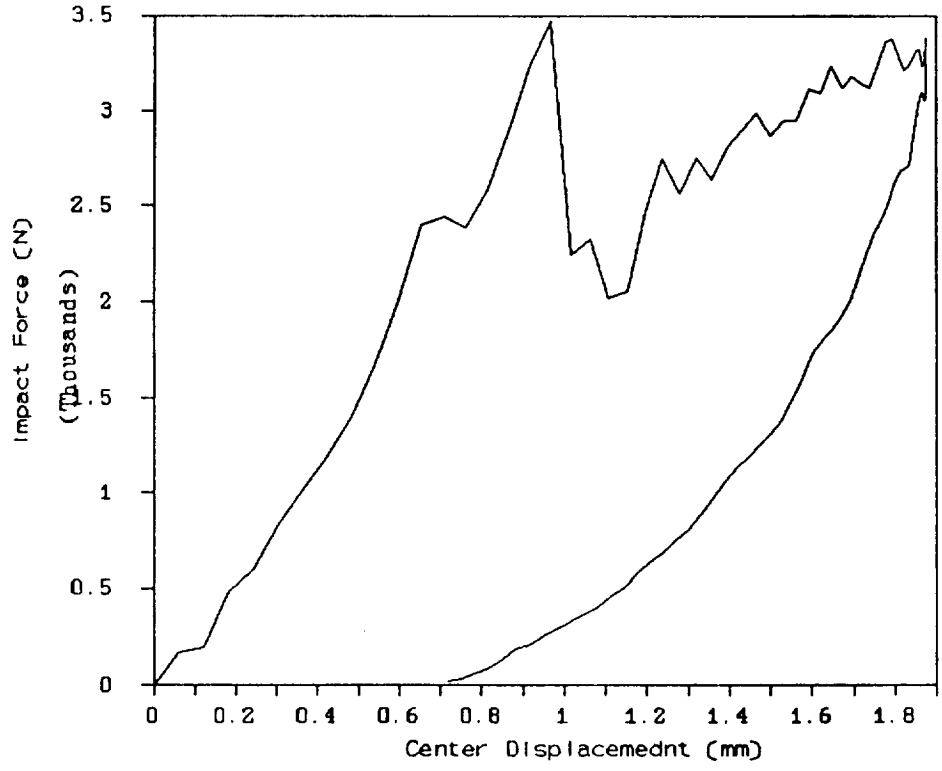

(b)

Figure E.15 Impact force history of IMPC2:(a) force vs. time and (b) force vs. displacement

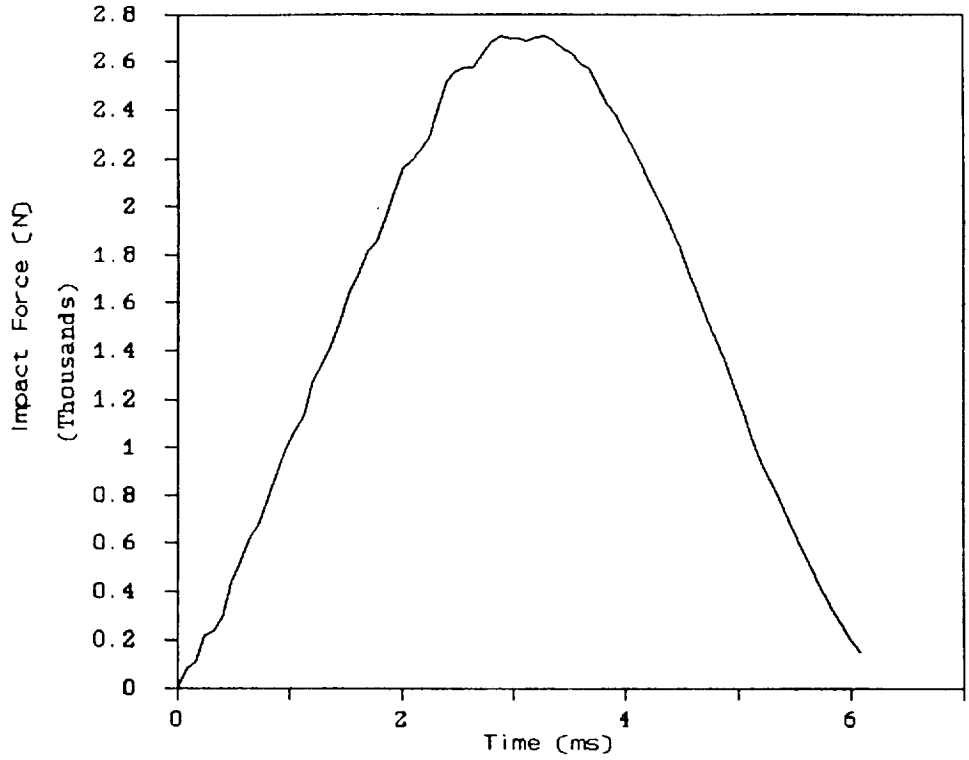

(a)

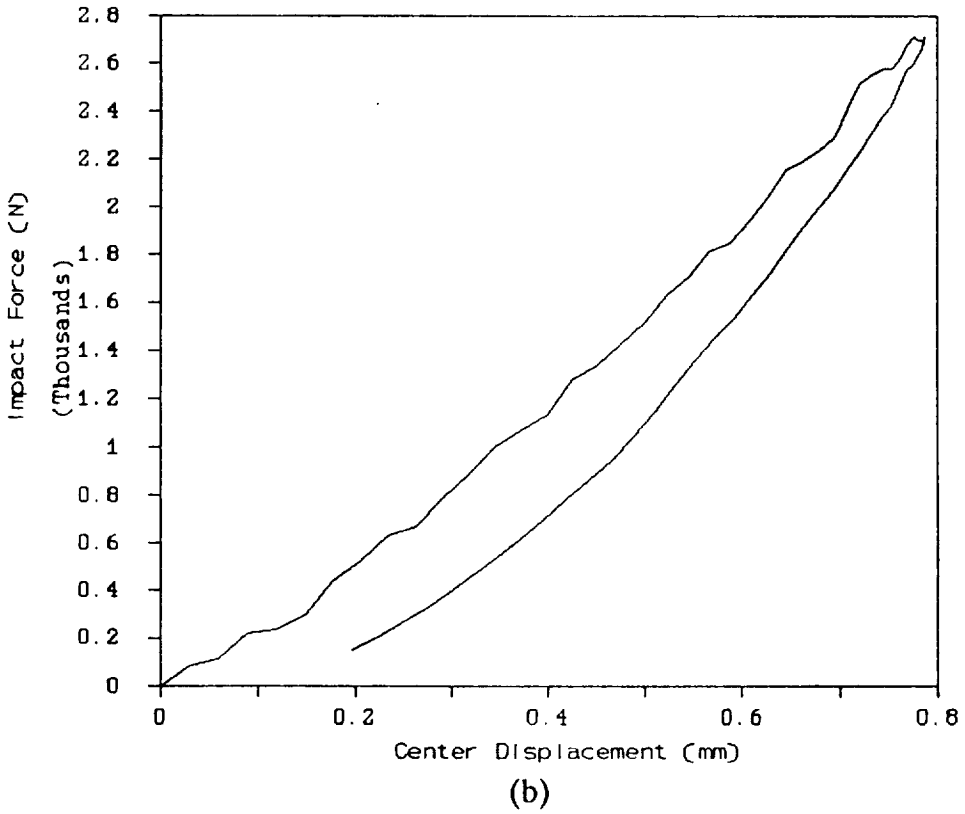

(b)

Figure E.16 Impact force history of IMPC3:(a) force vs. time and (b) force vs. displacement

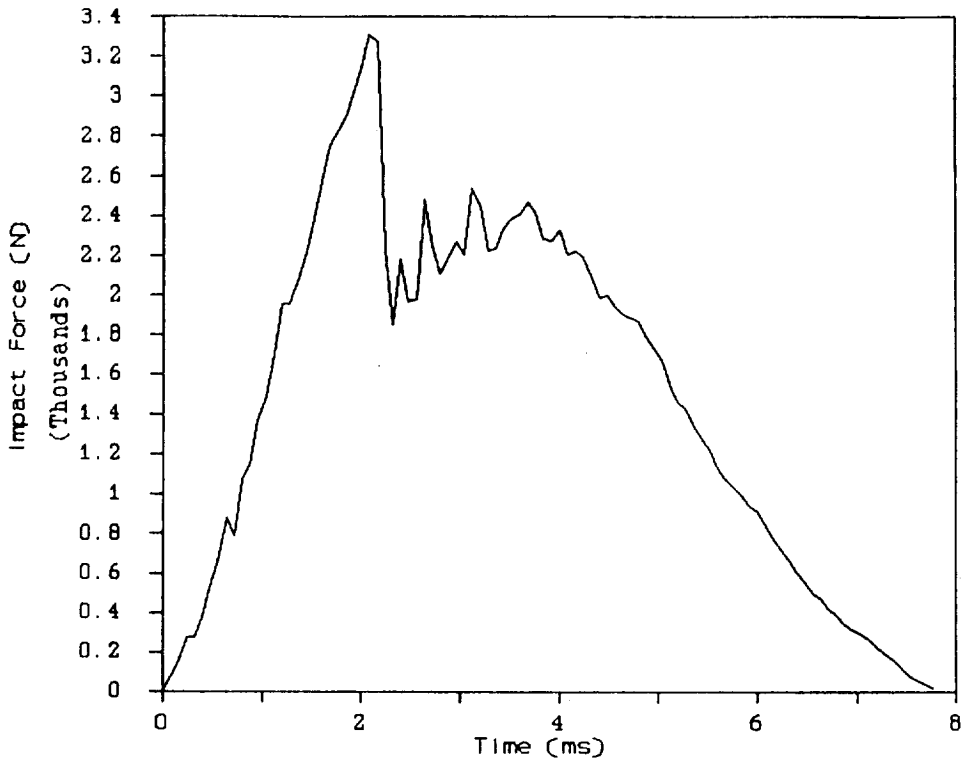

(a)

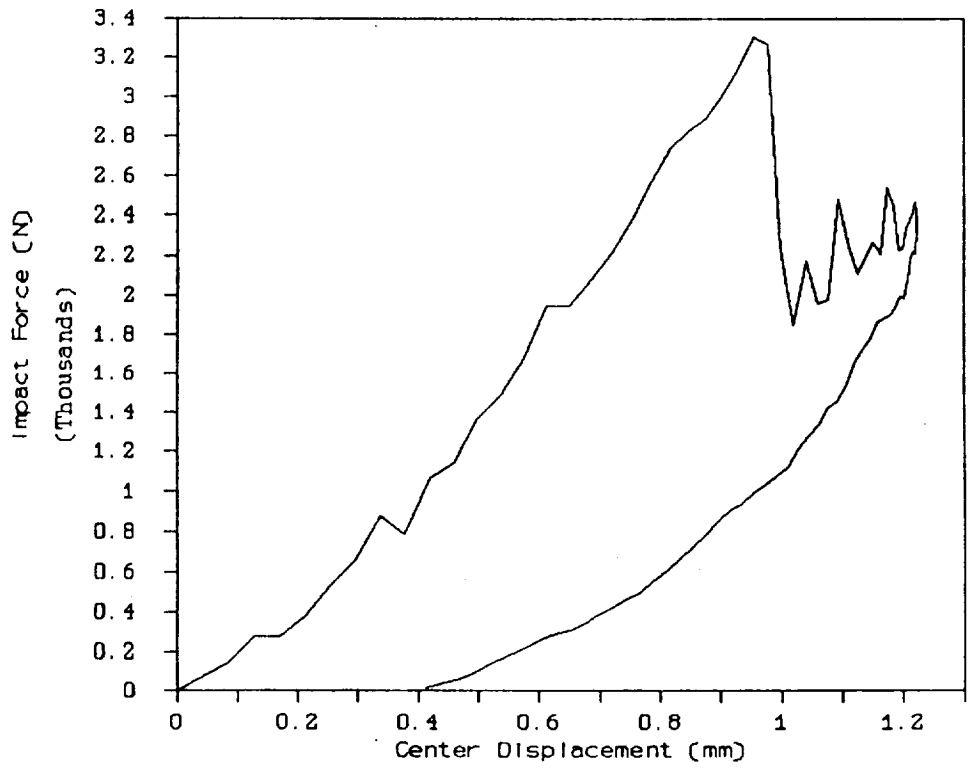

(b)

Figure E.17 Impact force history of IMPC4:(a) force vs. time and (b) force vs. displacement

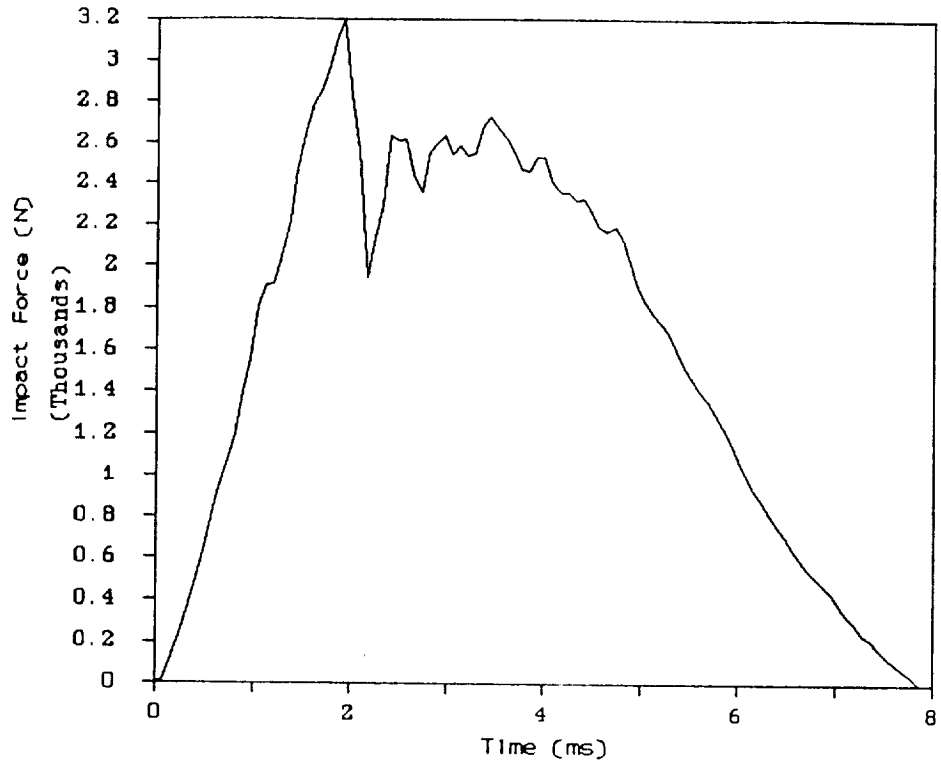

(a)

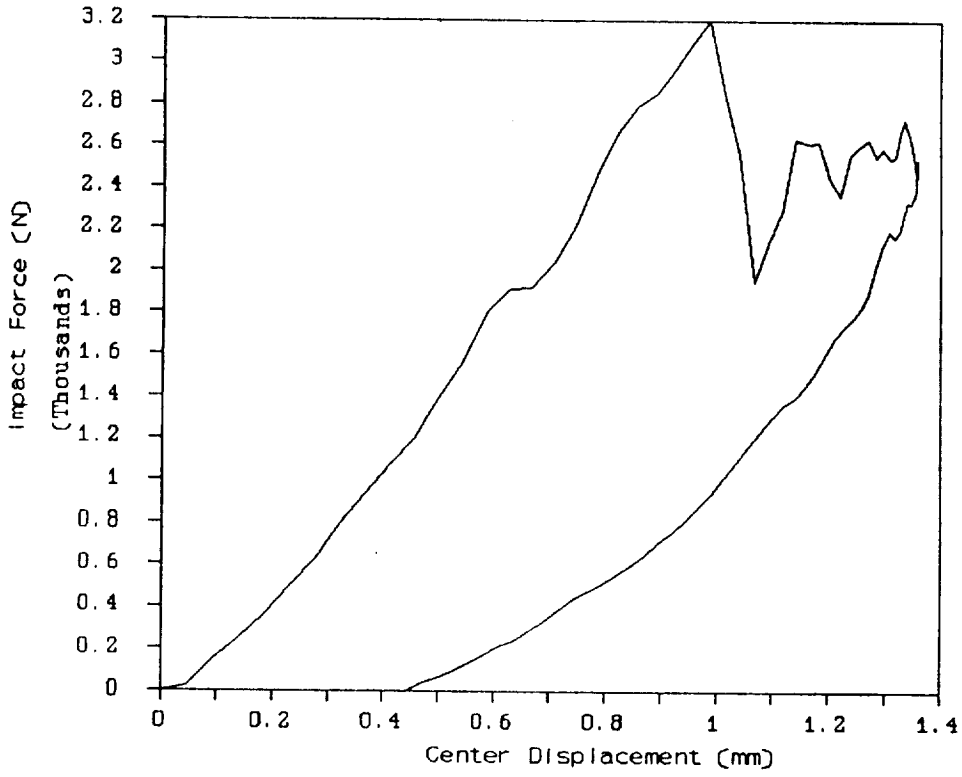

(b)

Figure E.18 Impact force history of IMPC5:(a) force vs. time and (b) force vs. displacement

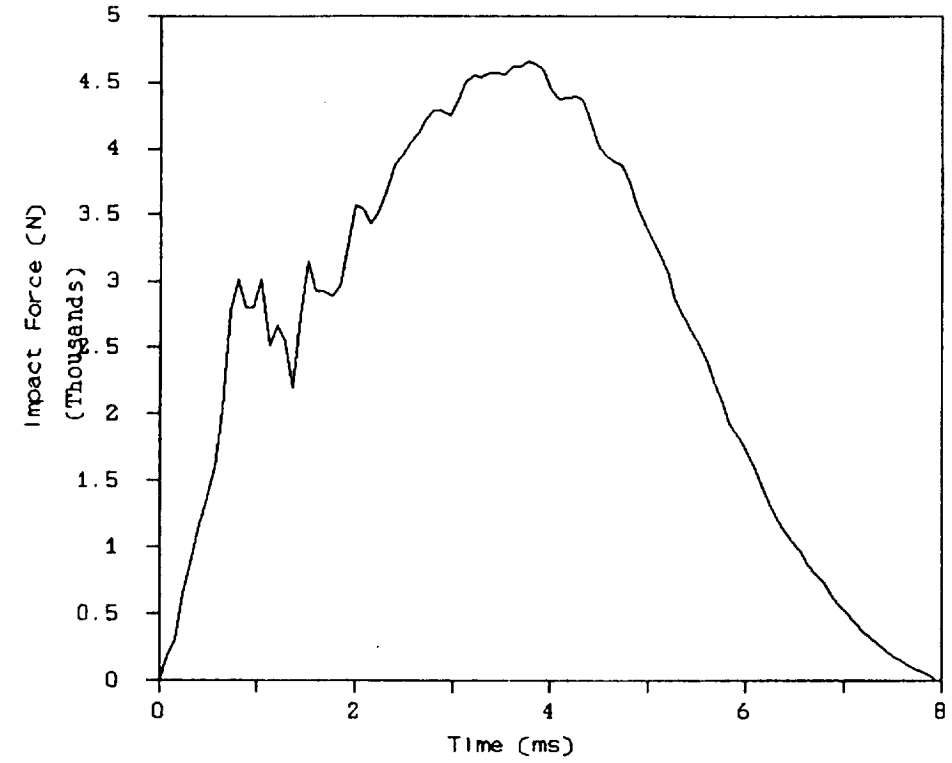

(a)

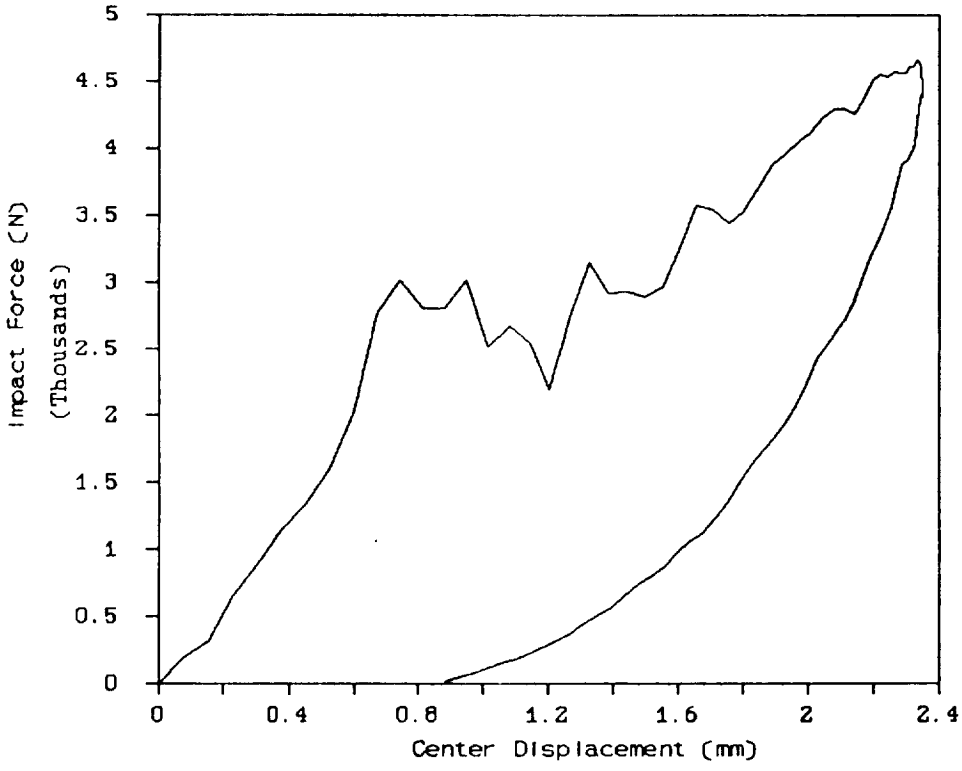

(b)

Figure E.19 Impact force history of IMPC6:(a) force vs. time and (b) force vs. displacement

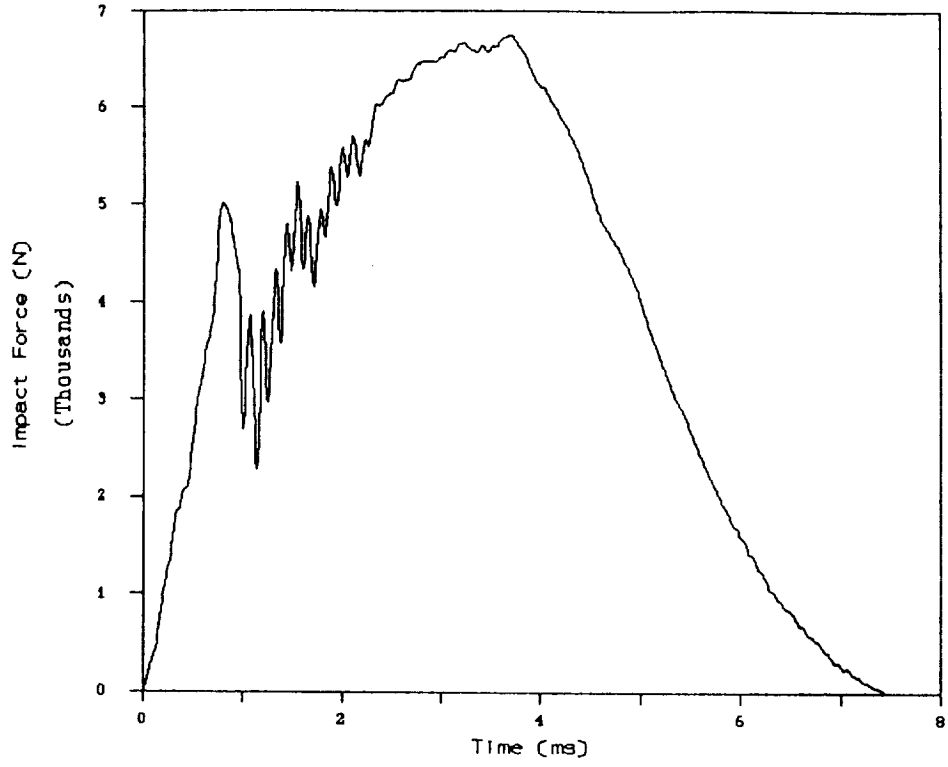

(a)

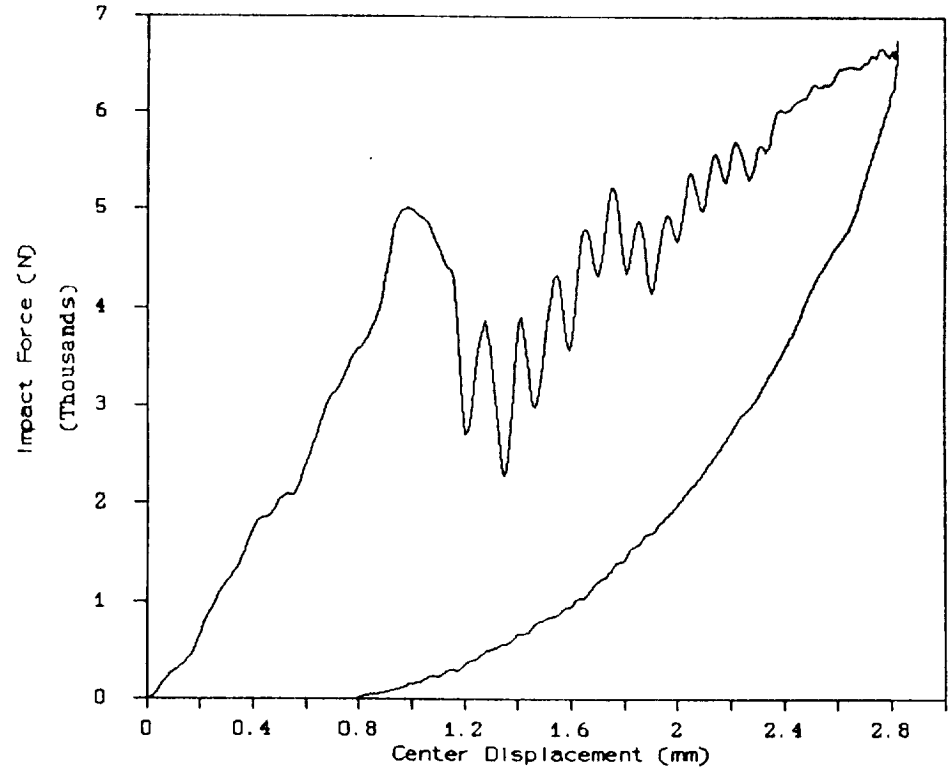

(b)

Figure E.20 Impact force history of IMPC7:(a) force vs. time and (b) force vs. displacement

REFERENCES

ASTM Designation: D 3039-76, "Standard Test Method for Tensile Properties of Fiber-Resin Composites," ASTM Standards and Literature References for Composite Materials, American Society for Testing and Materials, Philadelphia, 1987, pp. 35-40.

Bostaph G. M., and Elber, W., "Static Indentation Tests on Composite Plates for Impact Susceptibility Evaluation," Proceedings of the Army Symposium on Solid Mechanics, AMMRC MS 82-4, U.S. Army, Sept. 1982, pp. 288-317.

Dost, E. F., Ilcewicz, L. B., and Gosse, J. H., "Sublaminate Stability Based Modeling of Impact-Damaged Composite Laminates," Proceedings of the American Society for Composites 3rd Technical Conference, Seattle, Washington, September 1988, pp. 354-363.

Ireland, D. R., "Procedures and Problems Associated with Reliable Control of the Instrumented Impact Test," ASTM STP 563, 1974, pp. 3-29.

McConnell, V. P., "Composites after Defense: Where are the Opportunities?," Advanced Composites, Vol. 6, No.1, 1991, pp. 24-30.

Pinheiro, M. A. S., "Finite Elements for Free Edge Delaminations and Delaminated Anisotropic Beams," Ph.D Dissertation, University of Florida, Gainesville, Florida, 1991

Sankar, B. V., "Contact Law for Transversely Isotropic Materials," Proceedings of AIAA/ASME/ASCE/AHS 26th SDM conference, Orlando, Florida, 1985, pp. 516-521.

Sankar, B. V., "Interlaminar Shear Stresses in Composite Laminates Due to Static Indentation," J. Reinforced Plastics and Composites, Vol. 8, 1989, pp. 458-471.

Sankar, B. V., Ku, C., and Nguyen, P. T., "Nondimensional Impact Models for Composite Laminates," Proceedings of the American Society for Composites 5th Technical Conference, E. Lansing, Michigan, June 1990, pp. 600-610.

Sjöblom, P. O., Hartness, J. T., and Cordell, T. M., " On Low-Velocity Impact Testing of Composite Materials," J. Composite Materials, Vol. 22, 1988, pp. 30-52.

Timoshenko, S., and Woinowsky-Krieger, S., Theory of Plates and Shells, McGraw-Hill, New York, 1959.

REPORT DOCUMENTATION PAGE

Form Approved
OMB No. 0704-0188

1. AGENCY USE ONLY (Leave blank)	2. REPORT DATE	3. REPORT TYPE AND DATES COVERED
	March 1992	Contractor Report

4. TITLE AND SUBTITLE
Indentation-Flexure and Low-Velocity Impact Damage in Graphite/Epoxy Laminates

5. FUNDING NUMBERS
NAG-1-826
505-63-50-04

6. AUTHOR(S)
Young S. Kwon and Bhavani V. Sankar

7. PERFORMING ORGANIZATION NAME(S) AND ADDRESS(ES)
University of Florida
Department of Aerospace Engineering
Mechanics & Engineering Science
231 Aerospace Building
Gainesville, FL 32611-2031

8. PERFORMING ORGANIZATION REPORT NUMBER

9. SPONSORING / MONITORING AGENCY NAME(S) AND ADDRESS(ES)
National Aeronautics and Space Administration
Langley Research Center
Hampton, VA 23665-5225

10. SPONSORING / MONITORING AGENCY REPORT NUMBER
NASA CR-187624

11. SUPPLEMENTARY NOTES
Langley Technical Monitor: Wade C. Jackson

12a. DISTRIBUTION / AVAILABILITY STATEMENT
Unclassified-Unlimited

Subject Category 24

12b. DISTRIBUTION CODE

13. ABSTRACT *(Maximum 200 words)*

Static indentation and low-velocity impact tests were performed on quasi-isotropic and cross-ply graphite/epoxy composite laminates. The load-deflection relations in static tests and impact force history in the impact tests were recorded. The damage was assessed by using ultrasonic C-scanning and photo-micrographic techniques. The static behavior of the laminates and damage progression during loading, unloading, and reloading were explained by a simple plate delamination model. A good correlation existed between the static and the impact responses. It was found that results from a few static indentation-flexure tests can be used to predict the response and damge in composite laminates due to a class of low-velocity impact events.

14. SUBJECT TERMS	15. NUMBER OF PAGES
Indentation damage, Impact damage, Composite laminates, Graphite/epoxy; Delamination	171
	16. PRICE CODE A08

17. SECURITY CLASSIFICATION OF REPORT	18. SECURITY CLASSIFICATION OF THIS PAGE	19. SECURITY CLASSIFICATION OF ABSTRACT	20. LIMITATION OF ABSTRACT
Unclassified	Unclassified		